
# Flashback Detection and Suppression in Reheat Hydrogen Combustor

Master of Science Thesis Report

Mihnea Floris

TU Delft

# Flashback Detection and Suppression in Reheat Hydrogen Combustor

Master of Science Thesis Report

by

Mihnea Floris

Supervisors: Dr. A. K. Doan
Dr. I. Langella
Student number: 4663675

Faculty of Aerospace Engineering · Delft University of Technology

# Preface

I would like to express my sincere gratitude to my thesis supervisors, Dr. Anh Khoa Doan and Dr. Ivan Langella, for providing me with their guidance, expertise and valuable insights throughout the duration of this project. I would also like to thank them for giving me the opportunity to work on this exciting project, which has been a insightful journey. Their support has enriched my experience, influencing my academic and professional growth. Additionally, I would like to extend my gratitude to Dr. Konduri Aditya, Tadikonda Shiva Sai, and Dibyajyoti Nayak for their valuable insights and expertise. Our collaboration on the academic paper we published together was an integral part of this journey, enriching my understanding and contributing to the field.

I would also like to thank all of my friends here in Delft that have been with me throughout my whole journey, starting with the very first year of the Bachelor, all the way to the end of our studies, and all of those who came along the way. They have been there to help me in my academic journey, engaging in countless discussions from which we have learned together. Most importantly though, I would like to thank them for their support and the fun times we have shared together, as well as all of the experiences we have been through, which have shaped me throughout the years and made my time in Delft unforgettable. I am sure we will continue making memories for years to come.

Lastly, I would like to thank my parents, my brother and my girlfriend for their unwavering support throughout the years. They have made this journey possible and they have been there for me through thick and thin, for which I am most grateful.

# Abstract

This research contributes to addressing climate change challenges through the examination of hydrogen combustion. It investigates the flow dynamics within a simplified model of Ansaldo Energia's GT36 reheat combustor using Large Eddy Simulation (LES) at a high pressure of 20 bar, focusing on the autoignition flashback phenomena observed. More specifically, it explores predicting the apparition of this event through the use of a modularity-based clustering algorithm and its subsequent suppression by using water injection.

In the LES simulation, lean, premixed and high-pressure conditions are used, revealing an unsteady behaviour in the flame dynamics, i.e. an autoignition event in the mixing duct which repeats itself due to high-amplitude pressure waves and their subsequent convergence in the mixing duct. Using this simulation, time-series of multiple variables are acquired over the course of 8 flashback events. These variables are then pruned using a co-kurtosis PCA based dimensionality reduction technique. This method, by measuring the joint occurrence of outliers in the flow variables, identifies successfully which are the most important variables ($T$, $\rho$, $P$, $V_x$, $Y_{\mathrm{HO}_2}$ and $Y_{\mathrm{OH}}$) that introduce a lasting change in the system and are potentially useful in finding a precursor to the flashback event.

The time-series of these variables are then introduced in the modularity-based clustering algorithm. This algorithm tessellates the phase space of the system and then transforms it into a graph, thus retaining the information about the dynamics of the system. Then, it clusters this graph using a metric called modularity. The method proves effective in finding a precursor for the autoignition event, resulting in an average prediction time for the 8 flashback events of $t_{pred} = 32.12$ $\mu$s, which is over 50% of the time that the combustor is in the normal operating state. Furthermore, the algorithm performs very well in the number of false positives, and, due to a change made to the algorithm in this study, the number of true positives is increased to 100%. The algorithm is then put through several robustness tests, which include the use of different sampling locations, less features, unseen data and relying only on temperature and pressure information sampled at the combustor walls. Here, the algorithm retained its performance, with only a small decrease in the prediction time, demonstrating its potential towards its use in an online prediction scenario. Lastly, the level of fidelity of the LES simulation was increased by using the digital filter method to simulate turbulent fluctuations at the inlet and fully-developed velocity profile, where once again it was found that the algorithm retains a good prediction time.

For the second part of this research, a flashback event and its afferent prediction time were chosen to investigate the use of water injection and its potential at suppressing the flashback when the water is injected based on the prediction time. Here, following an empirical design approach, where the Sauter Mean Diameter (SMD), the mass flow, the diameter of the nozzle, the angles of the cone were varied, a preliminary design was sought. It was found that the SMD is highly influential towards the spread of the spray, with larger particles being preferred to their ability to retain their momentum and more quickly cover the mixing duct. In addition, large angles for the cone and a high injection velocity are again necessary for a good spread and a quick response time. An attempt was also

made to place a set of sprays at the walls of the mixing duct, where it was found that the flashback event now takes place upstream of the spray due to aerodynamic blockage. The design process culminates in a setup where six spray are placed at the inlet of the mixing duct. In this setup, the spray is able to quickly cover the mixing duct and the flashback is suppressed, while also retaining an evaporation efficiency of 96.3%.

# Contents

# Nomenclature

**List of Abbreviations**

AFOLU Agriculture, forestry and other land use

AMR Automatic Mesh Refinement

ARMA Auto-Regressive Moving Averages

ATDC After Top Dead Center

Auto-ML Automatic Machine Learning

BAT Best Available Techniques

BAT-AEELs BAT-associated energy efficiency levels

BC Boundary Condition

BL Boundary Layer

CC Climate Change

CFD Computational Fluid Dynamics

CIVB Combustion Induced Vortex Breakdown

CNN Convolutional Neural Network

CoK-PCA Co-kurtosis PCA

CPSC Constant Pressure Sequential Combustion

CSD Critical Slowing Down

DFA Detrended Fluctuation Analysis

DLN Dry-Low NOx

DNS Direct Numerical Simulation

EGR Exhaust Gas Recirculation

ESN Echo State Network

FVM Finite Volume Methods

GAN Generative Adversial Networks

GE General Electric

GHGs Greenhouse Gases

GNNs Graph Neural Networks

GRUs Gated Recurrent Units

GT Gas Turbine

HHV Higher Heating Value

HMMs Hidden Markov Models

IC Internal Combustion

IEA International Energy Agency

IRZ Internal Recirculation Zone

LES Large Eddy Simulation

LHV Lower Heating Value

LODI Local 1D Invsicid

LSI Low Swirl Injector

LSTMs Long Short-Term Memory

MET Mixing Exit Temperature

MHI Mitshubishi Heavy Industries

ML Machine Learning

MSE Mean Squared Error

NN Neural Networks

NSCBC Navier-Stokes Characteristic Boundary Condition

NZE Net-zero emissions

PCA Principal Component Analysis

PDFs Probability Distribution Functions

PISO Pressure Implicit with Splitting of Operators

POD Proper Orthogonal Decomposition

RANS Reynolds-Averaged Navier-Stokes

RC Reservoir Computing

RF Radiative Forcing

RNN Recurrent Neural Network

ROC Receiver Operating Characteristic Curve

SCR Selective Catalytic Reduction

SGS Sub-Grid Scale

SMD Sauter Mean Diameter

SOR Successive Over-Relaxation

SVD Singular Value Decomposition

TCNs Temporal Convolutional Networks

TFM Thickened Flame Model

UN United Nations

UNFCCC United Nation Framework Convention on Climate Change

WLE Wet Low Emissions

WPD Wavelet Package Decomposition

**List of Symbols**

$t$ Time

$\alpha$ Thermal Diffusivity

$\beta$ Volume Expansion Coefficient

$\Delta P$ Pressure Differential

$\Delta$ Cut-off Size

$\delta$ Kronecker Delta

$\delta_l$ Laminar Flame Thickness

$\dot{\omega}_k$ Reaction Rate of Species k

$\dot{m}$ Mass Flow

$\dot{Q}$ Heat Transfer Rate

$\epsilon_{sub}$ Subgrid Rate of Dissipation

$\eta_{ther}$ Thermal efficiency

$\mathcal{J}_j^k$ Molecular Diffusive Flux

$\mu$ Dynamic Viscosity

$\mu_L$ Liquid viscosity

$\omega$ Oscillation Frequency

$\phi$ Equivalence Ratio

$\Psi_{tol}$ Tolerance Threshold

$\rho$ Density

$\rho_a$ Ambient Density

$\rho_L$ Liquid Density

$\sigma$ Surface Tension

$\tau_k$ Kolmogorov Time Scale

$\tau_t$ Turbulence Time Scale

$\tau_{i,j}$ Viscous force tensor

$\tau_{ign}$ Autoignition delay time

$A_0$ Spray Outlet Area

| | |
|---|---|
| $C_D$ | Discharge Coefficient/ Drag Coefficient |
| $c_p$ | Specific Heat at Constant Pressure |
| $d_0$ | Spray outlet diameter |
| $Da$ | Damköhler Number |
| $E_a$ | Activation energy |
| $F$ | LES Filter |
| $F_i$ | Body Force |
| $F_{drag}$ | Drag Force |
| $h$ | Enthalpy |
| $h$ | Liquid Sheet Thickness |
| $k$ | Kinetic Energy |
| $k_{sub}$ | Subgrid Turbulent Kinetic Energy |
| $Ka$ | Karlovitz Number |
| $l_0$ | Spray Orifice Length |
| $l_k$ | Kolmogorov Integral Scale |
| $l_t$ | Turbulence Integral Scale |
| $Le$ | Lewis Number |
| $M_{coll}$ | Number of Collisions |
| $Nu$ | Nusselt Number |
| $P$ | Pressure |
| $Q_F$ | Total Calorific Value of the Fuel |
| $r_i$ | Particle Radius |
| $r_{32}$ | Sauter Mean Diameter |
| $Re$ | Reynolds Number |
| $S_L$ | Laminar flame speed |
| $S_T$ | Turbulent flame speed |
| $Sh$ | Sherwood Number |
| $T$ | Temperature |
| $t\tau_c$ | Combustion Time Scale |
| $t_d$ | Turbulent Correlation Time |
| $T_{in}$ | Inlet Temperature |
| $U$ | Axial Velocity |
| $u'$ | Velocity fluctuations |
| $u_k$ | Kolmogorov Velocity |
| $V$ | Cell Volume |
| $V$ | Tangential Velocity |
| $V$ | Velocity |
| $V_n$ | Velocity Normal to the Surface |
| $v_{inj}$ | Injection Velocity |
| $y$ | Drop distortion |
| $Y_k$ | Mass Fraction of species K |
| FN | Flow Number |
| N | Number of Droplets |
| Pr | Prandtl Number |
| Sc | Schmidt Number |
| We | Weber Number |

# List of Figures

# List of Tables

# 1

# Introduction

## 1.1. Overview

Over the past century, the surface air temperature has increased by 1°C, leading to the warmest period in the history of modern civilization. This apparently insignificant difference gives rise to a series of phenomena such as: extreme weather events, melting of the ice sheets, the displacement of natural habitats and ocean acidification. The review done by Abbass et al. [1] highlights the negative consequences of climate change (CC) on the viability of different industries worldwide.

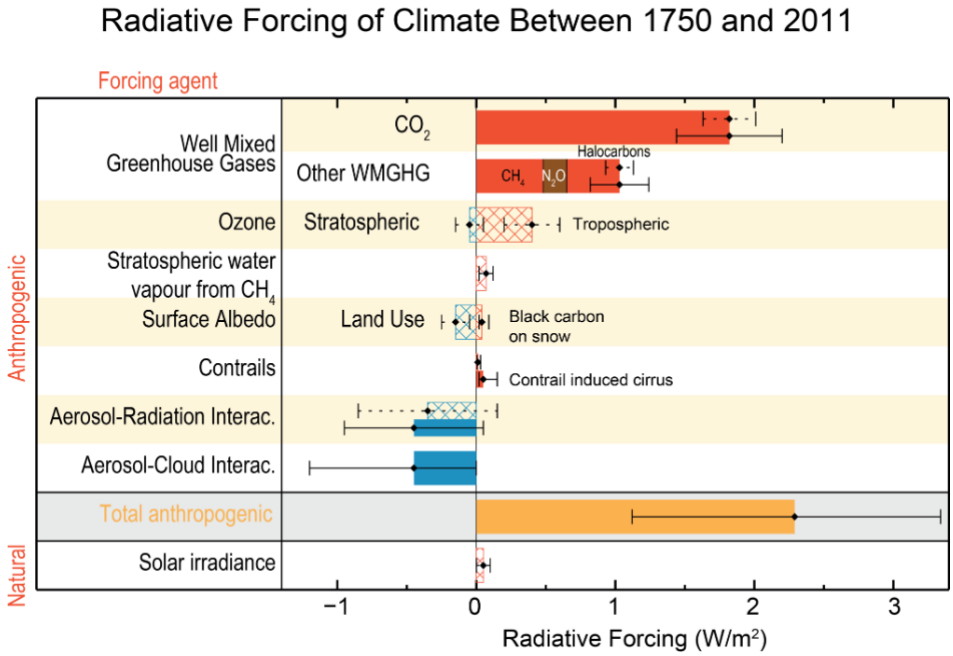


**Figure 1.1:** Radiative forcing (RF; hatched) and effective radiative forcing (ERF; solid) between 1750–2011. Uncertainties (5% to 95% confidence range) are given for RF (dotted lines) and ERF (solid lines) [2].

The thermal balance of the Earth is maintained through the absorption and reflection of sunlight, the emission of outgoing infrared radiation, and the absorption and subsequent re-emission of infrared radiation by the atmosphere, a process influenced by the presence of greenhouse gases (GHGs). Using radiative forcing (RF) as a metric, which is the

instantaneous change in net radiative flux following a change in a climate factor, the assessment done by Wuebbles et al. [2] concludes that it is this increase in GHGs, primarily caused by human activities, that is the main driving force of the observed warming and related phenomena (Figure 1.1).

The world's countries began their efforts to combat the GHG emissions in 1992 with the adoption of the UN Framework Convention on Climate Change (UNFCCC), which in turn lead to the Kyoto protocol and later to the Paris Agreement of 2015 [3], the most relevant climate action protocol to date. The Paris Agreement is a treaty that was adopted by 194 countries and it has the main objective of limiting the increase of global average temperatures to less than 2°C as compared to the pre-industrial era. Within this framework, each participating country submits their National Determined Contributions (NDCs), which are specific commitments of reducing GHG emissions across the different contributing industrial sectors. In 2018, the largest portion of global emissions came from the energy sector with 34%, followed by industry (production of metals, chemicals, cement and others) with 24%, agriculture, forestry and other land use (AFOLU) (21%), transport (14%) and the operation of buildings (6%) [4], where the yearly trend can be observed in Figure 1.2. With these unfavourable trends in mind, it is clear that radical solutions and technologies have to be researched and implemented. One such technology that could help alleviate the demands of the energy sectors is the hydrogen powered gas turbine.

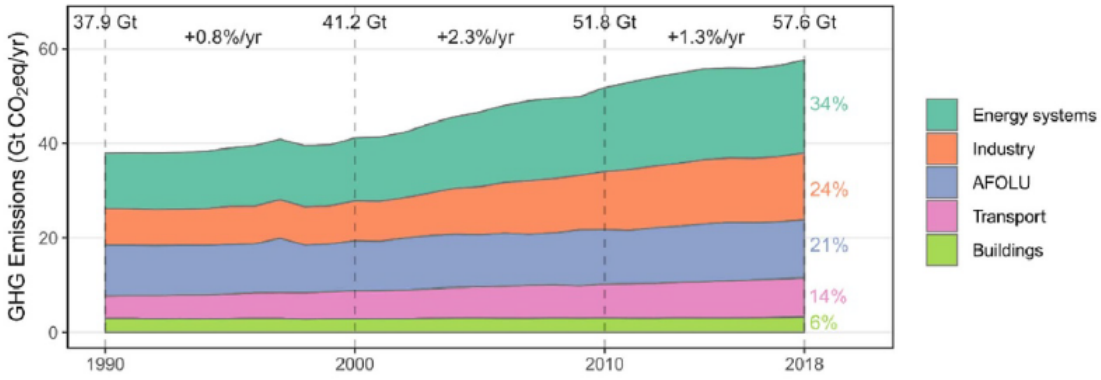


**Figure 1.2:** Global GHG emissions by sector [4]

## 1.2. Outlook

Hydrogen, due to its carbon-free structure, has been extensively studied and proposed as a promising alternative for conventional fuels in gas turbines (GTs). Besides the lack of carbon dioxide ($CO_2$) emissions and high energy content, considering its broad flammability range [5], hydrogen burnt under lean premixed conditions can also curb the release of harmful nitrogen oxides. In this mode, the excess air absorbs heat, effectively lowering temperatures and mitigating the production of nitrogen oxides or $NO_x$ through the thermal pathway [6]. Another advantage of hydrogen is its potential seamless integration within the renewable energy framework. As hydro, solar and wind energy are becoming more and more common, their intermittent nature can be turned from a disadvantage to an advantage by using the excess energy produced during peak production times for the production of hydrogen using electrolysis.

Indeed, these advantages have already been recognized in the industry, as certain manufac-

turers, such as Ansaldo Energia, Siemens and General Electric (GE), have already shown that some of their gas turbines are able to operate on 100% hydrogen fuel. This being said, the technology is still new, but, with sufficient attention, it could play an important role in the energy sector decarbonisation. In fact, the International Energy Agency (IEA), in their most optimistic scenario [7], where net-zero emissions (NZE) are achieved by 2050, predicts that hydrogen combustion could account for 2% of the total energy production in the world. In this scenario, leading economies such as the European Union, United States and Japan will adopt this technology and, by 2030, up to 190 GW of power will be produced from gas turbines retrofitted with hydrogen and/or ammonia dual fuel capabilities, with this figure rising to 580 GW by 2050.

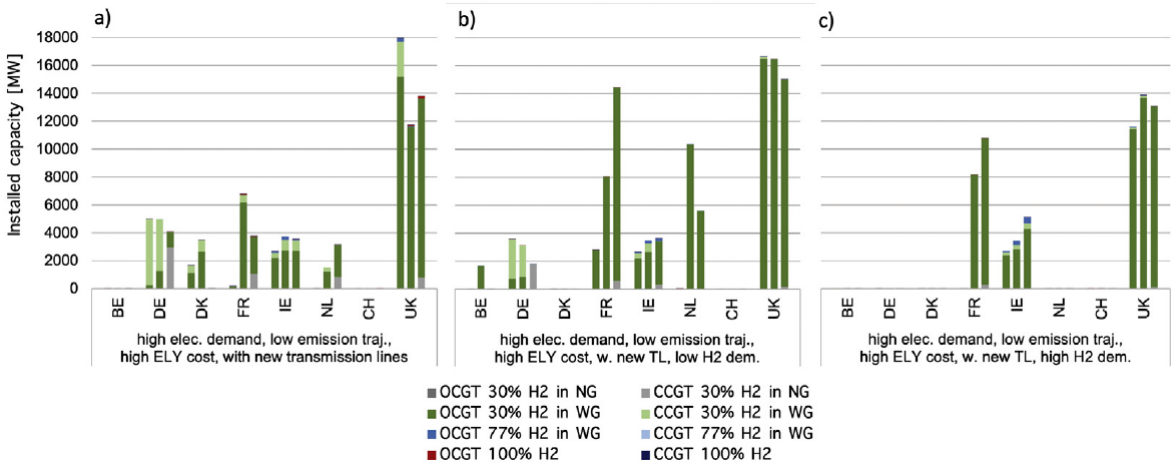


**Figure 1.3:** Hydrogen gas turbine predicted capacity by country for 2050. a) no hydrogen need, b) low hydrogen need, c) high hydrogen need. The three columns of each country represent assumed cost of natural gas and biogas where the middle column is the baseline and the left and right columns represent a 25% decrease and a 25% increase respectively [8]

Another study done by Öberg et al. [8] analysed the potential for hydrogen powered gas turbines by forecasting the installed capacity by 2050 in several Western and Central European countries. The results, shown in Figure 1.3, indicate that the adoption of this technology is highly dependent on the electricity demands and sources of each individual country, as well as on how much hydrogen will be required for other purposes such as aviation and industry. This claim is also supported by another study [9], which attributes these differences between the countries based on the availability of renewable energy. Their findings suggest that hydrogen powered gas turbines would be needed to meet the electricity demand in times of low renewable output, therefore creating a synergy between the two. For example, UK's significant 18 GW energy requirement is attributed to its dependency on wind power, a less predictable source of energy which can result in larger variability. On the other hand, countries like Spain, where solar power is more reliable, could turn to batteries to store the excess energy produced during peak production times.

## 1.3. Drawbacks

Unfortunately, the use of hydrogen fuel in gas turbine also presents several disadvantages. First off, although hydrogen is more than twice as energy dense on a mass basis as compared to $CH_4$, on a volume basis it is only one third as energy dense. This causes issues when

it comes to transporting and storing hydrogen effectively, a problem which is especially important for the aviation sector. Besides this, the low volumetric energy density means that GTs need to be adapted to provide the required volume flow [10].

From a safety point of view, hydrogen is less favourable than conventional fuels. First, a hydrogen flame is harder to detect visually as compared to a methane flame, thus requiring flame detection systems made specifically for hydrogen. Secondly, hydrogen's small atomic radius and its diffusive properties make it prone to slipping through seals. Moreover, $H_2$ induces embrittlement in numerous fuel plumbing materials [11], jeopardizing the integrity of various metals and materials typically utilized in gas turbines. These then have the potential to give rise to additional leaks and accelerate the deterioration of flow control and instrumentation equipment. Finally, hydrogen is more flammable than conventional fuels, meaning that, in the case of a fuel leak, it would ignite much easier. In comparison to $CH_4$, by mass, the lean flammability limit of $H_2$ is only 10% that of $CH_4$. This means that power plant procedure and safety regulations need to be changed when working with hydrogen [10] with implications in purging after a failed start and higher ventilation capabilities [12].

Furthermore, hydrogen's reactivity and its high thermal-diffusivity do pose notable challenges, such as an increase in adiabatic flame temperature when compared to conventional fuels. The increased adiabatic flame temperature, if not properly addressed, in turn leads to an increased $NO_x$ production, a greenhouse gas that is also harmful to human health. Coupled with these properties, the flame speed, which is an order of magnitude higher than conventional fuels, could make the hydrogen flame propagate upstream into the premixing zone, causing a flashback [12]. These issues lead to more stringent design requirements and a possibly limited operational range to mitigate high maintenance costs and damaged components [13]. This last drawback, i.e. the flashback phenomena, is the topic of research for this study as discussed in the following section.

## 1.4. Objectives

The objectives of this research are predicting and suppressing the flashback event observed in LES simulations of Ansaldo Energia's GT36 reheat combustion chamber model. As GTs, like the GT36, are designed to use higher proportions of $H_2$, as driven by the need for cleaner and more sustainable energy sources, they increasingly encounter the phenomenon of flashback. This adverse effect, characterized by the reverse flow of flames into the premixing tube, presents significant operational and safety issues. The focus of this thesis is to explore strategies for predicting and mitigating flashback, through the means of machine learning derived prediction methods and water injection, respectively. Successfully forecasting and controlling flashback could help with increasing $H_2$ content in GTs, advancing their potential towards clean power generation. The potential benefits of this are as follows: predictive measures would enhance the safety and reliability of these systems, reducing the risk of damage and extending their operational lifespan. The optimized use of water injection for flashback suppression, informed by ML predictions, could also lead to improvements in thermal efficiency, as water usage is tailored to the need of the system rather than used uniformly, allowing for this approach to not only warn against and mitigate flashback but to also improve the power output of the GTs. To summarize, the main research objectives of this study are as follows:

- Identify and apply a suitable machine learning-derived prediction method to determine in advance the apparition of the flashback event observed in the LES simulation.

- Find a suitable design for the water injection system and assess its capability in suppressing the flashback in the situation where the water is injected only after a flashback has been detected.

In addition, the secondary research objectives can also be formulated as follows:

- Use a dimensionality reduction technique to trim the number of flow variables coming from the LES simulation that can potentially be used in the prediction method.
- Assess the performance of the prediction method when it is constrained to conditions similar to those necessary for online prediction (limiting the available information, unseen data).

# 2

# Background

This chapter outlines the background of the problem, starting with the specific emission goals for power-generation gas turbines and what technologies have been developed by the industry to reach these goals. This is then followed by the specific details of the gas turbine studied here: Ansaldo Energia's GT36. Next, the different types of flashbacks and ways to mitigate them are discussed. Then, the flashback type encountered in the GT36 is discussed in detail. This is done by introducing general characteristics of hydrogen combustion and the autoignition phenomena, which lies at the heart of the flashback studied here. Lastly, other potential factors which can influence the autoignition process are discussed. These include high pressure effects, flame instabilities and how the flame regime affects flame instabilities. Lastly, a background is given for water injection system, as well as typical design parameters which are adjusted to fit the purpose.

| Type of combustion unit | BAT-AEELs (1) (2) | | | | |
|---|---|---|---|---|---|
| | Net electrical efficiency (%) | | Net total fuel utilisation (%) (3) (4) | Net mechanical energy efficiency (%) (4) (5) | |
| | New unit | Existing unit | | New unit | Existing unit |
| **Gas engine** | 39,5–44 (6) | 35–44 (6) | 56–85 (6) | No BAT-AEEL. | |
| **Gas-fired boiler** | 39–42,5 | 38–40 | 78–95 | No BAT-AEEL. | |
| **Open cycle gas turbine, ≥ 50 MWth** | 36–41,5 | 33–41,5 | No BAT-AEEL | 36,5–41 | 33,5–41 |
| **Combined cycle gas turbine (CCGT)** | | | | | |
| CCGT, 50–600 $MW_{th}$ | 53–58,5 | 46–54 | No BAT-AEEL | No BAT-AEEL | |
| CCGT, ≥ 600 $MW_{th}$ | 57–60,5 | 50–60 | No BAT-AEEL | No BAT-AEEL | |
| CHP CCGT, 50–600 $MW_{th}$ | 53–58,5 | 46–54 | 65–95 | No BAT-AEEL | |
| CHP CCGT, ≥ 600 $MW_{th}$ | 57–60,5 | 50–60 | 65–95 | No BAT-AEEL | |

**Figure 2.1:** BAT-associated energy efficiency levels (BAT-AEELs) for natural gas combustion [14]

## 2.1. Emissions regulations and gas turbine technologies

The latest regulations on land-based gas turbines were released by the European Union on the 31st of November 2021 [14]. In terms of efficiency, gas turbines are required to have a net electrical efficiency upwards of 50%, as seen in Figure 2.1, while for the $NO_x$ emissions the yearly average ranges from 10 to 55 mg/Nm$^3$, which is equivalent to 7.94 - 43.66 $NO_2$ ppm, assuming a 95% concentration of NO, see Figure 2.2.

| Type of combustion plant | Combustion plant total rated thermal input ($MW_{th}$) | BAT-AELs (mg/Nm³) (1) (2) | |
|---|---|---|---|
| | | Yearly average (3) (4) | Daily average or average over the sampling period |
| **Open-cycle gas turbines (OCGTs)** (5) (6) | | | |
| New OCGT | ≥ 50 | 15–35 | 25–50 |
| Existing OCGT (excluding turbines for mechanical drive applications) – All but plants operated < 500 h/yr | ≥ 50 | 15–50 | 25–55 (7) |
| **Combined-cycle gas turbines (CCGTs)** (5) (8) | | | |
| New CCGT | ≥ 50 | 10–30 | 15–40 |
| Existing CCGT with a net total fuel utilisation of < 75 % | ≥ 600 | 10–40 | 18–50 |
| Existing CCGT with a net total fuel utilisation of ≥ 75 % | ≥ 600 | 10–50 | 18–55 (9) |
| Existing CCGT with a net total fuel utilisation of < 75 % | 50–600 | 10–45 | 35–55 |
| Existing CCGT with a net total fuel utilisation of ≥ 75 % | 50–600 | 25–50 (10) | 35–55 (11) |

**Figure 2.2:** BAT-associated emission levels (BAT-AELs) for $NO_x$ emissions from natural gas combustion in GTs [14]

Along with these stringent requirements, the EU also gives a list of potential technologies to be added to existing GTs or incorporated in new GTs. These are advanced control systems which ensure optimum loading and efficiency at all times, water/steam addition, a method which is designed to reduce $NO_x$ emissions by lowering the overall temperature in the combution chamber, dry low-$NO_x$ burners (DLN), low-load design concepts and finally, selective catalytic reduction systems (SCR). All of these potential solutions have their drawbacks when hydrogen is incorporated, where, more often than not, flame stability is a key issue.

In their attempts to satisfy these requirements, as well as introducing hydrogen based combustion, large manufacturers of gas turbines have already started to adopt some of these technologies [12]. For example, Siemens and General Electric (GE) have adopted DLN in a variety of their models, already achieving more than 50% hydrogen concentrations. This figure is still limited due to hydrogen's complicated combustion dynamics, coupled with the lean premixed principle of DLN. GTs using this technology can be subject to phenomena such as undesired autoignition, flashbacks and thermo-acoustic instabilities. Nevertheless,

these companies were also able to achieve 100% $H_2$ content using this technology coupled with Wet Low Emissions (WLE). Furthermore, Mitsubishi Heavy Industries (MHI) has introduced a multicluster technology featuring a multicluster diffusion burner, which relies on micro-mix technology. As of right now, the technology is capable of accommodating up to 30% hydrogen content on the H-25 gas turbine, with plans to use 100% $H_2$ in 2024. Another gas turbine which has already successfully ran using hydrogen-containing fuel is Ansaldo Energia's sequential gas turbine, the GT36, which is the configuration of reference for this study.

## 2.2. Ansaldo Energia's GT36

The GT36 gas turbine, as shown in Figure 2.3, is the latest development in Ansaldo Energia's series of sequential gas turbines and a model of its reheat combustion chamber is the object of study for this thesis.

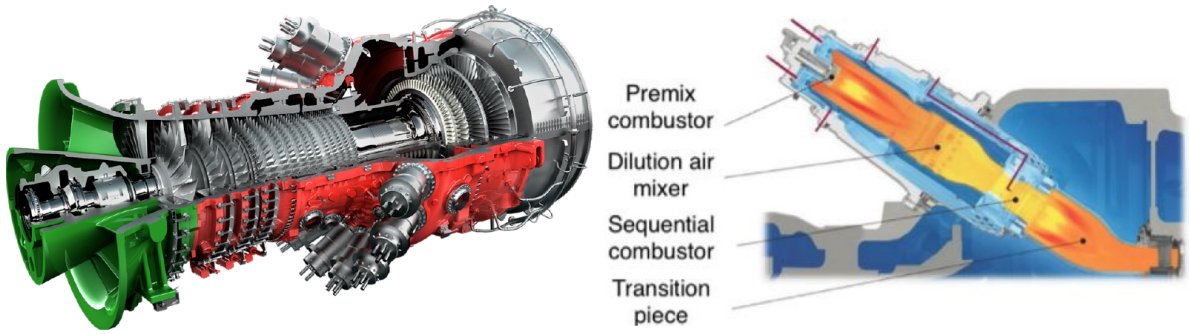


**Figure 2.3:** Render of the GT36 gas turbine and the CPSC system [15]

The initial development of sequential combustor technology can be attributed to Alstom, which introduced the first model, the GT24/GT26, utilizing this technology in 1994. In 2016, when Alstom was acquired by Ansaldo Energia, the two companies enhanced the sequential combustor design and recently unveiled the GT36. Sequential combustion involves two stages of combustors functioning in the lean premixed regime. In the initial stage, flame stability is maintained through flame propagation assisted by a vortex breakdown mechanism, while in the second stage (or the reheat stage), stabilization primarily relies on autoignition. This type of system, due to the flexibility of injecting different amounts of fuel in the two stages, proves advantageous when a high reactivity fuel, such as hydrogen, is used. A schematic of how this system works when hydrogen is added is shown in Figure 2.4. In this diagram, the progression of the temperature of the flow, as well as the position of the flame across the two stages is shown. The red line represent the baseline case, while the green line indicates the way in which the system can be adapted for using hydrogen as fuel, providing certain advantages while still retaining the original power and efficiency.

Firstly, this adaptation works by using less fuel in the first stage. This results in the flame being position more downstream, thus avoiding the risk of overheating the burner walls and decreasing the residence time in this first stage. Furthermore, due to the lower equivalence ratio, the flame temperature is also lower. This is advantageous because both the shorter residence time and the lower flame temperature reduce the formation of $NO_x$ through the thermal or Zeldovich pathway, which is the main mechanism through which $NO_x$ is produced. In this pathway, the main reactions that occur are $NO + O \leftrightarrows O + N_2$, $O + N_2 \leftrightarrows NO + N$ and $N + OH \leftrightarrows NO + N$. By lowering the residence time, there is less

time for these reactions to occur and thus the amount of $NO_x$ is reduced. Furthermore, the lower temperature decrease the kinetic energy of the molecules and thus, because the aforementioned reaction have a high activation energy (the energy of a collision needed to break the bonds of the reactants), in turn, it reduces the $NO_x$ formation.

Secondly, the unused fuel in the first stage can now be used in the second stage. In this stage, the position of the flame is independent of the amount of fuel, as it relies on autoignition to sustain the combustion. Autoignition is the spontaneous combustion of fuel. This phenomena typically occurs at a certain temperature, where the heat generated by the chemical reactions exceeds the heat lost to the surroundings. As such, the position of the flame relies only on the inlet temperature at this stage. Due to the lower mean exit temperature (MET) of the first stage and due to the dilution with air which takes place in between the two stages, the inlet temperature is thus lower and the position of the flame is again pushed downstream due to the increased ignition delay time (the time interval between when a fuel-air mixture reaches ignition conditions and the onset of spontaneous combustion). Once again, this reduces the residence time in the reheat stage and thus lowers the amount of $NO_x$ produced. Furthermore, due to the presence of water vapour coming from the products of the first stage, the production of $NO_x$ is further reduced. According to Le Chatelier's principle, if the equilibrium of a system is disturbed by a change, the system tends to adjust itself to a new equilibrium by counteracting as far as possible the effect of the change. Thus, by adding water, the reactions $2OH \leftrightarrows H_2O + O$ and $OH + H_2 \leftrightarrows H_2O + H$ are partially suppressed. Meanwhile, the production of $H_2O_2$ and the reduction in OH are in turn increased due to the reaction $H_2O_2 + H \rightleftarrows H_2O + OH$. This results in less O and OH radicals being available for the formation of $NO_x$ [16].

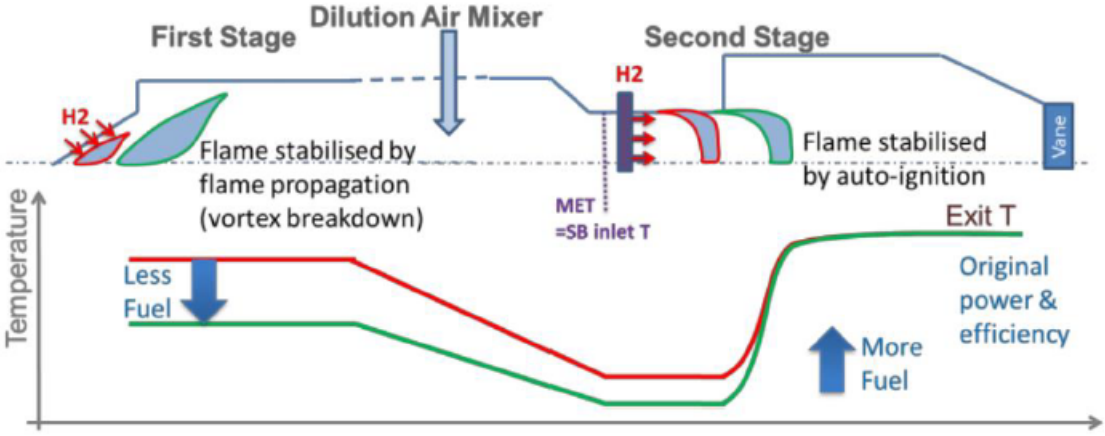


**Figure 2.4:** Temperature progression of the GT36 gas turbine [17]

In the first iteration of this gas turbine, the GT26, the two combustion stages are separated by a so-called interstage turbine. In the first stage, the fuel is burned at pressure over 30 bars, and, after passing through the turbine, the pressure drops to half of that. The GT36 improves upon this design by replacing the interstage turbine with a air dilution and mixing stage. By using this system, called Constant Pressure Sequential Combustion (CPSC), the same pressure level is maintained in the reheat combustor. This allows for H-class performance with low emissions, by injecting the fuel at around 1000°C, a firing temperature that is typically smaller than those found in F and H class gas turbines.

Besides the addition of the CPSC system, characteristic to the GT36 is also the cavity-trapped vortex combustor, a technology which is a key part in assuring flame stability for this GT. In the GT36's reheat combustor, two combustion modes coexist: an autoignition process and a deflagration (subsonic propagation of premixed flames) triggered by interactions between recirculation vortices and heat transfer to the walls of the combustion chamber. The efficient combustion dynamics hinge on the loss of heat to the mixing duct walls, causing reactants near the walls to be cooler than those in the main flow. As these cooler reactants enter the combustion chamber, their temperature is not favourable for autoignition. A sudden expansion in the chamber creates a recirculation region, promoting the propagation of flames towards unburned reactants. This mechanism stabilizes the flame and ensures efficient combustion [18]. A schematic of this system is shown in Figure 2.5.

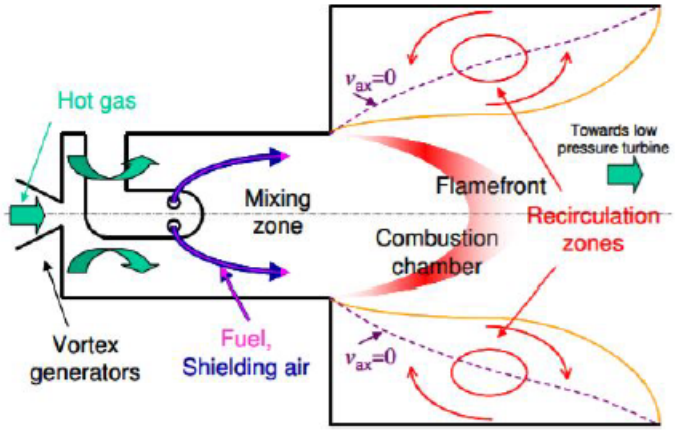


**Figure 2.5:** Schematic of the cavity-trapped vortex combustion system [18]

The next topic investigated here is the flashback phenomena, which is known to appear at high pressure conditions in LES simulations of a model of the reheat combustion chamber of the GT36 [19].

## 2.3. Flashback

A flashback is a critical phenomenon in combustion systems that involves the undesirable upstream propagation of the flame inside the mixing duct. Generally, this occurs when the turbulent flame velocity becomes higher than the velocity of the incoming reactant stream. As the trend in gas turbines leans towards lean premixed combustion and hydrogen addition, the flashback phenomena becomes an increasing concern. The occurrence of flashback is closely linked to the flame stabilization mechanisms and is influenced by other factors including flow velocity, mixture composition, temperature gradients, and the presence of obstacles or sudden expansions in the combustion chamber. The phenomenon is more prevalent in gaseous fuels with high hydrogen content due to their wide flammability limits and low quenching distances, making the understanding of flashback dynamics crucial for the development of efficient and safe combustion technologies.

Historically, the study of flashbacks has been a subject of extensive research due to its implications on the design and operation of combustion systems. The complex interplay between the turbulent flow structures and the flame's response to these structures governs the onset and progression of flashback. Theoretical models and empirical correlations

have been developed to predict the conditions under which flashback occurs, integrating parameters such as the laminar burning velocity, turbulence intensity, and scale of turbulence into predictive tools for flashback propensity.

There are five different types of flashback which are commonly encountered in gas turbines [20, 21]:

- **Core flow flashback:** Core flow flashback happens when turbulent flame speed $S_T$ surpasses local flow speed within the core [22], with the magnitude of $S_T$ being the main influencing factor. It occurs due to interactions between turbulent flames and chemistry, influenced by fuel composition and turbulence structures [23, 24]. Furthermore, flame stabilization methods in devices might inadvertently trigger core flashbacks by altering flow velocities and flame behavior. This type of flashback is more prominent in the case of hydrogen fueled combustion, due to its higher flame speed. There are several correlations which have been found to accurately model the turbulent burning velocity to predict core flow flashback, but they are usually dependent on the fuel composition, and thus they are difficult to generalize [25, 24, 23].
- **Combustion instabilities induced flashback:** Flashback from combustion instability results from large amplitude flow field fluctuations. Interactions between acoustic modes, heat release fluctuations, and flow patterns lead to pressure and velocity oscillations. These interactions can induce flame movement and generate vortices, potentially causing the flame to move upstream and trigger flashback. In an experimental study done by Keller et al. [26] it was found that the pulsation cycle of the flow structure lifted the flame from the edge of the expansion step, which later on induced flashback.
- **Combustion induced vortex breakdown (CIVB) flashback:** CIVB flashback is prevalent in swirl combustors. It occurs when the swirl number exceeds a threshold, leading to vortex breakdown and reverse flow regions [27]. Changes in velocity distribution due to azimuthal velocity increase induce vortex breakdown, altering flame and flow patterns. Whether flame propagation occurs upstream is dictated by the balance between volume expansion and baroclinic torque, where the flame position relative to the expanding bubble is crucial [28].
- **Boundary layer flashback:** Boundary layer flashback primarily happens in premixed flames such as jet/Bunsen flames. Flashback occurs where local burning velocity surpasses local flow velocity [29]. This typically happens in the boundary layer due to the small velocities at the wall. For confined boundary layer flashbacks (when the flame resides inside a channel) the concept of "critical velocity gradient" characterizes the propensity for flashback under specific conditions. Meanwhile, for unconfined BL flashback (when the flame resides after an expansion step), the variables which tend to dominate are velocity fluctuations and flame stretch [30].
- **Autoignition flashback:** Although not generally categorized as a flashback mechanism, autoignition can trigger the appearance of the flame in the mixing duct, with the same negative consequences on the gas turbine. As discussed in Section 2.4.3, autoignition occurs when the ignition delay time is less than the residence time in the mixing duct. In GTs, this may occur when there is a decrease in flow velocity or a local increase in temperature. This increase in temperature can occur due to convective/radiative heating, flame expansions and/or pressure waves [21].

To avoid these different types of flashback, different authors have suggested a multitude of methods which prove to be effective depending on the studied case. Key approaches include:

- Increasing Axial Velocity: Elevating the axial velocity reduces the likelihood of core and Convective Internal Vortex Breakdown (CIVB) flashbacks. This leads to a pressure loss, proportional to the square of the velocity change, impacting operational efficiency. Enhancing the axial fuel diameter strengthens the central jet, preserving downstream coherent structures and postponing vortex breakdown [31]. However, this negatively impacts $NO_x$ production and does not affect the boundary layer (BL) flashback, necessitating additional measures for its control [32].
- Reducing Swirl: While high swirl numbers aid in reactant mixing and emission reduction, they also diminish flashback resistance. Modifying the azimuthal opening jet angle at the mixing duct outlet induces negative azimuthal vorticity, promoting vortex breakdown. Conversely, reducing swirl lowers the combustion area in the burner, increasing axial velocity and flashback resistance.
- Preventing Boundary Layer Detachment: In turbulent, high-swirl flows, the stabilized flame penetrates closer to the burner walls than in laminar combustion. Nozzle geometry, determining quenching distance, influences flashback resistance. Maintaining a thin, attached boundary layer in critical areas like the mixing duct reduces BL flashback risks [33]. Techniques like micro-riblet structures to reduce skin friction or air effusion in walls to dilute the mixture help prevent flashback [32, 34, 35, 36]. Baumgartner and Sattlemayer [36] suggest that air injection up to 10% of the total flow near the burner outlet can divert flashback towards the rich central zone.
- Diluent Injection: Air humidification, by slowing reaction rates, can stabilize the flame. Pappa et al. demonstrate that a 10% water mass fraction dilution decreases hydrogen reactivity while maintaining flame speeds [37]. Exhaust gas recirculation as a diluent is also effective in reducing flashback risks and $NO_x$ emissions [38]. Nitrogen addition, as investigated by York et al. [39], lowers hydrogen content, enhancing flashback resistance.
- Fuel Momentum: The increased volumetric flow required for hydrogen substitution adds significant fuel momentum, influencing premixing flow. Reichel and Paschereit [40] define the momentum ratio $J$ as:

$$J = \frac{\rho_{\text{fuel}} u_{\text{fuel}}^2}{\rho_{\text{air}} u_{\text{air}}^2} \tag{2.1}$$

  Higher momentum ratios, achievable by maintaining constant air mass flow or preheating the air, move the flame front and vortex breakdown downstream, effectively preventing flashback [41]. These findings suggest that increasing the equivalence ratio, which initially seems counterintuitive, can be beneficial for flashback resistance when incorporated into combustor design.

From previous work [19], it is already known that at high pressure conditions, the flashback type observed in GT36's reheat combustor is of the autoignition type. Before moving on to flashback prediction and suppression techniques, a more in depth understanding of hydrogen combustion and autoignition is needed first.

# 2.4. Hydrogen combustion

## 2.4.1. General characteristics

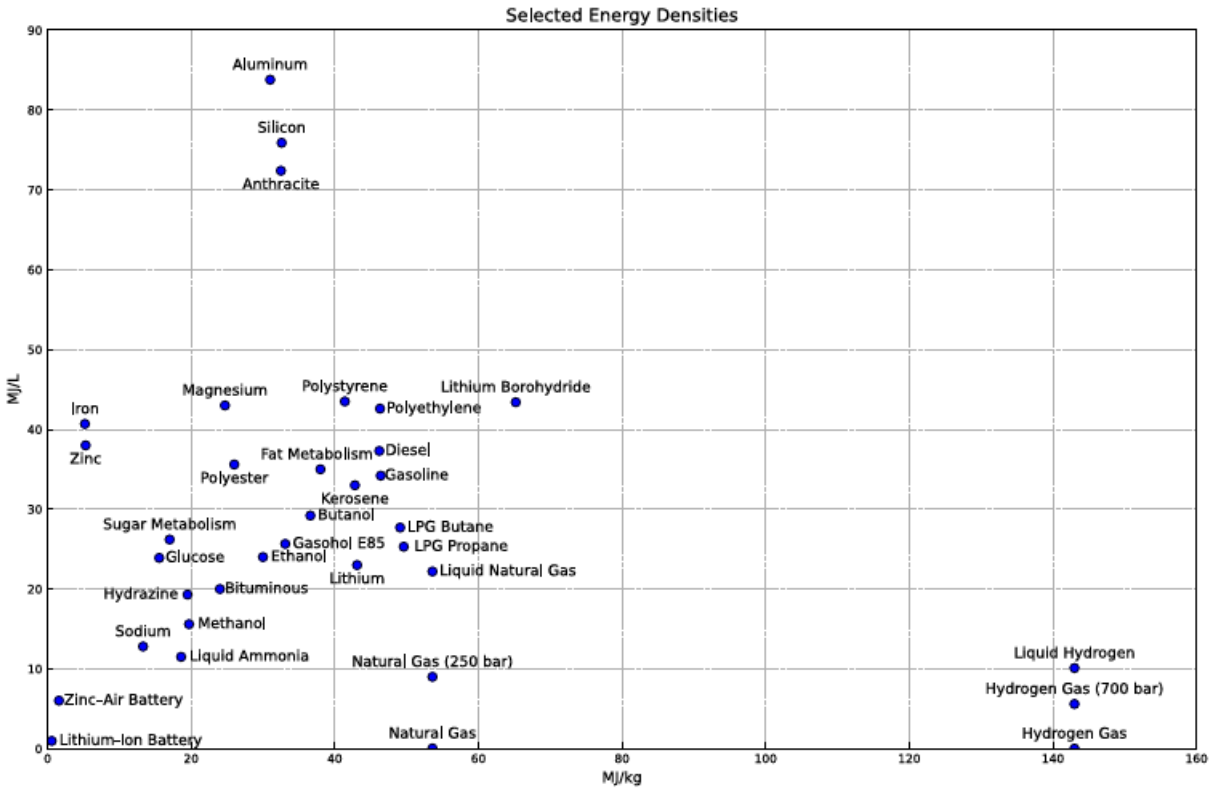


**Figure 2.6:** Energy densities of various sources of energy. [42]

Hydrogen, a chemical element found naturally as a diatomic gas at standard conditions, is a great candidate to be used as fuel due to its large higher heating value (HHV) (141.86 MJ/kg) and ease of production. It can be obtained through the process of steam reforming of natural gas and coal gasification, but also in a environmentally sustainable manner by using electrolysis with energy produced from renewable sources [43]. On the other hand, $H_2$ has low volumetric energy density with a HHV of only 0.01188 MJ/L, which is more than three times lower than the 0.0378 MJ/L HHV of natural gas at standard conditions. In comparison to other sources of energy, see Figure 2.6, $H_2$ again lies at the extreme end of spectrum, posing the highest mass energy density and the lowest volumetric energy density.

Furthermore, hydrogen also has a broader flammability range in comparison to natural gas, i.e. 4-75% compared to 3.5-15%, allowing for ultra-lean combustion where the equivalence ratio can be as low as $\phi = 0.1$. Other differences include a considerably larger adiabatic flame temperature, corresponding to 2318 K at stochiometric conditions, which can lead to higher NOx emissions. On the other hand, $NO_x$ can not form through the Fenimore and fuel pathways. $H_2$ also has a lower quenching distance than that of natural gas, at 0.64 mm and 2.1 mm, respectively, a property which can prove detrimental when it comes to the apparition of boundary layer flashback. Other aspects of $H_2$ also include a much thinner flame front as compared to natural gas, a Prandtl number of 0.701 under standard condition, compared to 0.707 for air, and an autoignition temperature which ranges from 793-1023 K, well within standard operating conditions of reheat combustion chambers. Also,

the diffusion coefficient of $H_2$ is 0.61 $cm^2/s$ in air at standard conditions, a value which is considerably larger than the 0.22 $cm^2/s$ of methane, resulting in more radicals being transported upstream of the flame. This also implies a small Lewis number, i.e. $Le_{H_2} = 0.3$, resulting in potential instabilities. Finally, $H_2$ has the fastest burning velocity among all fuels [44] and a small autoignition delay time [45], properties which, when coupled together, can lead to an unstable flame and an available residence time which may not allow for proper mixing. A summary of $H_2$'s properties, as compared to other fuels, can be found in Table 2.1. Furthermore, an in-depth view of how these properties affect the combustion dynamics, and consequently, the flashback phenomena, will be detailed in the following sections.

**Table 2.1:** Properties of $H_2$ and other fuels at 25°C and 1 atm. Superscripts denote the following: a - liquid at 0°C, b - stochiometric conditions, c - methane, d - vapor.

| **Property** | **Hydrogen** | **CNG** | **Gasoline** | **Methane** |
|---|---|---|---|---|
| Density (kg/m3) | 0.0824 | 0.72 | $730^a$ | 0.651 |
| Flammability limits (volume % in air) | 4-75 | 4.3-15 | 1.4-7.6 | 5.5-15 |
| Flammability limits ($\phi$) | 0.1-7.1 | 0.4-1.6 | 0.7-4 | 0.4-1.6 |
| Autoignition temperature in air (K) | 858 | 723 | 550 | 813 |
| Minimum ignition energy in air (mJ)$^b$ | 0.02 | 0.28 | 0.24 | 0.29 |
| Flame velocity (m/s)$^b$ | 1.85 | 0.38 | 0.37-0.43 | 0.40 |
| Adiabatic flame temperature (K)$^b$ | 2480 | 2214 | 2580 | 2226 |
| Quenching distance (mm)$^b$ | 0.64 | $2.1^c$ | $\approx 2$ | 2.5 |
| Stoichiometric fuel/air mass ratio | 0.029 | 0.069 | 0.068 | 0.058 |
| Stoichiometric volume fraction (%) | 29.53 | 9.48 | $2^d$ | 9.48 |
| Lower heating value (MJ/m3) | 9.9 | 32.6 | - | 32.6 |
| Lower heating value (MJ/kg) | 119.7 | 45.8 | 44.79 | 50.0 |
| Heat of combustion (MJ/kg air )$^b$ | 3.37 | 2.9 | 2.83 | 2.9 |

### 2.4.2. Chemical kinetics

Understanding the reactions that take place in hydrogen combustion is critical in understanding the autoignition flashback of this study. Describing the sequence of reactions occurring at molecular level during combustion through a chemical mechanism is vastly simplified when using hydrogen due to the absence of carbon species. There are different chemical mechanisms usually employed in simulations which posses different characteristics, making them suitable for different applications. In 2014, Olm et al. [46] conducted a comparative study of these mechanisms, ranking them based on an overall average error function value, as shown in Figure 2.7.

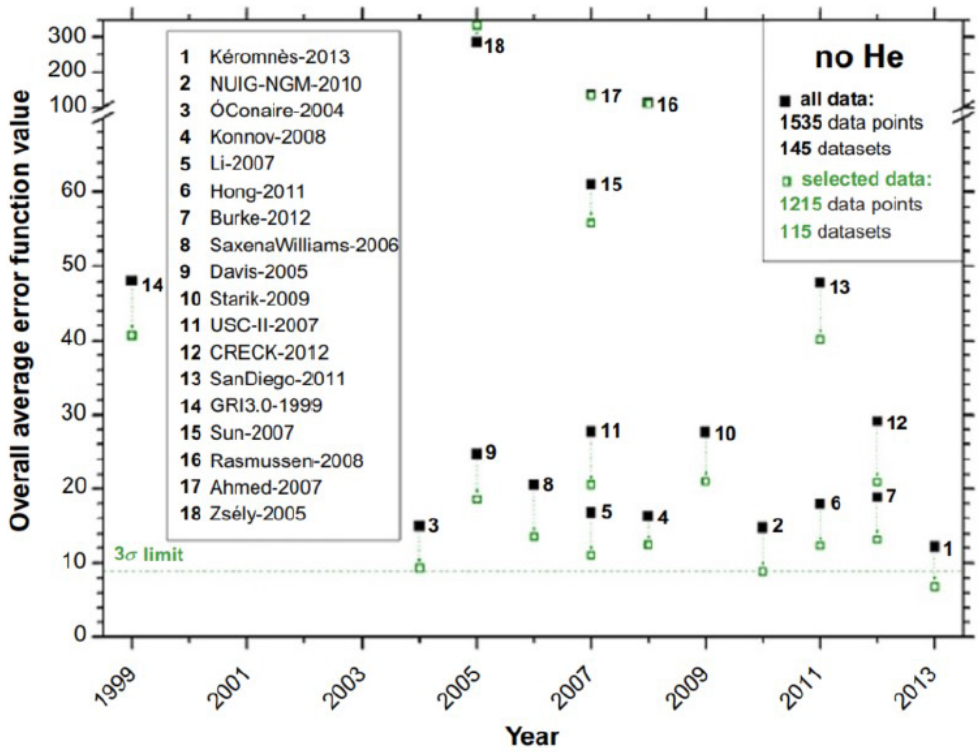


**Figure 2.7:** Overall performance of the different $H_2$ mechanism. The black squares represent all data and the green ones only the data also found in at least one other mechanism. The overall average error function value represents the deviation from experimental values of each individual chemical kinetic model, averaged across multiple datasets.

For the purposes of this study, the mechanisms of Li et al. [47] and Burke et al. [48] present the most interest due to their popularity, performance and ease of comparison to previous studies as done by Kruljevic et al [49]. Out of the two, the choice leaned in favour of the mechanism suggested by Li et al. due to its slightly better computational efficiency and demonstrated efficacy at predicting autoignition [19]. Furthermore, they also present a good performance at high pressures. The reactions involved in these mechanisms are shown in Table 2.2, where $A$ is the exponential factor, $n$ is a constant and $E_a$ is the activation energy as employed in the Arrhenius equation:

$$k = AT^n \exp\left(-\frac{E_a}{RT}\right) \tag{2.2}$$

**Table 2.2:** The reactions involved in the Li et al. mechanism. M can be either $N_2$, Ar or He [47]

| | | $A$ | $n$ | $E$ |
|---|---|---|---|---|
| | H2/O2 chain reactions | | | |
| R1. | $H + O_2 \rightleftarrows O + OH$ | $3.55 \times 10^{15}$ | -0.41 | 16.6 |
| R2. | $O + H_2 \rightleftarrows H + OH$ | $5.08 \times 10^{4}$ | 2.67 | 6.29 |
| R3. | $H_2 + OH \rightleftarrows H_2O + H$ | $2.16 \times 10^{8}$ | 1.51 | 3.43 |
| R4. | $O + H_2O \rightleftarrows OH + OH$ | $2.97 \times 10^{6}$ | 2.02 | 13.4 |
| | H2/O2 dissociation/recombination reactions | | | |
| R5. | $H_2 + M \rightleftharpoons H + H + M^a$ | $4.58 \times 10^{19}$ | -1.40 | 104.38 |
| | $H_2 + Ar \rightleftarrows H + H + Ar$ | $5.84 \times 10^{18}$ | -1.10 | 104.38 |
| | $H_2 + He \rightleftarrows H + H + He$ | $5.84 \times 10^{18}$ | -1.10 | 104.38 |
| R6. | $O + O + M \rightleftharpoons O_2 + M^a$ | $6.16 \times 10^{15}$ | -0.50 | 0.00 |
| | $O + O + Ar \rightleftarrows O_2 + Ar$ | $1.89 \times 10^{13}$ | 0 | -1.79 |
| | $O + O + He \rightleftharpoons O_2 + He$ | $1.89 \times 10^{13}$ | 0 | -1.79 |
| R7. | $O + H + M \rightleftharpoons OH + M^a$ | $4.71 \times 10^{18}$ | -1.0 | 0.00 |
| R8. | $H + OH + M \rightleftarrows H_2O + M^b$ | $3.80 \times 10^{22}$ | -2.00 | 0.00 |
| | Formation and consumption of HO2 | | | |
| R9. | $H + O_2 + M \rightleftarrows HO_2 + M^c$ | $6.37 \times 10^{20}$ | -1.72 | 0.52 |
| | $H + O_2 + M \rightleftarrows HO_2 + M$ | $9.04 \times 10^{19}$ | -1.5 | 0.49 |
| R10. | $HO_2 + H \rightleftarrows H_2 + O_2$ | $1.66 \times 10^{13}$ | 0.00 | 0.82 |
| R11. | $HO_2 + H \rightleftarrows OH + OH$ | $7.08 \times 10^{13}$ | 0.00 | 0.30 |
| R12. | $HO_2 + O \rightleftarrows OH + O_2$ | $3.25 \times 10^{13}$ | 0.00 | 0.00 |
| R13. | $HO_2 + OH \rightleftarrows H_2O + O_2$ | $2.89 \times 10^{13}$ | 0.00 | -0.50 |
| | Formation and consumption of H2O2 | | | |
| R14. | $HO_2 + HO_2 \rightleftarrows H_2O_2 + O_2$ | $4.20 \times 10^{14}$ | 0.00 | 11.98 |
| | $HO_2 + HO_2 \rightleftarrows H_2O_2 + O_2$ | $1.30 \times 10^{11}$ | 0.00 | -1.63 |
| R15. | $H_2O_2 + M \rightleftarrows OH + OH + M^d$ | $1.20 \times 10^{17}$ | 0.00 | 45.5 |
| R16. | $H_2O_2 + H \rightleftarrows H_2O + OH$ | $2.41 \times 10^{13}$ | 0.00 | 3.97 |
| R17. | $H_2O_2 + H \rightleftarrows H_2 + HO_2$ | $4.82 \times 10^{13}$ | 0.00 | 7.95 |
| R18. | $H_2O_2 + O \rightleftarrows OH + HO_2$ | $9.55 \times 10^{6}$ | 2.00 | 3.97 |
| R19. | $H_2O_2 + OH \rightleftarrows H_2O + HO_2$ | $1.00 \times 10^{12}$ | 0.00 | 0.00 |
| | $H_2O_2 + OH \rightleftarrows H_2O + HO_2$ | $5.80 \times 10^{14}$ | 0.00 | 9.56 |

[a] $\epsilon_{H_2O} = 12, \epsilon_{H_2} = 2.5, \epsilon_{Ar} = 0.75, \epsilon_{He} = 0.75$

[b] $\epsilon_{H_2O} = 12, \epsilon_{H_2} = 2.5, \epsilon_{Ar} = 0.38, \epsilon_{He} = 0.38$

[c] $\epsilon_{H_2O} = 11, \epsilon_{H_2} = 2, \epsilon_{O_2} = 0.78$

[d] $\epsilon_{H_2O} = 12, \epsilon_{H_2} = 2.5, \epsilon_{Ar} = 0.64, \epsilon_{He} = 0.64$

### 2.4.3. Autoignition characteristics

Autoignition refers to the phenomena where the fuel in a combustion chamber spontaneously ignites once it reaches a certain temperature, without the need for an external ignition source. This characteristic is used in Ansaldo Energia's GT36 and other GTs, for the operation of reheat combustion chambers due to the ideal conditions present there, i.e. high temperatures of more than 1000 K and high pressures 15-30 atm. A more exact definition is provided by Zeldovich (1980), which states the autoignition regime occurs when the inverse of the local ignition time is larger than the deflagration velocity but smaller than the speed of sound of the unburned gas [50].

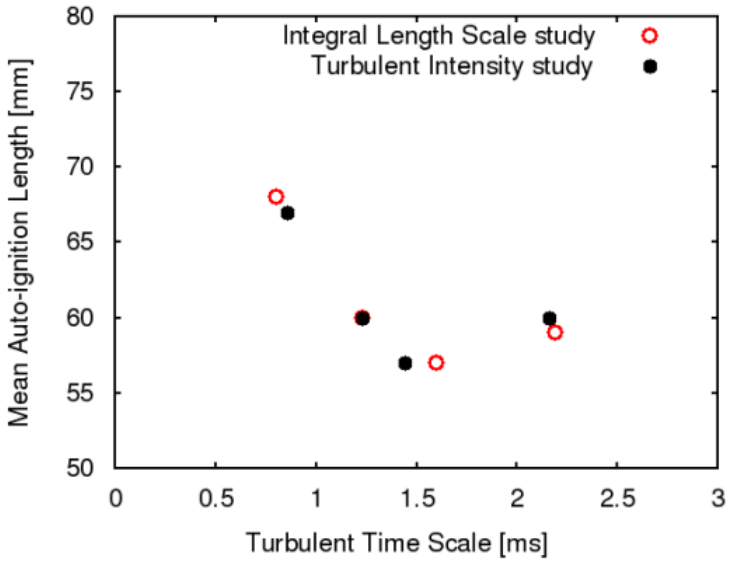


**Figure 2.8:** Co-flow LES parametric study of autoignition length with respect to turbulence intensity [51]

As such, it is the choice of an appropriate autoignition delay time which dictates the successful design of a reheat combustion chamber. In the case of premixed combustion, an autoignition delay time which is too short would results in the ignition of the flow happening in the mixing duct. This means that, to keep the flame at its design location, either the inlet conditions have to be changed or the mixing duct has to be shortened. Conversely, if the mixing duct is too short, then the reactants do not have enough time to mix to create the desired premixed conditions, resulting in a hotspot with a higher temperature and a higher predisposition for autoignition in the rest of the combustion chamber. These two competing aspects make the successful design of a reheat combustion chamber challenging. Moreover, to further complicate the problem, autoignition is also affected by strain. Moderate turbulence facilitates autoignition, while a large amount of turbulence has an impeding effect. This is illustrated in Figure 2.8, where the turbulent time scale is inversely proportional to the turbulence intensity [51].

Nevertheless, the main influence on the autoignition delay time is exerted by the inlet conditions: temperature, pressure and equivalence ratio, where of particular importance is the temperature, especially through the cross-over temperature, which will be defined in the upcoming paragraphs. These influences can be observed in Figure 2.9, where it can be seen that the autoignition delay time becomes smaller with an increasing temperature.

Furthermore, $\tau_{ign}$ presents a complex behaviour with pressure, where low pressures imply a higher $\tau_{ign}$ at low and high temperatures, and lower $\tau_{ign}$ in between. In the case of the GT36, the temperature falls in this in between regime, where the autoignition delay time benefits from the larger pressure, allowing for more time for reactant mixing.

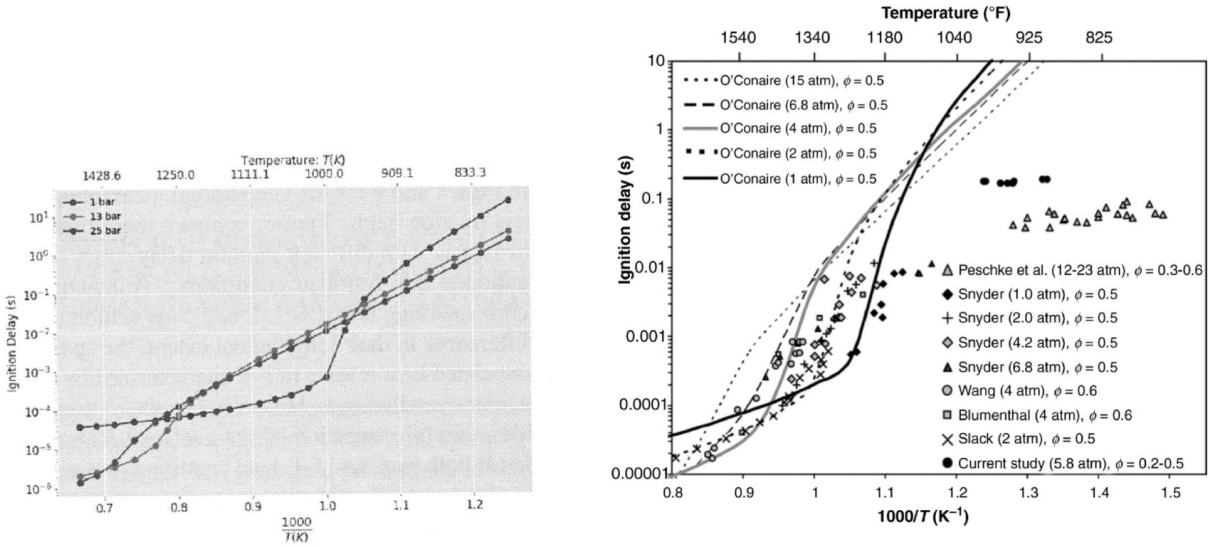


**Figure 2.9:** Ignition delay of premixed hydrogen as a function of pressure and temperature of the reactants. Left [52]: $\phi = 0.4$. At the highest temperature: the three curves are at 1, 13 and 25 atm from top to bottom. Right [50]: different simulations based on homogeneous, 0D, isobaric and adiabatic PFR models, as well as different experiments.

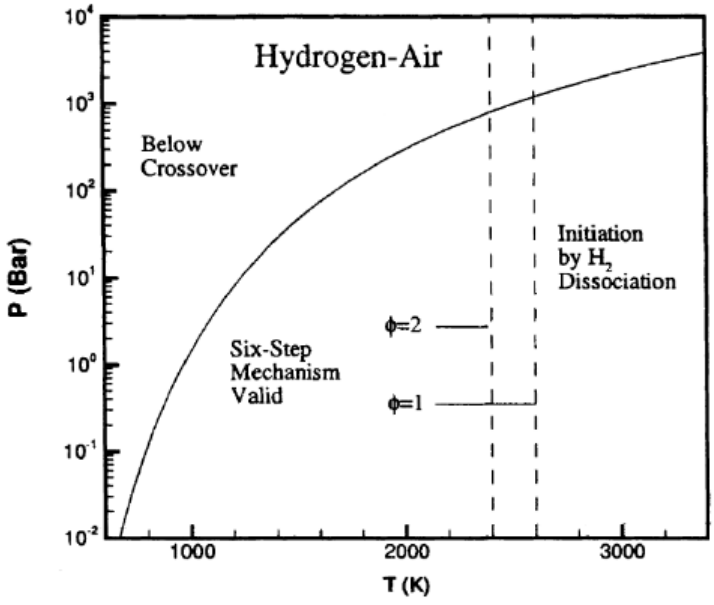


**Figure 2.10:** Cross-over temperature as a function of pressure. [53]

Also seen in Figure 2.9 is a section where the dependence of the autoignition delay time on the temperature is very high. This temperature range is commonly referred to as the cross-over temperature. Furthermore, it can be observed that this region presents a higher

slope, and therefore a higher dependence, for mixtures at a lower pressure. Álamo et al. [53] proposes an estimate of the cross-over temperature, see Figure 2.10, based on the range of validity of the six-reaction hydrogen-air mechanism.

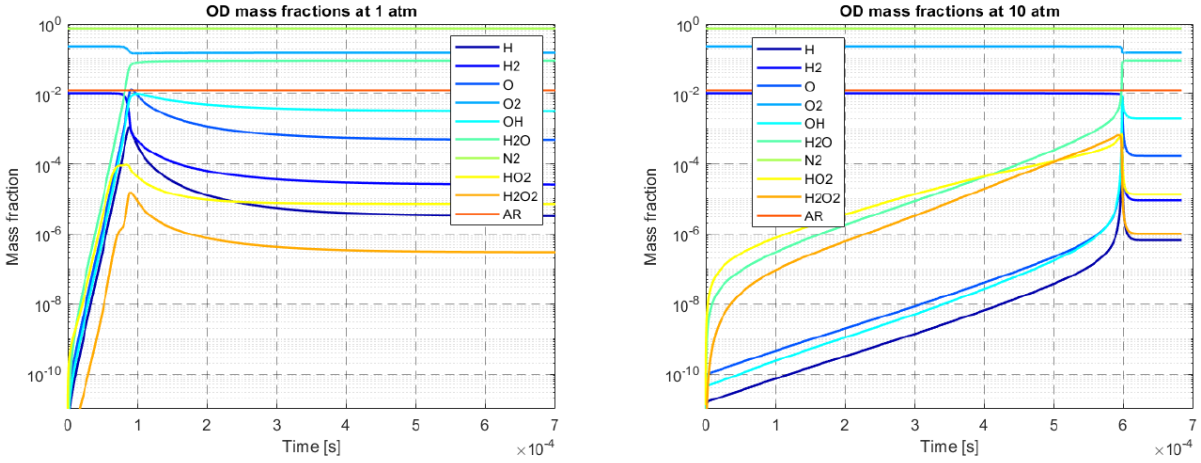


**Figure 2.11:** Mass fractions indicating the autoignition delay time for $\phi = 0.35$ and $T = 1100$ K [19].

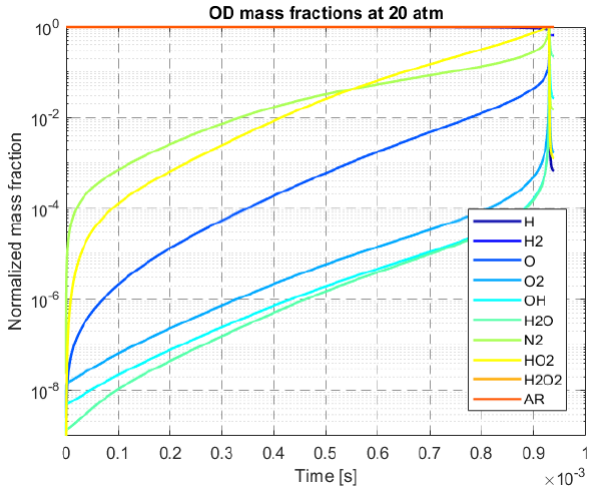


**Figure 2.12:** Mass fractions indicating the autoignition delay time for $\phi = 0.35$ and $T = 1100$ K [19].

To further distinguish between the different behaviours of the autoignition delay time with pressure, three ignition limits can be used as defined by Fleck et al. [54, 55] and Kreutz et al. [56]. Within the first limit, which is characterized by low pressure, the reactions $H + O_2 \longrightarrow OH + O, O + H_2 \longrightarrow H + OH$, and $H_2 + OH \longrightarrow H_2O + H$ compete with the production of HO2 through $H + O_2 + M \longrightarrow HO_2 + M$ (R9). In this regime, $HO_2$ and $H_2O$ act as sinks due to their low chemical reactivity and they are slowly transported out of the reaction zone. Furthermore, R9 is less present, indicating a potential for the mixture to ignite at lower temperatures due to the limited availability of the $HO_2$ sink. But, this is not the case because diffusion plays a larger role for the consumption of H and O radicals, resulting in a decrease in the ignition delay as the pressure increases.

For the second limit, corresponding to moderate pressures (10 atm), the radicals are produced by reactions $H_2 + O \rightleftarrows H + OH$ (R2) and $H_2 + OH \rightleftarrows H_2O + H$ (R3) and they are consumed by $H + O_2 \rightleftarrows O + OH$ (R1) and R9. In this regime, the diffusion loses are less pronounced and R9 is now the main factor for radical losses. This results in an increase in the ignition delay for an increase in pressure.

In the third autoignition limit, the concentration of $HO_2$ increases significantly, enabling the reaction $2HO_2 \longrightarrow H_2O_2 + OH$ (R14). Furthermore, $H_2O_2$ is also partly produced by the reaction $H_2O_2 + H \rightleftarrows H_2 + HO_2$ (R17). As a result, $H_2O_2$ now begins to act as a sink, replacing the role of $HO_2$, by dissociating through $H_2O_2 + M \longrightarrow 2OH + M$ (R15). This decomposition process, although limited by the convection of $H_2O_2$ outside of the reaction zone, leads to a reduction in ignition delay as the pressure increases [19]. At this limit, Rodhiya et al. [57] also observed an increased rate of movement of the flame, attributed to the higher sensitivity to temperature and pressure fluctuations. The mass fraction of the involved species at these three limits, indicating the autoignition delay time, can be observed in Figure 2.11 and Figure 2.12. A visualization of these ignition limits as found by Kreutz et al. [56] for heated air flowing against a mixture of 60% $H_2$ in $N_2$ can be seen in Figure 2.13. Here, the behaviour of the ignition temperature, which is linked directly to the ignition delay time as previously discussed, can be see for a range of pressures.

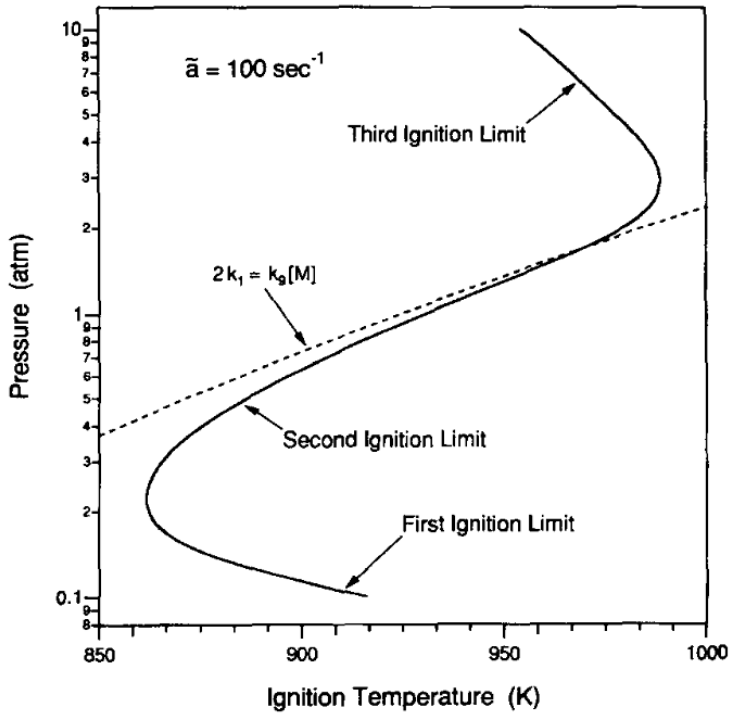


**Figure 2.13:** Ignition limits as a function of pressure for heated air flowing against a cold mixture with 60% $H_2$ in $N_2$ at a density-weighted strain rate of $\tilde{a} = 100$ s$^{-1}$ [56].

As previously mentioned, the corresponding pressure at which these limits are found changes depending on the temperature of the reactants. More precisely, for the case considered in this work, P. Rouco [19] found that at T = 1180 K, the chemical kinetics of the GT36 reside in the second ignition limit. This analysis provides valuable information for the species and reactions to consider when analyzing flashback precursors.

Another interesting finding of Rodhiya et al. [57] related to pressure scaling under reheat conditions is that, at high pressures, the consumption regime significantly changes. Whereas, at atmospheric pressures, 90% of the fuel was consumed by autoignition, this value drops down to 50% for 10 atm, indicating an increased importance of the flame propagation combustion regime of the shear layer.

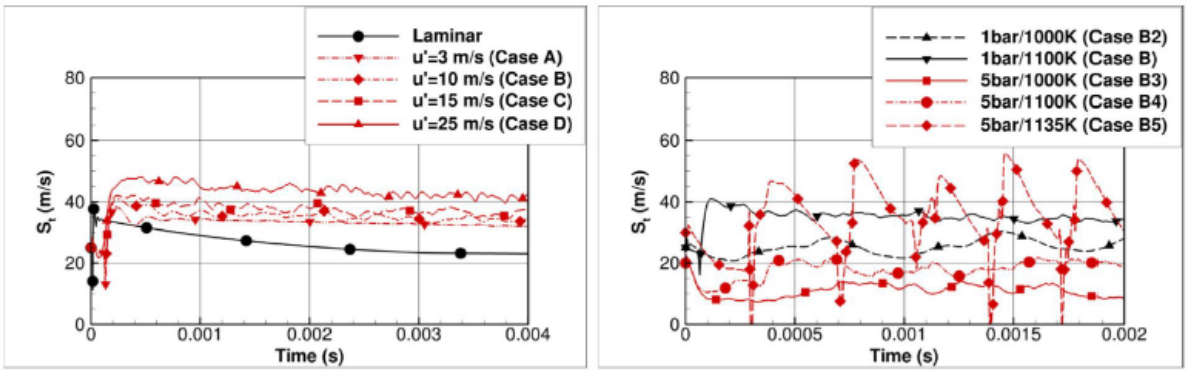


(a) (b)

**Figure 2.14:** Turbulent flame speed under varying levels of turbulence (left) and across different temperatures and pressures (right). DNS study of a hydrogen-fueled reheat combustor at $\phi = 0.35$ [58].

A noteworthy observation is also reported by Aditya et al. [59], where a 3D DNS simulation employing Chemical Explosive Mode Analysis (CEMA) was performed for a hydrogen-fueled sequential combustor ($\phi = 0.35$). Their findings revealed that in a stable state, combustion predominantly happens through autoignition aided flame propagation at various flame locations. Concurrently, they identified an unstable state characterized by periodic emergence of autoignition kernels within the mixing duct. In this state, the autoignition locally expands the gasses, inducing pressure waves in the upstream and downstream directions. Ultimately, these pressure waves converge in the mixing duct, locally compressing the gas, inducing a positive temperature fluctuation, followed by autoignition at this location. In this case, the flame travels upstream, as in the case of a flashback, and then moves back downstream. This phenomena highlights the importance of low frequency thermo-acoustic instabilities. Furthermore, Gruber et al. [58] explored similar phenomena through both two-dimensional and three-dimensional DNS of reheat burners. Their results highlighted a compressibility dependency, particularly at temperatures near the crossover point. This phenomenon was also observed in the variation in turbulent flame speed, when changing the inlet temperature from $T_{\text{in}} = 1000\,\text{K}$ to $T_{\text{in}} = 1135\,\text{K}$, as illustrated in Figure 2.14. Here, the local diffusion of H atoms and heat increases reactivity with increased turbulence intensity, resulting in a large turbulent flame velocity ranging from 30 to 60 m/s.

### 2.4.4. Flame instabilities

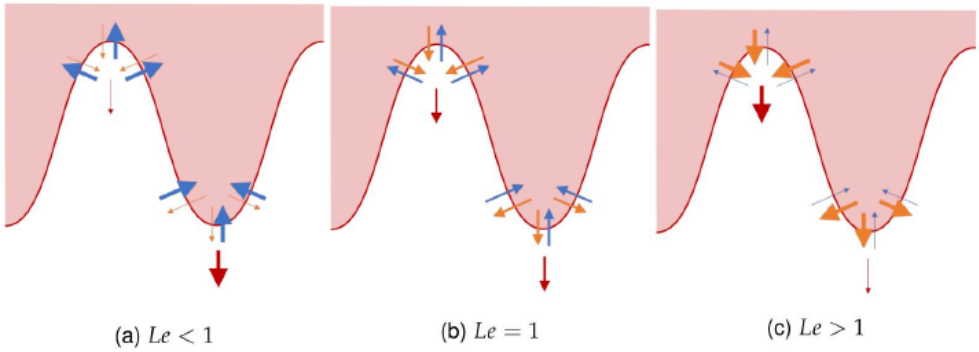


**Figure 2.15:** Illustration of thermo-diffusive instability with flame front expansions and contractions. The blue arrows represent the diffusion of species, the orange arrows represent heat diffusion and the red arrows indicate the decrease/increase of flame speed. [60].

- **Thermo-diffusive instabilities and pressure effects:** Combustion dynamics are significantly influenced by multiple types of instabilities. The foremost is the thermo-diffusive instability, which arises due to unequal diffusion rates of thermal energy and reactants within the combustion environment. As depicted in Figure 2.15, the flame front exhibits a series of expansions and contractions, respectively convex and concave toward the unreacted gases. These expansions increase the surface area of the flame relative to the reacted gases, resulting in considerable thermal energy loss from the flame (symbolized by orange arrows) and an influx of fresh gases (symbolized by blue arrows). In contrast, the contractions present reduced availability of reactants, leading to a thermal accumulation surrounded by hot combustion products. In the case of hydrogen, where Le $< 1$, the expansions rapidly attract new reactants compared to heat loss, enhancing the flame speed. Conversely, at the contractions, less hydrogen atoms are able to diffuse towards the flame front, and thus the flame speed is smaller. This results in an unstable flame, leading to increased curvature and self-generated wrinkling.

  Thermo-diffusive instabilities also present different behaviours when subjected to higher pressures. In a DNS study performed by Rieth et al. [61], the authors demonstrated that $H_2$ diffuses towards convex regions (expansions), while H diffuses towards concave regions (contractions). Furthermore, by analyzing a scenario where ammonia was used as fuel, they concluded that the diffusion of atomic hydrogen in concave regions under atmospheric conditions helps stabilize the flame by increasing the heat release. But, under higher pressures (10 atm), this effect was reduced as the concentration of H was lower due to the three body reactions $H + O_2 + (M) \rightleftarrows HO_2 + (M)$, leading to an increased propensity for thermo-diffusive instabilities and local enrichment.

  Other effects that influence the behaviour of the flame at elevated pressure include [62]:

  - The laminar flame speed and the laminar flame thickness tend to decrease.
  - The Peclet number also decreases, resulting in a predominance of diffusion over convection, exacerbating the predisposition to thermo-diffusive instabilities.

  - The Markstein length, which quantifies the distance over which diffusive-thermal processes, like heat and mass diffusion, influence the flame, gets smaller, indicating an increase in flame speed with negative curvature. This is associated with an increase in fuel consumption rates and a decrease in flame thickness.
  - Finally, the flames generally exhibit more wrinkles, the positive curvature regions becomes thinner, increasing the flame speed, and the negative curvature regions become thicker, leading to a decrease in flame speed and instabilities.

- **Thermoacoustic instabilities:** These happen in various types of thermodynamic engines. This instability typically arises from the interaction between irregular heat release and acoustic disturbances. It is known for creating continuous, large-amplitude oscillations that are self-sustaining. The fluctuating heat release acts as a powerful source for generating sound waves, which travel inside the engine, with some reflecting back from the engine walls. These reflected waves, once they return to the area where they were generated, cause further disturbances in the rate of heat release. If the irregular release of heat aligns with the sound pressure, it leads to a stronger variation in sound pressure. Eventually, some form of non-linear behavior in the burning process will limit the amplitude of these oscillations [63]. Thermoacoustic instabilities are not the focus of this work, but they are worthy of mentioning due to their similarity to the unstable autoignition state discussed in [59]. Furthermore, authors have shown interest in predicting these instabilities through the means of machine learning methods.

These types of instabilities make the flame particularly unstable in the case of hydrogen due to the small Lewis number, the thin flame front and its increased reactivity. This leads to a challenging design and analysis of combustion chambers using hydrogen, where classical methods of flame stabilization such as flame holders or step-like structures are often not enough to contain the movement of the flame. They are also particularly relevant for the autoignition phenomena. As previously explained in Section 2.4.3, the chemical kinetics under the cross-over temperature rely on the availability of H radicals to participate in exothermic reactions. As these instabilities, particularly thermo-diffusive instabilities, are responsible for diffusing H atoms away from the autoignition region in the case where $\mathrm{Le} < 1$, they can decelerate the autoignition process and increase the autoignition delay time. This is dependent on the location of the wrinkled flame fronts which appear in the flame propagation regime and the location of the autoignition zone in the premixing duct. If the autoignition zone is far away from this location, this effect is likely to be less pronounced.

## 2.5. Water injection systems

For the purpose of this research, it was decided that using a water injection system would be the means of suppressing the flashback. As such, to better understand these systems and the results of their application found in the various studies presented in Section 3.4, a background is given in the following.

Water injection is a process whereby $H_2O$, in the form of liquid droplets or steam, is introduced in combustion-driven power systems. It was first introduced in the Allison J33-A-35 engine with the purpose of providing additional power to the F-80 fighter jet [64]. The underlying idea was to increase the mass accelerated by the engine. The same principle was later also applied to the Boeing 707 aircraft to increase the thrust during

take-off. However, this technology was quickly abandoned partly due to the complications arising with the need of carrying water on board and partly due to the advancement of aero-engine technology which allowed them to produce more thrust [65]. The automotive sector has also introduced water injection over the years. For example both rally cars and Formula 1 cars have used to increase the power output. Furthermore, it has also been used in diesel engines to suppress the formation of $NO_x$ and finally the car manufacturer SAAB has also used it in the past on the I99 model to reduce the air temperature [66]. Finally, water injection was also introduced in the power generation sector with the purpose of reducing the $NO_x$ emissions in gas turbines. However, this technology was again abandoned in favour of dry premixed combustion because of the need of demineralised water [67]. Due to the increasingly stringent regulations on emissions, water injection has seen increased interest in all three of the aforementioned fields mainly because of its high potential of reducing $NO_x$.

The purpose of water injection systems in gas turbines depends on the injection location. When the water is injected in the compressor, the evaporation of the droplets lowers the flow temperature which in turn leads to higher densities and power output. Unfortunately, injecting water in the compressor leads to corrosion due to the humid air, especially if the water contains minerals. Furthermore, as the residence time in the compressor is very short, incomplete evaporation may lead to airfoil sputtering. Both of these effects can lead to an increased maintenance cost [68]. In the other case, when the water is injected in the combustion chamber, which is the case of interest for this study, the purpose shifts to stabilizing the flame and to reducing the $NO_x$ emissions. As a downside, however, thermal efficiency is decreased and fuel use is increased [69]. The main interest of this study is to see how efficient is the water spray in stopping the flame front from entering the mixing duct if it is activated at the time a flashback precursor has been detected. As such, water shall be injected in the combustion chamber where the design parameters of the spray shall be tuned for this purpose.

### 2.5.1. Spray design parameters

The effectiveness of the spray depends on several parameters related to the properties of the injected liquid water and the design of the spray itself. These are:

- **Atomizer:** The first choice in the design of the spray relates to its atomizer configuration. Atomization refers to the process whereby the liquid water is transformed into droplets. Common configurations are the plain orifice atomizer and the pressure swirl (simplex) atomizer. The plain orifice injects a solid spray cone through a small orifice by turning the pressure energy into kinetic energy. Meanwhile, the simplex atomizer uses outlet orifice in the form of a disk, through which water can be injected in the form of a swirled spray or a non-swirled spray. The two configurations can be seen in Figure 2.16. The resulting shape of the spray is annular. Both of these atomizers have found applications in combustion applications, but, generally, the hollow cone spray design is preferred in gas turbine applications due to its superior atomization potential [70].

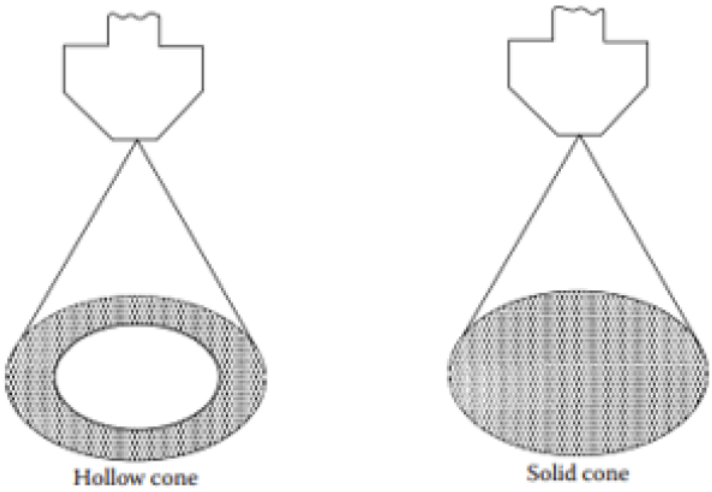


**Figure 2.16:** The solid and hollow cone spray configurations [70]

- **Injection velocity and pressure:** The injection velocity plays a critical role in determining the trajectory of the water droplets. Furthermore, it influences the residence time and consequently the time in which the droplets are able to evaporate. It can be estimated by applying Equation 2.3, where $\dot{m}_L$ is the mass flow of the liquid, $\rho_L$ is the density of the liquid and $d_0$ is the injection diameter.

$$v_{inj} = \frac{4\dot{m}_L}{\pi d_0^2 \rho_L} \tag{2.3}$$

  From the injection velocity the pressure difference between the spray outlet and the combustion chamber can also be obtained by applying Bernoulli's equation, as shown in Equation 2.4.

$$\Delta P = \frac{1}{2}\rho_L v_{inj}^2 \tag{2.4}$$

- **Water mass flow:** The water mass flow, appearing in Equation 2.3, is a critical parameter in determining the stability of the flame and the reduction in emissions. The more water that is added to the products of the first combustion chamber, the lower the adiabatic flame temperature will be, resulting in lower $NO_x$, as previously explained in Section 2.2
- **Sauter Mean Diameter (SMD):** The SMD is defined as the average diameter of a sphere which has the same volume to surface ratio as the typical particle of the spray. This parameter is highly influential towards the physics of the spray through it's impact on the evaporation efficiency and the spread of the spray. The first is increased when the residence time is long enough to allow for complete evaporation. Furthermore, smaller droplets also evaporate faster due to their decreased mass. Meanwhile, the distribution of the spray benefits from a larger SMD. This is because larger droplets have a higher momentum and thus the drop dispersion imposed by the nozzle is less affected by the surrounding flow.

  In general, the liquid surface tension and the liquid viscosity increases the SMD size. Furthermore, while the SMD increases with increasing flow rates and flow

numbers, it also decreases when the pressure differential gets larger. For the ambient medium properties, it was found that the SMD has a non-linear relationship with the ambient pressure, where it first increases until approximately 3 bar and then decreases again until 10 bar. Finally, a similar non-linear relationship was also found for the atomizer dimensions. Both the length/diameter ratio of the swirl chamber and the length/diameter ratio of the final orifice seem to first lead to an increase in the SMD, followed by a subsequent decrease as these ratios get larger.

- **Swirl number:** If one wishes to use a simplex injector where the flow is also swirled, the swirl number also becomes an important parameter that influences the flow dynamics and the effectiveness of the spray. Increasing the swirl tends to improve the mixing of the water with the ambient by promoting the break-up of droplets. However, in some cases, it can lead to decreased flashback resistance through the combustion induced vortex breakdown (CIVB) pathway. Nevertheless, it is important to note that an increase in swirl will lead to an increase in combustion efficiency and a smaller amount of water [71]. The influence of the swirl number on the SMD can be observed directly in the flow dynamics through the tangential component of the velocity and in the modification of the SMD through the adjustment of the pressure differential.
- **Atomizer geometry:** The geometry of the atomizer is composed of several parameters, depending on the desired configuration. For the solid cone atomizer, the parameters of interest are the length of the orifice, its diameter and the cone angle. Meanwhile, for the simplex injector, the thickness angle serves as an extra parameter which determines the ratio between the air core flow and the water flow. As seen in the previous sections, these parameters influence the SMD. In addition to that, the dispersion of the droplets throughout the combustion chamber is also highly influenced by the external angle and the thickness of the resulting annular sheet.
- **Injection location:** The performance of the spray in suppressing the flashback could also be highly influenced by the injection location. While the most common location is in the premixing duct, other studies [71, 72] have quantified the performance of the combustion when the spray was injected either in the ignition zone, after it, or in a combination of the three locations. As the autoignition flashback studied in this work travels close to the speed of sound, an injection location closer to the autoignition zone could prove useful in this scenario, minimizing the time needed for the particles to influence the temperature of the flow.

# 3

# Literature review

This chapter provides an overview on the state of the art research involved in the work of this thesis. First, the problem of predicting the flashback event is tackled. For this, a short description of dynamical systems exhibiting extreme events is given, followed by general machine learning algorithms that attempt to predict such dynamics. Then, a more in depth review containing methods that have been specifically applied to predicting events similar to flashback is given.

## 3.1. Dynamical systems

A dynamical system [73] is a mathematical framework used to describe a system whose state evolves over time according to a fixed rule. It encompasses any system, from simple mechanical systems to complex biological or financial systems, where the current state of the system uniquely indicates its future state. While simple systems can be approximated by a linear equation, others, which are nonlinear and high dimensional, may be harder to describe and even harder to predict.

The branch of dynamical systems which studies the underlying behaviour of such complex systems displaying aperiodic behaviour over time is called chaos theory. This theory states that the behaviour of such a system can be predicted only for a short duration, i.e. the predictability time. Central to chaos theory is the butterfly effect, which describes how infinitesimal disruptions in initial conditions can lead to vastly different result in deterministic nonlinear systems. This effect highlights the limited predictability in chaotic systems due to their sensitivity to initial conditions. This also indicates that approximating the present state shall not give an approximate view of the future [74].

Mathematically, this can be expressed by considering a dynamical system described by a set of equations. If $J(x(t))$ is the state of the system at a given time $t$ with the initial condition $x_0$, then, for two slightly different initial conditions $x_0$ and $y_0$, the states at a later time diverge according to:

$$|J(x(t)) - J(y(t))| \approx |J(x_0) - J(y_0)|\, e^{\lambda} t$$

where $\lambda$ is the largest global Lyapunov exponent, which, for chaotic systems, must be larger than 0. This equation signifies that as time progresses, the difference in the trajectories of the system, originating from these slightly different initial conditions, grows exponentially. This leads to unpredictable and divergent outcomes, indicative of chaotic behavior [73].

Prime examples of systems displaying this kind of behaviour are turbulent flows, the medium in which combustion takes place in gas turbines.

Although predicting the dynamics of chaotic systems is a challenging task, considerable attention has been given to these system due to their tendency to present extreme events. Extreme events are sudden, significant deviations in the dynamics of a system, often leading to substantial impacts [75]. Such events take place in a wide range of nonlinear, dynamic processes observed in daily life, including environmental phenomena like rogue waves and avalanches, as well as socio-economic occurrences like stock market crashes. The widespread nature and potential for severe consequences underscore the importance of understanding and predicting these events [76, 77, 78].

The complexity of these phenomena makes creating accurate mathematical models difficult. While simplifications can capture general process characteristics, they fall short in predicting rare and extreme events. A key challenge is data scarcity, as these events are infrequent, leaving insufficient data for developing and validating predictive algorithms [79].

The behaviour of chaotic systems often results in non-stationary time series [80]. These present a varying mean, variance and autocorellation. Some usual techniques that adjust a non-stationary time series to make it more predictable include the following: differencing, where the time series is transformed to the difference between one time step and the next, detrending, where long-term shifts in the data are removed and seasonal adjustment, where fluctuations in the data are accounted for. Nevertheless, these do not always manage to make a time series stationary. This is partly the reason why machine learning methods, which are more capable of learning non-stationary data, especially when helped by the aforementioned techniques, are becoming increasingly popular for tasks which involve predicting dynamical systems.

## 3.2. Machine learning

Machine learning is a branch of artificial intelligence dedicated to creating algorithms and statistical models that allow computers to carry out tasks by recognizing patterns and drawing conclusions from data, instead of adhering to explicit instructions. This field combines aspects of computer science and statistics to provide machines with the ability to make predictions or decisions adaptively as they are exposed to new data. At its core, machine learning involves training models on datasets, which then learn to make predictions or decisions that are refined through continuous exposure to new data.

The field encompasses a range of algorithms, each suited to different types of tasks and data. These algorithms can be categorized into three primary groups: supervised learning, where models are trained using labeled data; unsupervised learning, which involves finding patterns and links in unlabeled data; and reinforcement learning, which focuses on taking decisions based on a system of rewards and penalties. For applications that involve predicting the behaviour of dynamical systems, certain machine learning algorithms are particularly useful. They are adept at handling sequential data, extracting relevant temporal patterns and correlations crucial for effective forecasting and detecting anomalies. These can be divided into two classifications.

### 3.2.1. Approach towards predicition

The first classification of machine learning algorithms that are able to predict dynamical systems can be made based on the approach used to make the prediction. The two approaches available are time series prediction and precursor identification.

Time series prediction refers to the process of using historical data to forecast values in a sequence of time-orderd data points. It involves analyzing patterns in the historical data, such as trends, seasonal variations, and cycles, to predict future values. The primary focus of time series prediction is forecasting, which can range from short-term predictions (like stock prices for the next day) to long-term forecasts (like climate change effects over decades). Use of time series forecasting is widespread, with applications being found in finance, meteorology and other physical phenomena. Common techniques for time series prediction are classical methods such as autoregressive moving averages (ARMA) used for financial data and newer methods involving neural networks such as CNNs and LSTMs, transformers, generative adversial networks (GAN) and/or others.

Precursor identification, on the other hand, involves the detection of specific patterns or indicators within a time series that signal the likelihood of a significant event or change in the future. Unlike time series prediction, which forecasts specific future values, precursor identification focuses on recognizing the signs or conditions that often precede an event. This is particularly important in areas like healthcare, where identifying precursors can lead to early intervention for diseases, or in system monitoring, where detecting early signs of failure can prevent breakdowns. Here, common approaches include clustering-based, density-estimation-based and reconstruction-based methods.

### 3.2.2. Learning methodology

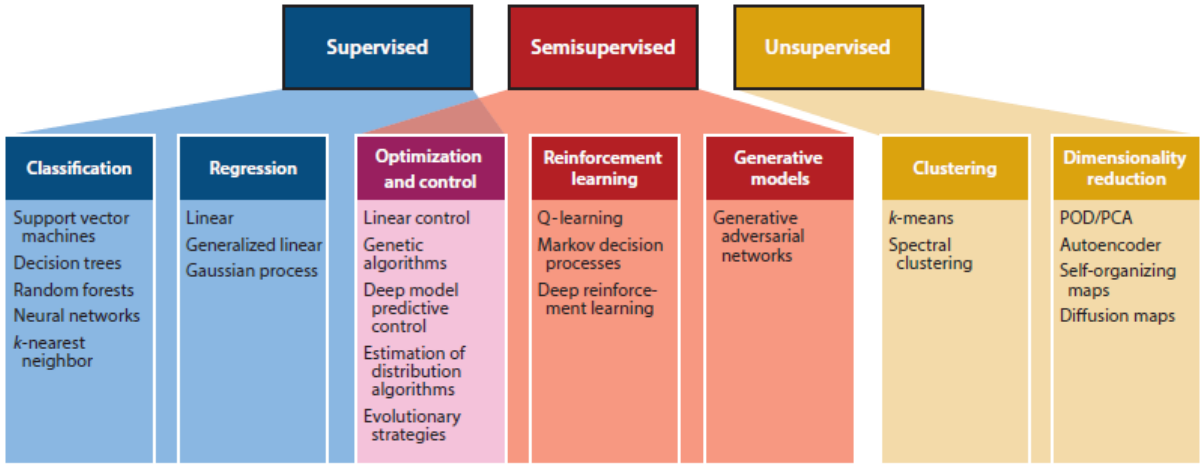


**Figure 3.1:** ML algorithm classified into supervised, unsupervised and semi-supervised [81]

The second classification is the type of machine learning used, supervised or unsupervised, both of which have been argued for in terms of viability for the prediction of a flashback-type event. The first, as previously explained, aims to create a map between inputs and outputs, usually through the means of classification or regression. The intuitive advantage of this method would be the inherent flexibility of such algorithms, which are able to learn any type of function, according to its own set of rules, as long as there is enough data to represent

that function. Unfortunately, this is potentially one of the problems of applying these types of algorithms for extreme events, due to their sparsity. This is where unsupervised machine learning could become useful, as this type of algorithm identifies the structure and patterns which the data follows on its own. Different machine learning algorithms which fall under these categories can be seen in Figure 3.1. An explanation for some of the most popular algorithms and their uses is detailed in the following paragraphs.

**Supervised learning**
In general, supervised learning implies using corrective information to minimize a cost function that in turn determines the correct parameters of the learning method. The most well-known methods within this category are neural networks (NNs), which can be described as function approximators. Their popularity stems from the universal approximation theorem [82], which states that a sufficiently large and deep neural network can approximate any given function. At its core, a NN is composed of layers of neurons connected by weights and biases, which are updated throughout the learning process using backpropagation.

In the context of predicting the behaviour of dynamical systems there are several types of neural networks which have been applied successfully, with some of them finding applications in predicting extreme events as well [80]. Some of the more popular ones are the following:

- **Convolutional neural networks (CNNs) [83]:** This type of neural network has an architecture that is generally composed of convolution, pooling and fully connected layers. In a CNN, a neuron is exclusively connected to a single input region and the neurons in a layer share a weight matrix. These particularities allow the network to detect patterns in the data, independent of the location in the 1D or the 2D field. This is useful for both precursor identification, by identifying peculiar features of the dataset, and time-series forecasting, by feeding the network a certain input and allowing it to complete the rest of the sequence using the learned patterns. The major shortcoming of CNNs for forecasting applications is the relatively short prediction horizon. Nevertheless, the extracting the relevant features using convolution and using them for points which are farther away can still be achieved by using temporal convolutional networks (TCNs), by graph neural networks (GNNs) and by other hybrid networks, such as combinations between CNNs and recurrent neural networks (RNNs).
- **Recurrent neural networks (RNNs) [83]:** RNNs implicitly take into account the relationship between the current sample of the time series and past ones, automatically determining how far behind to look in the past. They make use of recurrent layers, where one input time step is processed at a time. As traditional RNNs suffer from unstable training (the vanishing or exploding gradients), which prevents the network from understanding long term dependencies, currently, they are being replaced by more sophisticated rsions sveuch as echo state networks (ESNs), long short-term memory networks (LSTM), gated recurrent units (GRUs) and reservoir computing methods (RC).

There are many other models which have been developed recently, with some of the more popular being graph neural networks (GNNs) [84], deep gaussian processes (DGPs)[85], generative adversarial networks (GANs) [86], diffusion models and transformers.

Identified drawbacks of the aforementioned methods are as follows [80]. Firstly, deep learning methods, with the exception of DGPs, can not provide an uncertainty interval of

the model prediction. Secondly, when creating a deeper and more complex network, these architectures are subject to overfitting. Thirdly, there is a need for sufficiently long time series. Some deep learning architectures need to estimate millions of parameters, indicating thus the need for a large amount of training data. This problem has been partially solved by means of data augmentation, but the proposed methods are still lacking. Finally, the last problem is that most of the architectures assume that the time series is stationary over time. When the dynamical system is chaotic, a concept drift phenomena is observed, whereby the prediction accuracy is dramatically decreased.

**Unsupervised learning**
In supervised learning the task implies the extraction of feature or other relevant patterns from the data by specifying global criteria, without the need for labeled training data. Unsupervised learning deals with problems of dimensionality reduction, quantization and clustering [81].

Dimensionality reduction is a method of representing a dataset composed of multiple dimensions, such as a multi-variate time series, by a lower dimensional model. This technique is necessary when dealing with datasets which contain a large number of variables, such as combustion flows. Besides lowering the computational power necessary in the models, it also allows for the methods to focus on the variables (or characteristics arising from combinations of variables) that best represent an extreme event and its precursor. Some common methods include:

- **Proper orthogonal decomposition (POD) [87]**: POD, also known as Principal Component Analysis (PCA) and commonly used in the field of fluid dynamics, is an eigenvalue-based method which extract the dominant modes or features from a dataset. It identifies orthogonal modes which capture the most variance (or the maximum kinetic energy) by decomposing the data using methods such as singular value decomposition (SVD). Mathematically, this can be written as follows:

$$u(x,t) = \sum_{i=1}^{\infty} a_i(t)\phi(x) \tag{3.1}$$

  where $u(x,t)$ is the velocity vector field, $\phi_i(x)$ are deterministic spatial functions or modes, and $a_i(t)$ are the time-dependent coefficients.
- **Co-kurtosis PCA [88]:** This method was proposed to improve on the classical principal component analysis, as it was observed that PCA, which transforms the thermo-chemical state space into eigenvectors based on the co-variance of the data (much like POD), could fail when it comes to identifying localized chemical dynamics such as ignition kernels. Instead, this method proposes to use the fourth order statistical moment, the co-kurtosis tensor, to compute the principal vectors. In this way, the directions of these vectors now point towards the outliers contained in the dataset, which can locally indicate the appearance of ignition kernels. The method was tested on a synthetic dataset and proved to be better than PCA in terms of reconstruction error of the original thermo-chemical state. Furthermore, in [89], CoK-PCA was also successfully used for anomaly detection. In this algorithm, the data is decomposed into several spatial sub-domains, and the principal kurtosis tensors are computed in each sub-domain and at each time step to identify the relative importance of each features towards the overall co-kurtosis. By comparing the feature moment metric

distribution to its value at a regular time step/location, anomalies were identified for two turbulent auto-ignition combustion cases reliably.

- **Autoencoders [81]:** Autoencoders are a type of neural networks that particularly excel in dimensionality reduction and feature learning. The first component is an encoder, the part of the network which compresses the input data into a smaller dimensions. This part could be composed of different layers such as CNN layers or LSTM layers which allow for the network to capture different spatio-temporal patterns and features. The network's second component is the decoder, which aims to rebuild the original data based on the encoder's output. Training these networks involves reducing the error between the original data and the decoder's output, often employing a loss function such as Mean Squared Error (MSE). They can be used for denoising, anomaly detection (by learning to reconstruct normal data and failing to do so with anomalous data) and, similarly to the other dimensionality reduction techniques, they can be used to reduce the computational load of another method.

While most of the aforementioned methods in the supervised learning part have found applications in time-series forecasting, clustering, on the other hand, has found direct applications in precursor identification. Clustering is an unsupervised learning technique whereby data is clustered into similar groups. Common methods includes the following:

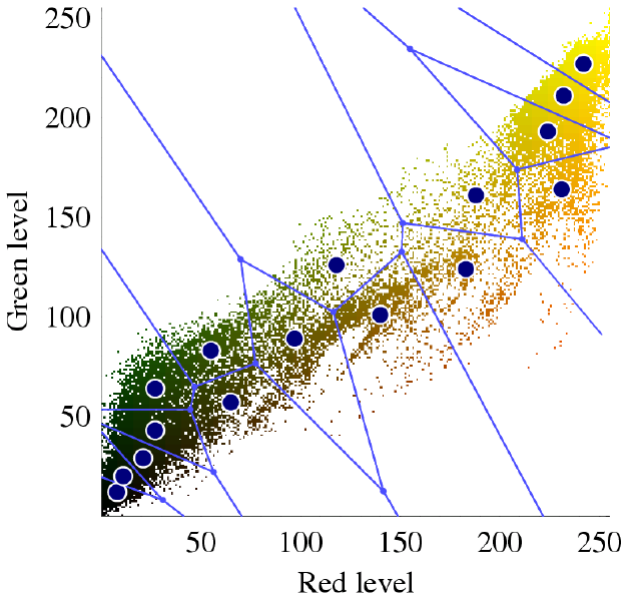


**Figure 3.2:** K-means algorithm applied to the colors in an image of a flower. Voronoi cells and their centroids are shown in blue. [90]

- **K-means clustering:** Initially introduced by Hartigan [91], this algorithm divides a dataset of $n$ points into $k$ clusters, where each observation is partitioned into the cluster with the nearest mean. This results in a tessellation into so-called Voronoi cells, as shown in Figure 3.2. While an improved version of this algorithm, *k-means++*, was applied in modelling the mixing layer of turbulent boundary layer with satisfactory results, this method has not actually been applied to chaotic systems showing extreme events, with the exception of Golyska [92] which shall be discussed shortly.
- **Spectral clustering [93]:** Spectral clustering is a widely used technique for grouping data. It operates by identifying communities of nodes and the connections (edges)

between them, akin to the principles seen in graph theory. The method involves computing the eigenvalues of the graph data's similarity matrix, which are then employed in the clustering process. This approach can be visualized as a two-dimensional system of masses and springs, where each data point is depicted as a mass, and the springs between them - with stiffness representing the edge weight - signify the similarity between data points. Despite its usefulness, spectral clustering is often considered resource-intensive due to the computational demands of calculating the eigenvalues of the similarity matrix.

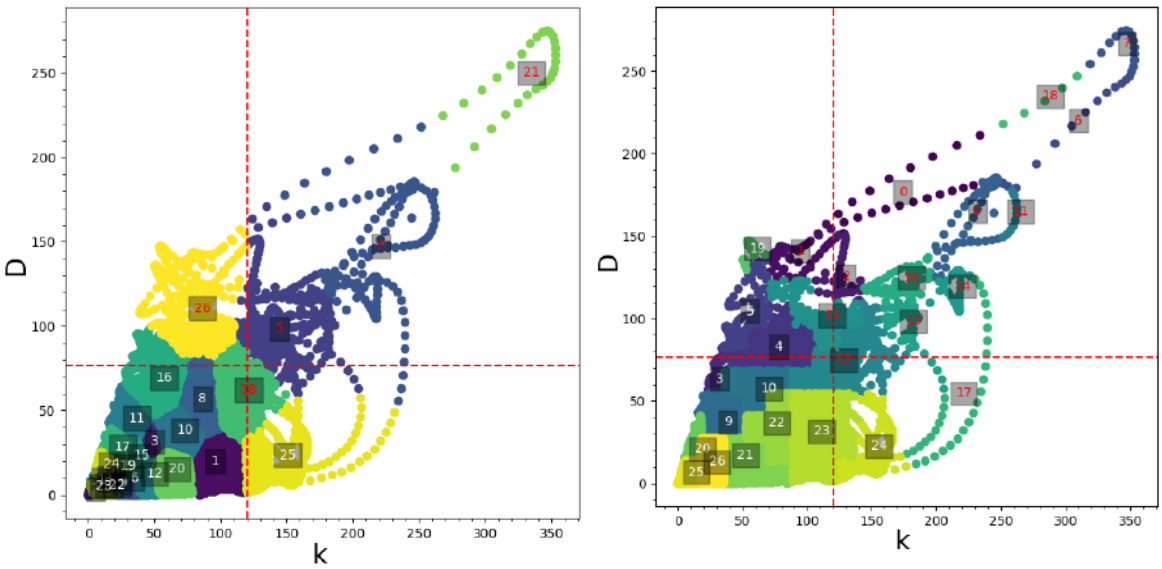


**Figure 3.3:** The clustered path of the Moehlis-Faisst-Eckhardt (MFE) system in the phase space. Left figure shows the clustering achieved with the *k-means++* algorithm and the right figure corresponds to the clustering achieved by the modularity-based algorithm. The clusters classified as extreme are indicated by red numbers for the cluster centers [92].

- **Modularity-based clustering:** This type of clustering technique, similarly to spectral clustering, is applied to graphs. It relies on maximizing modularity, which is a measure of strength of division into communities based on comparing the edges and the weights of the network in question to a network composed of the same nodes but with a random distribution of edges and weights. Maximizing this difference, this method finds communities which are similar to each other, where intra-connectivity is high and inter-connectivity with other communities is low. Of particular interest is the method proposed by Newman [94] due to its high modularity score as compared to other methods, relatively good complexity ($\mathcal{O}(N^2 \log\, n)$) [92] and the fact that it has already found applications in extreme event analysis [95]. The method of Newman [94] was in fact compared with the *k-means++* algorithm in a study performed by Golyska [92] where several systems exhibiting extreme events were studied. Although no conclusive difference was found in terms of prediction time (or the time spent by the system in the clusters prior to the extreme clusters), the modularity-based clustering approach resulted in better scores in the confusion matrix. This indicates that modularity-based clustering does a better job at identifying the dynamics of a system. Furthermore, Golyska [92] also indicated that if the approach is modified to

include only extreme nodes in extreme communities, these results should be further improved. The problem of not having this exact division between the extreme and non-extreme communities becomes evident by looking at Figure 3.3. Here, it can be seen that both clustering approaches result in extreme clusters which have little extreme nodes and non-extreme clusters which may contain extreme nodes. From these figures, one can also intuitively understand that a clustering algorithm which focuses on identifying the systems dynamics should outperform a method which merely relies on variance. This is because a precursor cluster identified based on variance should result in a large rate of false positives as compared to a precursor cluster identified based on the system dynamics. Nevertheless, if one wishes to accurately compare these two algorithms, the aforementioned change to the extreme clusters should be applied to both methods first.

## 3.3. Methods applied to chaotic systems

In this section, an overview of the existing method which are a close fit for autoignition flashbacks is presented. These methods have been chosen either due to their application to extreme events, in particular thermo-acoustic instabilities and turbulent flows exhibiting energy bursts, or due to their application to chaotic systems. In the following, they are split between unsupervised learning and supervised learning methods.

### 3.3.1. Unsupervised learning

A clustering-based, purely data driven approach aimed to fully describe dynamical systems was first introduced by Schmid et al. [95, 96] and then further developed by Golyska and Doan [92] to use it for precursor identification. Here, the Moehlis-Faisst-Eckhart model and the Kolmogorov flow model were represented in the phase space and then tesselated to reduce the system's size. Then, a transition probability matrix and modularity based clustering were used to describe the systems behaviour, resulting in communities with similar flow structures and the likelihood of transitioning between them. Finally, to predict the extreme events, communities were divided into normal clusters, precursor clusters and extreme clusters, and the prediction time is based on the time spent in precursor clusters which have a high probability of transitioning to an extreme cluster. Although showing a significant rate of false positives, by slightly altering the definition of extreme clusters and their detection, this algorithm seems like a good candidate which could be applied to flashbacks. While in this study the quantities represented in the phase space were the energy dissipation rate and the kinetic energy, the algorithm's flexibility allows for the use of any other representative variable, which for instance, in the case of autoignition flashback, could be pressure, temperature, certain species or velocity fluctuations.

The next method considered is based on recurrence quantification and was applied to pressure time series of a combustion experiment with the purpose of detecting an incoming flashback [97]. The authors stipulate that recurrence analysis should be able to identify patterns of deterministic and non-deterministic dynamics that signify the changes in the dynamics of a system appearing just before the extreme event. As such, the phase portrait was reconstructed using time delay embedding and after a recurrence threshold was chosen, the recurrence matrix was constructed and plotted. Finally, recurrence quantification analysis was performed using indicators such as recurrence rate, divergence and determinism, and flashback was predicted with 2-4 seconds prior to the event. As mentioned before, although

different in nature, the flashback event observed in the LES simulation does have similar characteristics in terms of pressure time series. As such, this method also look promising due to the robust detection and large prediction time. One disadvantage is the longer computational time, which might not be suitable for online detection. Furthermore, another drawback again lies in the simulation duration, i.e. because a lasting observable change has to be detected first, the time scale of recurrence analysis might not be small enough.

Different hybrid approaches involving complex networks were proposed by Murugesan et al. [98] and Kobayashi et al. [99] and applied to thermoacoustic instabilities, which is often a precursor to flashback [26]. Here, the authors of [99], use a synchronization index, which increases when the mutual coupling between pressure fluctuations and heat release rate strengthens to calculate the frequency of transition in the ordinal partition transition network. This network consists of order patterns expressing the relationship between the two time series in adjacent locations (how one increases/decreases with respect to the increase/decrease of the other and with respect to the increase/decrease of itself) and the frequency of transition between the patterns as weighted and directed edges. The network is expressed as an adjacency matrix. Then, PCA is applied to the probability distribution in the 16-dimensional transition patters in the ordinal transition networks and the vectors emerging from PCA are used as input to an SVM classifier, which classifies the data based on clusters generated through the k-means method. As for results, the synchronization index clearly shows a region of the combustion chamber where positive coupling between the pressure and heat-release-rate fluctuations emerges near the shear layer formed due to the large-scale vortices. Furthermore, the ordinal partition transition networks do successfully capture the beginning of the instabilities, and the same can be said by the PCA vectors. Finally the SVM manages to categorize the data into noise, transition and instability, and through it, online suppression is also achieved. Now although this is a hybrid approach, where the known behaviour of thermoacoustic instabilities was taken advantage of, these methods still present significant interest as the flashback phenomena of this study presents a somewhat similar behaviour, i.e. autoignition is induced due to the temperature fluctuations arising from pressure waves generated by heat release. Another drawback that should be mentioned is the significantly higher amount of data needed in the discussed study.

Another popular approach again employed for the detection of an incoming thermoacoustic instability is through the critical slowing down theory (CSD) [100]. CSD refers to a system which exhibits a reduced recovery rate to perturbations as a bifurcation is approaching. This study was able to detect CSD well before the amplitude of thermoacoustic oscillation increased, through both the variance and the lag-1 autocorellation coefficient applied to pressure time series, verifying both for statistical significance.

The unsupervised learning methods found show promise towards prediction the flashback event, with each of them presenting their own advantages and disadvantages. Firstly, the modularity-based clustering approach is a great candidate due to its insensitivity towards the underlying physical phenomena. Indeed, being purely data-driven offers and advantage, mitigating the need for data that fits certain criteria, while still capturing the true dynamics of the system due to the modularity-based clustering technique. This is reflected in the study of Golyska and Doan [101] in the application of the algorithm to multiple chaotic system, ranging from simple ones such as the Lorentz attractor to complex Kolmogorov flows. The next two methods discussed show promise due to their proven capabilities in an online setting. The issue is that they have been applied to thermo-acoustic instabilities, thus taking

advantage of the known behaviour of this phenomena. As such, although the autoignition flashback shares some common characteristics with thermo-acoustic instabilities, it remains a question whether or not this type of analysis fits the requirements. Lastly, the main disadvantage of CSD is that some of its indices, such as autocorellation, are known to under-perform on non-stationary time-series. This is the case of the autoignition flashback as the mean and the variance of the different variables change over time. All in all, for unsupervised learning, two points must be highlighted. Firstly, a large advantage is given by methods which are agnostic to the underlying physical phenomena and, secondly, the method chosen should be able to deal with non-stationary time-series to detect extreme events in chaotic systems.

### 3.3.2. Supervised learning

Another study that analyzed pressure time series of thermoacoustic oscillations was done by Bury et al. [102]. The authors, inspired by the critical slowing down theory, gathered a large dataset of systems presenting bifurcations and used it to train a convolutional neural network (CNN) combined with a long short-term memory (LSTM) network, with the idea that the NN could not only detect an incoming bifurcation, but it could also determine which type of bifurcation it is. As for the results, it was shown that the NN was able to detect an incoming instability with a better score on the receiver operating characteristic (ROC) curve, but it did not always assign the correct type of bifurcation. Postulating on the similarity between the pressure time series used in these studies and the pressure time series available from the LES simulation, either CSD or a CNN-LSTM combination, along with the training data set, could potentially be used to detect an incoming flashback. It should be mentioned that this sort of method, due to easily obtainable data, is preferable, as a non-intrusive pressure probe could be used in a real gas turbine with ease, thus achieving online prediction. Nevertheless, even though there is a considerable amount of data in this study which could be used, there is not data pertaining to autoignition flashback. This may prove problematic as the network might not be able to learn the new phenomena through the limited amount of data which can be supplied through LES simulations.

Asch et al. [103] sought out to predict extreme events in dynamical systems in a more data-driven way by using neural networks. The feedforward NN, the LSTM NN and the reservoir computing network were used in three separate dynamical systems, with good prediction times. A sensitivity analysis was carried out showing that the feedforward NN was the most sensitive to noisy data and model hyperparameters. The LSTM RNN was more robust in that sense, with minimal tuning of the hyperparameters needed and finally the RC network did consistently outperform the other two for the Kolmogorov flow. While these results are promising, the proposed method has one critical flaw, which is the lack of data availability for training that contains extreme events. To circumvent this, the authors performed computationally expensive simulations to gather enough data for these systems, which although applicable for simpler systems such as the ones analyzed here, is a more expensive task when it comes to LES simulations.

McCartney et al. [104] also studied precursor identification in thermoacoustic instabilities with the specific aim of online detection. To begin, they reviewed the existing methods stating that intermittency based methods such as recurrence plots and the Hurst Exponent do seem to provide good warning times but they are slow to compute and insufficient for an online detection. As such, the authors looked towards supervised machine learning methods. In particular, two methods of supervised learning are showcased and contrasted with the

Hurst exponent and Auto-Regressive (AR) models. In the first approach, the original dynamic pressure signal is fed into Hidden Markov Models (HMMs) to categorize its state. The second approach involves utilizing the signal that has undergone transformation through Detrended Fluctuation Analysis (DFA) as input. A universal machine learning classifier is applied to this transformed signal, with the classifier being chosen and optimized through the process of Automatic Machine Learning (AutoML), for the purpose of categorizing the signal's state. For the results, the ML methods initially outperform the AR and Hurst exponents methods, but their accuracy drops to similar levels as soon as the data is normalized. Finally, the ML methods completely fail to predict the incoming thermoacoustic instability when a point unseen during the training is fed as input. This again highlights the problem of supervised machine learning using a small set of training data, a problem that could also occur with the data available in this study. It should also be mentioned that the AR model involving CSD theory not only is more robust than the ML methods, but it also is quicker to calculate than the Hurst exponent and it requires much shorter time scales, which is of interest considering that the flashback event happens extremely fast.

Another method considered also making use of recurrence networks was developed by Ruiz et al. [105] and applied to the problem of thermoacoustic instabilities. Here, the aperiodic and periodic structures in the recurrence network were classified using a Convolutional Neural Network (CNN) which was further used to define the proximity of the dynamic state to the onset of the instability by making use of the knowledge that pressure fluctuations during normal operation are aperiodic and thermoacoustic instabilities are periodic. In terms of training, the lack of data could be circumvented by feeding the network periodic data coming from different sources and aperiodic data in the form of noise. Nevertheless, the use of information that is unique to thermo-acoustic instabilities is a disadvantage.

In a research done by Qi et al. [106], the authors used a densely connected CNN network model to detect extreme events arising in the truncated Korteweg-de Vries (tKdV) equation, which generates skewed distributions similar to outcomes from laboratory observations of shallow water waves encountering a sudden depth change. The method employs a data-driven architecture where the relative entropy loss function, together with empirical partition functions, is used to capture the differences in the shape of the density distribution functions of the output and the training data over both time and space. Here the dominant structures of the turbulent flow field are emphasized, such that the network does not get overwhelmed with learning small-scale dynamics. The network showed high skill in accurately predicting the statistical emergence of extreme events over a large number of statistical regimes. One particular merit of this method is that the NN was trained using data which was drawn only from the near-Gaussian regime of the tKdV model solutions. Another merit of this method consists in the CNN architecture used. The network employs convolutions with dilated kernels, by adding zeros between the elements of the original kernel. This dilation allows the network to capture structures at multiple scales more effectively, as it can adaptively include different spatial and temporal scales, making it able to better understand the multiscale nature of turbulent dynamics. Furthermore, the network architecture also incorporates dense connections. This means that the output from each layer is not just passed to the next layer, but is also used as input for all subsequent layers. In this way, information is integrated from various scales in each layer. One drawback of this solution when applied to reheat combustion dynamics is the need to pre-process the data and create appropriate probability distribution functions (PDFs) for the different variables obtained from the LES simulation. This is difficult due to the complexity of

combustion flows, which span a wide range of values over both time and space. Meanwhile, for the tKdV equation, the steady-state distribution can be characterized by the invariant Gibbs measure derived from statistical mechanics principles.

In a study done by Jiang et al. [107], the authors have developed a framework utilizing two deep convolutional neural network (DCNN) for data-driven prediction of extreme events in two-dimensional nonlinear physical systems, both temporally ("when") and spatially ("where"). This approach involves using two-dimensional snapshots or images as data or measurements. For effective training of the DCNN, a suitable labeling scheme is adopted, aimed at predicting extreme events within a specified time horizon. Once the DCNN predicts the likelihood of an extreme event within this time frame, a spatial labeling method is then employed to determine where the event is likely to occur. The effectiveness and accuracy of this machine-learning-based prediction framework are demonstrated and validated by the authors through synthetic data derived from the two-dimensional complex Ginzburg-Landau equation and empirical wind speed data from the North Atlantic Ocean. For the CGLE system, the time prediction was investigated for 10 time steps in advance resulting in 94.4 % AUC for the ROC curve metric for the better network out of the two (ResNet-50). When moving to 20 time steps in advance, ResNet-50 now resulted in a AUC value of 82%. In terms of the spatial accuracy, when trying to predict where the extreme event will happen inside a 2 x 2 grid, ResNet-50 achieved an AUC of 90%. When moving to a 5 x 5 grid, the AUC is not significantly smaller, with a value of 85%. The results are similar for the wind speed data, indicating an overall good performance of these networks. One mention here is the large amount of training data available in this study, corresponding to approximately 100.000 2D snapshots for the CGLE system and 44.000 snapshots of wind speed data.

A study done by Racca et al. [108] used echo state networks to predict and control extreme events in a chaotic shear flow. They indicate that the network was able to predict extreme events up to more than five Lyapunov times in the future. Furthermore, by training the NN with datasets containing non-converged statistics (short time series), they also showed that the NN is able to extrapolate the flow's long-term statistics. The network was also tested for robustness showing good behaviour over a wide range of Reynolds numbers. Another notable feature of this study is the use of Recycle Validation, which exploits Bayesian sampling, to select the hyperparameters of the NN. The authors indicate that the hyperparameters are key in the performance of the method.

Another study done by Ren et al. [109] demonstrated the performance of a CNN + LSTM neural network in predicting the evolution of a freely propagating turbulent premixed flame and BL turbulent premixed flame, when trained on DNS data. The authors used this type of architecture on the premises that the CNN model is able to capture the spatial dependencies, while the LSTM model is able to solve the temporal ones. Indeed, the results indicated that the performance of the CNN + LSTM architecture was much better than a stand-alone LSTM model. Training on average on 8 2D snapshots, the model was tasked with the prediction of the next snapshot, which was $0.012\tau_L$ for the freely propagating flames and $0.006\tau_L$ for the boundary layer flames away, where $\tau_L = 3.47$ ms is the laminar flame time for the freely propagating flame and $\tau_L = 0.31$ respectively for the BL turbulent premixed flame. For the mass fractions, the model retained a correlation coefficient between the DNS data and the CNN + LSTM prediction of 0.99 for the boundary layer flame and 0.93 for the freely propagating flames. This work demonstrates the capabilities of the discussed network to accurately predict the evolution of various turbulent flames. Although,

in the work of this thesis, autoignition is the phenomena of interest, the ability of this model to predict information about the mass fractions of different species makes it interesting for its application away from the flame region as well.

Another study which has compared neural networks to each other for time series forecasting of wind speed data was done by Liu et al. [110]. Here, the authors proposed a new network architecture based on wavelet-package decomposition (WPD), a CNN and a LSTM network. The WPD is utilized to break down the original wind speed time series into several sub-layers of varying frequencies. Subsequently, a CNN employing 1D convolution is applied to predict the high-frequency sub-layers, while a combined CNN-LSTM architecture is deployed for forecasting the low-frequency sub-layers. To verify the results of the proposed model, the authors compared it to the ARIMA model, SVM model, WPD-BP model, WPD-GRNN model, WPD-Elman model, WPD-ELM model, WPD-CEEMDAN-RBF model using four wind speed data sets. The results indicated that the WPD is effective in extracting the features of the signal and that their proposed model performs the best among all the others in terms of prediction accuracy. Furthermore, the proposed model also performed the best when the wind speed experienced sudden shifts.

It can be seen that supervised learning techniques have been widely applied with varying degrees of success to different kinds of time series, including chaotic systems presenting extreme events. Similarly to the modularity-based clustering technique [101], most of these methods are purely data-driven, making them agnostic to the underlying physical phenomena, which is partly the reason for their popularity. In terms of their prediction capabilities, it was observed that most of the employed methods are able to predict 10-20 time-steps in advance. This raises the problem of compromising between a time-step small enough to accurately capture the dynamics of the system and one that would give a larger prediction horizon. Furthermore, the major drawback of supervised learning methods is their dependency on training data. This is especially detrimental in the context of chaotic system presenting extreme events, due to the scarcity of these extreme states. As previously mentioned, they are fundamentally different in their approach, relying on time-series forecasting, rather than precursor identification. Lastly, similarly to statistical methods of time-series forecasting, supervised methods tend to perform better in a shorter time-frame and on stationary data.

The method chosen to predict the autoignition flashback needs to present several features. These features are computational speed for online detection, robustness, an actionable prediction horizon and ease of implementation in a real gas turbine. From the literature review on supervised and unsupervised machine learning method, it was seen that most of the methods compromise in one or more of these areas. The methods applied to thermoacoustic instabilities lack generalizability and the neural networks explored may lack extreme event containing training data in order for them to be accurate over a large enough prediction horizon. However, one emerging candidate should be considered further, i.e. the modularity-based clustering algorithm. This method shows promise due to being purely data-driven, as reflected in its success over several methods presenting extreme events. Furthermore, as this method relies on precursor identification instead of time-series forecasting, it should also be more robust to changes in the system. It should be although be noted that this method also has its own drawback. Like the neural networks, albeit less so, it needs a considerable amount of data which is sufficient for the convergence of the transition probability matrix. In addition, it does not have the best computational speed, indicating the need for a work-around to achieve online prediction.

## 3.4. Effect of water injection and its design parameters

As seen from Section 2.5.1, the effect of water injection depends on several parameters and it can be quantified through different metrics. There have been several studies made on the effects of water injection in both gas turbines an internal combustion engines. This section has the purpose of highlighting some of their findings.

In internal combustion engines, numerous studies found benefits when using water injection, particularly in terms of emissions. For example, Adnan et al. [111] studied the performance and emission of a hydrogen fueled compression engine with variable water injection timing. They found that injecting water after the compression stroke, i.e 20° ATDC for duration of 20° crank angle degrees lead to better engine performance by increasing the gross work and the thermal efficiency. Furthermore, they found that this configuration is also the best for reducing emissions, where a reducing of more than 50% was found for $NO_x$. Similar results were also obtained by Taghavifar et al. [112] when analysing both diesel fueled and hydrogen fueled IC engines through CFD. They found that when water is injected at 15% mass fraction and at a temperature of 60° the highest pressure peak, indicated torque and thermal efficiency were found. Furthermore, both soot formation and $NO_x$ emissions were reduced by an order of magnitude when water injection was used, but it was found that this reduction was smaller with an increase in water mass fraction.

Several authors have also quantified the effect of water injection in the case of gas turbines. For example, Amani et al. [71], using a 2D k-$\omega$ SST simulation of natural gas fueled gas turbine found several interesting results such as a reduction in $NO_x$ of 87%. They indicate that parameters which most influence the combustion efficiency and the emissions are the swirl number, where a high value (1.96) was found to be optimal. Outlet maximum temperature and water loading, however, were found to be more influenced by pre-injection and post-injection water mass flow rates. Here, a water-to-fuel ratio of 3.4 injected in a 80% majority in the post-flame region achieved the best results. The authors also note that in the case when flame instabilities arise due to pressure fluctuations, the water-to-fuel ratio should be reduced to 2. Another study using water injection on a methane fueled gas turbine was done by Farokhipour et al. [72]. Here, the authors found that the water droplets should not become entrained in the inner recirculation zone (IRZ) as this results in a lack of evaporation and participation in the combustion process due to the low temperature of this region. On the other hand, it was found that droplet entrapment in the swirling vortex increases the residence time, allowing for a more efficient evaporation. Finally, the authors also investigated the optimal injection location, indicating that post-ignition region best satisfies the aforementioned criteria. Another study done by Shahpouri et al. [113], using the same approach as the previous studies, compared the effectiveness of water injection and steam addition in natural gas turbines. It was found that injecting water was 1.69 times more efficient at reducing $NO_x$ than steam addition with the drawback of reduced thermal efficiency. Furthermore, it was found that optimal water to fuel ratio was close to 1, as using ratio higher than this greatly reduces the efficiency.

Other studies have also specifically looked at the stability of the flame when water injection is used. Pappa et al. [37] investigated the potential of water injection at preventing flashback in micro gas turbines when using natural gas enriched with hydrogen. Their findings indeed affirmed this assumption, but, the scope of the research was limited to a hydrogen concentration of only 10%. Another study, done by Tanneebrger et al. [69], experimentally investigated pure hydrogen combustion with steam injection. The authors

identified two distinct modes for the flow field: a stable low-swirl jet flame and high swirling flow that causes a recirculation region. Most interestingly, it was found that increasing the amount of steam dilution leads to a transition towards the recirculating flow regime due to the positive pressure gradient over the area expansion.

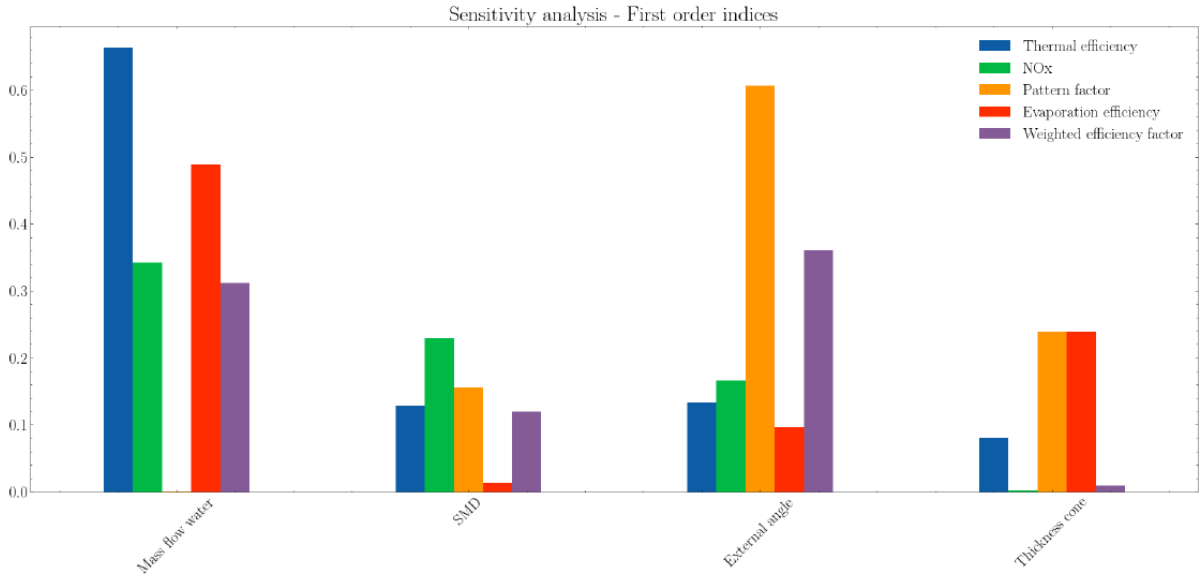


**Figure 3.4:** Sensitivity analysis of the different performance parameters to the design variables [19].

Studies with water injection were also performed on a model based on Ansaldo Energia's GT36 gas turbine. Here the authors studied a hydrogen fueled reheat combustion chamber through the means of LES simulations. Kruljevic et al. [49], simulating the flow at atmospheric pressure, found that water injection is effective in pushing the flame downstream, reducing its reactivity and the $NO_x$ emissions. This again came with the drawback of reduced thermal efficiency. Furthermore, this study also found that using direct water injection is more effective than steam addition in emission reduction. The authors also attempted to retrieve the original power output obtained without the addition of water by increasing the equivalence ratio, however it was found that this only increased the $NO_x$ emissions, with little impact on the combustion efficiency. Another notable result of this study was that the periodic flashback phenomena, which originally moved the flame front to the premixing duct, was suppressed by the water spray, resulting in the flame front no longer moving further upstream than the step location. While the authors of this study provide further insight into the effects of the design parameters of the spray, a similar parametric analysis was also done by P. Rouco [19] at high pressure (20 atm), which is the condition of interest for this study. Firstly, P. Rouco also found that the spray proved effective in lowering NOx levels and flame oscillations at the cost of reduced thermal efficiency. Unfortunately, unlike the 1 atm case, the flame front was not prevented from entering the premixing duct, but, nevertheless, the author suggests that with additional tunning of spray design parameters, this is also achievable in the high pressure case. For the sensitivity analysis, P. Rouco chose to vary the mass flow, the SMD, the external cone angle and thickness angle for a hollow cone spray with no swirl. Furthermore, the performance metrics chosen were the $NO_x$ production, the thermal efficiency, the pattern

factor and the evaporation efficiency. The main results of this sensitivity analysis are shown in Figure 3.4. For the thermal efficiency, the figure indicates that the main influencing factor is the water mass flow. The dispersion of particles, as characterized by the three other design parameters, also seems to affect the thermal efficiency but to a lesser extent. A similar behaviour can also be observed for the $NO_x$ production, but, this time, the dispersion of particles seems to be more influential than before. This is expected as a more uniform reduction in temperature better reduces the formation of hot spots and consequently the production of $NO_x$. What is interesting for this parameter is that the thickness angle of the cone seemingly plays no role. For the pattern factor, which is a better measure of the uniformity of the flow field, it is clear that only the dispersion of particles plays a role while the mass flow of water is irrelevant. From the remaining three parameters, the external angle is the most important. Finally, in terms of the evaporation efficiency, the water mass flow is again the most important, followed by the thickness angle and the external angle. Evidently, as more water is introduced, the evaporation efficiency decreases due to the lack of available heat. The thickness angle also plays an important role as tightly grouped droplets are less able to capture the surrounding heat. For the purpose of preventing the flame from entering the premixing duct, it can be inferred that both the amount of water and the droplet dispersion are important parameters. The flashback phenomena is initialized by autoignition and it acts on the whole transversal length of the premixing duct. As such, uniform cooling should be achieved with the water spray.

## 3.5. Research questions

For the purpose of this study, the modularity-based clustering algorithm for precursor identification developed by Schmid et al. [95] and Golyska et al. [101] is chosen as the prediction method. This approach has been selected due to its demonstrated potential as a data-driven technique applied to complex systems. In this thesis, its application towards turbulent reacting systems is further explored. These systems are chaotic and high-dimensional, which implies that there are a multitude of paths from which extreme events can originate, due to the wide range of spatio-temporal scales and perturbations. As such, this data-driven technique, which is insensitive to the underlying physical mechanisms, is though to be a good fit towards providing a precursor to the flashback events. In this study it will be applied to the obtained data from the LES simulations in multiple scenarios. Furthermore, to reduce the computational load for this method, the co-kurtosis PCA dimensionality reduction technique [88] shall be applied to limit the number of features used in the prediction algorithm.

To accompany this main goal, several tests for the precursor algorithm should be considered. Of interest is the performance of the algorithm in non-ideal scenarios. These include reducing the number of features available for the clustering algorithm and changing the sampling location such that it is further away from the ideal location (near the autoignition zone). Furthermore, another test shall be conducted to assess the performance on the algorithm on previously unseen data. Here, the clusters are computed based on a shorter time-series and then unseen data is classified based on its proximity to the previously computed clusters. This test assesses the performance of the algorithm when trained on a shorter time-series. In addition, it allows for computational speeds suitable for online prediction, thus making a first assessment of the algorithm in this setting. Another test further delves into the capabilities of the algorithm in online prediction. Instead of using the features indicated by the co-kurtosis PCA, the pressure at the wall is now fed to the

algorithm, along with the temperature. Lastly, the algorithm will be assessed based on data from an LES simulation where the flow is more turbulent. This checks the robustness of the algorithm towards fluctuation conditions.

In the last part of the thesis, the interest lies in assessing the capability of water injection in suppressing a flashback. For this purpose, the numerous design parameters will be tuned, with the purpose of finding a preliminary spray design. Using this spray, a new LES simulation will be done where the water spray is activated at the moment an incoming flashback has been detected. Based on this approach, it is now possible to formulate the research questions. The main research question is as follows:

**"Can the modularity-based clustering algorithm predict an incoming flashback event as observed in the high pressure reheat combustion LES simulations when using the features indicated by co-kurtosis PCA? "**

and the sub-questions accompanying this main goal are:

- **"How does this method perform for the following robustness tests: less features, shorter time-series and unseen data, relying on pressure data, fluctuation conditions and changing the sampling location?"**
- **"How well can a flashback be suppressed through the injection of water after an incoming flashback was detected?"**

# 4

# Methodology

This chapter delves into the methodology behind the approaches used in this study. The first part gives part about the details of the LES mathematical model, as implemented in Converge CFD. This covers the governing equations, Reynolds stress modelling, methods applied to the boundary conditions and the detailed chemistry model. In addition a short description of the spray model used for the water injection is given. Furthermore, the computational setup is given, where the geometry, the mesh, boundary and initial conditions are given, as well as the numerical solvers employed in this simulation. After a short description of how the data is extracted from the LES simulation, the second part of this chapter covers the dimensionality reduction technique used, in the form of co-kurtosis PCA and the precursor identification technique, in the form of the modularity-based clustering algorithm. The next section covers the robustness analysis employed to test the limits of the algorithm and explore its use in an online setting. Lastly, the final section of this chapter provides the guidelines used for the design of the spray. This methodology covers all of the steps from running the LES simulations, acquiring the data, pruning it to reduce the computational load and finally finding the precursor to the flashback event, which lastly, is used to time the injection of water and suppress the flashback event.

## 4.1. LES framework

In this section, the methodology for obtaining flashback data through Large Eddy Simulation (LES) and implementing flashback suppression via water injection is outlined. The description begins with an exposition of the mathematical model supporting the employed LES models. Following this, the mathematical models governing the spray are presented, and lastly, a detailed account of the computational setup is provided.

The importance of turbulent combustion modeling has grown significantly within the power generation and transportation industries, playing a crucial role in understanding and optimizing various combustion systems. Broadly, turbulent flame modeling faces a range of interconnected challenges, as explained by Veynante et al. (2002) [114]. These challenges include a solid grasp of the fluid mechanical properties inherent to the combustion system, necessary for modeling various transfer phenomena like heat transfer, molecular diffusion, and convection. Moreover, detailed chemical reaction schemes are needed to govern reactant consumption, product and pollutant species formation, as well as parameters like ignition delay time, and the stabilization and extinction of the flame. In some instances, the modeling scope extends to include two-phase flows, requiring a thorough representation of interactions between a liquid phase (e.g. fuel or water droplets) and the surrounding gaseous

medium. Finally, the complexity is further compounded in scenarios where radiative heat transfer models must be used to capture additional intricacies. As a result, a comprehensive approach to turbulent combustion modeling involves addressing these interconnected facets for a complete and accurate representation of the combustion processes under consideration.

### 4.1.1. Governing equations

The set of transport equations governing combustion flows is comprised of the Navier-Stokes equations, the species and the energy transport equations. Converge CFD uses the following formulations.

The compressible equations for mass transport and momentum transport are given by

$$\frac{\partial \rho}{\partial t} + \frac{\partial \rho u_i}{\partial x_i} = S \tag{4.1}$$

and

$$\frac{\partial \rho u_i}{\partial t} + \frac{\partial \rho u_i u_j}{\partial x_j} = -\frac{\partial P}{\partial x_i} + \frac{\partial \sigma_{ij}}{\partial x_j} + S_i \tag{4.2}$$

where the viscous stress tensor is given by:

$$\sigma_{ij} = \mu_t \left( \frac{\partial u_i}{\partial x_j} + \frac{\partial u_j}{\partial x_i} \right) - \frac{2}{3} \mu_t \left( \frac{\partial u_k}{\partial x_k} \delta_{ij} \right). \tag{4.3}$$

In the above equations, $u$ is velocity, $\rho$ is density, $S$ is the source term, $P$ is pressure, $\mu_t$ is turbulent viscosity, and $\delta_{ij}$ is the Kronecker delta. Furthermore, the energy equation is given by:

$$\frac{\partial \rho e}{\partial t} + \frac{\partial \rho e u_j}{\partial x_j} = -P \frac{\partial u_j}{\partial x_j} + \frac{\partial}{\partial x_j} \left( K_t \frac{\partial T}{\partial x_j} \right) + \sigma_{ij} \frac{\partial u_i}{\partial x_j} + \frac{\partial}{\partial x_j} \left( \rho \sum_m D_m h_m \frac{\partial Y_m}{\partial x_j} \right) + S \tag{4.4}$$

where $Y_m$ is the mass fraction of species $m$, $D_m$ is the species mass diffusion coefficient, $e$ is the specific internal energy, $K_t$ is the turbulent conductivity, and $h_m$ is the species specific enthalpy. The turbulent conductivity is given by:

$$K_t = K + c_p \frac{\mu_t}{Pr_t} \tag{4.5}$$

where $c_p$ is the specific heat at constant pressure, and $Pr_t = \frac{c_p \mu_t}{k_t}$ is the turbulent Prandtl number. The species conservation equation is given by:

$$\frac{\partial Y_m \rho}{\partial t} + \frac{\partial Y_m \rho u_j}{\partial x_j} = \frac{\partial}{\partial x_j} \left( \rho D_m \frac{\partial Y_m}{\partial x_j} \right) + S_m, \tag{4.6}$$

where $Y_m$ is the mass fraction of species $m$ and $S_m$ is a source term that accounts for evaporation, chemical reactions and other submodels. Furthermore, the local mixture-averaged diffusion coefficient is calculated as:

$$D_m = \frac{1 - X_m}{\sum_{j, j \neq m} \left( \frac{X_j}{D_{mj}} \right)} \tag{4.7}$$

where $X_m$ is the mole fraction of species $m$ and $D_{mj}$ is the binary diffusion coefficient for species $m$ and $j$. For turbulent applications, the turbulent mass diffusion coefficient $D_t = \nu_t / Sc_t$, is added to $D_m$. Finally, it should also be mentioned that the Redlich-Kwong equation of state is used indirectly in the PISO algorithm to couple pressure, density and temperature.

Finally, to arrive at the LES equations, where the large turbulence scales are resolved and the subgrid scales are modelled, relevant quantities $Q$ need to be filtered. In combustion flows, a mass-weighted, Favre filtering, is used as follows:

$$\bar{\rho}\tilde{Q}(\mathrm{x}) = \int \rho Q\left(\mathrm{x}^*\right) F(\mathrm{x} - \mathrm{x}^*)\, \mathrm{dx}^* \tag{4.8}$$

where $F$ is the LES filter and $\tilde{Q} = \overline{\rho Q}/\bar{\rho}$. In this application, $F$ is chosen as a box filter, where the cut-off size $\Delta$ is related to the size of the cell and is defined as $\Delta = \sqrt[3]{V}$, where $V$ is the volume of the cell. Using this approach, the following quantities still need to be modelled:

- Unresolved Reynolds stresses $\left(\widetilde{u_i u_j} - \tilde{u}_i \tilde{u}_j\right)$, which require a turbulence model for the subgrid scales.
- Unresolved species fluxes $\left(\widetilde{u_j Y_k} - \tilde{u}_j \tilde{Y}_k\right)$ and enthalpy fluxes $\left(\widetilde{u_j h_\mathrm{t}} - \tilde{u}_j \tilde{h}_\mathrm{t}\right)$.
- Filtered laminar diffusion fluxes $\overline{\mathcal{J}_j^k}, \overline{\mathcal{J}_j^h}$.
- Filtered chemical reaction rate $\overline{\dot{\omega}}_k$.

### 4.1.2. Subgrid stress modelling

For the purposes of this study, the one-equation viscosity model is chosen to resolve the subgrid scale Reynolds stresses. This model was formulated by Yoshizawa et al. in 1985 [115] and Menon et al. in 1996 [116] and it employs a sub grid kinetic energy equation for the turbulence viscosity modelling. The equation reads as follows, where the right hand side terms correspond to production, dissipation and diffusion, respectively:

$$\frac{\partial k}{\partial t} + \bar{u}_i \frac{\partial k}{\partial x_i} = -\tau_{ij} \frac{\partial \bar{u}_i}{\partial x_j} - \varepsilon + \frac{\partial}{\partial x_i}\left(\frac{v_t}{\sigma_k} \frac{\partial k}{\partial x_i}\right) \tag{4.9}$$

where the kinetic energy and the sub grid dissipation are represented by the following equations:

$$k = \frac{1}{2}(\overline{u_i u_i} - \bar{u}_i \bar{u}_i) \qquad\qquad \epsilon = \frac{C_\epsilon k^{3/2}}{\Delta}. \tag{4.10}$$

Furthermore, the turbulent viscosity, $\nu_t$, is given as $\nu_t = C_k \sqrt{k} \Delta$ and the SGS stress tensor is given by:

$$\tau_{ij} = -2\nu_t \bar{S}_{ij} + \frac{2}{3} k \delta_{ij}. \tag{4.11}$$

In these equations there are three model constants, i.e. the viscosity constant $C_k = 0.05$, the SGS dissipation constant $C_\epsilon = 1$ and the reciprocal SGS kinetic energy Prandtl number $\sigma_k = 1$, where their values are set as recommended by the authors of the model. Finally, $\bar{S}_{ij}$ is the velocity strain tensor, which can be calculated directly.

### 4.1.3. Turbulent inlet boundary condition

In some of the simulations, turbulent fluctuations are also imposed on the inlet velocity profile. To achieve this, the digital filter method developed by Klein et al. is used [117]. In this method, a velocity field signal is superimposed on the inlet velocity profile based on a statistical description.

The method starts with generating a turbulent velocity field from a white noise signal, $r_m$, with zero mean ($\overline{r_m} = 0$) and unity variance ($\overline{r_m r_m} = 1$), using the convolution operation. This operation blends a white noise signal with predetermined filter coefficients to generate a velocity field mimicking the statistical properties of turbulence.

$$u_m = \sum_{n=-N}^{N} b_n r_{m+n} \tag{4.12}$$

Here, $u_m$ represents the generated turbulent velocity at point $m$, $b_n$ are the filter coefficients, and $N$ signifies the convolution range, impacting the turbulence scale simulated. To accurately represent turbulence, it is necessary that different points in the generated signal are uncorrelated unless they coincide, necessitating $\overline{r_m r_n} = 0$ for $m \neq n$. This ensures the simulation's randomness. The link between the filter coefficients and the autocorrelation of the turbulent field is given by:

$$\frac{\overline{u_m u_{m+k}}}{\overline{u_m u_m}} = \frac{\sum_{j=-N+k}^{N} b_j b_{j-k}}{\sum_{j=-N}^{N} b_j^2} \tag{4.13}$$

This equation connects the filter coefficients with the turbulence's spatial structure, allowing the simulation to mimic realistic turbulence characteristics. The random variable's points $u_m$ and $u_{m+k}$ are interpolated between two grid points separated by a distance $k\Delta x$, where $\Delta x$ represents the grid spacing. The filter coefficients are chosen to reflect the length scales and essential correlation attributes, ensuring that $R_{uu}(\infty) = 0$ and $R_{uu}(0) = 1$. To apply this approach in three dimensions, the 1D filter coefficients are convolved in a manner such that $b_{ijk} = b_i \cdot b_j \cdot b_k$. The previous equation can then be iteratively solved using a Newton's method tailored for multidimensional problems.

### 4.1.4. Detailed chemistry model

The chemistry model used for this simulation is the SAGE detailed chemical kinetics solver, following the procedure laid out by Senecal et al. [118], which solves a system of ODEs to find out the reaction rates for each elementary reaction. According to Turns et al. [119], the chemical reaction mechanism can be described as follows:

$$\sum_{m=1}^{N} \nu'_{m,i} \chi_m \rightleftarrows \sum_{m=1}^{N} \nu''_{m,i} \chi_m \quad \text{for } i = 1, 2, \ldots, I \tag{4.14}$$

with $\nu'_{m,i}$ and $\nu''_{m,i}$ being the stoichiometric coefficient for the reactants and the products, respectively. Furthermore, $m$ represent the species and $i$ the reaction, $I$ is the number of reactions and $\chi_m$ is the chemical symbol for the respective species. The production rate of a certain species is described by:

$$\dot{\omega}_m = \sum_{i=1}^{I} \nu_{m,i} q_i \text{ for } m = 1, 2, ... \tag{4.15}$$

where $M$ is the total number of species and $v_{m,i} = v''_{m,i} - v'_{m,i}$. Next, the rate-of-progress parameter $q_i$ for reaction $i$ is given by:

$$q_i = k_{i,f} \prod_{m=1}^{N} [X_m]^{\nu'_{mi}} - k_{i,r} \prod_{m=1}^{N} [X_m]^{\nu''_{mi}} \tag{4.16}$$

where $X_m$ is the molar concentration of species m and $k_{i,f}$ and $k_{i,r}$ denote the forward and reverse rate coefficients in reaction $i$. Furthermore, $k_{i,f}$ is given by the Arrhenius equation:

$$k_{i,f} = A_i T^{\beta_i} \exp\left(\frac{-E_i}{RT}\right) \tag{4.17}$$

where $A_i$ is the pre-exponential factor, $\beta_i$ is the temperature exponent and $E_i$ is the activation energy (in cal/mol). For the reverse rate coefficient, either an equivalent formulation as the Arrhenius equation can be used or it can be expressed using the equilibrium coefficient $K_{i,c}$ in the following way: $k_{i,r} = \frac{k_{i,f}}{K_{i,c}}$. This in turn is evaluated based on thermodynamic properties as follows:

$$K_{i,c} = K_{i,p} \left(\frac{P_{atm}}{RT}\right)^{\sum_{m-1}^{M} v_{mi}} \qquad \text{with} \qquad K_{i,p} = \exp\left(\frac{\Delta S_i^0}{R} - \frac{\Delta H_i^0}{RT}\right) \tag{4.18}$$

In these equations, $P_{atm}$ is the atmospheric pressure and $T$ is the temperature. Furthermore, the change in entropy and enthalpy refers to the change that occurs when reactants are transformed into products:

$$\frac{\Delta S_i^0}{R} = \sum_{m=1}^{M} v_{m_i} \frac{S_m^0}{R} \qquad \text{and} \qquad \frac{\Delta H_i^0}{RT} = \sum_{m=1}^{M} v_{m_i} \frac{H_m^0}{RT} \tag{4.19}$$

Based on the above steps, the conservation equations for mass and energy can now be solved across the computational mesh. These are:

$$\begin{aligned} \frac{d[X_m]}{dt} &= \dot{\omega}_m \\ \frac{dT}{dt} &= \frac{\sum_m \left(\bar{h}_m \dot{\omega}_m\right)}{\sum_m \left([X_m]\, \bar{c}_{p,m}\right)} \end{aligned} \tag{4.20}$$

In these equations, $\dot{\omega}_m$ is based on Equation 4.15 and $\bar{h}_m$ and $\bar{c}_{p.m}$ are the molar specific enthalpy and the molar specific heat at constant pressure. The equations are solved at each time step and the concentration of the species is updated. The new temperature found from the energy equation is then used to update the forward and reverse reaction rate coefficients, repeating the process until convergence. The final temperature is then used to update the cell temperature.

### 4.1.5. Thickened flame model

The thickened flame model (TFM) complements the SAGE detailed chemistry solver and it acts upon the flame front dynamics. As the computational mesh is generally not fine enough to resolve the laminar flame thickness, the TFM model artificially thickens the flame without changing the laminar flame speed to get rid of the need for subgrid scale models. In CONVERGE, the TFM is implemented based on the description of Legier et al. [120]. This model dynamically changes the flame front and, subsequently, the turbulence chemistry interaction, by using the efficiency factor $E$ and a local thickening factor $F$, which multiplies the original flame thickness ($F \cdot \delta_l$). Furthermore, the diffusivity coefficient $D$ is also modified to $E \cdot F \cdot D$, the laminar flamespeed $s_L$ is converted to $E \cdot s_L$ and the pre-exponential factor of the Arrhenius formula $A$ is now $E \cdot A/F$. Using this reformulation, the flame front is resolved without the use of filters, similar to a DNS, while the processes far away from the flame front are not affected. As such, the equation for the scalar conservation is reformulated as follows:

$$\frac{\partial \rho Y_i}{\partial t} + \frac{\partial \rho Y_i u_j}{\partial x_j} = \frac{\partial}{\partial x_j}\left(\rho \cdot E \cdot F \cdot D \frac{\partial Y_m}{\partial x_j}\right) + \frac{E}{F}\dot{\omega}_i \tag{4.21}$$

The thickening factor $F$ can be expressed as:

$$F = 1 + (F_{max} - 1)S, \tag{4.22}$$

where $F_{max}$ is the maximum scaling factor and $S$ is the flame sensor, which determines the locality of the thickening operation. In these simulations, the number of grid points across the flame is specified directly ($n_{res} = 5$), resulting in a maximum scaling factor defined as:

$$F_{max} = \frac{n_{res}\Delta_x}{\delta_l}, \tag{4.23}$$

where $\Delta_x$ is the local grid spacing. An appropriate value for the flame sensor $S$ is determined using Equation 4.24, based on the properties of $H_2$. $|\overline{\dot{\omega}}_{sens}|$ is the local reaction rate as calculated by SAGE, $\Omega_{sens,o}(\phi)$ is the maximum reaction rate in the premixed laminar case for a given equivalence ratio based on a 1D simulation, and, finally, $\beta$ is a modelling coefficient that imposes a sensor thickness.

$$S = \max\left[\min\left(\beta\frac{|\overline{\dot{\omega}}_{sens}|}{\dot{\Omega}_{sens,0}(\phi)} - 1, 1\right), 0\right] \tag{4.24}$$

To further improve the sensor, the methodology described by Jaravel [121] is applied to detect species gradient at the extremities of the flame. This approach introduces a passive indicator function, $\tilde{\Psi}$, transported according to the following equation:

$$\frac{\partial \bar{\rho}\tilde{\psi}}{\partial t} + \frac{\partial \bar{\rho}\tilde{u}_j\tilde{\psi}}{\partial x_i} = \frac{\partial}{\partial x_i}\left(F\Xi_\Delta \bar{\rho}\widetilde{D}_\psi \frac{\partial \tilde{\psi}}{\partial x_i}\right) + \frac{\Xi_\Delta}{F}\overline{\dot{\omega}}_\psi. \tag{4.25}$$

In this equation, $\overline{\dot{\omega}}_\psi$ is a relaxation source factor, taking values as prescribed by Equation 4.26. This in turn is based on two relaxation times, $\tau_0$, taking on the value of the local

time-step of the solver, and $\tau_1$, which is defined as $\tau_1 = \alpha_1 \tau_c$. Next, $\tau_c$ is defined by the combustion time scale, as the ratio between the laminar flame thickness and the laminar flame speed ($\tau_c = \delta_L / s_L$). Finally, the parameter $\alpha_1$ changes based on the upstream/downstream sides of the flame, where the filtering is performed, thus taking different values based on temperature of the unburnt/burnt mixture. Using this method, the flame sensor $S$ now is updated as $S = \max[\min(\tilde{\psi}, 1), S]$.

$$\overline{\dot{\omega}}_{\psi} = \begin{cases} \frac{-\tilde{\psi}}{\tau_1} & \text{if } S < 0.05 \\ \frac{\psi_0 - \tilde{\psi}}{\tau_0} & \text{if } S > 0.8 \\ 0 & \text{if } 0.8 > S > 0.05, \end{cases} \qquad \alpha_1 = \begin{cases} \alpha_{1,\text{ cold}} & \text{if } T \leq T_s \\ \alpha_{1,\text{ hot}} & \text{if } T > T_s \end{cases} \tag{4.26}$$

Also appearing in Equation 4.25 is the sub-grid scale wrinkling precursor $\Xi_{\Delta}$, modelled following the methodology of Charlette et al. [122]. The purpose of this variable is to measure the loss in surface of the sub-grid flame that appears as a consequence of the thickening process and then to compensate for this by increasing the turbulent flame speed. The precursor is described by Equation 4.27, where $\Gamma_{\Delta}$ is an efficiency function which takes into account the strain effect caused by the subgrid turbulent scales. This in turn is dependent on the the Reynolds number $Re_{\Delta}$, the turbulent fluctuations $u'_{\Delta}$ and other flame characteristics [123].

$$\Xi_{\Delta} = \left(1 + \min\left[\frac{\Delta}{\delta_l} - 1, \Gamma_{\Delta}\left(\frac{\Delta}{\delta_l}, \frac{u'_{\Delta}}{s_l}, Re_{\Delta}\right)\frac{u'_{\Delta}}{s_l}\right]\right)^{\beta} \tag{4.27}$$

This wrinkling parameter is then used to determine the efficiency coefficient $E$ which appears in the reformulated scalar conservation equation, Equation 4.21, by comparing its value for a unthickened flame and a thickened flame:

$$E = \frac{\Xi|_{\delta=\delta_l}}{\Xi|_{\delta=F\delta_l}} \tag{4.28}$$

### 4.1.6. Laminar flame speed and flame thickness

To complement the thickened flame model, the laminar flamespeed and flame thickness also need to be determined and tabulated to be consequently introduced in the sub-grid scale wrinkling precursor and maximum scaling factor equations. This is achieved by running 1D simulations at a range of different inlet conditions, spanning different temperatures, equivalence ratios and pressures, the results of which are interpolated by the TFM. According to Turns [119], ($s_L^2 \propto \alpha\dot{\omega}/[H_2]$), where $\alpha$ is the thermal diffusivity of the mixture, $\dot{\omega}$ is the reaction rate and $[H_2]$ is the fuel concentration. Furthermore, the thermal diffusivity follows the following proportions: $\alpha \propto T_u \bar{T}^{3/2} P^{-1}$, where $\bar{T}$ is the mean temperature between the unburnt and the burnt mixtures. Next, the fuel concentration and the reaction rate can also be written as function of the temperature and the pressure as follows:

$$\dot{\omega} \propto T_b^n P^n \exp\left(\frac{-E_A}{RT_b}\right) \quad [F] \propto \frac{P}{T_u} \tag{4.29}$$

After substituting, the laminar flame speed can be expressed as a function of the burnt and unburnt mixtures temperatures and the pressure. The laminar flame thickness can then be inferred from $s_L$ based on $\delta_l = \alpha/2s_L$.

$$\begin{aligned} s_L &\propto \bar{T}^{0.375} T_u T_b^{-n/2} P^{(n-2)/2} \exp\left(\frac{-E_A}{RT_b}\right) \\ \delta &\propto \bar{T}^{0.375} T_b^{n/2} P^{-n/2} \exp\left(\frac{E_A}{RT_b}\right) \end{aligned} \tag{4.30}$$

For the purpose of this work, the flamespeed and the flame thickness table will be taken as calculated by P. Rouco [19]. These preliminary results present interesting behaviours of the two variables in question. Of particular interest is the influence of pressure on the flame speed, i.e. it decreases the flame speed at low temperature, but then it substantially increases it a higher temperatures, as a result of hydrogen diffusion. This is concerning when it comes to the flashback phenomena observed in this study as a higher flame speed means a higher flashback propensity of the flame. Furthermore, an increase in pressure also means a smaller flame thickness, i.e. $\delta_L$ is 20 times smaller for 30 atm as compared to 1 atm. It should also be mentioned here that the values for the thickness and the speed of the flame vary according to the chemical kinetics mechanism used. In this case, the mechanism created by Li et al. [47] is used throughout all the simulations and as such, the table does not need to be changed.

### 4.1.7. Spray Model

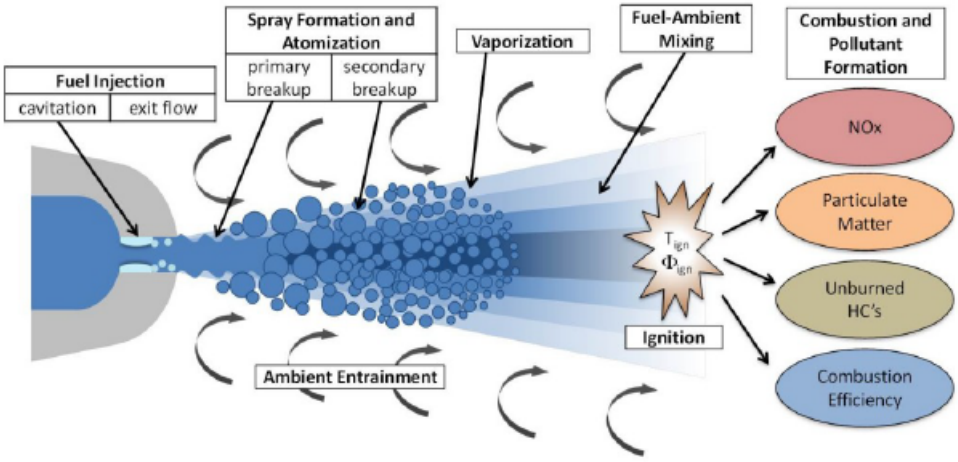


**Figure 4.1:** Spray breakup mechanisms inside a combustion chamber [124]

The subsequent section provides details the methodology of the spray model utilized for introducing water into the combustion chamber, aiming to assess its effectiveness in curbing the upstream propagation of the flame into the premixing tube. The process of injecting liquid in the form of a spray into a gas flow is a complex phenomenon, encompassing two-phase flows and various other physical mechanisms, as illustrated in Figure 4.1. After the water is injected into the nozzle, the first mechanism that could take place is that of cavitation, where sudden acceleration could lead to a static pressure drop, creating cavities in the flow, which in turn affects the spray breakup. Next, the flow is fragmented into

droplets as a result of gas-liquid instabilities in a mechanism known as primary breakup. Then, a secondary breakup causes large droplets to turn into smaller ones as a result of aerodynamic forces. Furthermore, in this stage, droplets may also collide, leading to coalescence and dispersion. In addition to these phenomena, the spray also evaporates due to the difference in pressure with respect to the ambient, it undergoes turbulent mixing and then participates in the combustion process when it reaches the flame front. As previously mentioned in Section 2.5.1, these processes are also highly influenced by the design parameters of the spray, highlighting the need for adequate models which are able to capture all of these phenomena.

As such, the modelling approach is based on the Eulerian-Lagrangian formulation. In this formulation, the first phase of the flow is considered to be continuous and it is therefore modelled using an Eulerian approach, where the flow properties are solved based on a control volume approach. In the second phase of the flow, the Lagrangian approach is used to describe the physics of the fluid droplets by tracking their individual motion, simulating their environment and potential collisions with other particles. The description of the different models used in the mathematical model of the spray as implemented in Converge [125] and used in this study is show in Appendix C.

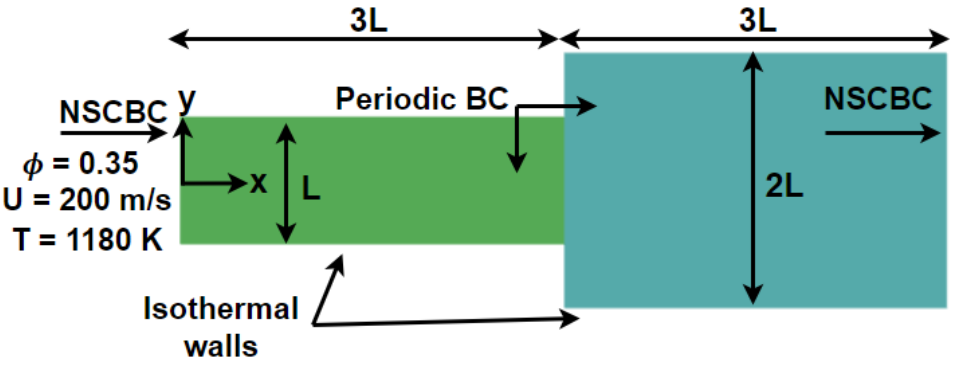


**Figure 4.2:** 2D represenation of the geometry of the reheat combustor

## 4.2. Computational setup

This section describes the setup of the various 3D LES simulations performed for the generation of flashback data, as well as the spray analysis. The geometry and the mesh are described, followed by the boundary and initial conditions. Then, an account of the spray setup is given followed by the numerical solvers chosen for the simulations.

### 4.2.1. Geometrical setup

The geometry used is a simplified version of Ansaldo Energia's GT36 reheat combustor, as displayed in 2D in Figure 4.2. Furthermore, the geometry follows the same shape as in the works of Aditya et al. [59], Kruljevic et al. [49] and P. Rouco [19]. The combustor is composed of a mixing duct with dimensions 3L x 1L x 1.5L, followed by the combustion chamber with dimensions 3L x 2L x 1.5L, where $L = 1$ cm. Also, some of the inlet parameters as well as the boundary conditions are visible in Figure 4.2. Their details shall be provided in the subsequent sections.

### 4.2.2. Computational mesh

In LES, the mesh choice significantly influences the precision of the outcomes. Using a coarse mesh might degrade the simulation's fidelity, possibly resulting in less accuracy than what is achievable with Reynolds-Averaged Navier-Stokes (RANS) simulations under comparable mesh conditions. The balance between computational efficiency and accuracy often involves applying the Pope criterion to evaluate the mesh's adequacy [126]. This criterion mandates that at least 80% of the kinetic energy should be resolved by the mesh, as shown in the formula:

$$M(x,t) = \frac{k_r(x,t)}{K(x,t) + k_r(x,t)} \tag{4.31}$$

Here, $K$ and $k_r$ denote the turbulent kinetic energy of the resolved motions and the energy within the subgrid scales, respectively, with $M$ indicating the level of turbulence captured by the mesh, all as functions of position and time. A value of $M$ lower than 0.2 is considered indicative of sufficient accuracy [126].

The computational grid features a baseline mesh size of 0.4 mm, which is significantly larger than the flame's thickness under conditions of 20 atm. This setup includes level 3 embedding at walls and leverages Automatic Mesh Refinement (AMR) based on subgrid-scale variations in velocity and temperature. The maximum level of detail for refinement, denoted as $s$, is capped at 3, yielding a new mesh size of $\Delta x_{\text{new}} = \Delta x_{\text{base}}/2^s$. The subgrid scalar field, represented as $\phi'$, is calculated by subtracting the resolved field $\bar{\phi}$ from the total scalar field $\phi$, using the second derivative term from a Taylor series expansion [127]:

$$\phi' \approx -\alpha_{[k]} \frac{\partial^2 \bar{\phi}}{\partial x_k^2} \tag{4.32}$$

This approach, initially applied to temperature and other scalar fields, is also extendable to vector fields. Mesh refinement occurs when the computed values exceed predefined thresholds and the total cell count remains under a set limit (for instance, 10 million cells to ensure computational manageability), while coarsening is applied when these values fall below 20% of the threshold.

Lastly, the TFM model also modifies the mesh by enforcing a minimum of 5 cells across the flame, ensuring refined resolution near the flame position. Of note here is that, compared to Kruljevic et al. [49], where a minimum value of 10 cells across the flame front is used, the higher pressure simulation in this case allows for only half of that due to the thinner flame front predicted. For illustration purposes, Figure 4.3 shows the mesh at an arbitrary time step.

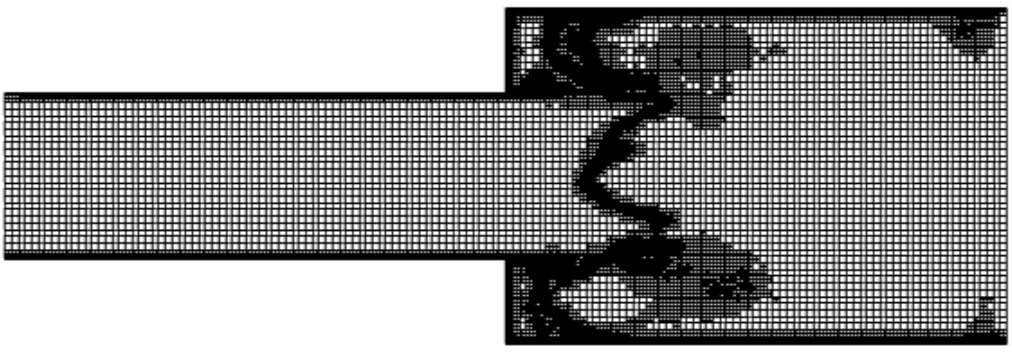

**Figure 4.3:** Computational mesh at an arbitrary time step where AMR is active.

### 4.2.3. Boundary Conditions

**Inlet**

The inlet boundary conditions are imposed based on the parts preceding the reheat combustion chamber. Following the case laid out by Aditya et al. [59], the mixture at the inlet consists of the products of the first combustion stage, i.e. $H_2O$ and a mixture of air and additional hydrogen. The velocity is uniformly set to $u = 200$ m/s and the equivalence ratio to $\phi = 0.35$. The pressure BC is of the Neumann type and the mass fraction are set as in Table 4.1.

**Table 4.1:** Species mass fractions at the inlet of the domain

| Species | Ar | $H_2$ | $H_2O$ | He | $N_2$ | $O_2$ |
|---|---|---|---|---|---|---|
| Mass fraction $Y$ | 0.01286 | 0.007855 | 0.05162 | $6.94\text{E}-07$ | 0.7496 | 0.1780 |

In distinction to the DNS simulation performed by Aditya et al. [59], the temperature at the inlet is now no longer 1100 K. This comes as a result of the discussion of Section 2.4.3 where the dependence of the autoignition delay time with the temperature and pressure was detailed. For the purpose of this work, to keep the flame at its design location, corresponding to a delay time of approximately 0.15 ms, a temperature of 1180 K is chosen [19].

Turbulent velocity fluctuations can also be imposed at the inlet through the digital filter method. For this, the turbulence intensity is set to 10 %, a common value for internal aerodynamics, to simulate fluctuations in the order of $u' = 20m/s$. The length scale is set to 0.7 mm on the assumption of a fully developed turbulent pipe flow, $l = 0.038d_h$, where $d_h$ is the hydraulic diameter. Then, in the one-equation closure model, the turbulent kinetic energy is determined as $k = 3/2(UI)^2$, where $U$ is the mean velocity and $I$ is the turbulence intensity. Finally, the Navier-Stokes Characteristic Boundary Condition (NSCBC) is also attributed to the inlet to reduce the reflection of acoustic disturbances. NSCBC methodology is detailed in Appendix A for brevity.

**Outlet**

For the outlet, the physical boundary condition prescribed is a Dirichlet BC corresponding to a pressure of 20 atm. Furthermore, the velocity is imposed as a Neumann BC and backflow is not taken into account. Similarly to the inflow, NSCBC is used with $\sigma = 0.25$.

**Walls**

For the walls, a non-slip isothermal boundary condition is applied where the temperature is set to 750 K. Furthermore, roughness is not considered and the law of the wall method is to model the unresolved sub-grid scales. In the z-direction (see Figure 4.2), translational periodic BCs are set. This choice was made to create a homogeneous direction which facilitates the sampling of statistics and therefore decrease the computational time.

### 4.2.4. Initial Conditions

To initialize the simulation and obtain a steady case, the flow field in the domain is initialized with a velocity of 200 m/s and a temperature of 1180K. Furthermore, the species are also the same as for the inflow and the equivalence ratio is again set to $\phi = 0.35$. The pressure is also set to 20 atm and, following the same procedure as in [19], the flow is developed in non-reacting conditions for the first millisecond, followed by activation of combustion with a slowly increasing equivalence ratio over the next 0.8 ms, as proposed by [52] and [49].

### 4.2.5. Numerical solvers

The Converge software [125] utilizes the Finite Volume Method (FVM) for solving the conservation equations. This well-known method involves updating the discrete cells of the domain based on the flux across the cell faces and contributions from internal sources.

Besides using the FVM method, the PISO algorithm (Pressure Implicit with Splitting of Operators) [128] is also employed. This algorithm assumes an initial pressure distribution, derived from a solution of the momentum equations at a previous time-step. Based on this, velocity field is updated to satisfy mass conservation through the momentum equation, by using the assumed initial pressure distribution. The velocity field is then updated again and the loop continues until convergence.

Furthermore, the solver also employs the Rhie-Chow algorithm [129] to circumvent the decoupling between pressure and velocity. Finally, to solve the set of discretized equations for each iteration, the SOR (Successive Over-Relaxation) technique is used. The different parts mentioned here involved in the numerical solver are detailed in Appendix B.

## 4.3. Data acquisition

As mentioned in Section 1.4, the first goal of this thesis is to use data from LES simulations of the GT36 to predict the flashback event using machine learning methods. These simulations output a large amount of data consisting of a number of variables sampled at every point of the mesh and at every time step. As using all of this data is unrealistic, it has to be reduced. As such, for the purposes of this work, 2D snapshots of the mid z-plane are saved at a frequency of 1 MHz. These snapshots contain the data points at the non-uniform mesh created by Converge's automatic mesh refinement (AMR) technique. Thus, to simplify the analysis and further reduce the size of the data, these snapshots are loaded into Tecplot. There, the mesh is linearly interpolated onto a evenly spaced 601 by 201 mesh and the number of variables is reduced. These new snapshots contain the data which is referred to in the following sections.

## 4.4. Co-kurtosis based dimensionality reduction

Before the precursor identification algorithm is applied to the LES data, it is necessary to reduce the number of variables to lessen the computational load required. This section explains the methodology behind the co-kurtosis based dimensionality reduction technique introduced by Jonnalagadda et al. [88], which is applied towards this purpose. As previously mentioned in Section 3.2.2, the co-kurtosis PCA improves on the classical PCA by computing the principal vectors using the fourth order statistical moment, i.e. the co-kurtosis tensor. The benefit of this approach is that the vectors now point in the direction of the outliers of a particular dataset (see Figure 4.4). Using this insight, it can be seen how this approach may be useful in detecting anomalies or extreme events, as prior to these events, there may be variables which contain outliers. For example, for an combustion dataset, fleeting ignition kernels at a particular location may be indicative of an incoming autoignition event [89].

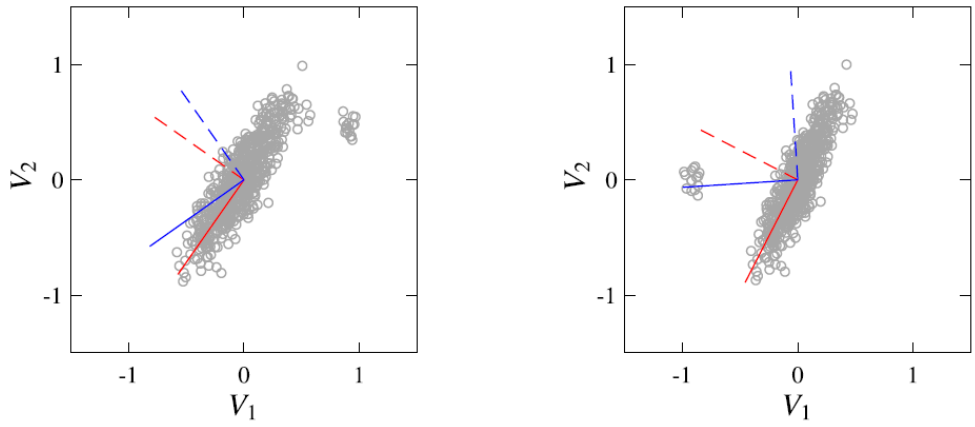


**Figure 4.4:** A Gaussian dataset with a few samples converted to outliers in different locations. The first (solid line) and second (dashed line) PCA vectors are shown in red, while the co-kurtosis PCA vectors are shown in blue [89].

To apply this algorithm, the principal vector of the fourth order moment must be computed at every time-step for a given dataset containing different variables across a grid. As such, at each time-step, thermo-chemical variables in a region near the autoignition zone are used. The region differs from case to case and it will be shown later in Section 5.2.

The initial phase of the algorithm encompasses a data preprocessing stage. During this stage, for a single time-step, the data from each feature is scaled by subtracting its mean and then dividing by its absolute spatial maximum. For the next step, consider a feature vector $\mathbf{V}$ of dimension $N_f$ with $n_s$ samples. The joint fourth order moment tensor can be calculated as:

$$\tau_{ijkl} = \frac{1}{n_s} \sum_{n_s} v_i v_j v_k v_l, \quad 1 \leq i, j, k, l \leq N_f \tag{4.33}$$

where $v_i \in \mathbf{V}$. Then, the tensor of interest, containing only the excess kurtosis is obtained by subtracting the excess variance as follows:

$$\begin{aligned}[C_4^y]_{i_1 i_2 i_3 i_4} = \mathbb{E}[y \otimes y \otimes y \otimes y] - \mathbb{E}\left[y_{i_1} y_{i_2}\right] - \mathbb{E}\left[y_{i_3} y_{i_4}\right] - \\ \mathbb{E}\left[y_{i_1} y_{i_3}\right] \mathbb{E}\left[y_{i_2} y_{i_4}\right] - \mathbb{E}\left[y_{i_1} y_{i_4}\right] \mathbb{E}\left[y_{i_2} y_{i_3}\right]\end{aligned} \tag{4.34}$$

where $1 \leq i_1 \ldots i_4 \leq q$ and $\mathbb{E}$ is the expectation operator. The next step is reshaping the cumulant tensor $C_4^y$ into a matrix $M^y$ which can be decomposed into principal vectors and eigenvalues using singular value decomposition (SVD) [130, 131].

$$\mathrm{mat}\left(C_4^y\right) \equiv M^y = \sum_{i=1}^{\mathrm{q}} \kappa_{\mathrm{i}} \mathrm{a}_{\mathrm{i}} \otimes \mathrm{vec}\left(\mathrm{a}_{\mathrm{i}} \otimes \mathrm{a}_{\mathrm{i}} \otimes \mathrm{a}_{\mathrm{i}}\right) \tag{4.35}$$

where the vector $a_i$ are determined from the SVD of $M^y$. Here, the mat and vec denote the matricising and vectorising operation of a tensor. With this the principal vectors are obtained. An extra step can be made in this algorithm to find out the contribution of each individual feature towards the co-kurtosis and quantify the change in this contribution over

time. This is a featurization step where a feature moment metric $F_i^{j,n}$ is defined for each feature $i$ in a given domain $j$ and time-step $n$. $F_i^{j,n}$ is computed as follows:

$$F_i^{j,n} = \frac{\sum_{k=1}^{N_f} \lambda_k \left(\hat{e}_i \cdot \hat{v}_k\right)^2}{\sum_{k=1}^{N_f} \lambda_k} \tag{4.36}$$

Here, $\hat{e}_i \cdot \hat{v}_k$ corresponds to the $i^{th}$ entry in the $k^{th}$ vector $\hat{v}_k$. By definition, the set of vectors $\hat{v}_k$ is orthonormal. Furthermore, the sum of all feature moment metric values of the different variables is equal to 1 for a single time-step. Qualitatively, the FMMs indicate the individual contribution of each variable towards the principal vectors. For the application in this work, it is stipulated that the variables which present high values for the feature moment metrics are the ones that have the most outliers and therefore the highest amount of change just before the autoignition flashback. Thus, using these variables is likely to create an unique path in the phase space which can be picked up by the modularity-based clustering to create a reliable precursor.

## 4.5. Modularity-based clustering precursor identification

As mentioned in Section 3.3, this algorithm was first introduced by Schmid et al. [95, 96] and then further developed by Golyska and Doan [101]. This approach consists of describing a complex system as a weighted graph in the phase space, with the aim of identifying communities which could serve as precursor states leading to an extreme event. The methodology of this algorithm is detailed in the following sections.

### 4.5.1. Data selection and phase space representation

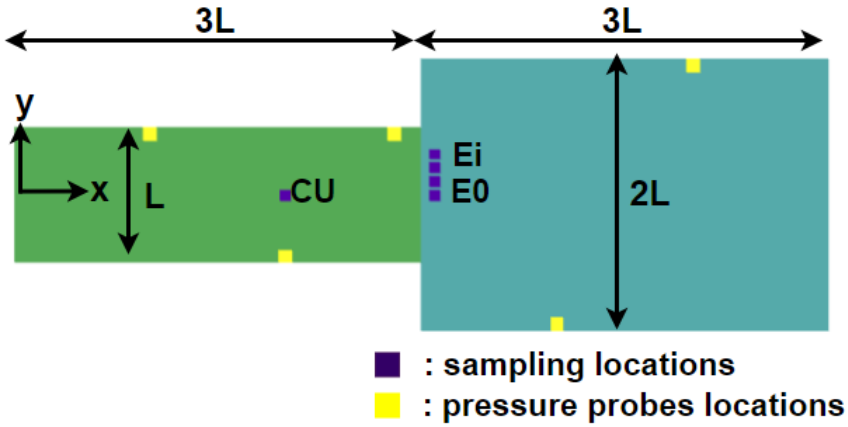


**Figure 4.5:** Geometry of the GT36 at the mid z-plane showing the sampling locations for the clustering-based algorithm

The first step of the algorithm consists in choosing the right data out of the available LES simulations, where the sampling location and the different flow variables are of interest. First, the sampling location for the desired time series is chosen according to the definition of a flashback, i.e. when the flame is present in the mixing duct. This corresponds to the step location $E_0$ (x = 3.1 and y = 0 cm) shown in Figure 4.5, which is taken as a baseline case to be later compared to off-centre locations $E_i$ (where i = 1, 2, 3) and $CU$. The second

part of this step consists in identifying the right flow variables which would best represent the dynamics of the system and lead to the correct identification of a precursor to flashback. This part is based on the dimensionality reduction technique presented in Section 5.2.

The time series of the chosen variables are then represented in the phase space, which allows for an easy identification of the extreme events. An example is shown in Figure 4.6, where a two-dimensional system (not related to the reheat combustion chamber) represented by variables $x_1$ and $x_2$ is plotted.

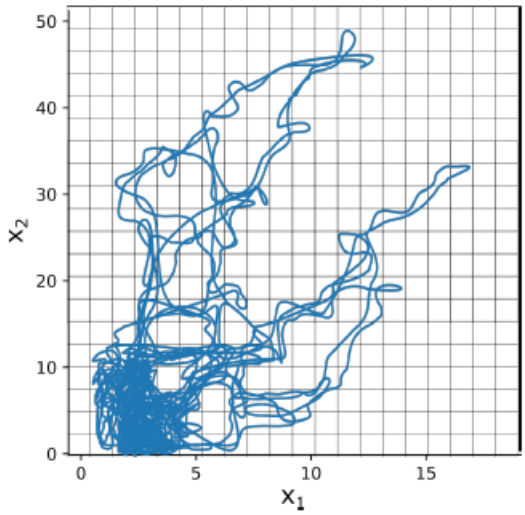


**Figure 4.6:** An example of the evolution of a system represented in the phase space [92].

### 4.5.2. Tessellation

To compress the description of the system's path, the phase space is subdivided into smaller segments, with $M$ divisions along each axis, where the resulting volumes are called *hypercubes*. The initial step involves normalizing the phase space across all dimensions, simplifying the process of identifying which hypercubes contain specific trajectory points. Following this, the trajectory's time series in the phase space is examined. This analysis converts the original data into hypercube indices. The outcome is a time series that maps the system's path, denoting the relevant hypercubes at each time interval. For efficiency, the tessellation process utilizes sparse matrices. This approach ensures that only the non-empty hypercubes are recorded in memory, with each assigned a distinct index. This enables the accurate discretization of the system's trajectory without any overlap or voids, as seen in Figure 4.7.

At this stage of the algorithm, the extreme states of the system are also defined by marking the hypercubes as extreme. Golyska [92] uses a broad definition based on how many standard deviations a point in the time series is away from the mean. This is done for any number of dimensions of the phase space and it allows for the algorithm to remain the same when considering different systems presenting extreme events. In the case of a reheat combustor, this is unfortunately not as applicable. As such, for the definition of the flashback event, only the temperature dimension is considered at the step location, where an extreme event is marked as such if the value surpasses a certain threshold. This threshold was chosen as 1300 K based on observation of the temperature time series as it was seen that at this point the gradient becomes sufficiently steep to consider flashback as

inevitable. This value is close to the cross-over limit of 1350 K, but it provides an earlier warning of the incoming flashback, without inducing any false positives.

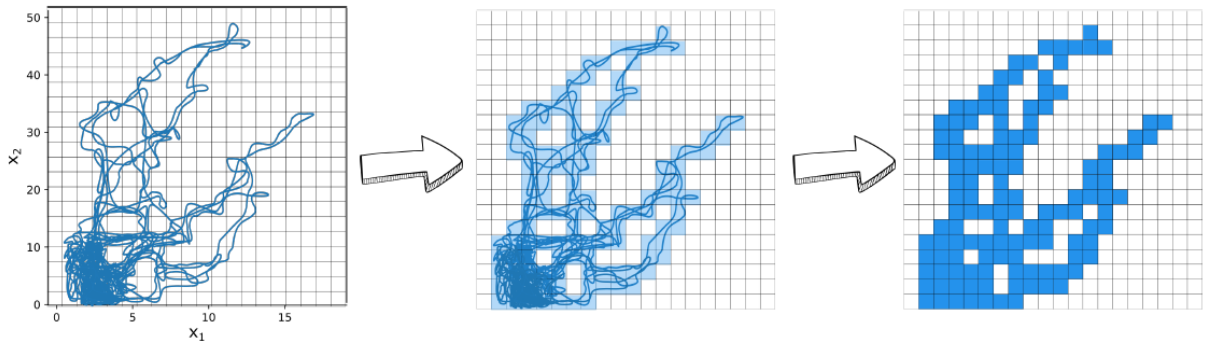


**Figure 4.7:** The tesselation process of an example system's trajectory. [92]

### 4.5.3. Transition probability matrix

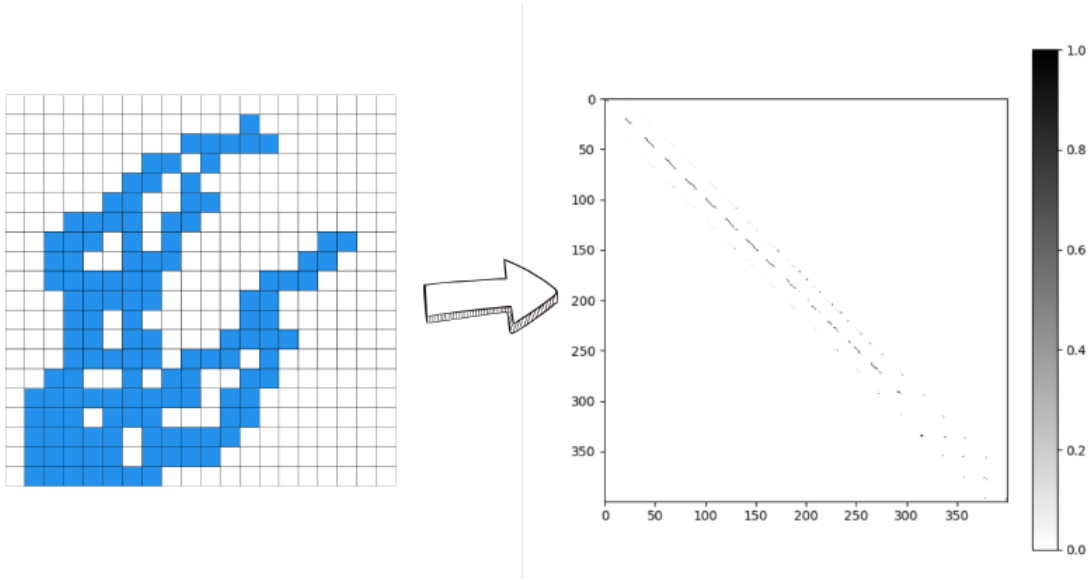


**Figure 4.8:** Transformation of the tessellated space into a transition probability matrix [92].

The next step of the algorithm is translating the tessellated data into a transition probability matrix. The *classic* method calculates the elements of this matrix as follows:

$$P_{ij} = \frac{m\left(B_i \cap \mathcal{F}^1\left(B_j\right)\right)}{m\left(B_i\right)} \quad i,j = 1,\ldots,N \tag{4.37}$$

where $P_{i,j}$ denotes the probability of hypercube $B_i$ to transition to hypercube $B_j$, N denotes the total number of hypercubes and $\mathcal{F}^1$ is the temporal forward operator denoting the state of the system at the following time step. Furthermore, $m\left(B_i\right)$ indicates the number of phase space points contained in hypercube $B_i$. The *backwards* method, as implemented in Schmid et al. [95], can also be used for the probability transition matrix:

$$P_{ij} = \frac{m\left(B_j \cap \mathcal{F}^{-1}\left(B_i\right)\right)}{m\left(B_j\right)} \quad i,j = 1,\ldots,N \tag{4.38}$$

where now $\mathcal{F}^{-1}$ is the temporal backstep operator, indicating the state of the system at the preceding time step. The final result of this step is a sparse transition probability matrix $\mathcal{P}$ of size $M^n$, where $n$ is the number of dimensions of the phase space. A visualization of $\mathcal{P}$ is shown in Figure 4.8, where it can be seen that the matrix is highly diagonal, indicating that the trajectory lies in a given hypercube for multiple time steps at a time. The off-diagonal non-zero terms represent transitions to other hypercubes.

### 4.5.4. Graph interpretation

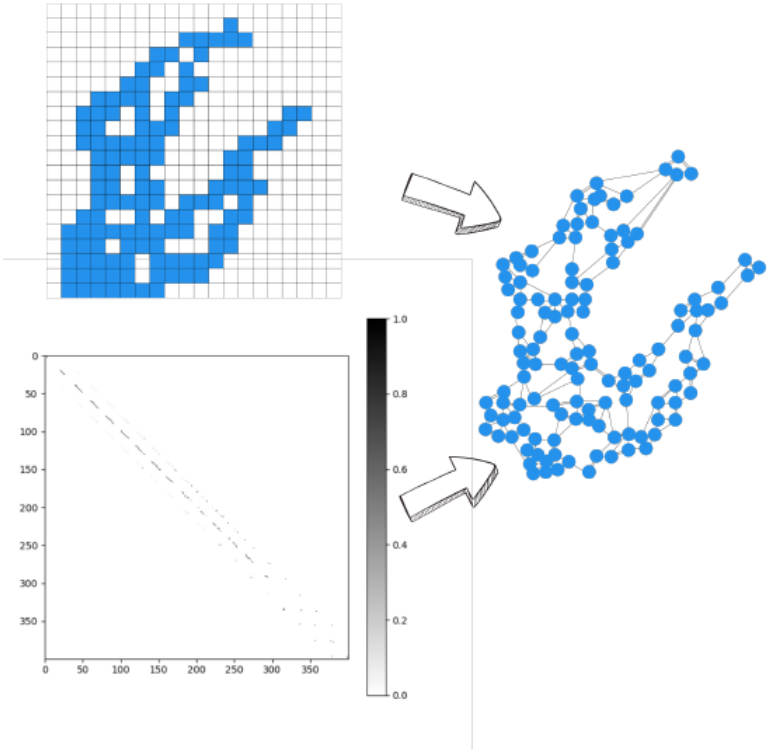


**Figure 4.9:** Network representation of the tessellated phase space [92].

The transition probability matrix can subsequently be transformed in a weighted and directed graph. In this graph, the nodes are the hypercubes of the tessellated trajectory and the edges represent the transitions between one hypercube to another. Furthermore, the edge weights represent the probabilities of transitioning. An example of how such a graph looks is shown in Figure 4.9.

### 4.5.5. Modularity-based clustering

In this step of the algorithm, the obtained network is clustered based on a metric called modularity. The Python Modularity Maximization library [132] is used, which implements this method based on the works of Newman and Leicht [94, 133]. Furthermore, a change involving the computational speed made by Golyska [92] is also kept here.

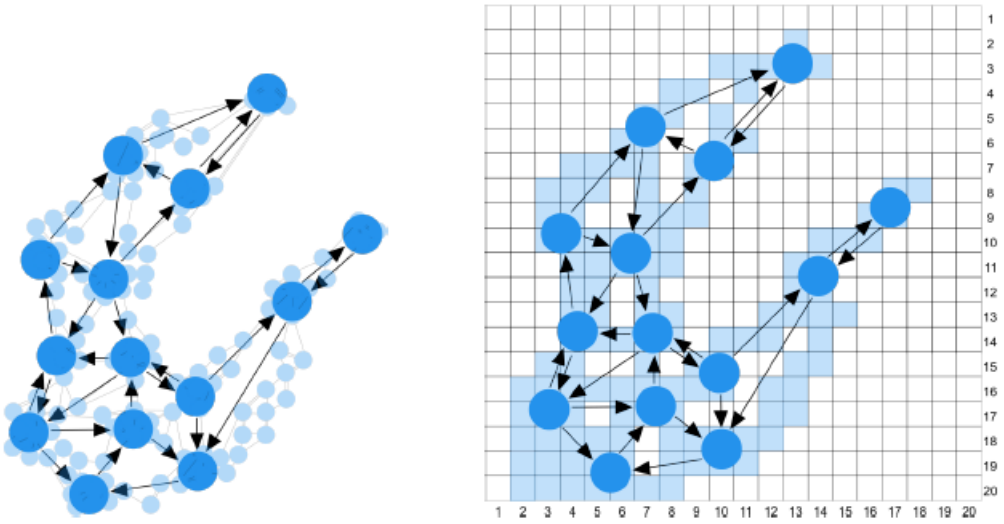


**Figure 4.10:** Example of the final network obtained after the clustering process (left), superimposed on the tessellated phase space (right) [92].

The algorithm works by maximizing modularity, which is a measure of the strength of division into communities, defined as the difference between the fraction of edges within communities and the expected fraction of such edges. The idea behind this parameter is that a division is good when the number of edges between divided communities is smaller than expected, and not just small. In essence, what distinguishes a division between communities as interesting is the deviation from a random distribution in the expected number of edges.

The calculation of the expected number of edges is performed by creating a random network that mirrors the degree sequence of the original network. This involves assigning each node a degree $k_i$, conceptualized as a half-link. As a result, the aggregate of all these half-links sums up to $\sum k_i = 2m$, where $m$ represents the total count of edges within the network. A given half-link is capable of connecting to any one of the $2m-1$ other half-links, excluding a connection to itself. For another node $j$ with $k_j$ half-links, the probability of connection to node $i$ is uniform, resulting in a connection probability of $\frac{k_j}{2m-1}$, which can be approximated as $\frac{k_j}{2m}$ in large networks. Hence, the chance of a connection between node $i$ and node $j$ can be expressed as $\frac{k_i k_j}{2m}$. When considering the interaction between a node pair $i, j$, modularity, as detailed in Equation 4.39, reflects the difference between the actual adjacency $A_{ij}$ and the expected connection $\frac{k_i k_j}{2m}$, with $A_{ij}$ being an adjacency matrix entry that signifies the presence (1) or absence (0) of an edge between them. This treatment precludes the possibility of multiple edges between the same pair of nodes. Aggregating this calculation across all node pairs for a graph split into two communities, where $n$ denotes the total number of vertices, gives us the modularity equation:

$$Q = \frac{1}{2m} \sum_{i,j} \left( A_{ij} - \frac{k_i k_j}{2m} \right) \delta_{s_i, s_j} \tag{4.39}$$

In this formula, $s_i$ and $s_j$ represent the community affiliations of nodes $i$ and $j$ respectively, with the modularity contribution coming solely from node pairs within the same community, as indicated by the Kronecker delta function $\delta_{s_i, s_j}$.

This equation can be modified to account for the directness of the graph:

$$Q = \frac{1}{m} \sum_{ij} \left( A_{ij} - \frac{k_i^{in} k_j^{out}}{m} \right) \delta_{s_i, s_j} \tag{4.40}$$

In this formula, $k_i^{in}$ and $k_j^{out}$ are the in- and out-degrees of the vertices. The probability of an edge from vertex $j$ to vertex $i$ is $\frac{k_i^{in} k_j^{out}}{m}$. Unlike Equation 4.39, the factor of 2 is omitted in the denominator due to the graph's directness.

The method used in [94] reduces the challenge to partitioning the network into two communities. For computational efficiency, Equation 4.40 is rephrased in vector form as:

$$Q = \frac{1}{2m} \sum_{ij} \left( A_{ij} - \frac{k_i^{in} k_j^{out}}{m} \right) (s_i s_j + 1) = \frac{1}{2m} \sum_{ij} s_i B_{ij} s_j = \frac{1}{2m} \mathbf{s}^T \mathrm{Bs}$$

In this scenario, $s_i$ takes on a value of 1 or -1, reflecting the community to which the node belongs, where $\delta_{s_i, s_j} = \frac{1}{2}(s_i s_j + 1)$. The vector $\mathbf{s}$ contains the values of $s_i$, and $\mathbf{B}$ represents the modularity matrix, with its components $B_{ij}$ defined accordingly:

$$B_{ij} = A_{ij} - \frac{k_i^{in} k_j^{out}}{m}$$

The algorithm aims to maximize $Q$ for a given matrix $\mathbf{B}$. For directed graphs, where $\mathbf{B}$ is asymmetric, symmetry is restored by adding its transpose:

$$Q = \frac{1}{4m} \mathbf{s}^T (\mathbf{B} + \mathbf{B}^T) \mathbf{s}$$

This is treated as an eigenvalue problem, where $s = \sum_1 a_1 v_1$ is a linear combination of the eigenvectors $\mathbf{v}_1$ of $(\mathbf{B} + \mathbf{B}^T)$, and $a_1 = \mathbf{v}_1^T \cdot \mathbf{s}$. The modularity can be rewritten in terms of the eigenvalues $\beta_i$ and corresponding eigenvectors $\mathbf{v}_1$:

$$Q = \sum_i a_i \mathbf{v}_1^T (\mathbf{B} + \mathbf{B}^T) \sum_j a_j \mathbf{v}_j = \sum_i \beta_i (\mathbf{v}_1^T \cdot \mathbf{s})^2$$

The highest value of $Q$ is reached when vector $s$ aligns with the eigenvector of the largest eigenvalue. The closest solution is sought, given the constraint that $s_i = \pm 1$. The eigenvector's signs define the nodes' community affiliations, facilitating the division process. The algorithm iteratively divides the network into two communities, stopping when no further division increases overall modularity. The change in base modularity, rather than modularity itself, is considered for each subdivision:

$$\Delta Q = \frac{1}{4m} \mathbf{s}^T (\mathbf{B}^{(g)} + \mathbf{B}^{(g)^T}) \mathbf{s}$$

With:

$$B_{ij}^{(g)} = B_{ij} - \delta_{ij} \sum_{k \in g} B_{ik}$$

where $g$ is the subgraph being considered. In this algorithm, the clustering runs iteratively. The communities are found based on maximizing the modularity, the transition probability matrix is deflated as in the following step, a new network is formed based on the new matrix and clustering begins again. The process continues until either the maximum number of iterations is surpassed or the number of communities decreases to a user-defined threshold. An example of the clustering process is shown in Figure 4.10 where the final network obtained is compared with the original one.

### 4.5.6. Matrix deflation

In this step, a community affiliation matrix D is created, which connects the obtained clusters from the previous step, to the nodes of the original graph. Using this matrix, the original probability transition matrix is deflated, resulting in a new matrix $P_{(1)}$, which describes the dynamics of the new network. This is the point of the algorithm in which the iterative process starts, as explained in the previous section.

$$P_{(1)} = D^{T}PD \tag{4.41}$$

The original probability transition matrix and the resulting deflated matrix are shown in Figure 4.11.

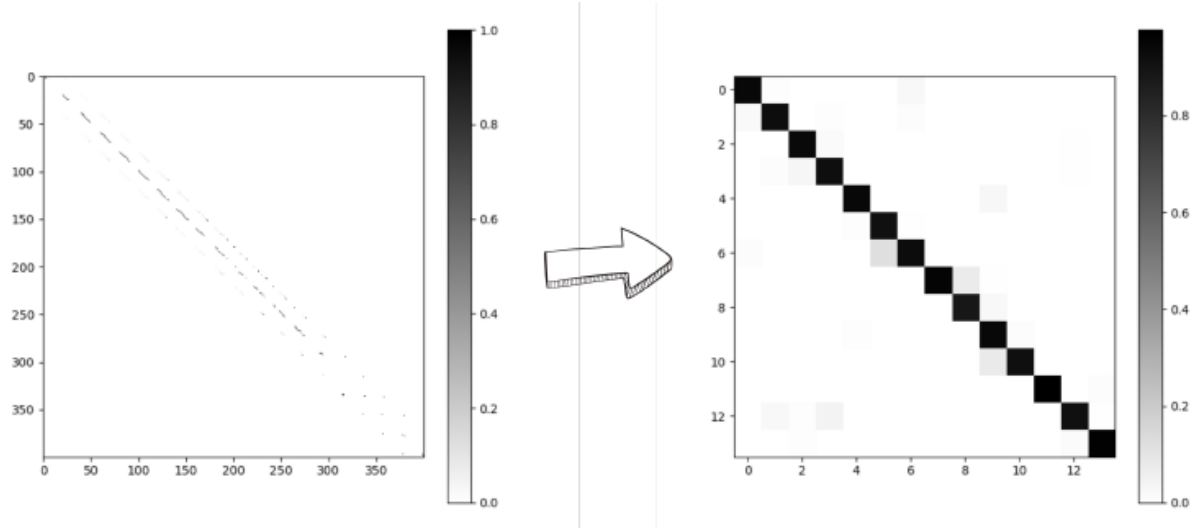


**Figure 4.11:** Transformation of the transition probability matrix after the deflation step [92].

### 4.5.7. Cluster classification

The last step of the algorithm consists of identifying the extreme clusters and the precursors clusters. The extreme clusters are classified as such based on the tessellation step, where the extreme hypercubes were marked, and the precursor clusters are defined as the clusters which transition into extreme clusters, as indicated by the final transition probability matrix. Any cluster which has a probability of transition into an extreme one is identified as a precursor cluster, no matter the actual the probability value. A visualization of the identification of extreme and precursor clusters is shown in Figure 4.12 and Figure 4.13.

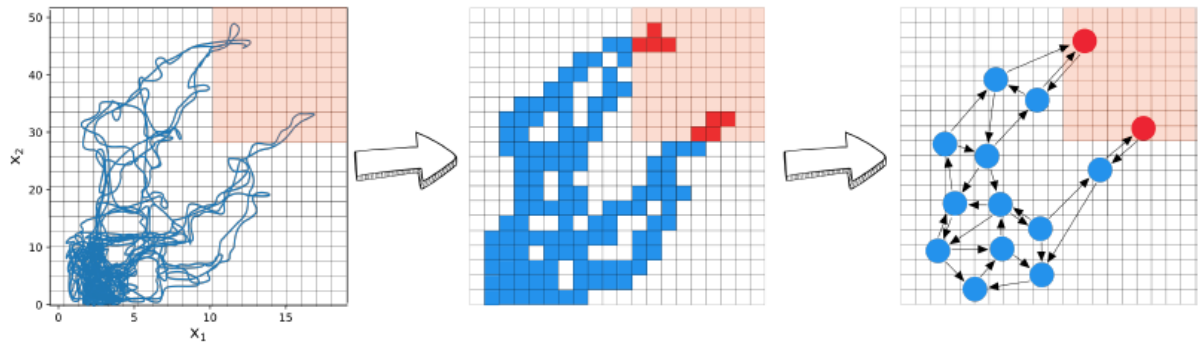


**Figure 4.12:** In this example, the extreme region of the phase space is shown in red across the phase space, the tessellated phase space and the final network. [92]

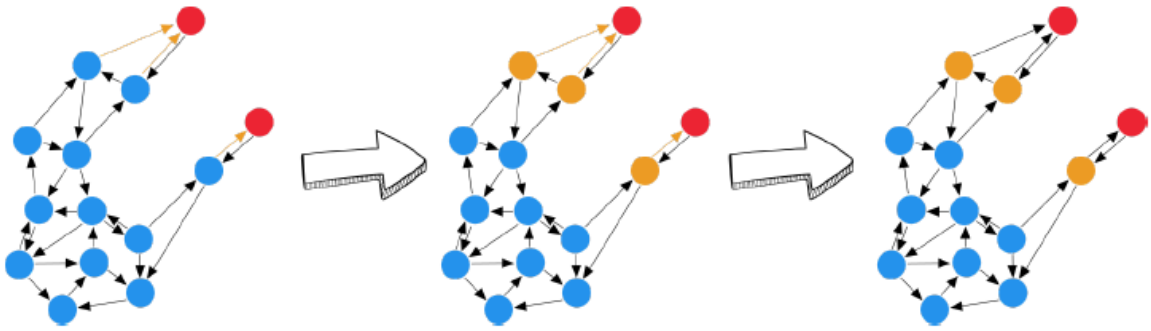

**Figure 4.13:** The process of identifying the precursor clusters. The transitions to the extreme clusters (red) are shown in orange, based on which the precursor clusters (orange) are identified. [92]

### 4.5.8. Addition to the algorithm

One flaw of the original algorithm is that the condition set in the tessellation step that identifies extreme clusters is not satisfied anymore as the network gets coarser. More precisely, the clustering step is not restricted in grouping non-extreme nodes and extreme nodes together, leading to clusters containing both types of nodes. This results in a vague definition of extreme events where a precursor cluster does not transition into an extreme event, even though it indicates the transition towards an extreme cluster. This also influences the results by leading to erroneous statistics (false positives, false negatives, etc.).

As such, a change was made to the clustering step of the algorithm, whereby, instead of initializing the clustering process with a single community, the nodes of the network were initialized into two distinct communities: an extreme community, containing the extreme nodes, and a non-extreme one, containing the rest of the nodes. In this way, the distinction is kept through the clustering process. On the next iteration of the algorithm, the newly found normal and extreme clusters are identified and used to initialize the clustering process again.

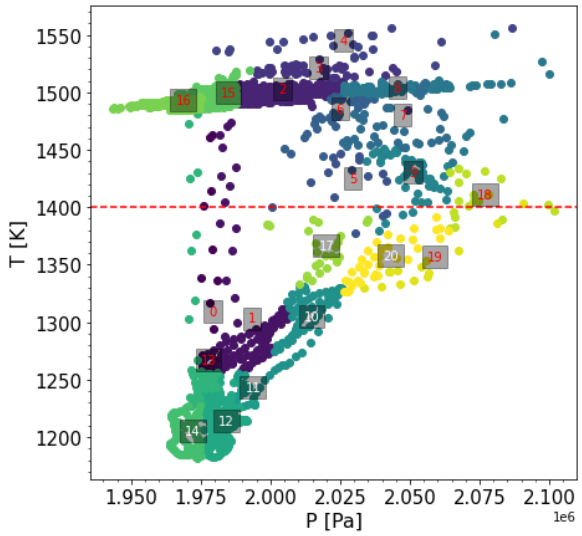


**Figure 4.14:** Example clustered phase space without the change

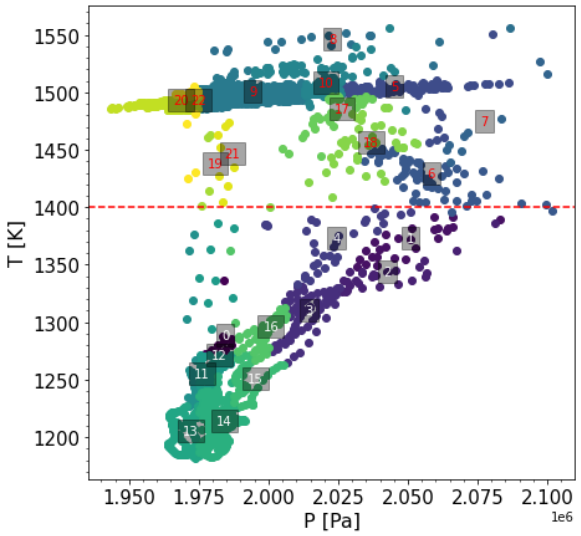


**Figure 4.15:** Example clustered phase space with the change

Figure 4.14 and Figure 4.15 showcase a clustered phase space, with and without the change, where the limit identifying extreme events lies at $T = 1400$ K. It can be seen that on the right hand side, the extreme clusters (identified by red number) do not contain non-extreme nodes anymore, as clusters 0, 1, 12 and 19 did on the left hand side. In this way, the precursor clusters are more precisely identified, leading to a reduced rate of false positives. Furthermore, when the system enters an extreme cluster, it also transitions to an extreme event, resulting in a correct rate of correct positives.

### 4.5.9. Post-processing

After the algorithm is finished, the results are post-processed to make a statistical analysis. First, some properties are saved for each cluster:

- The list of nodes belonging to the cluster
- The nature of the cluster: normal, precursor or extreme
- Clusters which can transition to the considered cluster
- Clusters towards the considered cluster can transition
- Center of the cluster in the phase space
- Center of the cluster in the tessellated phase space
- Average time spent in the cluster before a transition happens
- Number of times the trajectory of the phase space enters the cluster (number of instances)
- The percentage of time spent in the cluster from the entire time series

Using these properties, the following statistical measures can be calculated:

- Prediction time: defined as the average time spent in the precursor clusters.
- Rate of false negatives: defined as the ratio between the number of instances an extreme event did not have a precursor and the number of extreme events, expressed as a percentage.

- Rate of correct positives: defined as the ratio between the number of instances an extreme event did have a precursor and the number of extreme events, expressed as a percentage.
- Rate of false positives: defined as the ratio between the number of instances a precursor cluster did not lead to an extreme cluster and the number of times the system entered a precursor cluster, expressed as a percentage.

Besides these metrics, it is possible to do a more detailed analysis of all the clusters in the system. The probability of transitioning to an extreme event is saved not only for precursor clusters, but for all the clusters in the system. For these clusters, the probability is calculated as the product of the probabilities of transitioning to all the clusters found on the path to an extreme cluster. For each cluster, there may be different paths leading to an extreme event and as such, for the previous statistical measure, the path with the highest probability is considered. Likewise, the minimum average time to an extreme cluster is also computed by taking the sum of the average residence times on one particular path and then choosing the path with the smallest time.

## 4.6. Robustness Analysis

This section presents the robustness tests which will be employed to analyze the performance of the modularity-based clustering algorithm in non-ideal scenarios.

**Sampling location**

The first robustness test is based on varying the sampling location for the time series of the features. In addition to the location E0, four additional points from the LES simulation will be used to compile the data. These points can be seen in Figure 4.5. This test will be a good indication of the performance of the algorithm when the sampling is not done at the ideal location, where the first autoignition kernels emerge.

**Future unseen flashbacks**

The second robustness test employed for the modularity-based clustering algorithm investigates the prediction performance when the algorithm is used in an online setting and with less data. As the clustering algorithm has a significant computing time due to the large complexity involved in converging the probability transition matrix, it is not possible for the algorithm to perform the clustering process in real-time, i.e. recalculate the probability transition matrix each time a new data point is added to the time series. As such, it is interesting to determine whether or not the algorithm has enough robustness to predict the behaviour of unseen data, based on previously seen time series.

For this purpose, the data containing the time series of the different features shall be split into so called training sets and test sets. The algorithm then performs the clustering based on the training data, resulting in a set of normal, extreme and precursor clusters, as well as their probability transition matrix. The centroids of all of the clusters are then recorded. These centroids are then used to classify the state of the test data. This shall be done by computing the distance between the state of the new incoming data to the previously identified clusters using the following formula:

$$\epsilon = \sqrt{\sum_{i}^{n} (\tilde{\phi}_i - \tilde{\phi}_{i,cluster})^2} \tag{4.42}$$

where $\tilde{\phi}_i$ is the current state of the incoming data, $n$ is the number of features and $\tilde{\phi}_{i,cluster}$ represents the centroids of all the previously computed clusters. To properly account for the influence of the different features, the states of the test data and the centroids of the clusters are normalized using min-max normalization. Once the closest cluster has been identified, the current state receives the labelling of that cluster. The precursor to the extreme event is then found when the data is labeled to belong to a precursor cluster. In this way, it is possible to achieve "online" prediction and assess the robustness of the algorithm. Moreover, this test is also a good indicator of the performance of the clustering-based method when only shorter time series are available.

**Features availability**
The following test is composed of two different parts:

- Firstly, the available data is again limited, not through the length of the time series or by not feeding it to the algorithm, but through the number of features. More specifically, the number of features will be varied and some key features will be removed from the available data to assess the prediction time. This way, it is possible to investigate which features give the best indication of an incoming flashback and see whether or not these are the same features indicated by the literature on autoignition.
- Secondly, this test will also look at a specific test case where the features will be limited to pressure time series at the walls and the temperature at location E0. Using pressure time series at the walls represent a step towards achieving true online prediction as collecting this sort of data at a high sampling frequency is possible by using pressure probes. The sampling locations are denoted by the yellow points in Figure 4.5. Unfortunately, removing the temperature time series altogether is a difficult task as the definition of the extreme event relies on it.

**Fluctuating conditions**
Generally, gas turbines can have either large or small fluctuations in their operating conditions. For example, fluctuations in power output, vibrations and noise, increased temperature at the compressor outlet and increased fuel consumption can induce a different behaviour in the combustion chamber. As such, it is important to determine the robustness of the precursor identification algorithm under these conditions. For this purpose a new LES simulation will done based on the same setup, but with different inlet conditions. Now, the digital filter method will be used to impose turbulent fluctuation at the inlet, as described in Section 4.2.3 and a realistic velocity profile will also be used, as discussed in Appendix D. Using the data generate by this new simulation, the same procedure will be applied to find the prediction time for the autoignition flashback.

## 4.7. Spray design

In order to find a suitable spray configuration which successfully stops the flashback, the design must focus on a few key parameters, while still adhering as much as possible to certain limitations. As previously mentioned in Section 2.5.1, there are several parameters which can be tuned. These parameters are the choice of atomizer, the injection location, the diameter of the spray $d_0$, the mass flow $\dot{m}_L$, the SMD, the angle of the cone, $\beta$, and finally the thickness angle of the cone, $\tau$. These parameters, in turn, influence the injection velocity, which can be considered as another critical design parameter. The swirl number is not considered here due to the tendency of swirled flows to induce CIVB flashback and to focus

on the effects created only by the autoignition flashback. In the following, each of these parameters are considered independently, focusing on the procedure taken to maximize the potential of the spray to stop the flashback. It should be mentioned that this procedure does not represent a thorough sensitivity analysis as only a preliminary design is sought.

Before moving on to the design parameters, the liquid water spray properties are shown in Table 4.2. Here, $\mu_L$, $\rho_L$, $\sigma$ and $C_p$ are the viscosity, the density, the surface tension and specific heat capacity of liquid water, respectively.

**Table 4.2:** Properties of liquid water

| T [K] | $\mu$ [Ns/m$^2$] | $\rho$ [kg/m$^3$] | $C_p$[ J/(kgK)] | $\sigma$[N/m] |
|---|---|---|---|---|
| 300 | 8.276e − 04 | 995.210 | 4180.2 | 71.175e − 03 |

**Injection velocity**

In a spray for which the main purpose is the suppression of the flashback, the injection velocity is one of the most important parameters. This is because it influences the response time of the water spray. Depending on the location of the spray and the external angle, the velocity necessary to stop the flashback ($V_{response}$) before it reaches the mixing duct can be determined. For example, if the spray is injected at the inlet ($x = 0$, $y = 0$ and $z = 0$ cm) with a hollow cone configuration, the velocity can be determined as follows (see Figure 4.16):

$$V_{response} = \frac{1}{cos(\beta - \tau)} \frac{\Delta x}{t_{pred}} \tag{4.43}$$

where $\Delta x$ is the distance the spray has to travel to the sampling location and $t_{pred}$ is the prediction time. Meanwhile, the actual injection velocity of the spray, $V_{inj}$, is calculated as follows:

$$V_{inj} = \frac{4\dot{m}_L}{\pi d_0^2 \rho_L} \tag{4.44}$$

In reality, the velocity of the spray is influenced by a multitude of factors and it will not equal $V_{inj}$, but, nevertheless, the value of $V_{response}$ can be taken as a first hand estimate for $V_{inj}$. As such, following Equation 2.3, the water mass flow and the nozzle diameter are tuned such that the $V_{inj} \approx V_{response}$. The other factors which influence the spray velocity are the external angle and the thickness angle due to way in which they position the flow relative to the reactant flow. Lastly, the SMD also plays an important role because, as previously discussed, large particles carry higher momentum and are thus less influenced by the drag of the surrounding flow. In this study, the influence of the SMD and the injector geometry is explored by trial and error.

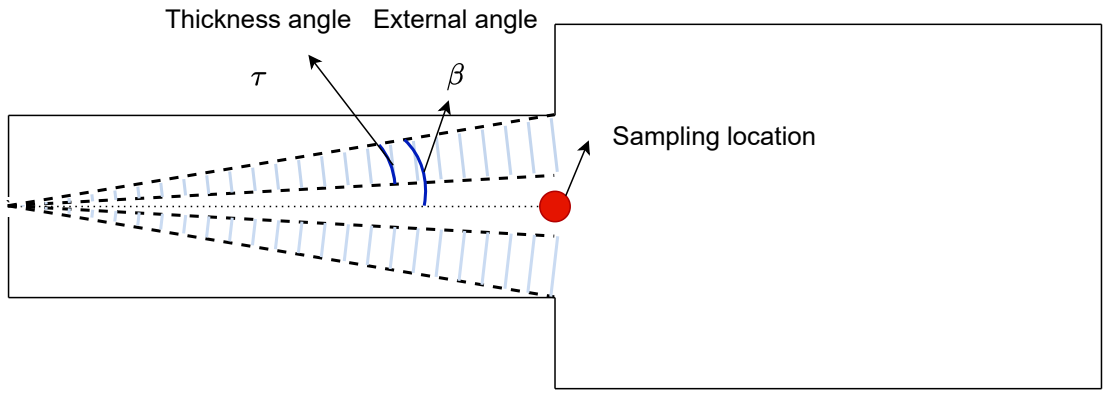


**Figure 4.16:** Schematic of the spray geometry when the injector is located at the inlet.

**Sauter Mean Diameter (SMD)**

The Sauter Mean Diameter, besides its influence on the drag of the particles, plays an important role in the particle's ability to evaporate. The SMD dictates how long it takes for the liquid particles to turn into gas and cool the surrounding flow by absorbing its heat. Generally, in a water spray which is not focused on flashback suppression, the SMD should not exceed a certain value beyond which the droplets do not have enough time to evaporate as this leads to a lower efficiency. For this design, although, the main focus is on stopping the flashback and as such this value will be merely used as a guideline. An estimation of the SMD can be obtained based on the study of Estes and Mudawar [134]:

$$\begin{gathered} d_{32} = 3.67 d_0 \left[ We_{d_0}^{1/2} Re_{d_0} \right]^{-0.259} \\ We_{d_0} = \frac{\rho_\mathrm{a} \left( 2\Delta P / \rho_\mathrm{L} \right) d_0}{\sigma} \qquad Re_{d_0} = \frac{\rho_\mathrm{L} \left( 2\Delta P / \rho_\mathrm{f} \right)^{1/2} d_0}{\mu_\mathrm{L}} \end{gathered} \tag{4.45}$$

**Atomization regime**

In this study, the Rosin-Rammler (RR) particle distribution is used and the break-up phenomena is neglected. As such, it is important to determine whether or not the atomization regime of the spray fits this assumption. For this purpose, the guidelines laid out by Reitz [135] are followed. Here, the author indicates that there are four atomization regimes which are encountered sequentially as the injection velocity rises. In the Rayleigh Jet Breakup Regime, droplets form due to axisymmetric surface oscillations caused by surface tension, with droplet diameters larger than the jet. In the First Wind-Induced Breakup Regime, surface tension is assisted by static pressure differences from jet and ambient gas velocities, causing breakup several jet diameters from the nozzle and producing droplets roughly the size of the jet. The Second Wind-Induced Breakup Regime features enhanced short wavelength surface waves from increased relative velocity of the two-phase flow, leading to droplet formation. Finally, in the Atomization Regime, small droplets form immediately upon exiting the nozzle, effectively atomizing the jet. The four regimes are displayed in Figure 4.17.

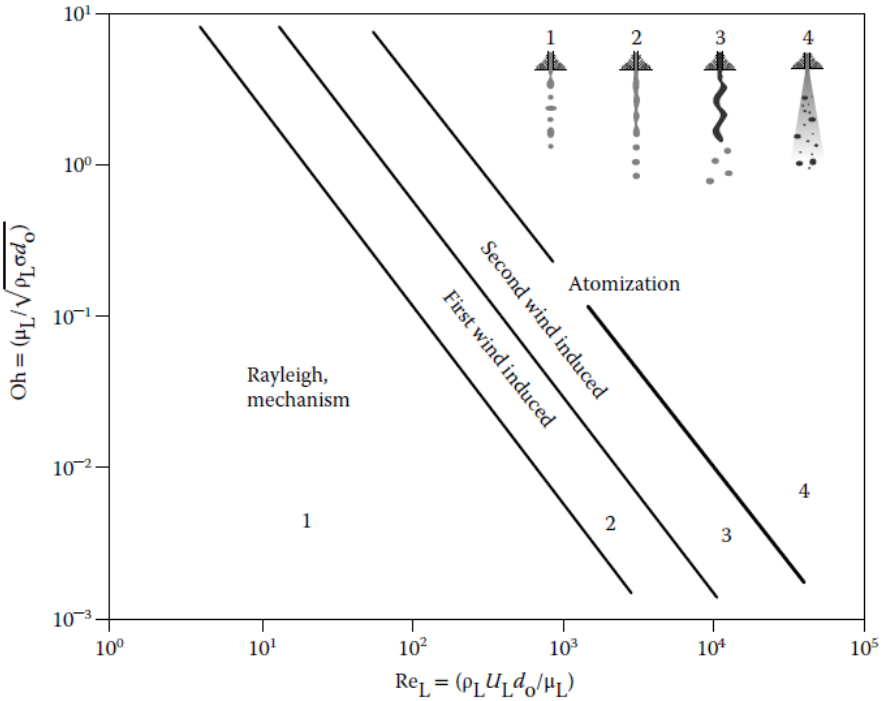


**Figure 4.17:** Break-up regimes based on the Ohnesorge number and the Reynolds number [135].

As such, a constraint of this design is to ensure that the spray is in the atomization regime. For this purpose, the design parameters of the spray shall be tuned such that the values of Oh and $\mathrm{Re_L}$ fit this criteria. These numbers are calculated as follows:

$$\begin{aligned} \mathrm{Re_L} &= \frac{\rho_L V_{inj} d_o}{\mu_L} \\ \mathrm{Oh} &= \frac{\mu_L}{\sqrt{\rho_L \sigma d_0}} \end{aligned} \tag{4.46}$$

**Injector geometry**

The remaining parameters not discussed yet are the diameter of the spray $d_0$, the angle of the cone $\beta$ and the thickness angle $\tau$. Similarly to the SMD, the influence of these parameters shall be explored empirically. What is mainly sought here is that the spread of the particles, as dictated by the two angles, is wide enough to cover the whole area of the premixing duct, effectively stopping the flashback from advancing upstream.

# 5

# Results

In this chapter, the results aimed at answering the research questions are presented and discussed. Firstly, the LES simulation and the observed phenomena are discussed, where emphasis is made on the flashback and autoignition precursors. Secondly, the dimensionality reduction technique is applied and the results are discussed, resulting in a final choice for the features to be used in the precursor algorithm. Then, the results from the modularity-based clustering algorithm are discussed, along with the robustness tests detailed in Section 4.6. Lastly, the use of water injection to suppress the flashback is discussed.

## 5.1. 3D LES simulation

The first part of this chapter consists of analyzing the high pressure 3D LES simulation of the simplified GT36 combustor. For this simulation, the case setup is described in Section 4.2, with the exception of using the digital filter method to impose turbulent fluctuations at the inlet. This choice was made to simplify the analysis and for this simulation to serve as a first demonstrator for the modularity-based clustering precursor identification algorithm. Later on, a realistic case where turbulent fluctuation are super-imposed at the inlet along with a fully-developed pipe flow velocity profile is also put to the test. As a summary, the most important conditions for this simulation are as follows:

- Pressure BC at the outlet: $P = 20$ atm
- Inlet velocity: $V = 200$ m/s
- Inlet temperature: $T = 1180$ K
- Equivalence ratio: $\phi = 0.35$
- Turbulence intensity at the inlet: $I = 10\%$

The simulation has a base grid with a $\Delta x = 0.4$ mm, 10 million cells in total when AMR is activated and at a minimum 5 cells across the thin flame front by using the TFM model. In addition, to verify the adequacy of the simulation, Pope's criteria is shown in Figure 5.1, which corresponds to a time-step where the flame is located in the combustor. The calculation was done using Equation 4.31, where $K(x,t)$ was calculated as $K = \frac{1}{2}(\tilde{u}^2 + \tilde{v}^2 + \tilde{w}^2)$, with $\tilde{u}$, $\tilde{v}$, $\tilde{w}$ being the time-averaged RMS values of the fluctuations of the velocity components. It can be seen how almost the entire domain is below the 0.2 threshold, which is generally considered as acceptable for LES. The only regions which come close to this value are the IRZs, where the velocity and the sub-grid scale velocities are closer to 0, making the ratio of turbulent kinetic energies less precise.

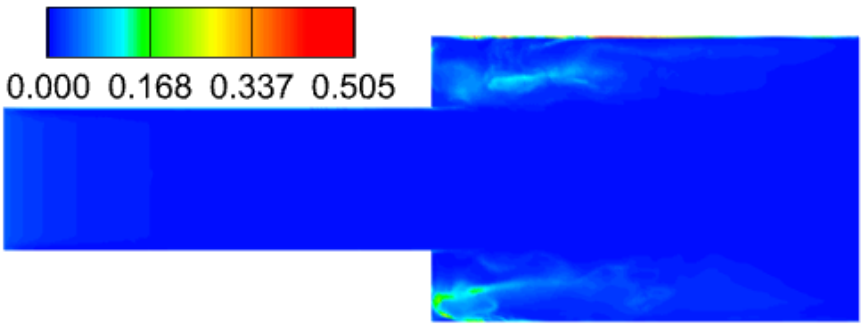


**Figure 5.1:** Pope's criterion at an arbitrary time step.

This simulation is similar to the cases analyzed by P. Rouco [19] and Kruljevic et al. [49], at 20 atm and 1 atm, respectively. Their likeness can be verified by inspecting Figure 5.2. The simulation exhibits the same characteristics, showing a central divergence zone (CDZ), formed due to the expansion of the gas and represented by the divergence of the streamlines. Furthermore, the outer recirculation zones (ORZ) are also present, which form due to the sudden expansion of the combustion chamber and the consequent large vortical structures which appear in the corners. In between these regions, the shear layer is also found.

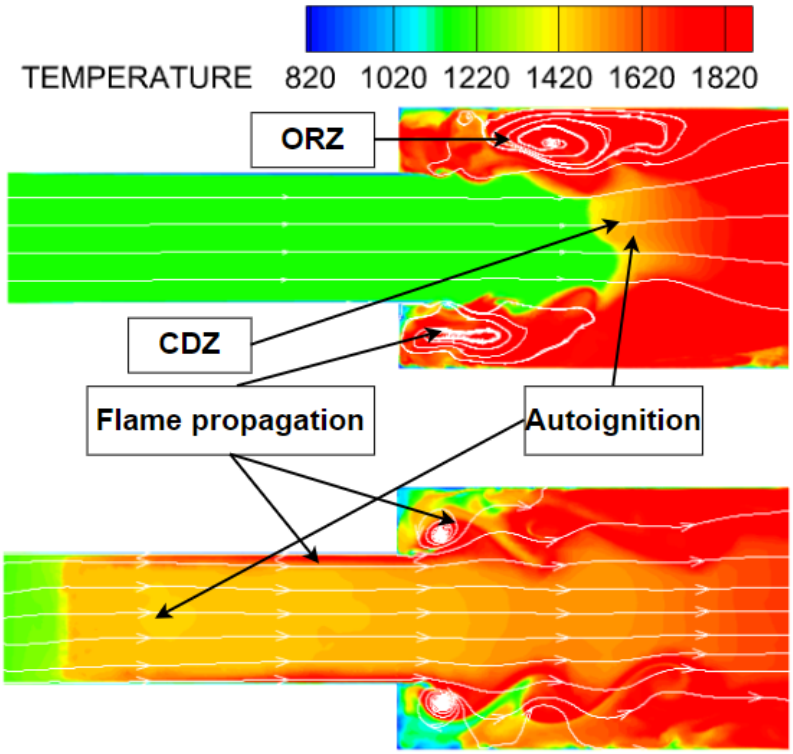


**Figure 5.2:** Flame contour plot for two positions of the flame. The figure depicts the autoignition and flame propagation zones in the two scenarios, as well as the central divergence zone (CDZ) and the outer recirculation zones (ORZ).

Also seen in Figure 5.2 are the two distinct mechanisms which sustain the flame: the deflagration flame which propagates and stabilizes at the corners and the other, the self-sustaining autoignition process in the central area of the burner. The propagation of the

flame is driven by the creation of recirculation zones, where the balance between heat loss at the walls and the heat produced by burning the reactants aided by the influx of energy coming from the high temperature burnt gasses, keeps the flame at a stable position. This ORZ is isolated from the instabilities occurring in the autoignition zone due to its position. Meanwhile, at the central part of the flame, autoignition is the dominant regime, driven by the high temperature of the reactants. This regime does not appear in the ORZ due to the heat of the reactants being lost to the walls. It does however present significant fluctuations as explained in the following section.

### 5.1.1. Flashback in Anslado Energia GT36 reheat combustor

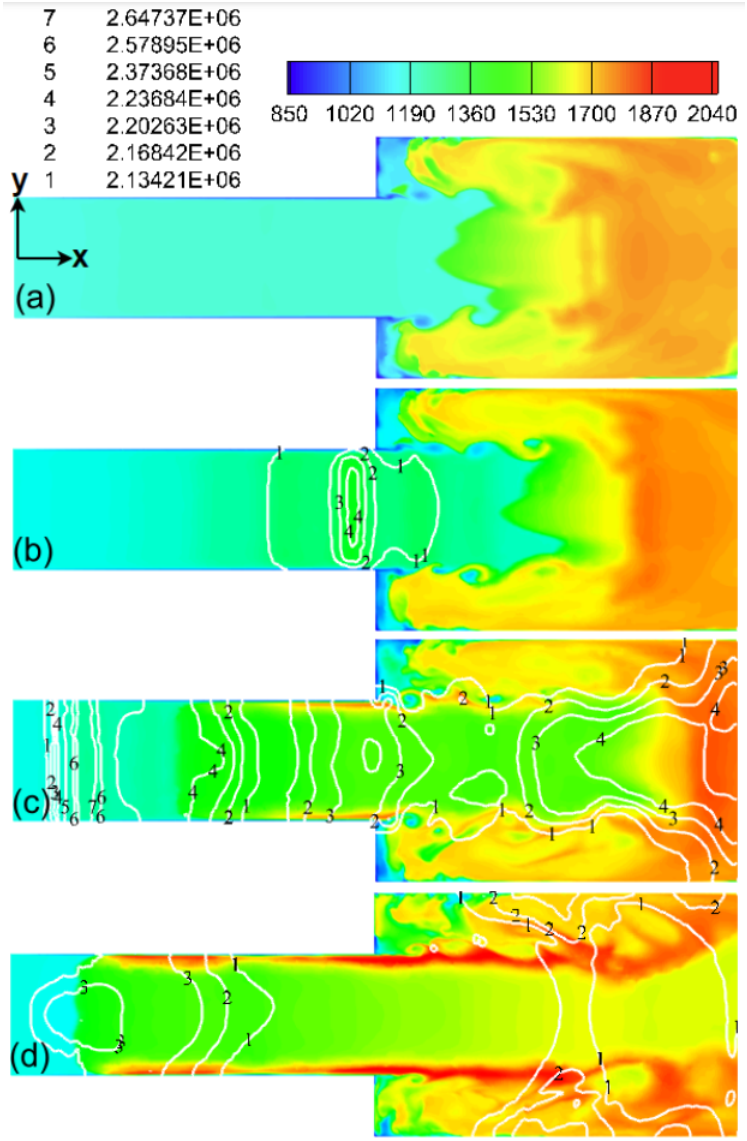


**Figure 5.3:** Contour of temperature [K] during a typical flashback event (top to bottom), where the white lines represent pressure [Pa] isolines.

In this simulation, combustion is set to start at 1 ms, after the inert flow is fully developed in the combustion chamber. Shortly after, the flow ignites through the autoignition process and the base of the flame settles at the expansion step. This is the design location of the

flame as calculated by the balance between the autoignition delay time and the flow-through time. The autoignition is accompanied by a pressure wave generated by the heat release, which expands the gases in its vicinity. This pressure waves then travels both downstream and upstream of the flame location, reflecting at the walls of the combustion chamber. The reflected pressure waves then form a constructive interference pattern, converging at the centerline and sending these pressure waves periodically upstream. This behaviour leads to a positive temperature fluctuation due to compressive heating (Figure 5.3, b). The temperature then rises, eventually resulting in an early autoignition event, accompanied by a pressure wave which travels upstream, imposing an unfavourable pressure gradient on the incoming flow, creating the so-called piston effect. The flow is then heated through compression, allowing for autoignition in the rest of the mixing duct (Figure 5.3, c). As seen from (Figure 5.3, d), the boundary layer is the most susceptible in this case and flame propagation also appears, resulting in a boundary layer flashback. The flame travels almost all the way to the inlet, corresponding to the point where the residence time matches the new ignition delay found under the significantly higher pressures and temperatures. Once the pressure wave reaches the inlet, the piston effect ceases, resulting in a relaxation phase, where the temperature and the pressure return to normal operating conditions. The flame is then flushed back, this time further downstream than the original location (Figure 5.3, a). Nevertheless, ignition kernels quickly start to appear again and the process repeats itself.

In this case, autoignition, the predominant regime of flame propagation for the GT36, is highly sensitive to temperature fluctuations. As previously mentioned, the autoignition delay time has a strong dependence on temperature, especially near the cross-over point. As the reactants' inlet temperature is 1180 K, it only takes a relatively small increase in temperature such that the flame changes its location. Furthermore, the cross-over temperature, which is approximately 1350 K, is also easily reached once ignition kernels start to appear. This temperature is in fact the temperature found slightly upstream of the step location, just before the flow fully autoignites in the whole premixing tube. Also interesting to mention here is that the pressure wave has a large amplitude, reaching 26.5 atm at the inlet, and it travels at nearly 650 m/s, which is the speed of sound in medium formed by the reactants. This creates a powerful piston effect, slowing the incoming flow more than half of its initial velocity, i.e. 100 m/s. Furthermore, this phenomena is also negatively impacted by larger equivalence ratios and inlet bulk velocities. Whereas a higher value for the inlet bulk velocity generally results in an increased resistance to flashback, in this case, it leads to more compressive heating, allowing for easier autoignition. Similarly, the equivalence ratio was found to generate stronger pressure waves for values above $\phi = 0.2$ [58].

The boundary layer flashback can also prove detrimental in this scenario by aiding the upstream movement of the flame through an increase of the temperature near the wall. This type of flashback occurs when the balance between the turbulent burning velocity and the local flow velocity near the wall shifts in favour of the propagating flame. This can happen for a multitude of reasons such as fluctuation in the turbulent burning velocities and vortices leading to the separation of the boundary layer. Furthermore, in the case of hydrogen, this phenomena is more prone to appear due to the small quenching distance (the distance from a wall at which the flame is extinguished) of only 0.64 mm. According to Hoferichter [30], the turbulent flame speed, velocity fluctuations and other parameters such as the quenching distance are a good indicator of the propensity of the flow for boundary layer flashback. In this simulation, the boundary layer flashback is aided by the autoignition

in the mixing duct through the resulting heating of the ambient flow and the smaller velocity present due to the piston effect. Nevertheless, predicting the appearance of BL flashback is not of interest in this study, as this phenomena happens only as a result of the autoignition process. This being said, to fully suppress any flame propagation within the mixing duct, this type of flashback must also be suppressed.

### 5.1.2. Autoignition precursors

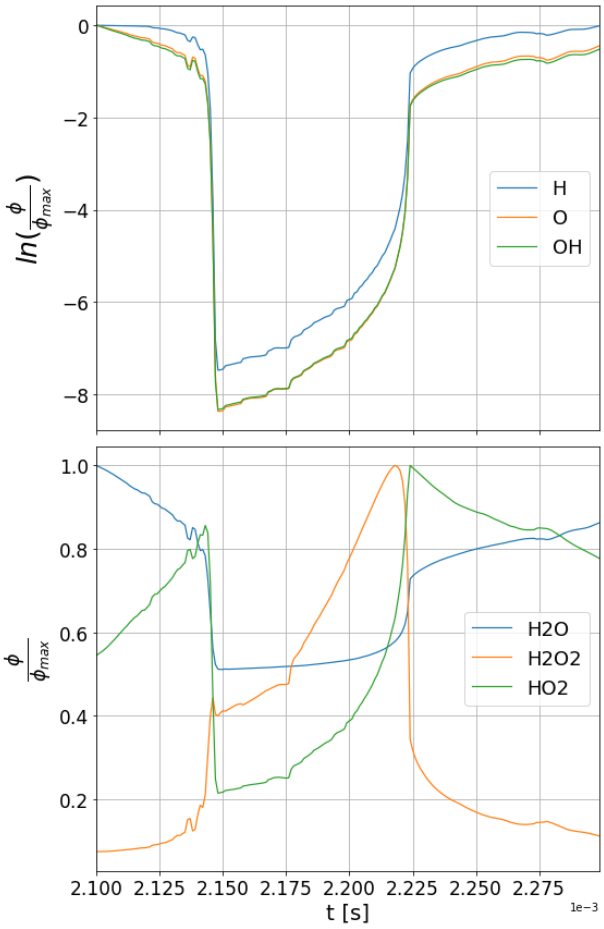


**Figure 5.4:** Species mass fractions over the course of a typical flashback event taken at the sampling location E0 (see Figure 4.5)

A complementary analysis to the one shown in Section 2.4.3 can be performed here based only on the LES simulation data to find what flow variables are a good indicator of flashback. In particular, scalars of interest are plotted at the intersection of the centerline axis and the step plane over the course of a typical flashback event (see Figure 5.4). Key moments of this figure happen around $t = 2.14$ ms, where the flame is flushed downstream of the considered point and $t = 2.22$ ms which approximates the time when the cross-over temperature (T = 1350 K) is surpassed and autoignition happens almost instantly in the whole premixing duct. From the figure, it is clear that $H_2O_2$, $HO_2$ and $H_2O$ present a significant increase during the relaxation period before the following flashback, where $H_2O_2$ and $HO_2$ follow a similar pattern. Furthermore, although not as visible, H, O and OH also present a coupled increase, as evident when the natural logarithm is plotted.

As such, the following analysis can be split into the chemical kinetics below and above cross-over, which Trevino [136] identified as a thermal runway and branched-chain explosion, respectively. The most important reactions below cross-over are shown in Equation 5.1 [137], while the ones which are most important above cross-over are displayed in Equation 5.2 [138].

$$\begin{aligned} \mathrm{H} + \mathrm{O_2} + \mathrm{M} &\rightleftarrows \mathrm{HO_2} + \mathrm{M} \quad (R9) \\ \mathrm{HO_2} + \mathrm{HO_2} &\rightleftarrows \mathrm{H_2O_2} + \mathrm{O_2} \quad (R14) \\ \mathrm{H_2O_2} + \mathrm{M} &\rightleftarrows \mathrm{OH} + \mathrm{OH} + \mathrm{M} \quad (R15) \\ \mathrm{H_2O_2} + \mathrm{H} &\rightleftarrows \mathrm{H_2} + \mathrm{HO_2} \quad (R17) \end{aligned} \tag{5.1}$$

$$\begin{aligned} \mathrm{O_2} + \mathrm{H} &\rightleftarrows \mathrm{O} + \mathrm{OH} \quad (R1) \\ \mathrm{O} + \mathrm{H_2} &\rightleftarrows \mathrm{H} + \mathrm{OH} \quad (R2) \\ \mathrm{H_2} + \mathrm{OH} &\rightleftarrows \mathrm{H_2O} + \mathrm{H} \quad (R3) \\ \mathrm{H} + \mathrm{O_2} + \mathrm{M} &\rightleftarrows \mathrm{HO_2} + \mathrm{M} \quad (R9) \\ \mathrm{HO_2} + \mathrm{H} &\rightleftarrows \mathrm{H_2} + \mathrm{O_2} \quad (R10) \end{aligned} \tag{5.2}$$

Central to the discussion are radicals, specifically focusing on the chain-branching step R1, $\mathrm{H} + \mathrm{O_2} \rightarrow \mathrm{OH} + \mathrm{O}$, and the chain-termination step R9, $\mathrm{H} + \mathrm{O_2} + \mathrm{M} \rightarrow \mathrm{HO_2} + \mathrm{M}$. Both steps involve the same reactants, yet the latter requires an additional third body, M. The branching step's rate escalates markedly with an increase in temperature, whereas the termination rate remains relatively unchanged with temperature variations. This indicates that at a certain elevated temperature, the branching rate surpasses the termination rate. Conversely, at temperatures below this threshold, the branching rate is markedly lower than the termination rate. This specific temperature, where the rates of both reactions intersect, is in fact the crossover temperature. Its significance lies in its role in dictating autoignition chemistry; above this temperature, radical concentrations during autoignition escalate substantially, while below it, the termination process keeps these concentrations minimal [138]. Nevertheless, autoignition below cross-over is enabled by an alternative branched-chain path. This consists of the formation of $\mathrm{H_2O_2}$ from R14 and the subsequent formation of OH from $\mathrm{H_2O_2} + \mathrm{M} \rightleftarrows \mathrm{OH} + \mathrm{OH} + \mathrm{M}$ (R15). Furthermore, to a smaller extent, autoignition is also helped by the creation of H radicals through the reverse of reaction R17 [137]. This explanation proves satisfactory when tracking the mass fraction of Figure 5.4, but, this being said, it is possible that there are other reactions involved in the autoignition process below the cross-over temperature. While it is clear that the cross-over temperature is reached through the means of exothermic reactions, aided by the availability of H radicals, there is no single species which could be considered as a precursor for flashback. As such, different combinations of the species $\mathrm{HO_2}, \mathrm{H_2O_2}, \mathrm{H}, \mathrm{O}, \mathrm{OH}$ shall be investigated, where a larger number of species is preferred.

It should also be mentioned here that thermo-diffusive instabilities may also influence the autoignition process. These instabilities hinder the autoignition process due to the preferential diffusion of hydrogen towards the flame front in wrinkled flames, and at the same time it facilitates it through the expansion of the flame attributed to the hydrogen diffusion, which in turn increases the temperature near the autoignition region. However, as autoignition seems to appear relatively far away from the flame front, this appears to be of little relevance for this simulation. Nevertheless, for different initial conditions

(i.e. $\phi \approx 0.15$), the autoignition process was also observed to appear closer to the flame front and as such, in these cases importance may also be attributed to flow variables that influence the wrinkling process.

## 5.2. Dimensionality reduction

Using this first base simulation, it was seen that there are several scalars which may be of interest for the precursor identification algorithm, as indicated in Section 5.1.2. Nevertheless, the LES simulation outputs many different variables which may also be used. To avoid the curse of dimensionality in the modularity-based clustering, it is thus needed to trim the number of variables to a manageable number. This section shows the results of the dimensionality reduction procedure, following the methodology laid out in Section 4.4.

Before this step, some of the variables can already be eliminated based on either insight into the physical phenomena or their lack of practicability. Firstly, only variables which are inherent to the thermo-chemical and physical state of the system should be considered, as these are the variables that can potentially be measured in a real life. This excludes variables that pertain to the LES model, such as the magnitude of the turbulent velocity, sub-grid scale velocities and sub-grid scale kinetic energy and dissipation rate.

Secondly, the velocities in the transversal axes with respect to the direction of the flow and the vorticity vector can also be excluded. These variables, although an indicator of the turbulent mixing present in the flow, can be disregarded because the consequence of this mixing can be taken directly in the form of the mass fractions of the different species. Furthermore, due to their large variation over the short period of time in between two autoignition events, these variables do not constitute a solid basis for the co-kurtosis analysis as the distribution of the samples also varies significantly within the region of interest. Lastly, these variables would also not form a strong basis for the clustering procedure as they can vary significantly from one flashback to the other in a non coherent fashion which would not assist the clustering algorithm in finding a precursor to the autoignition event.

Third and lastly, quantities which are averaged over space or time such RMS or mean values should also be disregarded. This is due to the fact that the phenomena of interest is inherently dynamic, happening over a very small time period. If the fluctuations in the variables of interest are averaged out then the modularity-based clustering would find less differences between the different states in the system and would thus have a lower chance of finding a precursor. The remaining variables to consider are thus as follows:

- Temperature ($T$)
- Density ($\rho$)
- Pressure ($P$)
- Axial velocity ($V_x$)
- Mass fractions of the species: OH, O, H, $O_2$, $H_2$, $H_2O$, $H_2O_2$, $HO_2$

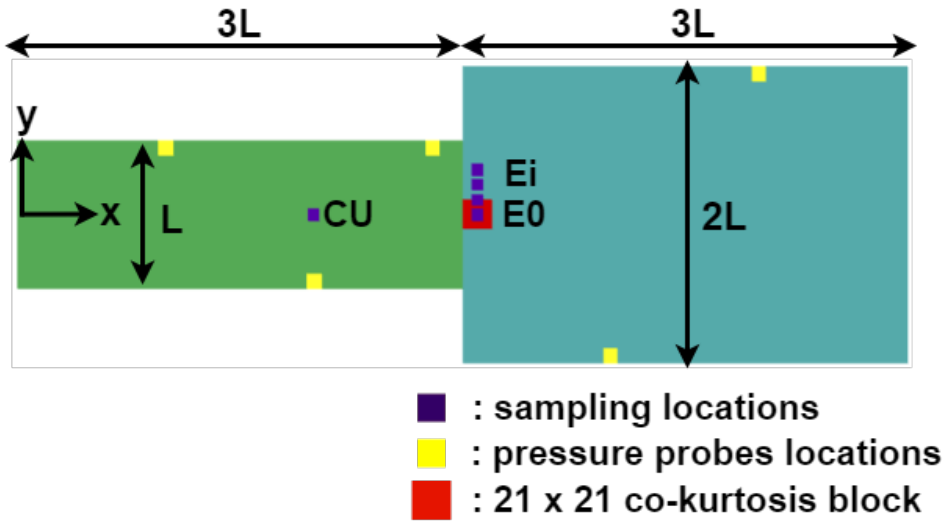


**Figure 5.5:** 2D geometry showcasing the co-kurtosis sampling block

The next step in the dimensionality reduction procedure consists of applying the co-kurtosis algorithm. Towards this purpose, the block shown in red in Figure 5.5 is sampled at every time step for the variables mentioned above. This block consists of a grid of 21 x 21 sampled from the Tecplot 601 x 201 data obtained from the post-processing of the LES. This results in 441 samples over a region of 2.1 x 2.1 $mm^2$, ensuring a region of interest which contains enough samples to be statistically significant, but at the same time, focusing on the autoignition region, such that there are no data points coming from regions where there is already a flame.

### 5.2.1. Kurtosis

Before moving on to the co-kurtosis, it is also interesting to calculate the kurtosis of the dataset. Kurtosis is also calculated on the same domain for each time step using Equation 5.3, where $n$ denotes the number of samples, $s$ is the standard deviation and $X_{avg}$ is the mean.

$$K = \frac{n(n+1)}{(n-1)(n-2)(n-3)} \frac{\sum_{i=1}^{n} \left(X_i - X_{\text{avg}}\right)^4}{s^4} - \frac{3(n-1)^2}{(n-2)(n-3)} \tag{5.3}$$

The resulting value from this formula denotes the excess kurtosis, meaning that distributions with $K > 0$ are leptokurtic, having a fatter tail or a significant amount of outliers. The result is shown over the course of a typical flashback event and for the period shortly after it in Figure 5.6, where the evolution of features ($\phi$) are plotted alongside the evolution of the kurtosis. The results are divided into three different graphs, grouped by the features which show similar behaviour in the kurtosis. The features themselves are shown scaled by their maximum such that they can be plotted together. The kurtosis values should give a good indication of what features tend to have outliers at the same time, thus allowing for a better understanding of the co-kurtosis analysis.

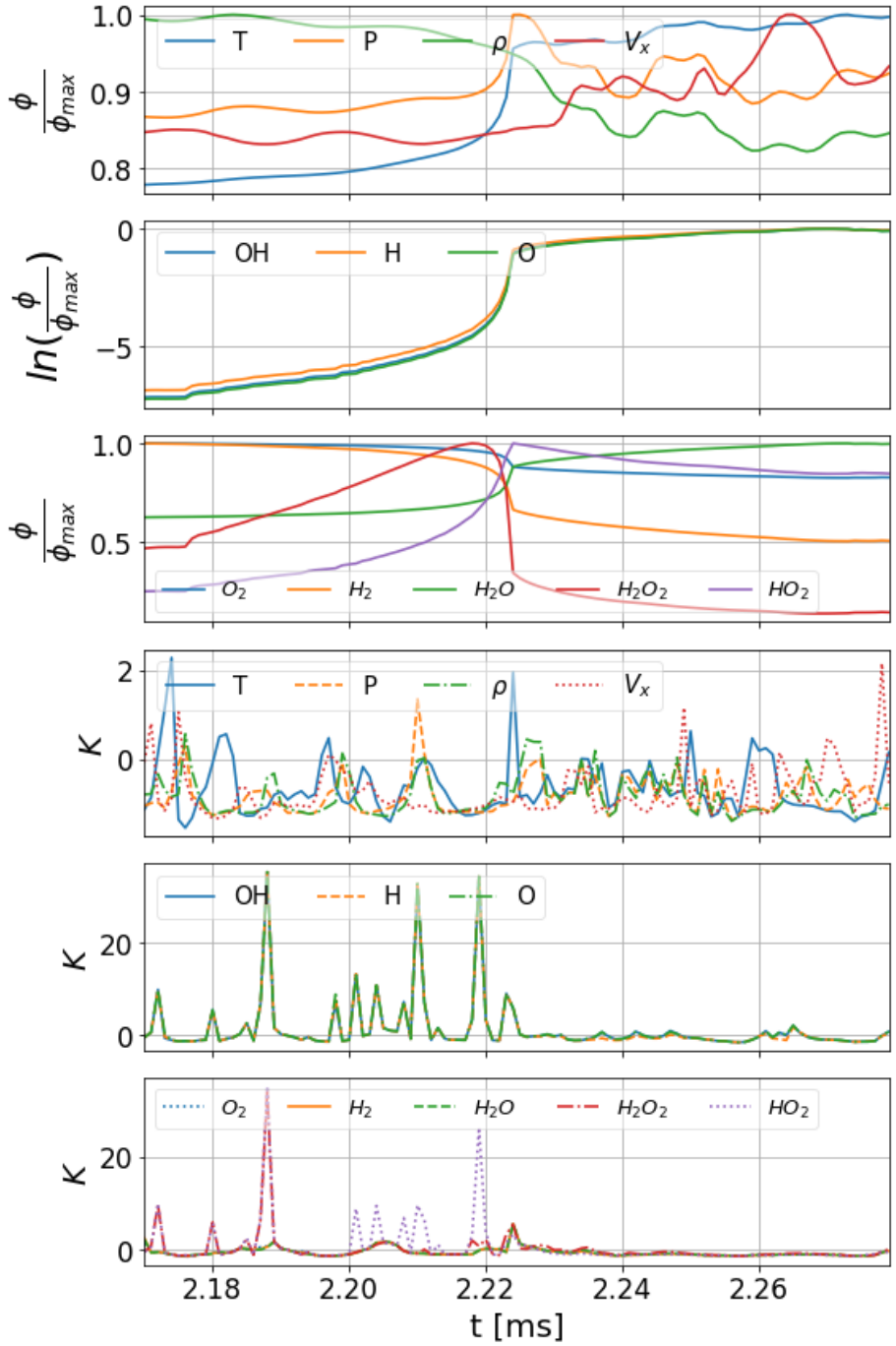


**Figure 5.6:** Variables of interest and their kurtosis values during a typical flashback event.

Regarding the features, it can be seen how the pressure, the temperature and the mass fractions of several species slowly increase, culminating in a exponential increase right before the flashback event. Then, for the period after autoignition, it can be seen how the flashback event, accompanied by the large magnitude pressure wave, creates a highly unstable and fast varying state for $T$, $P$, $\rho$ and $V_x$. Meanwhile, the behaviour of the mass fractions is almost uniform as now the autoignition front has moved upstream.

For the kurtosis values, firstly, the temperature, the pressure, density and velocity in the x-direction generally have low values of kurtosis, with rare exceptions in which $K > 0$,

out of which, the most significant exceptions occur for temperature. This is expected as all of these variables should generally not vary significantly within the region of interest in a stable state. This also holds true for the period after the flashback. Here, although the features have a significant temporal variation, the spatial variation is limited within the region of interest. Secondly, the kurtosis for the mass fractions of OH, H and O show extremely high valued peaks of kurtosis for distinct times across the time series. This is indicative of reactions occurring below the cross-over temperature which happen locally in the region of interest, or of the propagation of an ignition kernel which happened outside this region. The next set consists of the mass fractions of $O_2$, $H_2$, $H_2O$, $H_2O_2$ and $HO_2$. Here, most of the mass fractions have values close to 0, with the exception of $H_2O_2$ and $HO_2$, out of which $HO_2$ has more peaks of high kurtosis. It should be noted that the activity of $H_2O_2$ and $HO_2$ is closely aligned with that of OH, O and H, but the peaks of the former are generally less pronounced. Most interesting, the period after the flashback shows almost no values of $K > 0$ for any of the species. This is already promising with regards to the use of co-kurtosis because there is a clear distinct behaviour between the two periods. This further confirms the intuition that kurtosis and co-kurtosis can capture the activity of species before an autoignition event.

The behaviour of the kurtosis of the mass fraction of the different species can be further explained by considering Figure 5.7, Figure 5.8 and Figure 5.9. These figures show the evolution of the distributions of $H_2$, OH and $H_2O$ over 12 time-steps ($t = 2.170 - 2.181$ ms) between two peaks of high kurtosis for OH and $H_2O$. These species have been chosen based on their position in the reaction chain, such that reactants, intermediate species and products are all represented. Any of the other species which fit these categories could have been chosen instead, as their behaviour is similar. In general, the intermediate species which appear in the reaction chain have a higher predisposition of showing outliers.

Starting with the histograms of OH, one can link the distributions at $t = 2.172$ and $t = 2.180$ ms with peaks shown in the kurtosis time-series. On one hand, these distributions are rather uniform due to the large peak containing numerous samples in a small range of values. Furthermore, the presence of outliers at these two time-steps can also be observed far away from the mean. Putting these together, the distribution formed resembles a fat-tailed distribution which is bound to show high values of kurtosis. It is interesting to note that there are other time-steps, such as $t = 2.170$ and $t = 2.177$ ms, which have a distribution of this form, without presenting such high values for the kurtosis. This is due to the mean of the distribution being closer to the outliers. This brings into perspective the way kurtosis is calculated. Being a fourth-order moment, the distance from the mean is amplified significantly. Meanwhile, the distributions of $H_2O$ and $H_2$ better resemble a Gaussian distribution, and, as such, they do not present high values of kurtosis.

There is another important distinction to be made regarding the value of kurtosis. It may not necessarily be attributed to the apparition of ignition kernels. Considering the histograms of the mass fraction of OH at $t = 2.172$ and $t = 2.180$ ms, it can be seen that the first has the outliers to the left of peak, while the second has the outliers to the right. Relating the distributions to the contour plot at those time-steps, as shown in Figure 5.10, the reason for this difference in behaviour becomes evident. At $t = 2.172$ ms, the sampling region, denoted by the black borders, contains outliers at a lower value than the rest of the region, due to the incomplete propagation of OH molecules from an autoignition kernel placed upstream. Meanwhile, at $t = 2.180$ ms, the sampling region indeed captures the apparition of an ignition kernel located slightly downstream. This means that not every

kurtosis peak indicates the apparition of an ignition kernel. Furthermore, depending on where the sampling region is located, the time-steps at which high kurtosis values appear will change significantly. Nevertheless, even though it is not possible to tell exactly what is the underlying phenomena that triggers high kurtosis values without closely examining all of the time-steps, the important part is that kurtosis can indicate an evolving field. Thus it should be a good indicator for which values present the highest activity before the flashback.

Shifting the discussion to the actual evolution of the distributions in time, certain correlations can be observed between the reactants, the products and the intermediate species. One can see that the mass fraction of $H_2$ decreases between $t = 2.170 - 2.181$ ms and the distribution shifts from having the peak more towards the right, to having the peak towards the left. This indicates that more and more $H_2$ is being consumed, allowing for intermediate species to be formed and for the autoignition kernel to appear at $t = 2.180$ ms. In contrast, the mass fraction of $H_2O$ has its peak shifted from the left to the right. This indicates an increased rate in the formation of products from the reactions under the cross-over temperature, facilitating autoignition by releasing heat. As previously mentioned, the distributions of $H_2O$ and $H_2$ have a more Gaussian form. This is likely due to their slower spread as a result of autoignition. For example, while for OH, the region of interest is fully covered with the higher mass fraction OH in just 3 time-steps, for $H_2O$, this takes over 8 time-steps, resulting in a more uniform spread in the distribution.

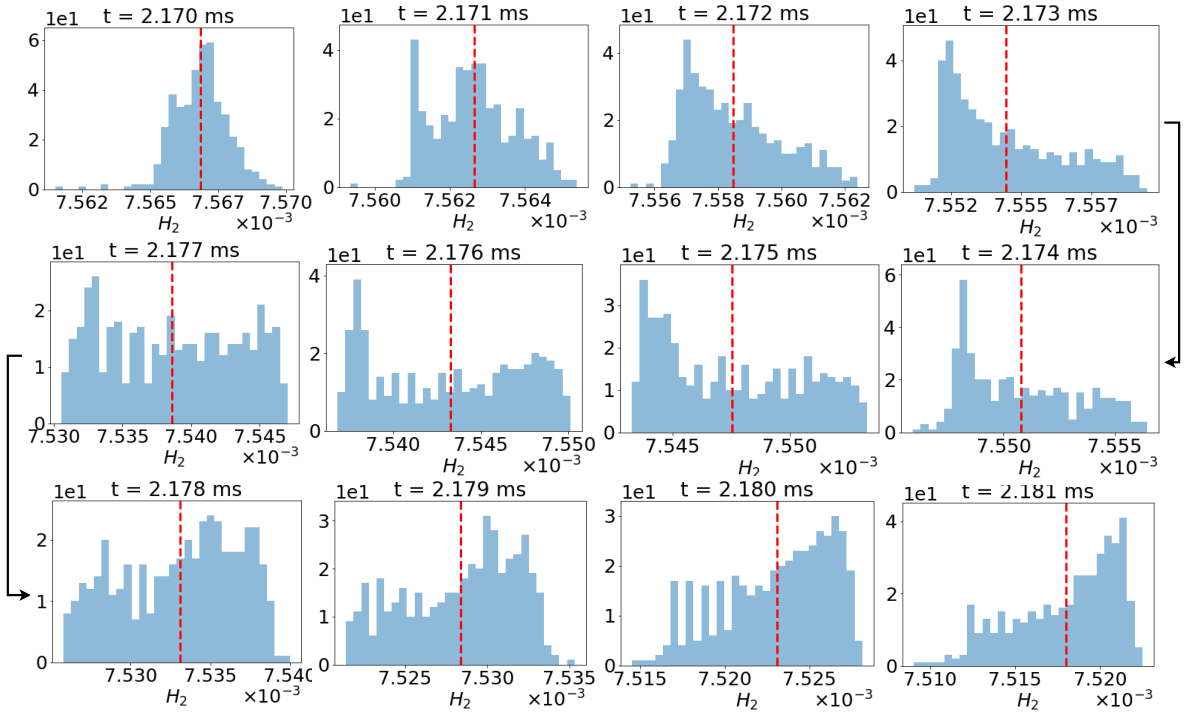


**Figure 5.7:** Histograms showing the evolution of the distribution of $H_2$ mass fraction in the sampling region after the apparition of an ignition kernel. Red line is the mean.

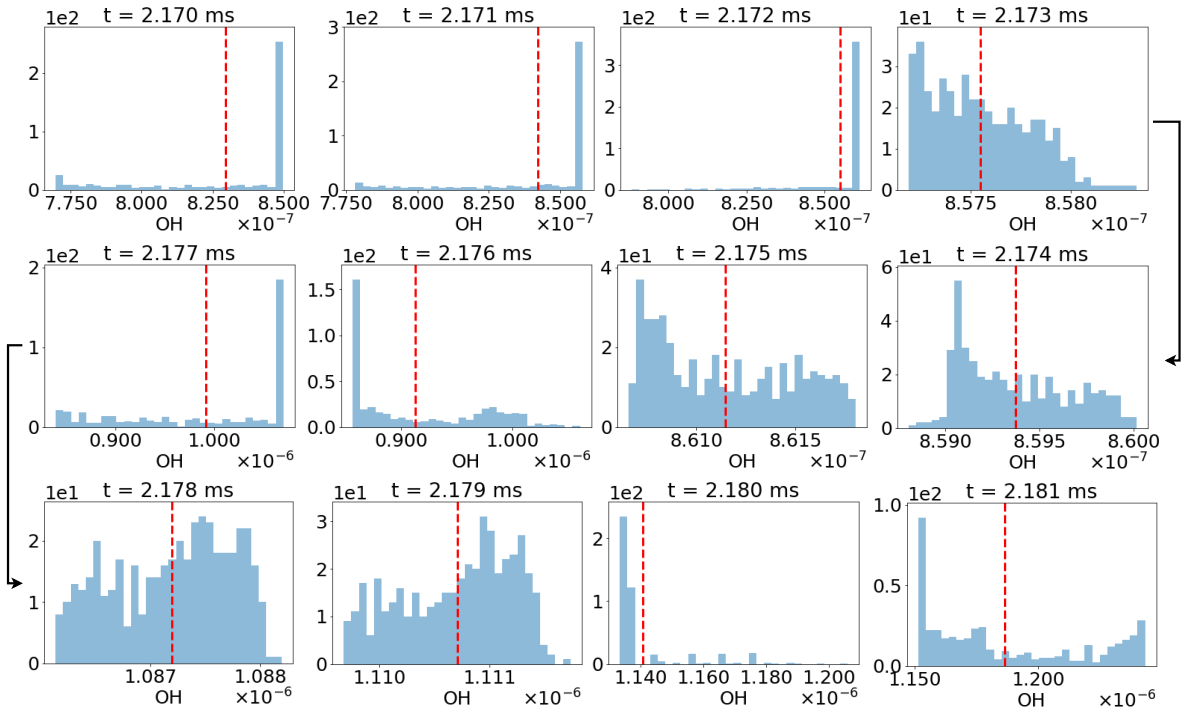


**Figure 5.8:** Histograms showing the evolution of the distribution of OH mass fraction in the sampling region after the apparition of an ignition kernel. Red line is the mean.

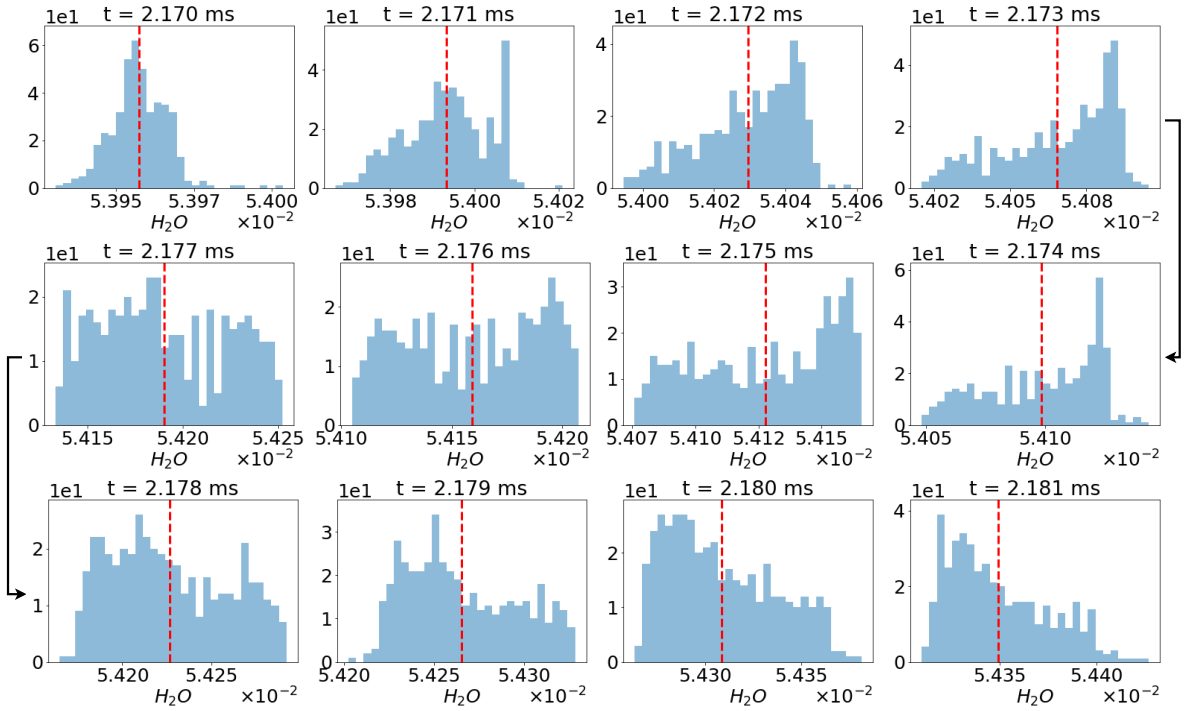


**Figure 5.9:** Sequence of histograms showing the evolution of the distribution of $H_2O$ mass fraction in the sampling region after the apparition of an ignition kernel. Red line is the mean.

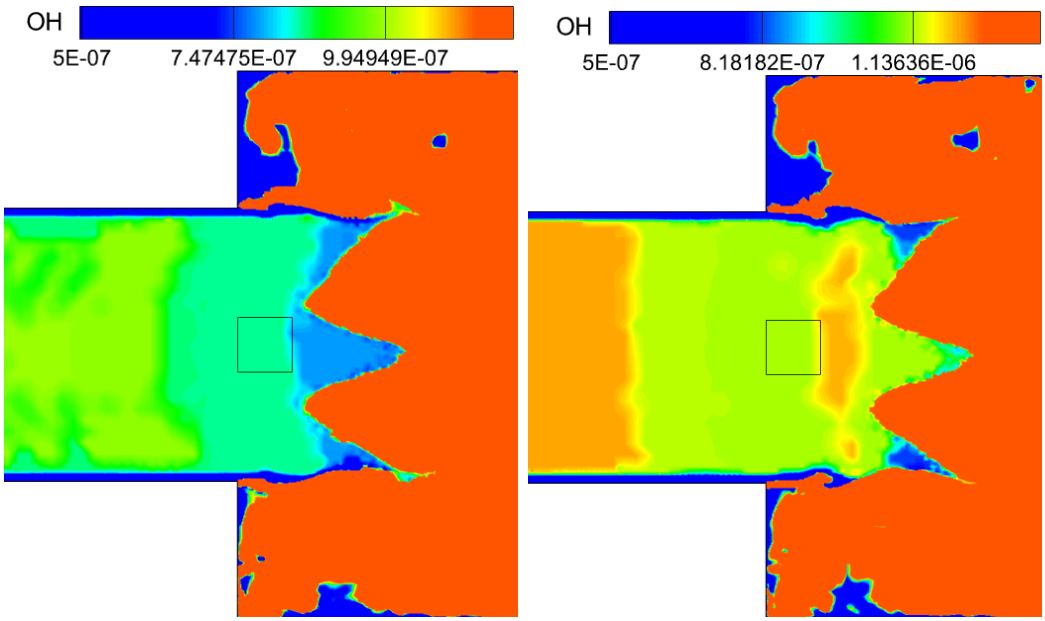


**Figure 5.10:** Contour plot showing the mass fraction of OH in and around the sampling region (shown with the black edge box) at $t = 2.172$ and $t = 2.180$ ms.

### 5.2.2. Co-Kurtosis PCA

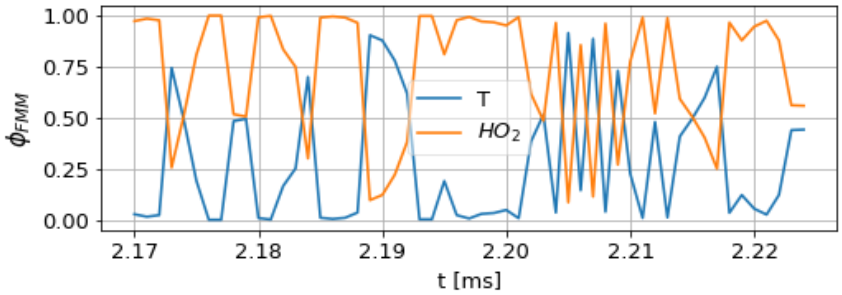


**Figure 5.11:** Feature moment metrics of T and $HO_2$ taken individually over the course of a typical flashback event.

Co-kurtosis PCA has proven to be useful for both dimensionality reduction of combustion datasets and for detecting ignition kernels [88] [89]. While kurtosis was able to identify important changes in the individual features which make up the system, the idea behind using co-kurtosis is to build on this by identifying the relationship between these features and assess which ones are the most important. This would effectively allow for a reduction in the number of useful features, making the use of the modularity-based clustering algorithm more viable. As previously explained in Section 4.4, for a given time step and a given physical domain, the data is first scaled and then the co-kurtosis tensor is computed. The co-kurtosis tensor indicates how much correlation is there between the apparition of outliers in one variable with respect to the rest. The next step in the procedure is to unfold the co-kurtosis tensor into matrix and then perform the singular value decomposition (SVD) operation to obtain the principal vectors and the principal values, which point in the direction of outlier co-occurence. Finally, the last step is computing the feature moment

metrics (FMMs) for all of the features of the dataset. One can interpret the FMMs as the individual contribution of each feature towards the principal vectors.. This indicates that usually, the feature with a dominating presence of outliers is also likely to have a higher FMM value. This may although not be the case. For example, given two distributions of features X and Y, even if X individually does not always exhibit outliers (low kurtosis), it may still have a high FMM value if the outliers of X, when they occur, align with the principal direction of co-occurrence captured by the principal vector.

To better understand the way in which the co-kurtosis tensor and the feature moment metrics are related, one can consider Figure 5.11. Here, only the temperature and the mass fraction of $HO_2$ are taken into consideration. The figure shows the FMMs over the period of a typical flashback event. Firstly, it can be seen that the FMM of $HO_2$ is higher for a greater portion of the time-series. Based on the results shown in the kurtosis analysis, this is expected, as $Y_{HO_2}$ shows more outliers and higher $K$ values. Based on the FMMs presented in this time-series, specific time-steps are investigated as shown in Figure 5.12. Here, the scatter plots of the two variables, as well as the principal vectors coming from the Co-Kurtosis PCA analysis and from a simple PCA analysis are shown. The reason for which only two variables are taken in this initial analysis is that it makes visualizing the scatter plot and the principal vectors possible.

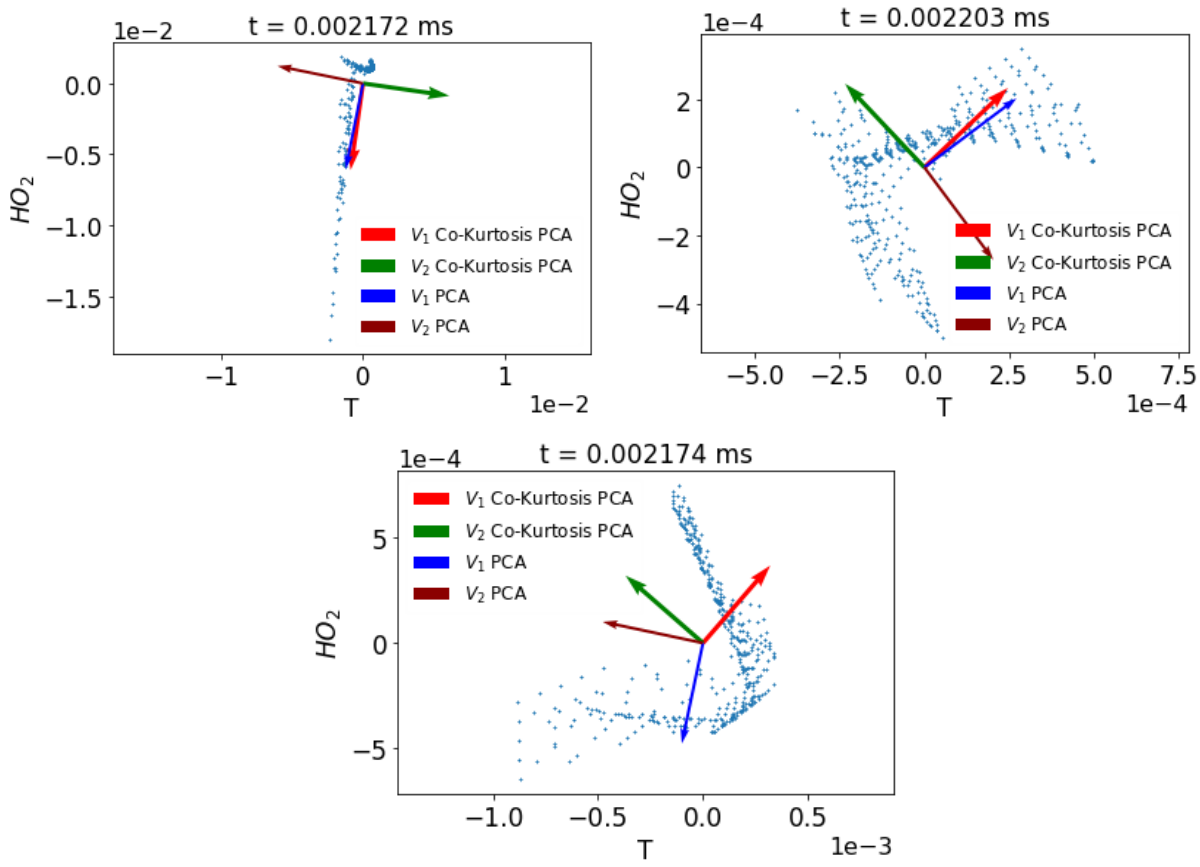


**Figure 5.12:** Scatter plots of $T$ and $HO_2$ showing the PCA and co-kurtosis PCA principal vectors at different time-steps.

The time-steps chosen for this figure correspond to times when the FMM is higher for $Y_{HO_2}$ ($t = 2.172$ ms), the FMM is approximately equal between the two variables ($t = 2.203$ ms)

and to when the FMM is higher for $T$ ($t = 2.174$ ms). As can be seen, the first principal vector resulting from co-kurtosis PCA points towards the direction of the outliers in all of these cases. Furthermore, it can also be seen how the FMMs are able to capture the contribution of the outliers of each individual feature towards the principal vectors, as reflected by their higher values for each particular case. Lastly, it is interesting to note how, for the case at $t = 2.203$ ms, the spread of the outliers makes it such that the principal vector lies in between the two variables. The figure also provides a comparative visualization of PCA and co-kurtosis PCA, with the principal vectors indicating the direction of maximum variance in the multivariate outlier pattern. Here, the vectors from co-kurtosis PCA diverge from standard PCA, emphasizing the importance of outlier values and their co-occurrence, rather than the average spread of data.

Finally, the evolution of the FMMs during the period prior to the flashback event is shown in Figure 5.13. The FMM values are again high for the intermediate species OH, H and O. This is in line with the expectations created by the kurtosis analysis as it was seen that these species have a high level of activity and a tendency to present outliers. Interestingly, $\rho$, $P$ and $V_x$ also present high values for several time-steps. This suggests that when the intermediate species do not present high values, it is the outliers of these features which make the main contribution towards the principal vector, driving the pattern of outlier co-occurrence. Finally, as expected, because the outliers of $HO_2$ and $H_2O_2$ tend to occur at the same time as the ones from the other intermediate species, but have lower $K$ values, these two species present higher FMM values for a smaller amount of time-steps. However, unexpectedly, the FMMs of the reactant $H_2$ and the product $H_2O$ follows the trend of $HO_2$ and $H_2O_2$. This suggests that the distributions of these features is linked to each other.

From a physical perspective, the feature moment metrics confirm the physical intuition given by the observed flashback mechanism. The effect of the pressure waves that converge at the centerline and move upstream is reflected in both the change in the pressure FMM and in the FMM of the streamwise velocity. The early ignition kernels resulting from these pressure waves, that appear in the mixing tube give rise to the change in the intermediate species. The effect of which can also be reflected in the FMMs. In fact, the FMM time series suggests that there is seesaw effect between the two groups. While the FMM of the intermediate species is high, the opposite is true for $P$, $V_x$ and $\rho$. This further highlights the correct interpretation of physical mechanism by the FMMs. There are however two distinct moments where the $H_2O$, $H_2$, $O_2$, $H_2O_2$ and $HO_2$ group also has a significant contribution to the FMM. From a physical perspective, this could be attributed to the different chemical timescales of the reactions and their spread across the sampling region.

With these points in mind, the choice of the features that shall be used in the modularity-based clustering algorithm can be made. As previously mentioned, the way in which the features are chosen is based on whether or not they have high FMM values. This criteria is chosen based on the interpretation that high FMM values suggest an increased level of activity prior to a flashback event and/or a high dependency of other variables on this feature. Firstly, since the OH, H and O group all present an almost identical behavior, their behaviour should be captured by only one of them. For this reason, only OH is taken from this group. Secondly, from the $H_2O$, $H_2$, $O_2$ $H_2O_2$ and $HO_2$ group, the mass fraction of $HO_2$ is taken. This is because, although it does not show the highest peaks, it is more consistent, having higher values for a larger portion of the time-series. Finally, all of the features from the remaining group are taken. This is because, with the exception of $T$, all of them present high FMM values, and, unlike OH, H and O, they are fundamentally

different quantities. As such, it is thought that their different behaviours would benefit the clustering algorithm more than taking H and O for example. The reason for which $T$ is taken is because it is fundamental to the definition of the extreme event in the precursor identification procedure. The final set of features consists of $T$, $\rho$, $P$, $V_x$, $HO_2$ and OH.

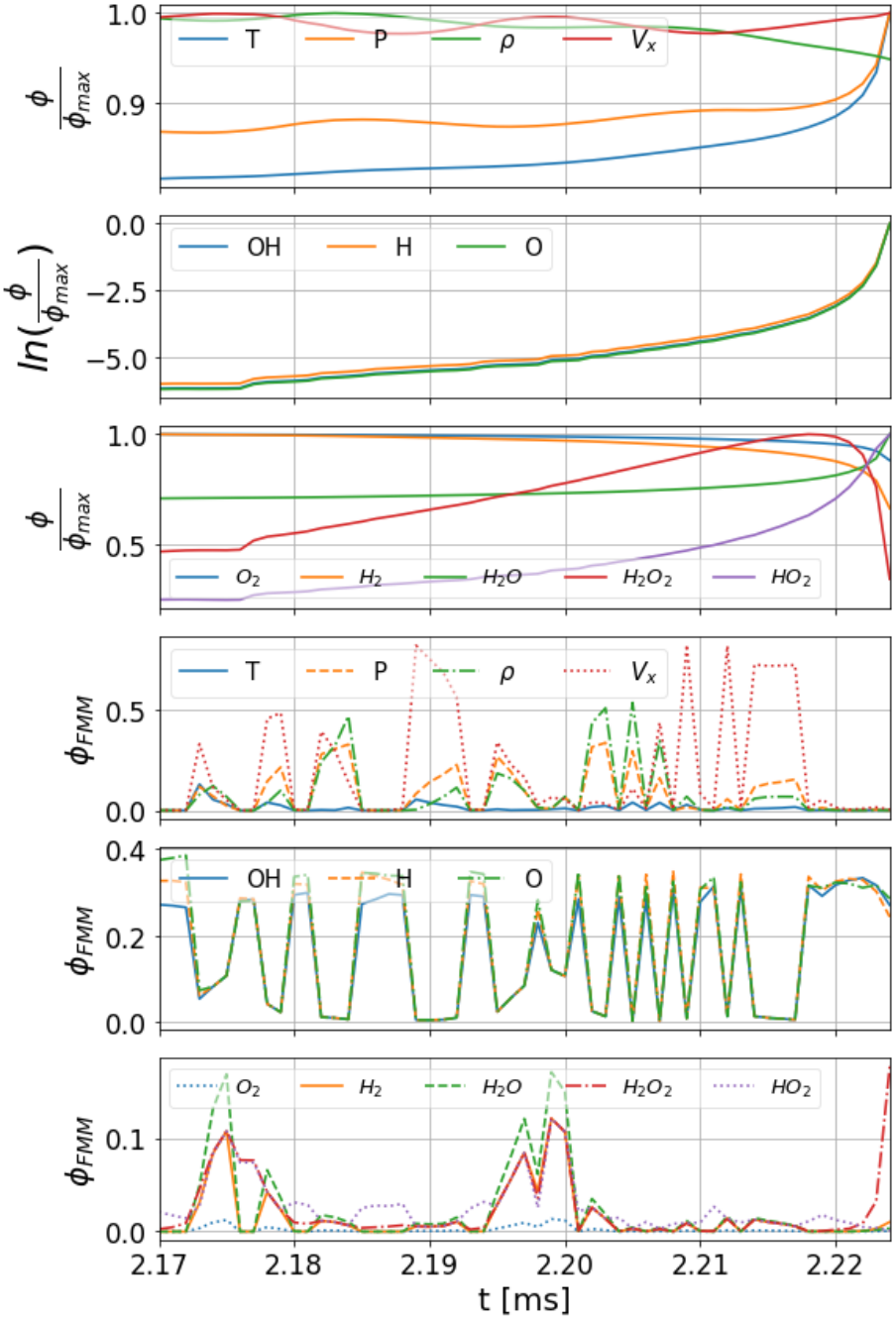


**Figure 5.13:** Evolution of the normalized variables of interest and of their respective FMMs during a typical flashback event.

### 5.2.3. Sensitivity to the sampling time and sampling region

To assess the influence of the sampling region and of the sampling time on the outcome of the co-kurtosis analysis, several tests were conducted. For the influence of the sampling region, the same analysis was done with 2 larger regions. The first one spanned from $x \in [2, 2.8]$

cm and $y \in [-0.4, 0.4]$ cm, resulting in 6400 samples for each time step. The second one stretched from $x \in [1.2, 2.8]$ cm and $y \in [-0.4, 0.4]$ cm, resulting in 13041 samples. It was found that there are not significant differences in the outcome of the analysis with respect to the smaller sized region spanning from $x \in [3, 3.2]$ cm and $y \in [-0.1, 0.1]$ cm. To support this conclusion, one can consider the $K$ values and the FMM values shown in Figure 5.14 for the same period before a flashback event. Here, it can be seen that the kurtosis is similar to before for all of the considered values. The only difference comes in the number of peaks that appear across the time-series.

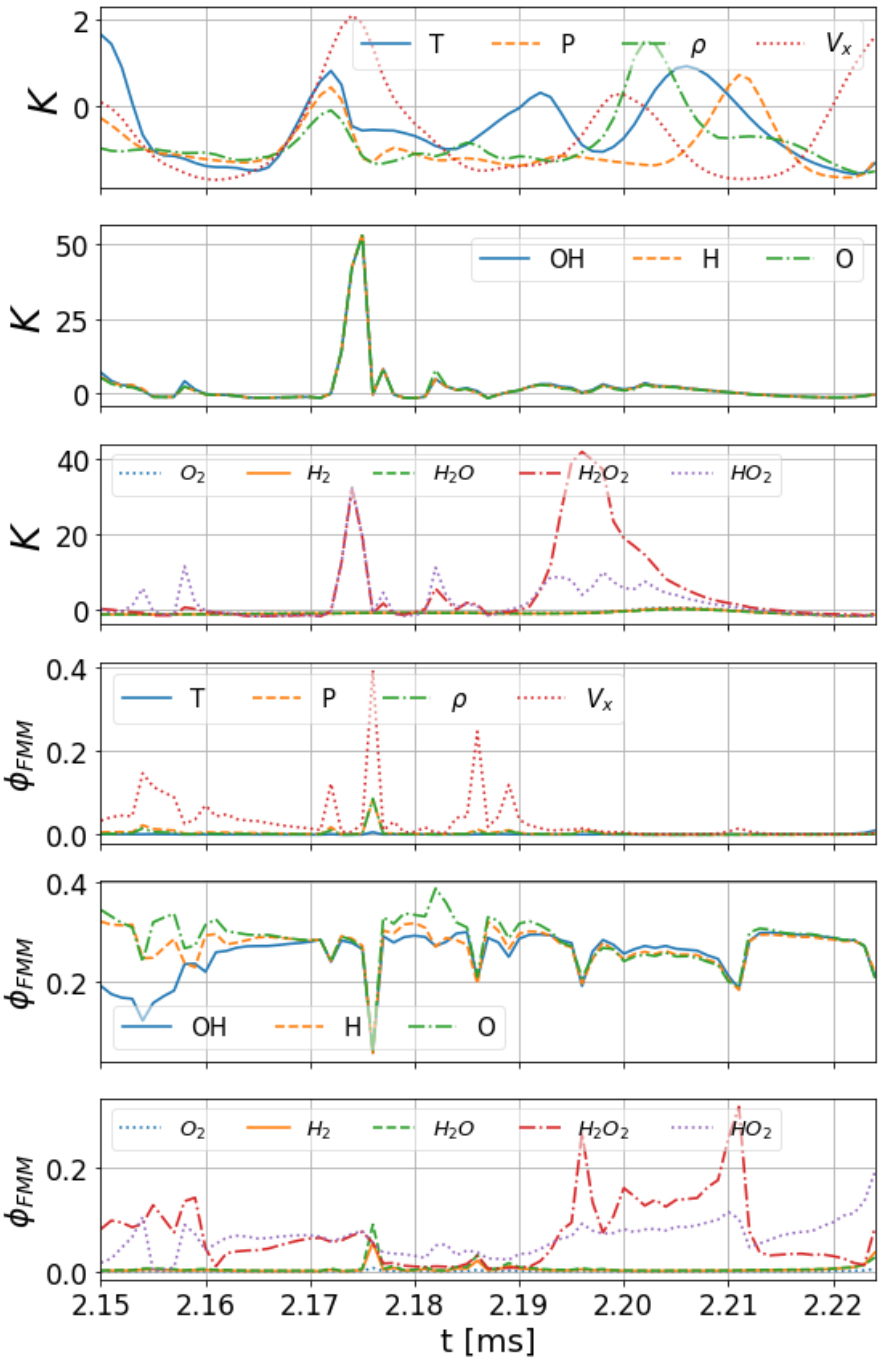


**Figure 5.14:** FMMs and $K$ for the $x \in [1.2, 2.8]$ cm and $y \in [-0.4, 0.4]$ cm region over the period prior to a flashback event.

With regards to the FMMs, the differences in the number of peaks from the kurtosis analysis is reflected in a more constant high FMM value for OH, H and O. Furthermore, $P$, $\rho$ and $H_2O$ show a decreased activity. These changes can all be explained by the increased number of samples of this region. Because it spans a larger area, the distributions of the features have a lot more variation within them. As such, to be able to detect for example the apparition of an ignition kernel, there is not enough uniformity across the sampling region to make the higher $Y_{OH}$ values stand out. In conclusion, even though the features chosen would have not been changed, the smaller region may perhaps be better than these larger regions as it provides more points of reference that indicate an increased amount of activity for the features. Its smaller size allows for more uniformity which allows for a better detection of outliers when they do appear.

Regarding the sampling time, an additional test that was done was using the original sampling region and a $dt = 10^{-7}$ s instead of the original $dt = 10^{-6}$ s. It should be mentioned that another LES simulation was used for this test (hence the different time). The intuition behind this was that the lower time step would perhaps allow for a more accurate detection of the progression of ignition kernels and consequently the outliers. As such, it should be seen if the feature selection is influenced by this. By inspecting Figure 5.15, it can be seen that this is true up to a certain extent. For example, the $K$ values of H, O and OH now have a smoother progression from one time-step to the other, instead of shortly peaking for one time-step and then returning to a small value in the rest of the time. Furthermore, the $K$ values do not exhibit such large values as before, this is likely not a consequence of the smaller sampling time, but rather from the autoignition phenomena itself. The same sort of smoother progression can also be observed for the other set of species.

With regards to the feature moment metric values, $V_x$ seems to be more dominant. This is due to stronger pressure waves before this autoignition event, which in turn induce a stronger variation in $V_x$. In addition, from the features of the last set, consisting of $H_2O$, $H_2$, $O_2$, $H_2O_2$ and $HO_2$, only the last two present high FMM values in this test. Nevertheless, the choice of features again does not change in this scenario. The only feature that could be disregarded is $HO_2$ in favour of $H_2O_2$ as now the latter shows more activity. Even so, due to their similar behaviour, the results is not likely to change significantly. It should although be mentioned that is highly unpractical to use such a small time-step for this analysis as acquiring snapshots for a longer time-series would result in very high memory requirements.

To conclude this section, it was seen that the feature moment metrics can serve to accurately identify features of high activity prior to the flashback event. Furthermore, they are robust to the size of the sampling region and the sampling time. Nevertheless, applying kurtosis and co-kurtosis PCA is highly linked to the phenomena of interest. For this case, where the flame is fluctuating, selecting a region of interest close to the autoignition region is a requirement that should be met. Furthermore, high kurtosis values in intermediate species can not be interpreted only as ignition kernels, as their propagation through the region of interest can also trigger such values. In addition, it was seen that the kurtosis and FMM values can vary in magnitude at different time-steps when the sampling region and the sampling times are changed. Although it was seen that this did not influence the choice of features, as the features which were most active throughout the time-series remained the same, one should be careful about drawing conclusions about certain time-steps based solely on the statistical analysis.

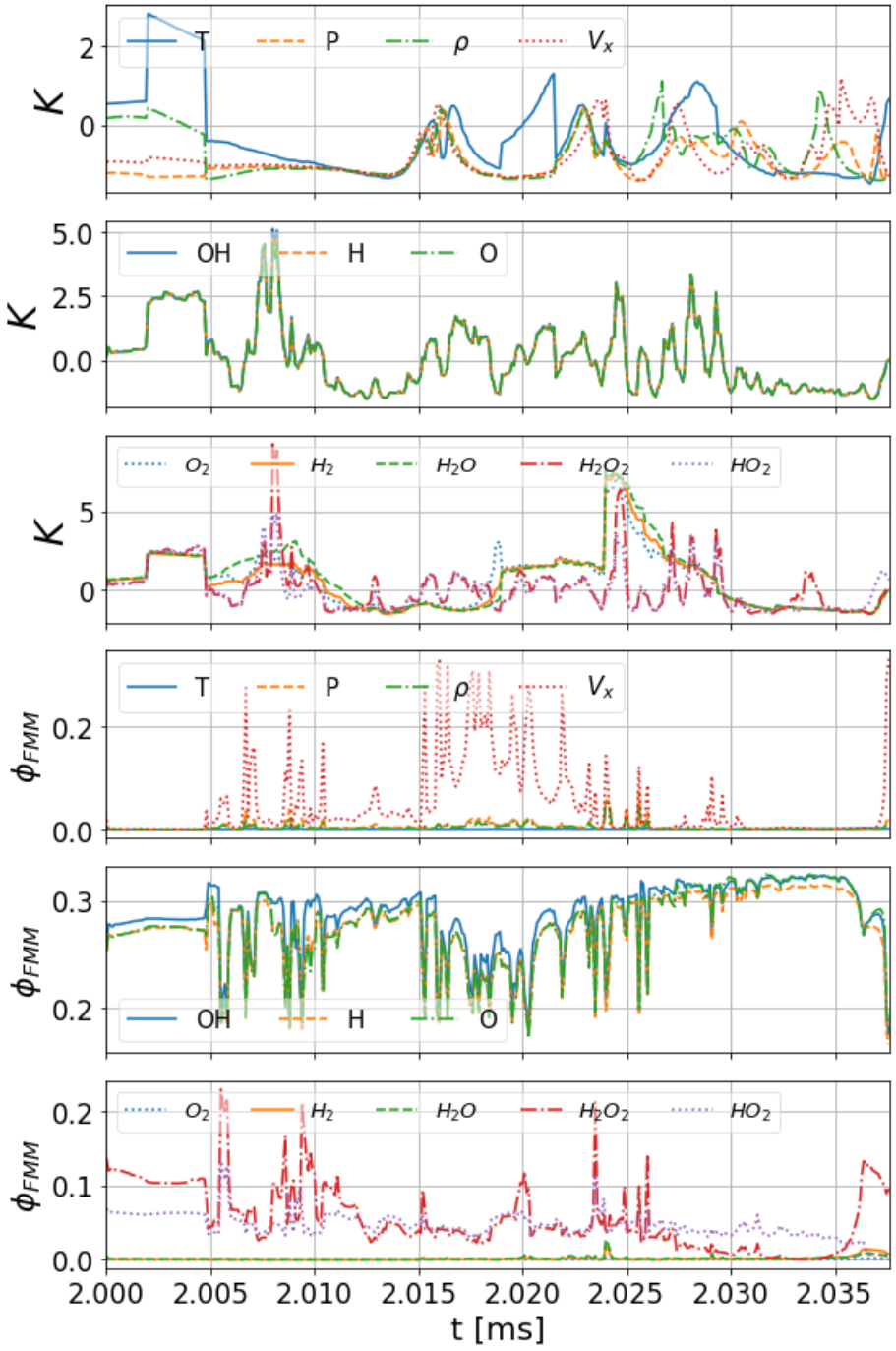


**Figure 5.15:** FMMs and $K$ for a sampling time of $dt = 10^{-7}$ over the period prior to a flashback event.

## 5.3. Precursor identification

In this section, the features retained from the dimensionality reduction analysis, namely $T$, $\rho$, $P$, $V_x$, $HO_2$ and OH, are used in the application of the precursor identification technique. The modularity-based clustering technique, whose methodology is detailed in Section 4.5, describes the multi-dimensional phase space of a system as a weighted and directed graph. This graph is then ultimately clustered with the aim of finding communities which act as a precursor state prior to an extreme event. For the first part of this section, the individual

steps of this algorithm, as applied to the autoignition event in the reheat combustor, are shown. For the next part, the results are discussed in depth and the robustness tests of Section 4.6 are applied to the system.

One of the robustness tests applied to the system consists in varying the number of features used. As such, as it shall be seen shortly, different combinations of the features identified earlier are tested using the clustering algorithm. For the illustration of the following results, the combination of features which yielded the highest prediction time is used. This retains the follows variables: $T$, $V_x$, $P$, $\rho$, OH. Furthermore, in all of these combinations, because the variations of $Y_{\mathrm{OH}}$ and $Y_{\mathrm{HO_2}}$ can be better captured in the tessellation space by using the natural logarithm function, these are transformed to $ln(Y_{\mathrm{OH}})$ and $ln(Y_{\mathrm{HO_2}})$. Proceeding with the results, even though all of the aforementioned features are used, the graphs depicting the different steps in the algorithm contain only two features ($T$ and $P$) for visualization reasons. Lastly, the time-series used has 2500 time-steps, over the course of which, 8 flashback events take place.

To begin, the phase space of this time-series is shown in Figure 5.16. After min-max normalization, this phase space is then tessellated as shown in Figure 5.17. Here, using the definition of a flashback, i.e. $T > 1300$ K, the extreme sections are also saved separately to initialize the clustering algorithm with two different communities, an extreme one and a non-extreme one, as explained in Section 4.5.8. This results in a time-series of the section's indices. The choice of the number of tessellation sections as $M = 20$ is based on a trade-off between computational speed and how accurate the phase space trajectory is represented by the tessellated phase space. Similarly to the analysis done by Golyska [92], it was found that with a low number of tessellation sections, the dynamics of the system are not preserved in enough detail to find any meaningful distinction between the normal clusters and the precursor ones. Conversely, for a large number of sections, the computational cost increases significantly (as the system scales with $M^{N_f}$, where $N_f$ is the number of features). In addition, no improvement was found towards the prediction time.

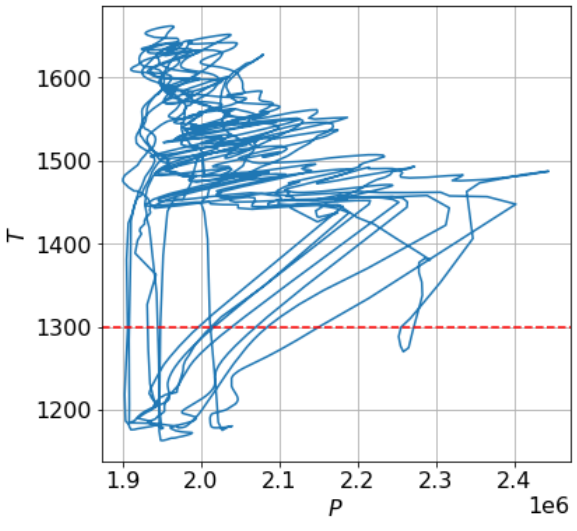


**Figure 5.16:** Projected evolution in the $T$-$P$ phase space of the features sampled at location E0 (right). The red line indicate the definition of a flashback, i.e. $T > 1300$ K.

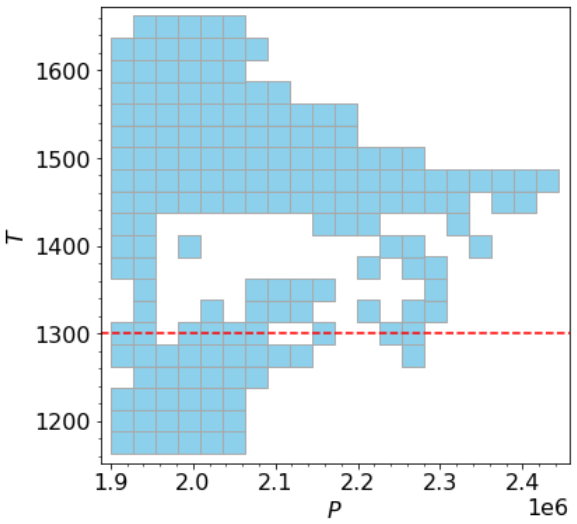


**Figure 5.17:** The tessellated phase space with $M = 20$ tessellation sections in each dimension.

In the next step, the algorithm begins the loop where the system is transformed into a transition probability matrix, followed by a graph, which is then clustered using the modularity-based approach. The reduced graph is then transformed back into a transition probability matrix and the loop continues. At the end of the loop, the transition probability matrix and the reduced graph determine the final state of the system, as shown in Figure 5.18 and Figure 5.19, respectively. The loop continues until either the maximum number of iterations is reached or until the number of clusters falls below a set minimum. The maximum number of iterations was set to 5 as it was observed that the system does not change anymore after this point and the minimum number of clusters was set to 20 to retain an accurate representation of the dynamics of the system.

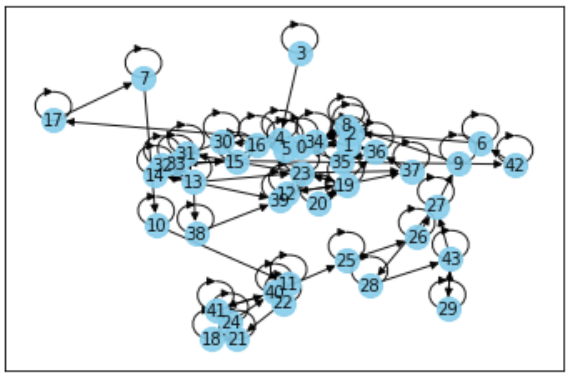

**Figure 5.18:** The weighted and directed graph at the end of the clustering loop.

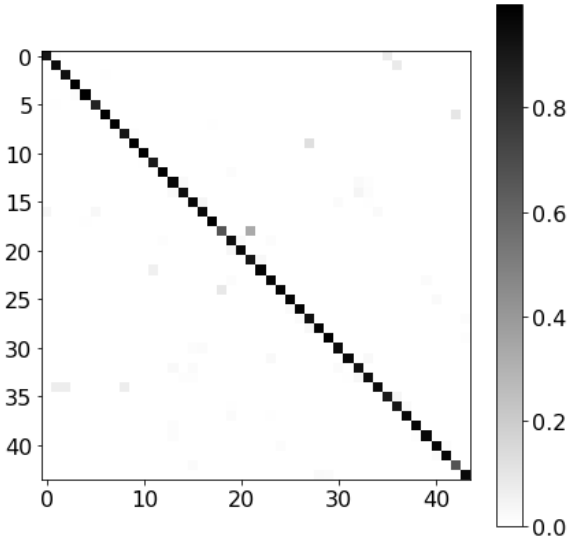


**Figure 5.19:** The transition probability matrix at the end of the clustering loop.

The resulting clusters identified are shown in both the phase space and the tessellated phase space in Figure 5.20. The algorithm finds 43 clusters, out of which 7 are normal clusters, 7 are precursor clusters and the rest are extreme. The precursor clusters identified are 0, 1, 2, 5, 8, 9, 10 and 18. The clustered phase space already gives a good idea of the capabilities of this algorithm. With the naked eye, it would not be possible to tell which are the paths leading to the extreme event.

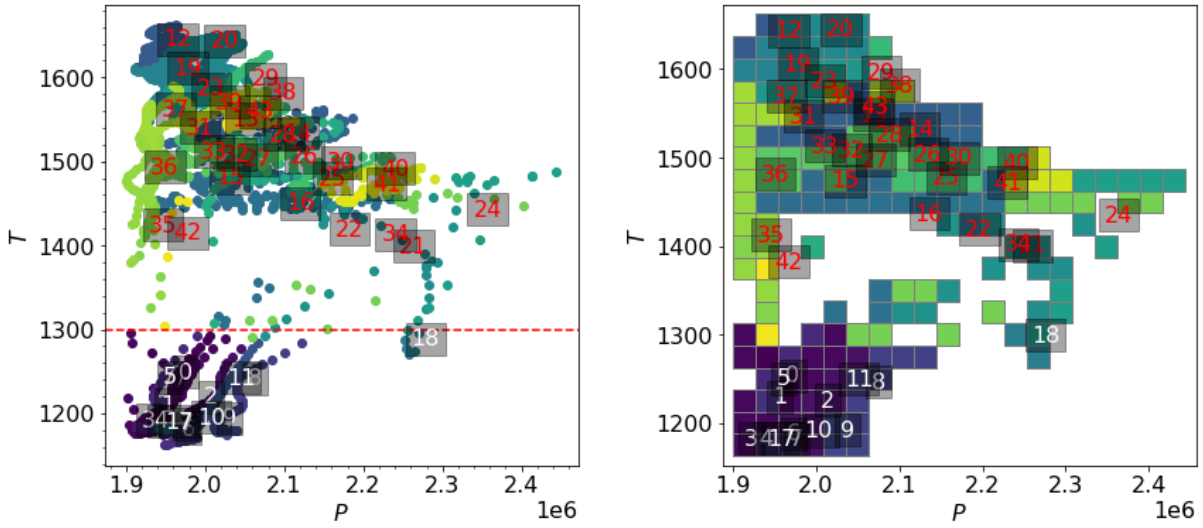


**Figure 5.20:** The trajectory of the system in the $T - P$ space (left) and tessellated $T - P$ space (right) showing the final clusters obtained. The clusters are denoted by their number, placed at the centroid of each cluster. The color of the cluster's index shows its extreme/non-extreme state.

From the transition probability matrix, it is also possible to calculate some statistics regarding the final state of the system. Firstly, for the discussed combination of features, the mean time between the moment the combustor enters the precursor clusters until it reaches the extreme clusters can be calculated as $t_{pred} = 32.13$ $\mu$s. Although this prediction time may seem small, it actually corresponds to a temperature of 1208 K at location E0. This is a very small departure from the inlet temperature of 1180 K. In addition, the flashback phenomena is very fast due to the strongly unstable nature of the combustor. On average the time between two flashbacks, i.e. when the combustor is in a "normal" operating state, is only 60 $\mu$s. This translate to a prediction time equal to over 50 % of the "stable" time. In addition, the components of the confusion matrix (number of false positive, false negatives, correct positives and correct negatives) can also be calculated. Firstly, due to the construction of the precursor clusters, where each one is defined as directly preceding an extreme cluster, the false negative rate is always 0%. Secondly, for this case, the false positive rate is also 0%, meaning that each time the system enters a precursor cluster, it does not turn back to a normal state and an extreme event follows. Lastly, due to the change applied to the clustering algorithm, whereby the extreme clusters can not contain non-extreme states, the true positive rate is 100%. To conclude this part, the temperature evolution sampled at location E0 is also shown in Figure 5.21. Here, the background color indicates the type of cluster in which the combustor is in (blue: normal, orange: precursor and red: extreme). This is where it can be clearly seen that the algorithm identifies a precursor state ahead of the large increase in temperature denoting the flashback event. This shows that it could potentially be used as an early warning system for this type of event. Furthermore, it is clear from this figure that the algorithm clusters the system based on its trajectory rather than the position of the points in the phase space.

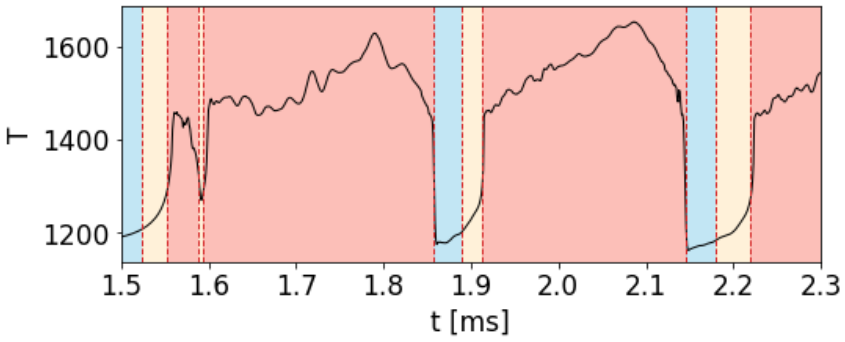


**Figure 5.21:** Temperature evolution during the first 3 flashback events when using [$T$, $V_x$, $P$, $\rho$, $HO_2$] for clustering. Background color indicates the type of cluster the combustor is in (blue: normal; orange: precursor; red: extreme)

### 5.3.1. Robustness analysis

To better understand the overall performance of the modularity-based clustering algorithm„ it has been put through several robustness tests. These tests are detailed in Section 4.6.

**Features availability**

The first test performed consists in limiting the number of features available to the clustering procedure. One particular combinations of features, the one which yielded the best prediction time has already been detailed in the previous section. As such, from the 6 features identified in the dimensionality reduction analysis, namely $T$, $\rho$, $P$, $V_x$, $HO_2$ and OH, combinations of 4, 5 and 6 are taken. The results are reported in Table 5.1. The prediction time ranges from 8.38 $\mu$s to 32.1 $\mu$s, which corresponds to 14% to 53.5% of the 60 $\mu$s "stable" time between two flashbacks. Given the time scale of the flashback event, this results is again promising. Furthermore, it can be seen that when only four features are used, the prediction time seems to generally decrease. This is expected as the clustering algorithm has fewer features available to differentiate between the normal and precursor states. This however is in contrast with the prediction time seen when using five features. Generally, this time is higher than the time found when using all of the six features $t_{pred} = 15.7$ $\mu$s. This could be attributed to the limited amount of data available for the clustering algorithm which only contains 8 flashback events and, due to the nature of the phenomena, less time spent in the normal state with respect to the extreme states. This may lead to a not fully converged probability transition matrix used in the graph representation, due to the smaller amount of points per tessellation hypercube. In turn, this ultimately leads to a decreased performance in the clustering procedure. As such, a balance has to be struck between the number of features and the length of time-series of the available dataset.

**Table 5.1:** Prediction time ($t_{pred}$) and false positives (FP) for different combinations of the important features. Sampling location E0 ($x = 3.1$ and $y = 0.0$ cm in the mid-$z$ plane). FP reported as number of events.

| **Features used** | $t_{pred}$ [$\mu$s] | FP |
|---|---|---|
| $T$, $V_x$, $P$, $\rho$, $HO_2$, OH | 15.7 | 0 |
| $T$, $V_x$, $P$, $\rho$, $HO_2$ | 32.1 | 0 |
| $T$, $V_x$, $P$, $HO_2$, OH | 16.0 | 0 |
| $T$, $V_x$, $P$, $\rho$, OH | 20.9 | 0 |
| $T$, $V_x$, $\rho$, $HO_2$, OH | 17.1 | 0 |
| $T$, $P$, $\rho$, $HO_2$, OH | 14.1 | 1 |
| $T$, $V_x$, $P$, $HO_2$ | 15.8 | 0 |
| $T$, $V_x$, $P$, $\rho$ | 18.1 | 0 |
| $T$, $V_x$, $P$, OH | 24.5 | 0 |
| $T$, $V_x$, $\rho$, $HO_2$ | 12.6 | 0 |
| $T$, $V_x$, HO2, OH | 12.5 | 0 |
| $T$, $V_x$, $\rho$, OH | 15.0 | 0 |
| $T$, $P$, $\rho$, $HO_2$ | 18.6 | 1 |
| $T$, $P$, $HO_2$, OH | 11.1 | 1 |
| $T$, $P$, $\rho$, OH | 13.1 | 1 |
| $T$, $\rho$, $HO_2$, OH | 8.38 | 0 |

Also interesting to note here is that some of the combinations to present 1 false positive (FP) event. For a clustering algorithm, this is expected, as the precursor states and the normal states are usually very close to each other in the phase space, and thus, hard to tell apart. Nevertheless, the resulting false positive rate is relatively small for these cases at only 12.5%. It was observed that these false positives occur at the moment the flame front is flushed back in to the combustion chamber, past the sampling point. This is likely due to similarity of some features at that moment to the moments right before the flashback. As such, one possible improvement would be to use the gradients of some of these problematic features in the clustering process. This would be beneficial as now the algorithm could clearly distinguish between the time when the flame front is flushed out (and most of the variables decrease in magnitude) and when a flashback is about to happen (and the variables increase in magnitude).

**Sampling location**

The next test was to investigate the importance of the sampling location with regards to the prediction time. For this purpose, the time-series were sampled at several different locations, as shown in Figure 4.5. These locations correspond to three points at the same $x$ position as E0, but offset from the centerline (Ei), and a location placed in the mixing tube (CU). Again, the combination of features which previously yielded the best results is taken. It can be seen that, overall, the prediction times are slightly smaller. This is expected as these location are further away from the autoignition zone, and thus the precursor information has a larger lag. This ultimately results in a smaller prediction time. With

regards to the CU location, a larger decrease in the prediction time is observed. Although the same ignition kernels appear around the location, resulting in visible changes in most of the variables, the main ignition kernel which starts the flashback happens further away. This results in larger delay in the propagation of the flame and consequently the increase in temperature.

**Table 5.2:** $t_{pred}$ and FP for the $[T, p, u, \rho, \mathrm{HO}_2]$ case sampled at different locations. FP reported as number of events.

| **Location [cm]** | $t_{pred}$ $[\mu s]$ | FP |
|---|---|---|
| E0: x = 3.1; y = 0.0 | 32.1 | 0 |
| E1: x = 3.1; y = 0.1 | 20.6 | 2 |
| E2: x = 3.1; y = 0.2 | 32.0 | 1 |
| E3: x = 3.1; y = 0.3 | 20.4 | 0 |
| CU: x = 2.0; y = 0.0 | 13.9 | 0 |

**Data availability**

This section is concerned with investigating the robustness of the algorithm with respect to the length of the time-series. As previously explained in Section 4.6, this also consists of a first step in using the algorithm in an online setting. As it is not possible to aggregate information and change the clusters in real time due to the computation time required, this test assess the performance on unseen data, based on clusters computed on previously seen time-series. For this, the new points will be categorized as normal, precursor or extreme based on their distance to the closest cluster from the previously computed group. Then, the prediction time is calculated in the same way as before.

As such, the first 1.1 ms (1100 time-steps) out of the available 2.5 ms (2500 time-steps) are used in the clustering process with the features $T$, $\rho$, $P$, $V_x$ and OH. The clustering in this case still performs relatively well with a prediction time of 14 $\mu$s. The resulting time-series of temperature with the background color indicating the type of cluster is shown in Figure 5.22. It should be noted that the prediction time in this case, and in all of the other cases, is affected by the first flashback event. As previously discussed, this flashback event happens very soon after the autoignition event present in the combustion chamber which locates the flame front at the step location. This happens at approximately 1.6 ms, and, as it can be seen from the figure, the ”stable” time is very short. This also results in a small prediction time which brings the average down. This is especially noticeable in this case since there are only 3 precursor clusters. To be exact, the system is in the first precursor 9 $\mu$s, 6 $\mu$s in the second and 27 $\mu$s in the third.

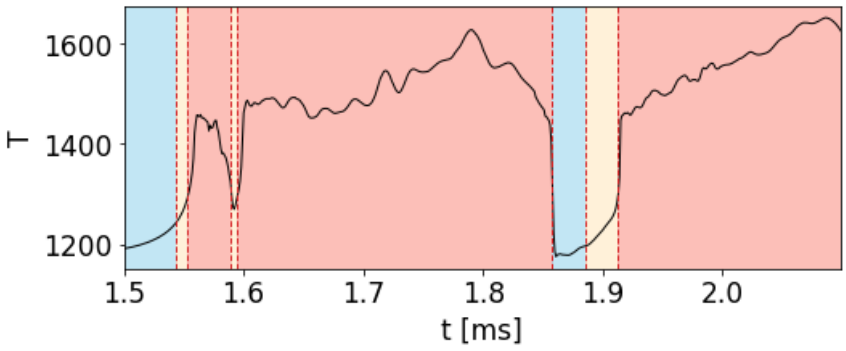


**Figure 5.22:** Time-series of $T$ when the clustering algorithm uses only 1100 time-steps.

Using the centroids of the clusters computed here, the clusters of the remaining time-series containing the unseen flashback events are now determined. The average prediction time in this case is 23.6 $\mu$s, which represents a decrease of 26% with respect to the baseline case. This indicates that the algorithm is still able to identify reliable precursor based on a short time-series and when using previously unseen data. The time-series of $T$ corresponding to this test is shown in Figure 5.23. It should be noted that although each flashback event is different, the algorithm is still able to find a precursor that is general enough to be applied to all of these events.

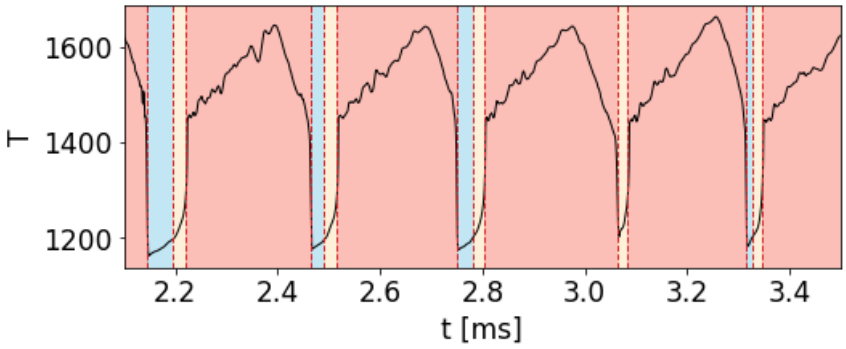


**Figure 5.23:** Time-series of $T$ for the five remaining flashbacks events.

**Precursor based on pressure time series**

Once again, with this approach, the idea is to move closer to the prediction in an online scenario. As such, the performance of the modularity-based clustering algorithm is assessed using measurable quantities. Specifically, the temperature at location E0 (retained for the definition of the extreme event) and five wall pressure measurements in the locations highlighted with yellow in Figure 4.5 are used. The same methodology is applied as before and the average precursor time is now 23.75 $\mu$s. This implies a 25% decrease with respect to the best case in Table 5.1. This reduction in prediction time is expected as now the clustering algorithm has less information available to segregate the clusters. This highlights the importance of the features found in the previous section and through the co-kurtosis PCA analysis in the flashback mechanism observed in this reheat combustor. Furthermore, by inspecting Figure 5.24, it can be seen that the length of the precursor clusters is not as consistent as before. This is likely due to the highly fluctuating nature of the pressure waves. Generally, because of the relaxation phase of the previous flashback (i.e. when

the flame front is being flushed out of the mixing tube), the pressure is decreasing right before a flashback, with the occasional increase due to the heat release of ignition kernels. This introduces a fluctuation which makes it hard for the clustering algorithm to find a reliable precursor. Nevertheless, the order of the prediction time remains similar as in the previous best precursor, indicating that the clustering algorithm is still able to identify specific combinations of pressure signals which indicate an incoming flashback.

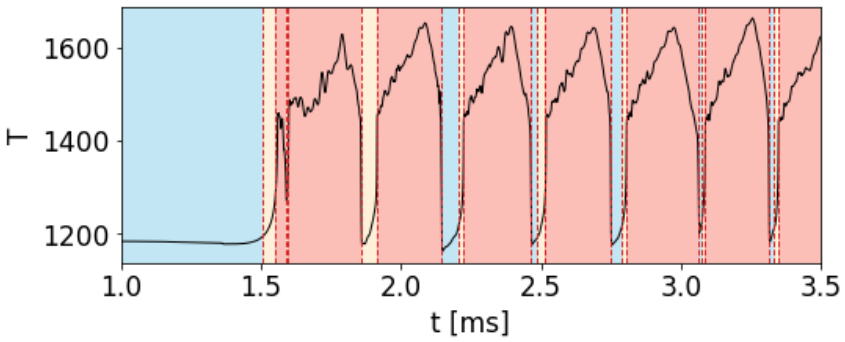


**Figure 5.24:** Time-series of $T$ sampled at location E0 for the clustering based on pressure measurements.

### 5.3.2. Fluctuating conditions

To further assess the capabilities of the modularity-based clustering algorithm the data is now obtained from a new LES simulation. The change made to this simulation are two-fold. Firstly, the digital filter method (see Section 4.1.3) is used to superimpose turbulent fluctuations at the inlet as detailed in Section 4.2.3. Secondly, an inlet velocity profile approximating a fully-developed channel flow is also imposed at the inlet, as detailed in Appendix D. This is a more realistic scenario as compared to the previous simulation, which better represents real-world conditions, thus allowing for a fair assessment of the algorithm. Furthermore, it will be interesting to see whether or not the clustering algorithm performs as well when the state of the system is changing constantly, as a result of the turbulent fluctuations.

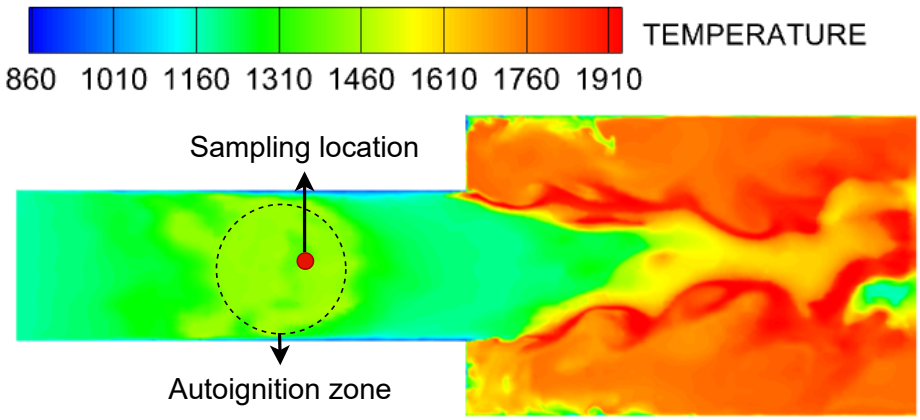


**Figure 5.25:** Contour plot of the temperature showing the upstream location of the autoignition event.

Firstly, it should be mentioned that the autoignition phenomena has a slightly different

behaviour with respect to the previous simulation. Now, the autoignition event which triggers the flashback is located more upstream, as shown in Figure 5.25. This could be attributed to the heat released through turbulent dissipation and the effects of strain on the reaction rates. After this autoignition event, the mixture in the mixing duct is ignited and, eventually, the flame front is flushed out in the combustion chamber and the cycle continues.

In order to capture this more upstream position of the autoignition kernels, the sampling location is moved to $x = 1.86$ and $y = 0$ cm on the mid z-plane. After running the simulation long enough to capture six flashback events, the same procedure as before is applied, where the features taken are again $T$, $V_x$, $P$, $\rho$ and OH. The resulting prediction time is $t_{pred} = 3.417$ $\mu$s and the number of false positives is 0. The temperature time-series with the background color indicating the type of cluster is shown for the first three flashback events in Figure 5.26. As seen, the clustering algorithm also performs well in this scenario.

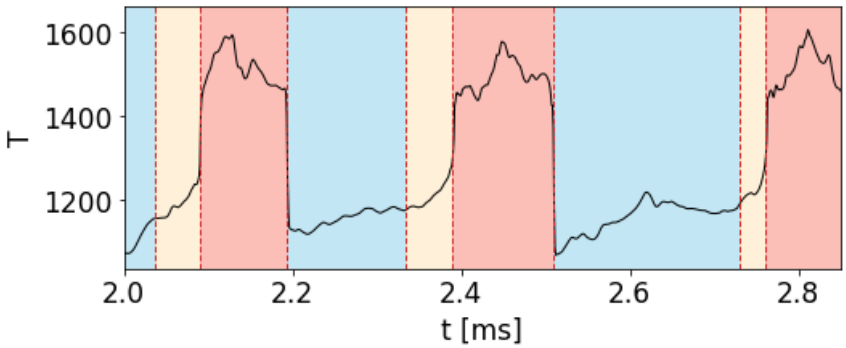


**Figure 5.26:** Time-series of $T$ sampled at $x = 1.86$ and $y = 0$ cm for the clustering based on LES simulation with fluctuating velocity at the inlet.

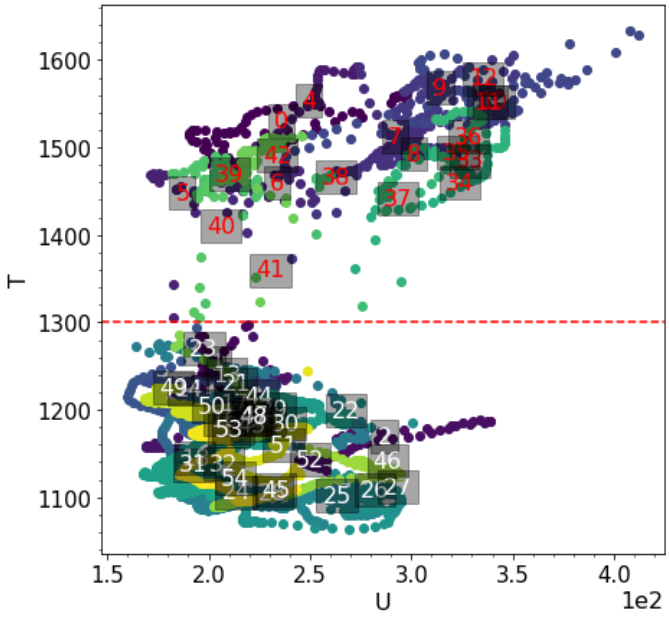


**Figure 5.27:** Trajectory of the system in the $T - V_x$ space showing the final clusters obtained.

Furthermore, it is also interesting to highlight the trajectory of the system in the phase space, as shown through the features $T$ and $V_x$. Here, the precursor clusters are 1, 3, 14 and 44. It can be seen that, although the features present highly fluctuating values, the algorithm is still able to identify a set of clusters that accurately capture the precursor to the flashback event. This simulation also present more data points in the non-extreme category, thus further highlighting the ability of the algorithm at segregating these states.

### 5.3.3. Analysis of the features selected

In this section, the features chosen through the dimensionality reduction procedure are compared to different combinations of the remaining features in their performance in the precursor algorithm. The purpose of this comparison is to assess whether the features selected through co-kurtosis PCA are indeed the best fit for the modularity-based clustering algorithm. As a reminder, the features from the LES considered initially are as follows:

- $T$, $P$, $\rho$ and $V_x$
- Mass fractions of H, O, OH, $O_2$, $H_2$, $H_2O$, $HO_2$ and $H_2O_2$

and the features selected through the dimensionality reduction procedure are: $T$, $V_x$, $P$, $\rho$, OH and $HO_2$.

For this purpose, a set of combinations containing $T$, $V_x$, $P$, $\rho$ and logarithm of one of the mass fractions of the species is tested, as shown in Table 5.3. The first four features, $T$, $V_x$, $P$, $\rho$, are kept in this test as it is assumed that they are essential for the precursor algorithm due to their distinct behaviour in the phase space. Furthermore, by keeping these features, it allows for a fair comparison between all the other species. This makes it possible to assess the whether species chosen through co-kurtosis PCA (OH, $HO_2$) are indeed the best fit. As previously mentioned, these species were chosen based on their activity, as indicated by their changing state and the apparition of outliers. Nevertheless, even though these species show the highest activity, it is interesting to see whether or not the other species are also able to segregate the normal and precursor states in the phase space.

Considering the first three rows of Table 5.3, where the features OH, H and O are tested, it can be seen that they all have similarly high prediction times. This is expected as the co-kurtosis analysis indicates that they all have a similar level of activity. For the next five rows in the table, corresponding to the other set of species, it can be seen that the prediction time is again relatively high. For $HO_2$, $H_2O_2$ and $H_2O$ this is expected all of these species have a high level of activity, but, contrary to expectations, $O_2$ also has a high prediction time despite the low FMM. Interestingly, looking back at Figure 5.13, this is the only species that does not present a high FMM value when the sampling region spans from $x \in [3, 3.2]$ and $y \in [-0.1, 0.1]$ cm. This is indicative of its distinct behaviour with respect to the other species and perhaps the reason why using this mass fraction can also be beneficial at segregating the states in the phase space.

Nevertheless, the test done here to verify the performance of the features chosen with respect to the remaining features is not extensive enough to draw any further conclusions. To achieve this, all of the other combinations would need to be tested, requiring a large amount of time. Nonetheless, the dimensionality reduction technique achieves its purpose successfully, avoiding a large computation time when keeping many features, while still providing the features among which the highest prediction time from all of the combinations tested was found.

**Table 5.3:** Prediction time ($t_{pred}$) and false positives (FP) for combinations containing $T$, $V_x$, $P$, $\rho$ and one species. Sampling location E0 ($x = 3.1$ and $y = 0.0$ cm in the mid-$z$ plane). FP reported as number of events.

| **Features used** | $t_{pred}$ [$\mu$s] | FP |
|---|---|---|
| $T$, $V_x$, $P$, $\rho$, OH | 20.9 | 0 |
| $T$, $V_x$, $P$, $\rho$, H | 22.6 | 0 |
| $T$, $V_x$, $P$, $\rho$, O | 20.4 | 0 |
| $T$, $V_x$, $P$, $\rho$, $O_2$ | 28.4 | 0 |
| $T$, $V_x$, $P$, $\rho$, $H_2$ | 18.4 | 0 |
| $T$, $V_x$, $P$, $\rho$, $H_2O$ | 19.5 | 0 |
| $T$, $V_x$, $P$, $\rho$, $HO_2$ | 32.1 | 0 |
| $T$, $V_x$, $P$, $\rho$, $H_2O_2$ | 22.1 | 0 |

## 5.4. Flashback suppression

In this section, the results of the flashback suppression part of this study are presented and discussed. To reiterate, the goal here is to assess to which extent can a flashback be suppressed by injecting water at the moment the precursor algorithm indicates its approach. For this purpose a new LES simulation was done with the same settings as indicated by Section 4.2, where the use of a fully developed inlet velocity profile and the digital filter method for turbulent fluctuations at the inlet is omitted. In this new simulation, the state was saved prior to the apparition of the flashbacks and subsequent simulations which include the water spray are started from these states. By limiting the time in which the simulation is developing, it is ensured that the prediction time found from the dry simulation (without spray) corresponds to the apparition of the flashback in the wet simulations (with spray).

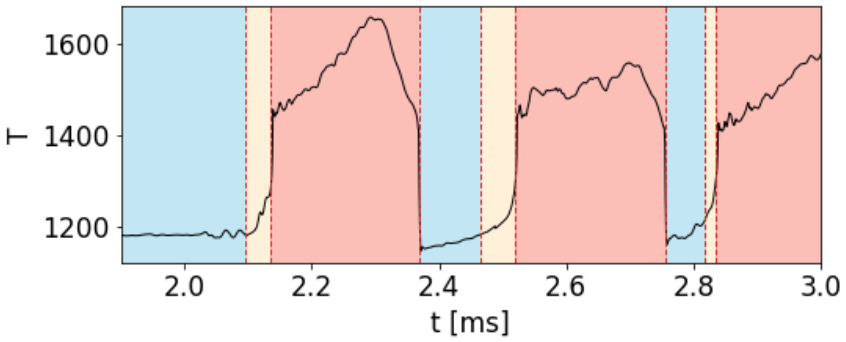


**Figure 5.28:** Time-series of $T$ sampled at $x = 3$ and $y = 0$ cm where the background color indicates the type of cluster (blue: normal, orange: precursor, red: extreme).

This simulation ran long enough to capture five flashback events. Sampled at $x = 3$ and $y = 0$ cm, on the mid z-plane, with a time-step of $dt = 10^{-6}$ s, the data was acquired and the modularity-based clustering algorithm was applied in the same way as before. For the features $T$, $V_x$, $P$, $\rho$, $HO_2$, the average prediction time is 35.2 $\mu s$. The resulting temperature time-series, where the background color indicates the type of cluster the system resides in, is shown in Figure 5.28. As such, using this simulation, the $2^{nd}$ flashback in this time-series

is picked for the water spray simulation. This flashback happens at $t = 2.516$ ms and the prediction time is $t_{pred} = 56$ $\mu$s, resulting in the water injection taking place at $t = 2.46$ ms.

As such, the methodology laid out in Section 4.7 is followed in order to reach a preliminary spray design. As this process is mostly empirical, the most important simulations which led to the preliminary design are showed here chronologically. Furthermore, the design parameters are showed and discussed, along with the theoretical values for the SMD which ensure complete evaporation and the check regarding the atomization regime.

### 5.4.1. Inlet sprays

**Case I**

The first spray design attempts to locate the injector at the inlet, positioned halfway between the walls and the periodic boundaries at $x = 0$, $y = 0$ and $z = 0$ cm. The design procedure starts with calculating the value of the response velocity as explained in Section 4.7. This value is equal to $V_{response} = 653$ m/s, as shown in Table 5.4. Then, the injection velocity is made approximately equal to the response velocity by adjusting the water mass flow and the diameter of the nozzle. The external angle and the thickness angle take usual values, following the results of P. Rouco [19]. In addition, the SMD is set to the value indicated by Equation 4.45. Lastly, the evaporation efficiency is calculated as shown in Equation 5.4 and reported in the table. This efficiency denotes the excess of liquid water that reaches the outlet of the combustor. It should be noted that this efficiency is based on the liquid water mass flow at the outlet shortly after the spray reaches the outlet, at $t = 2.81$ ms. As such, after the initial large heat release coming from the flashback subsides, the evaporation efficiency is likely to decrease until the next flashback appears. This is the same behaviour that occurs in the study of P. Rouco [19]. Nevertheless, in this study, the water spray is not used continuously, as it is activated only at the moment a flashback appears and then deactivated after the flashback has been suppressed. This means that calculating the efficiency as previously described is the best approach because the average efficiency over time is not of interest. This approach is used throughout the following cases. With regards to the actual value of the efficiency, $\eta_e = 99.3\%$, it can be seen that the water almost completely evaporates. This is expected as the SMD value is tuned for this purpose.

$$\eta_e = 1 - \frac{\dot{m}_{\mathrm{H_2O(L),outlet}}}{\dot{m}_{\mathrm{H_2O,injector}}} \tag{5.4}$$

Also reported Table 5.4 are the values of $\mathrm{Re_L}$ and Oh which indicate that the spray does reside in the atomization regime (see Figure 4.17) and the use of the Rosin-Ramler (RR) distribution is indeed justified. As the injection velocity is very large, it is expected that all of the following cases reside in the atomization regime.

Figure 5.29 shows the contour plot of $T$ showcasing the influence of the spray on the flashback. Firstly, it should be noted that, even though the flashback does happen at the expected time, it also appears slightly more upstream. Secondly, it can be seen that the values for the cone angles and the injection velocity are not reflected in the actual behaviour of the spray due to the influence of the surrounding flow. Lastly, it can be seen that the water spray does not manage to stop the flashback, as the flame simply moves around the cooler region. It is expected that the main culprit in the poor spread of the water spray is

the small SMD, as the smaller particles carry less momentum are thus less able to overcome the surrounding flow.

**Table 5.4:** Design parameters for the first iteration of the inlet spray

| Parameter | Value | Units |
|---|---|---|
| $d_0$ | 0.16 | mm |
| $\dot{m}_L$ | 0.013 | $kg/s$ |
| SMD | 4.73e-6 | m |
| $\beta$ | 57 | deg |
| $\tau$ | 17 | deg |
| $V_{response}$ | 653 | $m/s$ |
| $V_{inj}$ | 652 | $m/s$ |

| Parameter | Value | Units |
|---|---|---|
| $Re_L$ | 1.25e5 | - |
| Oh | 7.7e-3 | - |
| SMD [134] | 4.73e-6 | m |
| $\eta_e$ | 99.3% | - |

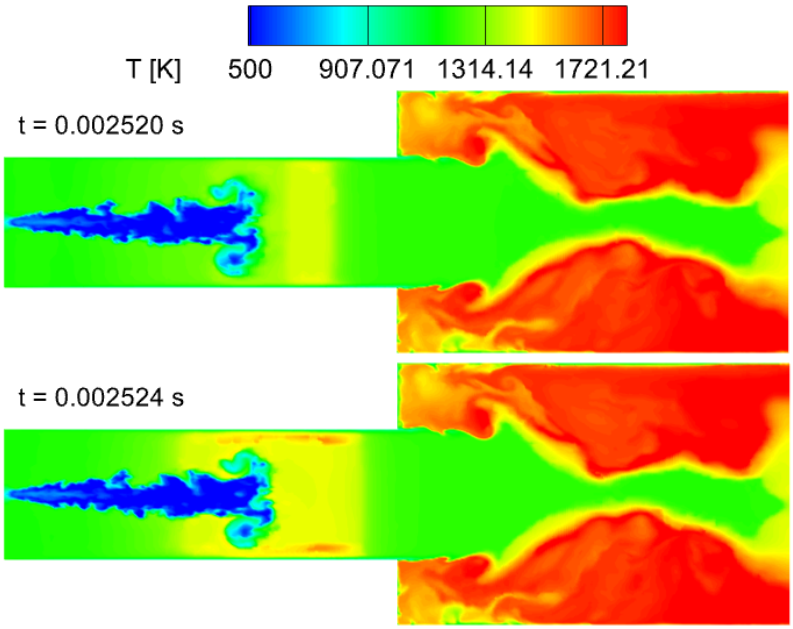


**Figure 5.29:** Contour plots of $T$ showcasing the influence of the spray on the flashback for the first iteration of the inlet spray

**Case II**

The next iteration of the inlet spray design followed based on the observation that the spray did not spread as expected. As such, to counteract this, the SMD is increased, allowing for the water droplets to keep their momentum for longer and reach the walls of the premixing duct. Even though this might decrease the evaporation efficiency, it is deemed reasonable as the focus of this spray is on stopping the flashback. The design parameters are shown in Table 5.5. The only change with respect to the previous case is in the SMD, where the value has now increased to 2e-5 m. The values of $Re_L$ and Oh are the same as before, corresponding to the correct atomization regime. Surprisingly, the evaporation efficiency is slightly higher than before, at 99.4%. This is likely due to the better spread of the droplets, which capture more of the heat coming from the flashback, as shown in Figure 5.30.

**Table 5.5:** Design parameters for the second iteration of the inlet spray

| Parameter | Value | Units |
|---|---|---|
| $d_0$ | 0.16 | mm |
| $\dot{m}_L$ | 0.013 | $kg/s$ |
| SMD | 2e-5 | m |
| $\beta$ | 57 | deg |
| $\tau$ | 17 | deg |
| $V_{response}$ | 653 | $m/s$ |
| $V_{inj}$ | 652 | $m/s$ |

| Parameter | Value | Units |
|---|---|---|
| $Re_L$ | 1.25e5 | - |
| Oh | 7.7e-3 | - |
| SMD[134] | 4.73e-6 | m |
| $\eta_e$ | 99.4% | - |

Once again, as seen in Figure 5.30, the water spray is not able to stop the flashback from propagating in the mixing duct. While the spread is better, with the spray reaching the walls in the mid-z plane, it is not fast enough to cover the whole $yz$ plane. Thus, the flame simply moves past the water spray in the z-axis.

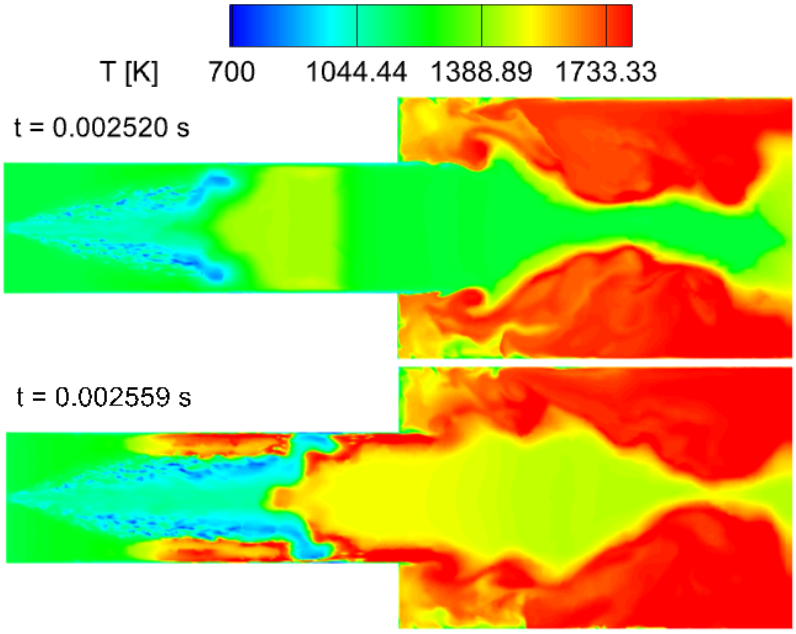


**Figure 5.30:** Contour plots of $T$ showcasing the influence of the spray on the flashback for the second iteration of the inlet spray

### 5.4.2. Wall spray

Based on the poor performance of the inlet spray in covering the mixing duct, the next iteration of the design attempts to place the three sprays at the walls. These are shown in Figure 5.31. Here, the sprays are located at $x = 1.8$ cm and oriented upstream. It should be mentioned that these choice are based on a previous iteration of the wall spray setup, not shown here for brevity. The idea behind this placement is that, given the smaller distance they need to cover, these spray could cover the whole $xy$ plane faster than the inlet spray. Furthermore, they are oriented upstream in order to account for the incoming reactant flow and thus redirect the water to have a somewhat perpendicular path to this flow.

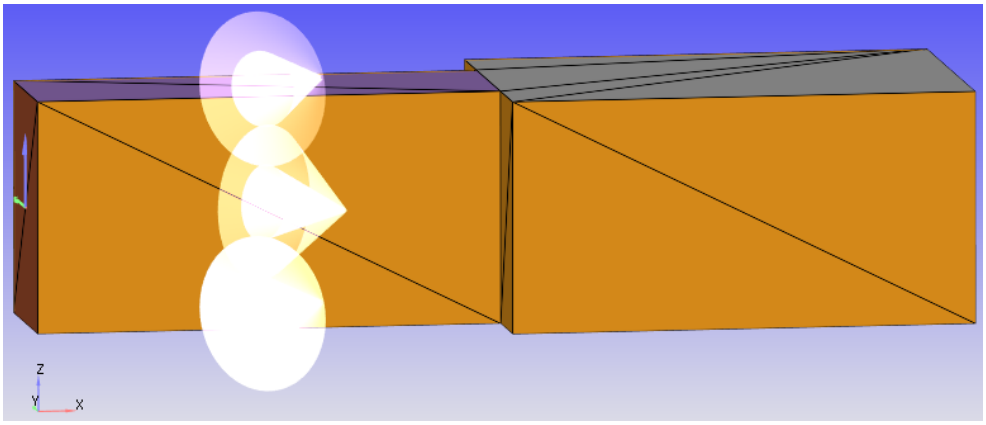

**Figure 5.31:** Configuration of the wall spray setup.

The design parameters for these sprays are shown in Table 5.6. Most of the parameters are the same, with the mass flow of water now split between the three nozzles. With a diameter of $d_0 = 0.18$ mm, this now again results in the injection velocity being approximately equal to the response velocity. The SMD is kept at $2e-5$, such that the particles better retain their momentum.

**Table 5.6:** Design parameters for the wall spray setup

| **Parameter** | **Value** | **Units** |
|---|---|---|
| $d_0$ | 0.16 | mm |
| $\dot{m}_L$ (per nozzle) | 0.0043 | $kg/s$ |
| SMD | 2e-5 | m |
| $\beta$ | 57 | deg |
| $\tau$ | 17 | deg |
| $V_{response}$ | 178 | $m/s$ |
| $V_{inj}$ | 171 | $m/s$ |

| **Parameter** | **Value** | Units |
|---|---|---|
| $Re_L$ | 1.11e5 | - |
| Oh | 7.33e-3 | - |
| | | |
| | | |
| SMD[134] | 5.7e-6 | m |

By inspecting Figure 5.32, it can be seen that a higher injection velocity would have perhaps been useful since the sprays are now in a cross-flow configuration and they do not reach the walls of the mixing duct. But, nevertheless, this is not the main reason for which this configuration does not stop the flashback. As it can be seen, the flashback now appears upstream of the spray. This can be attributed to aerodynamic blockage. In this setup, the incoming reactant flow is blocked by the formation of the spray, forcing it to go around the cone. This results in a longer residence time and a more compressed reactant flow, which, together, ultimately lead to an earlier autoignition of the flow.

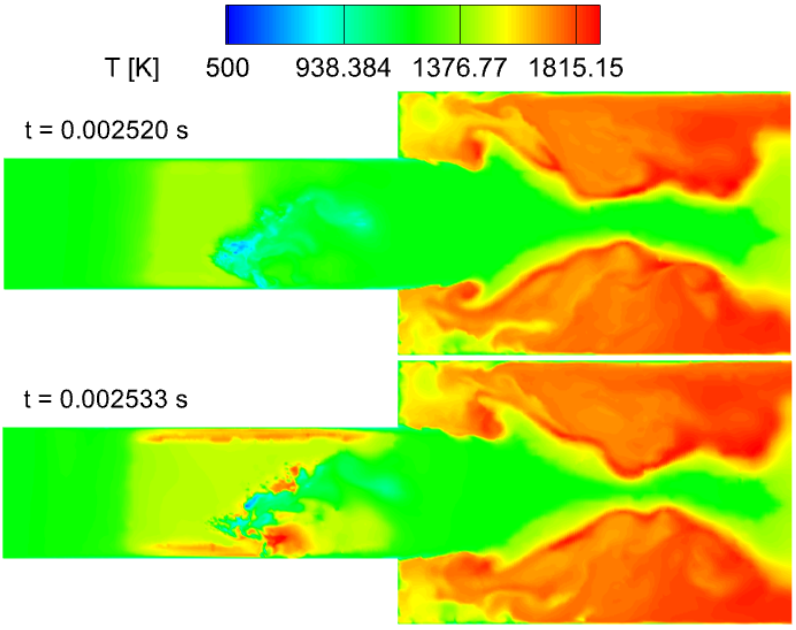


**Figure 5.32:** Contour plots of $T$ showcasing the influence of the spray on the flashback for the wall spray setup

### 5.4.3. Multiple inlet sprays

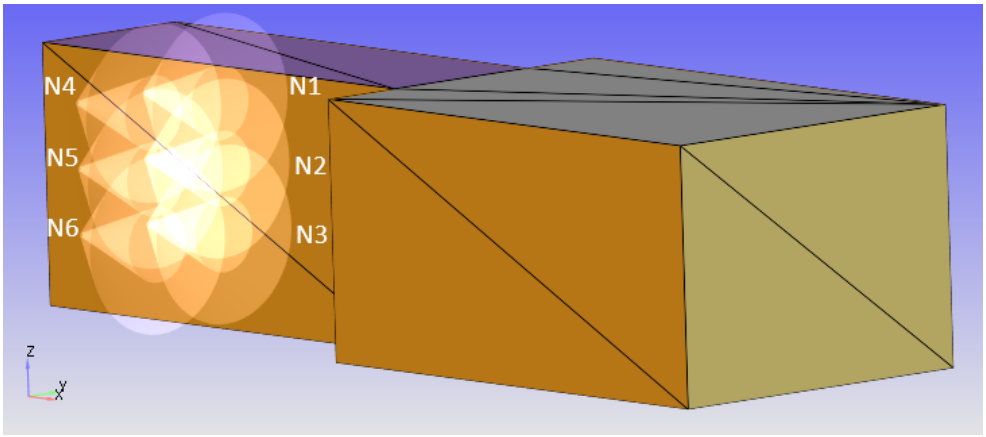


**Figure 5.33:** Configuration with multiple sprays at the inlet

The next iteration in the design builds upon the inlet spray setup by using six sprays instead of one, arranged symmetrically at the inlet as shown in Figure 5.33. The injector coordinates for these six nozzle are shown in Table 5.7. The idea behind this setup is that using multiple sprays allows for a faster coverage of the mixing duct.

**Table 5.7:** Coordinates of the injection locations for the multiple inlet sprays setup

| Nozzle | N1 | N2 | N3 | N4 | N5 | N6 |
|---|---|---|---|---|---|---|
| x [cm] | 0 | 0 | 0 | 0 | 0 | 0 |
| y [cm] | 0.25 | 0.25 | 0.25 | -0.25 | -0.25 | -0.25 |
| z [cm] | 0.375 | 0 | -0.375 | 0.375 | 0 | 0.375 |

**Case I**

**Table 5.8:** Design parameters for the first iteration of the multiple inlet sprays configuration

| Parameter | Value | Units |
|---|---|---|
| $d_0$ | 0.15 | mm |
| $\dot{m}_L$ (per nozzle) | 0.013 | $kg/s$ |
| SMD | 2e-5 | m |
| $\beta$ | 55 | deg |
| $\tau$ | 20 | deg |
| $V_{response}$ | 610 | $m/s$ |
| $V_{inj}$ | 739 | $m/s$ |

| Parameter | Value | Units |
|---|---|---|
| $Re_L$ | 1.33e5 | - |
| Oh | 8.02e-3 | - |
| SMD[134] | 4.25e-6 | m |
| $\eta_e$ | 30.5% | - |

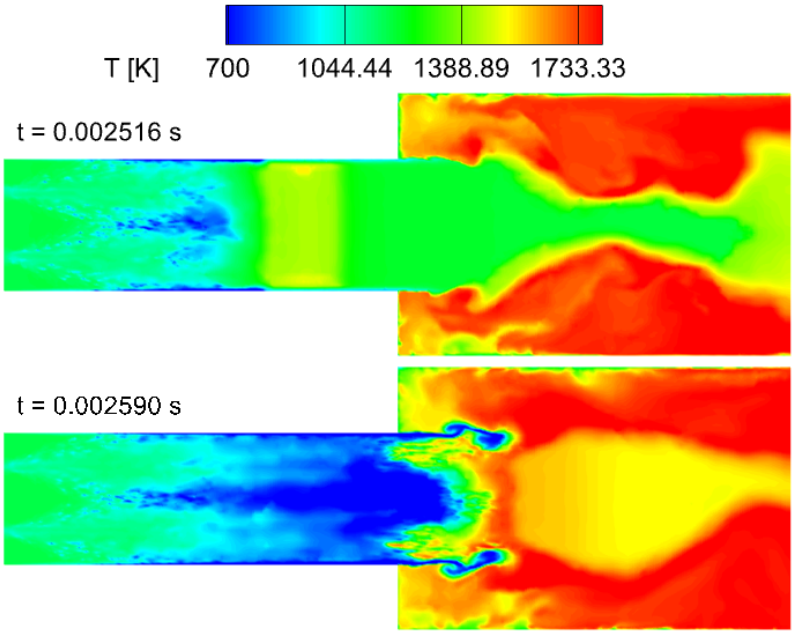


**Figure 5.34:** Contour plots of $T$ showcasing the influence of the spray on the flashback for the multiple inlet spray setup (first iteration).

The design parameters for the first attempt at this configuration are shown in Table 5.8. Here, a notable change is in the injection velocity, which was increased with respect to the response velocity to account for the effect of the surrounding flow. The rest of parameters are similar to the second iteration of the inlet spray cases, where the external angle was slightly decreased and the thickness angle slightly increased due to the closer positioning of the sprays to the walls. Furthermore, the mass flow of water was increased by 6 times, as each nozzle has the same mass flow as in Table 5.5.

As seen in Figure 5.34, the water spray is indeed now able to fully suppress the flashback, managing to completely push the flame out of the mixing duct at $t = 2.59$ ms. This results in only 74 $\mu$s where the flame still resides in the mixing duct. Unfortunately, the spray velocity, which can be approximated at 330 m/s, is still not high enough such that the

water completely covers the full length of the mixing duct before the flashback appears. One weak point of this setup is the poor evaporation efficiency of only 30.5%.

**Case II**

**Table 5.9:** Design parameters for the second iteration of the multiple inlet sprays configuration

| Parameter | Value | Units |
|---|---|---|
| $d_0$ | 0.1 | mm |
| $\dot{m}_L$ (per nozzle) | 0.006 | $kg/s$ |
| SMD | 2e-5 | m |
| $\beta$ | 55 | deg |
| $\tau$ | 20 | deg |
| $V_{response}$ | 610 | $m/s$ |
| $V_{inj}$ | 767 | $m/s$ |

| Parameter | Value | Units |
|---|---|---|
| $\mathrm{Re_L}$ | 0.92e5 | - |
| Oh | 9.8e-3 | - |
| | | |
| | | |
| SMD[134] | 3.26e-6 | m |
| $\eta_e$ | 96.3% | - |

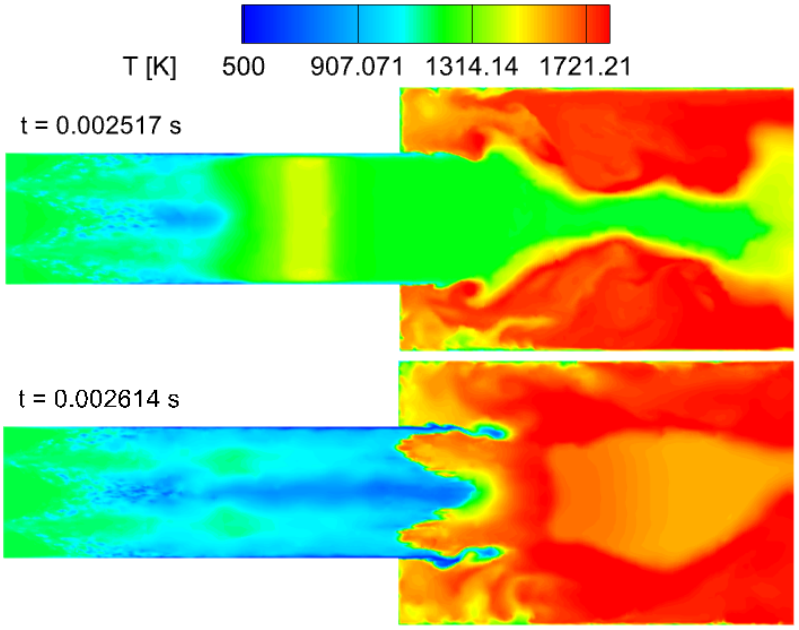


**Figure 5.35:** Contour plots of $T$ showcasing the influence of the spray on the flashback for the multiple inlet spray setup (second iteration).

The final setup tested in this study builds upon the previous case by improving on the poor evaporation efficiency. To achieve this, the mass flow of water is now reduced to $\dot{m}_L = 0.006$ kg/s per nozzle. In addition, to keep the same injection velocity as before, the diameter of the nozzle is decreased to $d_0 = 0.1$ mm. As seen from Figure 5.35, the water sprays are still able to stop the flashback successfully and push the flame out of the mixing duct in a similar time frame as in the previous case, despite the lower mass flow. Although, in this simulation, the evaporation efficiency is now $\eta_e = 96.3\%$, indicating that almost all of the water is evaporated successfully.

In conclusion, by employing this empirical approach, a satisfactory spray design was found which is able to successfully suppress the flashback. This design is although only preliminary and can be improved upon. For example, the injection velocity could be increased further such that the water spray covers a larger area of the mixing duct before the flashback appears. This is although not trivial, as it was seen that increasing the mass flow of water leads to a poor evaporation efficiency. The other option, which is to decrease the nozzle diameter, is also eventually restricted, as a dimension of $d_0 = 0.1$ mm already approaches the limit where the nozzle is likely to be subjected to blockage due to foreign particles [70]. Furthermore, an in-depth optimization of $d_0$, $\dot{m}_L$, SMD, $\beta$, $\tau$ could also be performed given enough computational resources.

# 6

# Conclusion and Recommendations

## 6.1. Conclusion

This study addresses a part of the challenges related to climate change by studying hydrogen combustion. More specifically, the flow inside a simplified version of Ansaldo Energia's GT36 reheat combustor is studied using LES simulation at high pressure (20 bar), where the autoignition flashback observed is of particular interest. The goal of this study is to explore the prediction and suppression of this flashback event. For the first part, the prediction of this flashback event is sought to be achieved using a machine learning method, while for the second part, the flashback suppression, a water spray is introduced in the LES simulations.

In the LES simulation, lean, premixed and high-pressure conditions are used, revealing an unsteady behaviour in the flame dynamics. Pertaining to the models employed, of note are the use of the Thickened Flame Model (TFM), NSCBC boundaries and the SAGE detailed chemistry solver. It was found that the initial autoignition event triggers high amplitude pressure waves, which reflect of the combustor walls and converge at the centerline of the premixing duct. These pressure waves result in heat release due to compressive heating effects, which accelerate the chemical kinetics, triggering an early autoignition event in the premixing duct. After the flame front is flushed back out into the combustor, this phenomena repeats itself. Next, the behaviour of the species prior to the autoignition events are investigated, where the reactions below and above the cross-over temperature are highlighted.

Towards this purpose, several machine learning methods are explored in the literature review and the modularity-based clustering technique first introduced by Schmid et al. [95] and then further developed in this study and by Golyska and Doan [101] is selected due to its demonstrated potential and its insensitivity to the physical phenomena addressed. Before applying the algorithm, the dimensions of the system are reduced using co-kurtosis PCA [88]. This method, by measuring the joint occurrence of outliers in the flow variables, indicates which are the most important variables that introduce a lasting change in the system and are potentially useful in finding a precursor to the flashback event. By applying the method and, at the same time, calculating the kurtosis of each individual feature, it was found the most important features of the flow field are $T$, $\rho$, $P$, $V_x$, $Y_{\mathrm{HO_2}}$ and $Y_{\mathrm{OH}}$. Furthermore, the importance of these features remained the same when the sampling time and the sampling region of the co-kurtosis PCA method were varied.

After performing dimensionality reduction using co-kurtosis PCA, the time-series of the emergent features of the flow field ( $T$, $\rho$, $P$, $V_x$, $Y_{\mathrm{HO_2}}$ and $Y_{\mathrm{OH}}$) are used in the prediction

method. This algorithm tessellates the phase space of the system and then transforms it into a graph, thus retaining the information about the dynamics of the system. Then, it clusters this network using modularity, a metric which indicates how different the connections of particular node are from what is expected in a graph with the same nodes but with randomly distributed edges and weights. This method proves effective in finding precursors to the flashback event, resulting in an average prediction time for the 8 flashback events of $t_{pred} = 32.13$ $\mu$s, which is over 50% of the stable time, or the time in which the combustor is in the normal operating state. Furthermore, the algorithm performs very well in the number of false positives, and, due a change made to the algorithm in this study, the number of true positives is increased to 100%.

The modularity-based clustering algorithm is also put through a robustness analysis involving several tests. Firstly, by testing different combinations of 4, 5 and 6 features, it was found that the algorithm generally performs better when five features are used instead of four. However, when using all of the six features, the prediction time deteriorates. This is attributed to the lack of complete convergence of the eigenvalue problem encountered in the transition probability matrix, which could be solved by using longer time-series. The second robustness test was regarding the sampling location for these time-series. This location was varied, taking data points further away from the autoignition zone, and it was found that the prediction time slightly decreases. This is expected as the information from the features only arrives later at the sampling location. Furthermore, in the third robustness test, the potential of the algorithm in online prediction was explored. Here, the algorithm identified the precursor clusters based on only three flashback events and the remaining data points were classified into either normal, precursor or extreme based on their proximity in the phase space to these clusters. Using this method, the prediction time for the remaining five flashbacks was 23.6 $\mu$s, which represents a decrease of 26% with respect to the baseline case. The fourth test also explored online prediction by using only the temperature time-series and five pressure time-series sampled at the wall of the combustor, to mimic a set of pressure probes. In this case, the prediction time was 23.75 $\mu$s. This decrease was attributed to the lack of information from the other features and the fluctuating nature of the pressure time-series. Finally, the last robustness test employed was the application of the precursor algorithm to a new LES simulation, in which turbulent fluctuations are imposed at the inlet along with a fully-developed channel flow velocity profile. The aim here was to test the algorithm in a more realistic scenario, which better approximates conditions found in a real combustor. The prediction time in this case is was $t_{pred} = 34.2$ $\mu$s, indicating that although the features present highly fluctuating values, the algorithm is still able to accurately identify the precursor to the flashback event.

In the second part of this study, the aim was to find a preliminary spray design which is able to stop the flashback from entering the mixing duct. Here, the water is injected at the moment an incoming flashback is detected by the precursor algorithm. As such, taking one of the flashback events and its afferent prediction time, a mostly empirical design procedure was followed. Here, the injection velocity of the spray (influenced by the diameter of the nozzle and the mass flow) was made approximately equal to the response velocity desired (i.e. the velocity needed for the spray to reach the sampling point in the given prediction time). Furthermore, the Sauter Mean Diameter (SMD) was initially taken as indicated by experimental studies to ensure a complete evaporation of the droplets. In addition, by checking whether or not the spray is in the atomization regime, the assumption that break-up phenomena can be neglected was verified. Lastly, the influence of the angle of the

cone and the thickness angle were explored empirically.

The first attempts for the design of the spray placed it at the inlet of the mixing tube. Here, it was found that using a higher SMD than indicated by experimental studies improves the spread of the spray due to the higher momentum of the particles, which allows them to better retain their trajectory. In addition, the higher SMD actually improves the evaporation efficiency for this particular case. This is because the larger spread also allows for the spray to capture more of the heat resulting from the flashback. Nevertheless, this initial design was not successful in stopping the flashback as the single spray is not able to spread throughout the whole mixing tube, in all three dimensions. In the next attempts, three spray were placed at the walls of the combustion chamber, near the autoignition zone. In this case, it was found that the spray is not able to stop the flashback, as it now appears upstream of the injection location. This was attributed to aerodynamic blockage, where the incoming reactant flow is blocked by the formation of the spray, forcing it to go around the cone. This results in a longer residence time and compression on the reactant flow, leading to an early autoignition event. In the next iterations of the spray, six injectors are placed at the inlet, arranged symmetrically. Here, the external angle was decreased, the thickness angle was increased and the injection velocity was increased based on the observation that the velocity of the spray quickly decreases when encountering the surrounding flow. Using this design, the flashback is successfully suppressed while still achieving an evaporation efficiency of 96.3%.

## 6.2. Recommendations

This study has delved deeper into the problem of predicting and suppressing the appearance of an autoignition flashback event in a reheat combustor. It has looked at the importance of the features both from a physical perspective and through the co-kurtosis PCA dimensionality reduction technique and then used the most important features in the modularity-based clustering algorithm to successfully predict the flashback event. Lastly, a preliminary spray design was found which was able to stop the propagation of the flashback in the mixing duct. Nevertheless, there are several topics which still need to be addressed further. These are discussed in the following recommendations for future work.

To begin, the modularity-based clustering algorithm could benefit from even more tests in the application of predicting autoignition events in reacting flow. Firstly, the performance of the algorithm should be assessed for the flashback that is bound to appear after the previous flashback has been suppressed with water and the spray has been stopped. This should give a better indication of how much does the state inside the combustor change and of how this combined system can be used repeatedly. Secondly, beyond the addition of turbulent fluctuations and a velocity profile, the LES model, and thus the real-life similitude, could be improved by considering an imperfect mixing of the reactants. Here, commonly used mixing methods from gas turbines could be used such as the ones that make use of swirled flows. Beyond testing the precursor algorithm on this setup, the behaviour of the boundary layer flashback would be interesting to analyze, as the reactants should be poorly mixed in that region and thus its effect should be weaker.

Furthermore, it was seen that the conditions for the LES simulation resulted in highly unstable combustion dynamics. It could perhaps be interesting the assess the performance of the precursor algorithm in a case where the combustion is more stable and the flashback happens more rarely. The idea behind this is that in a real gas turbine, the desired operation

would of course not contain these oscillation and perhaps this kind of a system would be used as a fail-safe. Thus, the aforementioned conditions would better approximate this kind of behaviour. Lastly, the use of this algorithm in an online setting should be further explored. Here, sensors that can measure the activity inside a combustor should be explored in order to determine what other features might be measurable at a high sampling rate. Particularly, sensors that detect heat release, pressure fluctuations, luminescence, and the presence of ions and electrons may offer valuable data for this purpose.

For the second part of this study, the first recommendation that could be made is to perform an optimization for the spray design in which the evaporation efficiency, the thermal efficiency and other performance metrics are taken into account, as well as how fast flashback is suppressed. Secondly, increasing the injection velocity to minimize the response time should also be further assessed. Here, it is important to strike a balance between the diameter of the nozzle and the mass flow of water, as the first can not be decreased indefinitely, while increasing the second reduces the evaporation efficiency.

Lastly, the response time of such an online system should be investigated. This system includes a chain of several electronic components and most importantly, a mechanical one, in the form of the valve used for the water spray. Given the small time scale of the flashback phenomena, it is important to assess how fast all of the involved components can communicate with each other to activate the water spray.

# References


[1] Kashif Abbass et al. "A review of the global climate change impacts, adaptation, and sustainable mitigation measures". In: *Environmental Science and Pollution Research* 29.28 (June 2022), pp. 42539–42559. ISSN: 0944-1344, 1614-7499. DOI: 10.1007/s11356-022-19718-6.

[2] USGCRP. *Climate Science Special Report*. U.S. Global Change Research Program, Washington, DC, pp. 1–470.

[3] *The Paris Agreement | UNFCCC*. URL: https://unfccc.int/process-and-meetings/the-paris-agreement (visited on 10/04/2023).

[4] William F. Lamb et al. "A review of trends and drivers of greenhouse gas emissions by sector from 1990 to 2018". In: *Environmental Research Letters* 16.7 (June 2021). Publisher: IOP Publishing, p. 073005. ISSN: 1748-9326. DOI: 10.1088/1748-9326/abee4e.

[5] Peter Therkelsen et al. "[3] Evaluation of a Low Emission Gas Turbine Operated on Hydrogen". In: *Volume 1: Combustion and Fuels, Education*. ASME Turbo Expo 2006: Power for Land, Sea, and Air. Barcelona, Spain: ASMEDC, Jan. 1, 2006, pp. 557–564. ISBN: 978-0-7918-4236-2. DOI: 10.1115/GT2006-90725.

[6] D.J. Wuebbles et al. *Executive summary. Climate Science Special Report: Fourth National Climate Assessment, Volume I*. U.S. Global Change Research Program, 2017. DOI: 10.7930/J0DJ5CTG.

[7] *Outlook for electricity – World Energy Outlook 2022 – Analysis*. IEA. URL: https://www.iea.org/reports/world-energy-outlook-2022/outlook-for-electricity (visited on 10/08/2023).

[8] Simon Öberg et al. "Exploring the competitiveness of hydrogen-fueled gas turbines in future energy systems". In: *International Journal of Hydrogen Energy* 47.1 (Jan. 1, 2022), pp. 624–644. ISSN: 0360-3199. DOI: 10.1016/j.ijhydene.2021.10.035.

[9] Simon Öberg et al. "The value of flexible fuel mixing in hydrogen-fueled gas turbines – A techno-economic study". In: *International Journal of Hydrogen Energy*. GCGW-21 - Global Warming Reduction by Hydrogen 47.74 (Aug. 29, 2022), pp. 31684–31702. ISSN: 0360-3199. DOI: 10.1016/j.ijhydene.2022.07.075.

[10] Dr Jeffrey Goldmeer. "Fuel Flexible Gas Turbines as Enablers for a Low or Reduced Carbon Energy Ecosystem". In: ().

[11] M. R Louthan et al. "Hydrogen embrittlement of metals". In: *Materials Science and Engineering* 10 (Jan. 1, 1972), pp. 357–368. ISSN: 0025-5416. DOI: 10.1016/0025-5416(72)90109-7.

[12] David Noble et al. "Assessment of Current Capabilities and Near-Term Availability of Hydrogen-Fired Gas Turbines Considering a Low-Carbon Future". In: *Journal*

*of Engineering for Gas Turbines and Power* 143.4 (Apr. 1, 2021), p. 041002. ISSN: 0742-4795, 1528-8919. DOI: 10.1115/1.4049346.

[13] L.Y.M. Gicquel et al. "[4] Large Eddy Simulations of gaseous flames in gas turbine combustion chambers". In: *Progress in Energy and Combustion Science* 38.6 (Dec. 2012), pp. 782–817. ISSN: 03601285. DOI: 10.1016/j.pecs.2012.04.004.

[14] *Commission Implementing Decision (EU) 2021/2326 of 30 November 2021 establishing best available techniques (BAT) conclusions, under Directive 2010/75/EU of the European Parliament and of the Council, for large combustion plants (notified under document C (2021) 8580) (Text with EEA relevance)*. Legislative Body: ENV, COM. Nov. 30, 2021.

[15] *Photo gallery*. URL: https://www.ansaldoenergia.com/about-us/media-center/photo-gallery (visited on 11/14/2023).

[16] Jinfei Wang et al. "Numerical investigation of water injection quantity and water injection timing on the thermodynamics, combustion and emissions in a hydrogen enriched lean-burn natural gas SI engine". In: *International Journal of Hydrogen Energy* 45 (May 1, 2020). DOI: 10.1016/j.ijhydene.2020.04.146.

[17] Mirko R. Bothien et al. "Toward Decarbonized Power Generation With Gas Turbines by Using Sequential Combustion for Burning Hydrogen". In: *Journal of Engineering for Gas Turbines and Power* 141.12 (Dec. 1, 2019), p. 121013. ISSN: 0742-4795, 1528-8919. DOI: 10.1115/1.4045256.

[18] K. Michael Düsing et al. "Development of GT24 and GT26 (Upgrades 2011) Reheat Combustors, Achieving Reduced Emissions and Increased Fuel Flexibility". In: *Volume 1B: Combustion, Fuels and Emissions*. ASME Turbo Expo 2013: Turbine Technical Conference and Exposition. San Antonio, Texas, USA: American Society of Mechanical Engineers, June 3, 2013, V01BT04A034. ISBN: 978-0-7918-5511-9. DOI: 10.1115/GT2013-95437.

[19] P. Rouco et al. "FLASHBACK PREVENTION IN A HYDROGEN-FUELED REHEAT COMBUSTOR BY WATER INJECTION OPTIMIZED WITH GLOBAL SENSITIVITY ANALYSIS". In: *Proceedings of ASME Turbo Expo 2024*. GT2024-127332 (June 2024).

[20] Alireza Kalantari et al. "Boundary layer flashback of non-swirling premixed flames: Mechanisms, fundamental research, and recent advances". In: *Progress in Energy and Combustion Science* 61 (July 2017), pp. 249–292. ISSN: 03601285. DOI: 10.1016/j.pecs.2017.03.001.

[21] Ali Cemal Benim et al. *Flashback Mechanisms in Lean Premixed Gas Turbine Combustion*. Boston: Academic Press, 2015. ISBN: 978-0-12-800755-6.

[22] S.L. Plee et al. "Review of flashback reported in prevaporizing/premixing combustors". In: *Combustion and Flame* 32 (1978), pp. 193–203. ISSN: 00102180. DOI: 10.1016/0010-2180(78)90093-7.

[23] Hiroyuki Kido et al. "Influence of local flame displacement velocity on turbulent burning velocity". In: *Proceedings of the Combustion Institute* 29.2 (Jan. 2002), pp. 1855–1861. ISSN: 15407489. DOI: 10.1016/S1540-7489(02)80225-5.

[24] A.N. Lipatnikov et al. “Molecular transport effects on turbulent flame propagation and structure”. In: *Progress in Energy and Combustion Science* 31.1 (Jan. 2005), pp. 1–73. ISSN: 03601285. DOI: 10.1016/j.pecs.2004.07.001.

[25] James F. Driscoll. “Turbulent premixed combustion: Flamelet structure and its effect on turbulent burning velocities”. In: *Progress in Energy and Combustion Science* 34.1 (Feb. 1, 2008), pp. 91–134. ISSN: 0360-1285. DOI: 10.1016/j.pecs.2007.04.002.

[26] J. O. Keller et al. “Mechanism of Instabilities in Turbulent Combustion Leading to Flashback”. In: *AIAA Journal* 20.2 (Feb. 1982), pp. 254–262. ISSN: 0001-1452, 1533-385X. DOI: 10.2514/3.51073.

[27] Paul Billant et al. “Experimental study of vortex breakdown in swirling jets”. In: *Journal of Fluid Mechanics* 376 (Dec. 10, 1998), pp. 183–219. ISSN: 0022-1120, 1469-7645. DOI: 10.1017/S0022112098002870.

[28] Marco Konle et al. “Simultaneous high repetition rate PIV–LIF-measurements of CIVB driven flashback”. In: *Experiments in Fluids* 44.4 (Apr. 2008), pp. 529–538. ISSN: 0723-4864, 1432-1114. DOI: 10.1007/s00348-007-0411-2.

[29] Bernard Lewis et al. “Stability and Structure of Burner Flames”. In: *The Journal of Chemical Physics* 11.2 (Feb. 1, 1943), pp. 75–97. ISSN: 0021-9606, 1089-7690. DOI: 10.1063/1.1723808.

[30] Vera Hoferichter. “Boundary Layer Flashback in Premixed Combustion Systems”. In: ().

[31] Marco Konle et al. “Interaction of heat release and vortex breakdown during flame flashback driven by combustion induced vortex breakdown”. In: *Experiments in Fluids* 47 (Oct. 1, 2009), pp. 627–635. DOI: 10.1007/s00348-009-0679-5.

[32] F. A. Hatem et al. “Enhancing flame flashback resistance against Combustion Induced Vortex Breakdown and Boundary Layer Flashback in swirl burners”. In: *Applied Energy* 230 (Nov. 15, 2018), pp. 946–959. ISSN: 0306-2619. DOI: 10.1016/j.apenergy.2018.09.055.

[33] Tim Lieuwen et al. “Burner Development and Operability Issues Associated with Steady Flowing Syngas Fired Combustors”. In: *Combustion Science and Technology - COMBUST SCI TECHNOL* 180 (May 15, 2008), pp. 1169–1192. DOI: 10.1080/00102200801963375.

[34] Samuel Martin et al. “Modeling and optimization of shark-inspired riblet geometries for low drag applications”. In: *Journal of Colloid and Interface Science* 474 (July 15, 2016), pp. 206–215. ISSN: 0021-9797. DOI: 10.1016/j.jcis.2016.04.019.

[35] Yu-Chun Lin et al. “Turbulent Flame Speed as an Indicator for Flashback Propensity of Hydrogen-Rich Fuel Gases”. In: *Journal of Engineering for Gas Turbines and Power* 135.111503 (Sept. 17, 2013). ISSN: 0742-4795. DOI: 10.1115/1.4025068.

[36] Georg Baumgartner et al. “Experimental Investigation on the Effect of Boundary Layer Fluid Injection on the Flashback Propensity of Premixed Hydrogen-Air Flames”. In: ASME Turbo Expo 2013: Turbine Technical Conference and Exposition. American Society of Mechanical Engineers Digital Collection, Nov. 14, 2013. DOI: 10.1115/GT2013-94266.

[37] Alessio Pappa et al. “Can Water Dilution Avoid Flashback on a Hydrogen-Enriched Micro-Gas Turbine Combustion?—A Large Eddy Simulations Study”. In: *Journal of Engineering for Gas Turbines and Power* 143.4 (Apr. 1, 2021), p. 041008. ISSN: 0742-4795, 1528-8919. DOI: 10.1115/1.4049798.

[38] Charles Lhuillier et al. “Hydrogen-Enriched Methane Combustion Diluted With Exhaust Gas and Steam: Fundamental Investigation on Laminar Flames and NOx Emissions”. In: ASME Turbo Expo 2017: Turbomachinery Technical Conference and Exposition. American Society of Mechanical Engineers Digital Collection, Aug. 17, 2017. DOI: 10.1115/GT2017-64885.

[39] William D. York et al. “Development and Testing of a Low NOx Hydrogen Combustion System for Heavy-Duty Gas Turbines”. In: *Journal of Engineering for Gas Turbines and Power* 135.22001 (Jan. 8, 2013). ISSN: 0742-4795. DOI: 10.1115/1.4007733.

[40] Thoralf G. Reichel et al. “Interaction mechanisms of fuel momentum with flashback limits in lean-premixed combustion of hydrogen”. In: *International Journal of Hydrogen Energy* 42.7 (Feb. 16, 2017), pp. 4518–4529. ISSN: 0360-3199. DOI: 10.1016/j.ijhydene.2016.11.018.

[41] J. Sangl et al. “Dynamic Adaptation of Aerodynamic Flame Stabilization of a Premix Swirl Burner to Fuel Reactivity Using Fuel Momentum”. In: *Journal of Engineering for Gas Turbines and Power* 133.71501 (Mar. 16, 2011). ISSN: 0742-4795. DOI: 10.1115/1.4002659.

[42] Hideaki Kobayashi et al. “Science and technology of ammonia combustion”. In: *Proceedings of the Combustion Institute* 37.1 (Jan. 1, 2019), pp. 109–133. ISSN: 1540-7489. DOI: 10.1016/j.proci.2018.09.029.

[43] Mengdi Ji et al. “Review and comparison of various hydrogen production methods based on costs and life cycle impact assessment indicators”. In: *International Journal of Hydrogen Energy* 46.78 (Nov. 2021), pp. 38612–38635. ISSN: 03603199. DOI: 10.1016/j.ijhydene.2021.09.142.

[44] Fritz Ullmann. *Ullmann’s encyclopedia of industrial chemistry*. 6th ed. ; Release 2000-. OCLC: 46878292. New York: Wiley, 2000. ISBN: 978-3-527-30673-2.

[45] D. J. Beerer et al. “Autoignition of Hydrogen and Air Inside a Continuous Flow Reactor With Application to Lean Premixed Combustion”. In: *Journal of Engineering for Gas Turbines and Power* 130.5 (Sept. 1, 2008), p. 051507. ISSN: 0742-4795, 1528-8919. DOI: 10.1115/1.2939007.

[46] Carsten Olm et al. “Comparison of the performance of several recent hydrogen combustion mechanisms”. In: *Combustion and Flame* 161.9 (Sept. 2014), pp. 2219–2234. ISSN: 00102180. DOI: 10.1016/j.combustflame.2014.03.006.

[47] Juan Li et al. “An updated comprehensive kinetic model of hydrogen combustion”. In: *International Journal of Chemical Kinetics* 36.10 (Oct. 2004), pp. 566–575. ISSN: 0538-8066, 1097-4601. DOI: 10.1002/kin.20026.

[48] Michael P. Burke et al. “Comprehensive H2/O2 kinetic model for high-pressure combustion - Burke - 2012 - International Journal of Chemical Kinetics - Wiley

Online Library". In: *International Journal of Chemical Kinetics* 44.7 (2011), pp. 444–474. DOI: https://doi.org/10.1002/kin.20603.

[49] Boris Kruljevic et al. "LES OF REHEAT HYDROGEN COMBUSTION WITH WATER/STEAM INJECTION". In: (2023).

[50] Ya. B. Zeldovich. "Regime classification of an exothermic reaction with nonuniform initial conditions". In: *Combustion and Flame* 39.2 (Oct. 1, 1980), pp. 211–214. ISSN: 0010-2180. DOI: 10.1016/0010-2180(80)90017-6.

[51] Rohit Kulkarni et al. *LES Based Investigation of Autoignition in Turbulent Co-flow Configurations*. Vol. 17. Journal Abbreviation: Combustion Theory Modelling Publication Title: Combustion Theory Modelling. Jan. 1, 2011.

[52] Andrea Gruber et al. "A Numerical Investigation of Reheat Hydrogen Combustion in a Simplified Geometrical Configuration From Atmospheric Pressure to Full Load Conditions". In: ASME Turbo Expo 2022: Turbomachinery Technical Conference and Exposition. American Society of Mechanical Engineers Digital Collection, Oct. 28, 2022. DOI: 10.1115/GT2022-83218.

[53] GONZALO DEL ÁLAMO et al. "Hydrogen–Oxygen Induction Times Above Crossover Temperatures". In: *Combustion Science and Technology* 176.10 (Oct. 1, 2004). Publisher: Taylor & Francis _eprint: https://doi.org/10.1080/00102200490487175, pp. 1599–1626. ISSN: 0010-2202. DOI: 10.1080/00102200490487175.

[54] Julia M. Fleck et al. "[39] Autoignition of hydrogen/nitrogen jets in vitiated air crossflows at different pressures". In: *Proceedings of the Combustion Institute* 34.2 (2013), pp. 3185–3192. ISSN: 15407489. DOI: 10.1016/j.proci.2012.05.039.

[55] J. Fleck et al. "Autoignition Limits of Hydrogen at Relevant Reheat Combustor Operating Conditions". In: *Journal of Engineering for Gas Turbines and Power* 134.41502 (Jan. 25, 2012). ISSN: 0742-4795. DOI: 10.1115/1.4004500.

[56] T. G. Kreutz et al. "Ignition in nonpremixed counterflowing hydrogen versus heated air: Computational study with detailed chemistry". In: *Combustion and Flame* 104.1 (Jan. 1, 1996), pp. 157–175. ISSN: 0010-2180. DOI: 10.1016/0010-2180(95)00121-2.

[57] Akash Rodhiya et al. "Simulations of flame structure in a reheat burner: pressure scaling". In: *AIAA Propulsion and Energy 2021 Forum*. AIAA Propulsion and Energy Forum. American Institute of Aeronautics and Astronautics, July 28, 2021. DOI: 10.2514/6.2021-3448.

[58] Andrea Gruber et al. "Direct Numerical Simulation of hydrogen combustion at auto-ignitive conditions: Ignition, stability and turbulent reaction-front velocity". In: *Combustion and Flame* 229 (July 2021), p. 111385. ISSN: 00102180. DOI: 10.1016/j.combustflame.2021.02.031.

[59] Konduri Aditya et al. "Direct numerical simulation of flame stabilization assisted by autoignition in a reheat gas turbine combustor". In: *Proceedings of the Combustion Institute* 37.2 (Jan. 1, 2019), pp. 2635–2642. ISSN: 1540-7489. DOI: 10.1016/j.proci.2018.06.084.

[60] James Bailey. “Analysis and modelling of boundary-layer flashback processes for hydrogen-rich gas-turbine combustion”. PhD thesis. University of Southampton, July 2021. 215 pp.

[61] Martin Rieth et al. “Enhanced burning rates in hydrogen-enriched turbulent premixed flames by diffusion of molecular and atomic hydrogen”. In: *Combustion and Flame*. A dedication to Professor Kenneth Noel Corbett Bray 239 (May 1, 2022), p. 111740. ISSN: 0010-2180. DOI: 10.1016/j.combustflame.2021.111740.

[62] Martin Rieth et al. “The effect of pressure on lean premixed hydrogen-air flames”. In: *Combustion and Flame* 250 (Apr. 1, 2023), p. 112514. DOI: 10.1016/j.combustflame.2022.112514.

[63] Dan Zhao. “Chapter 1 - Introduction of self-sustained thermoacoustic instability”. In: *Thermoacoustic Combustion Instability Control*. Ed. by Dan Zhao. Academic Press, Jan. 1, 2023, pp. 1–112. ISBN: 978-0-323-89910-9. DOI: 10.1016/B978-0-323-89910-9.00011-9.

[64] Paul Howard Wilkinson. *Aircraft Engines of the World, 1957*. Google-Books-ID: bf9luAEACAAJ. P.H. Wilkinson, 1957. 320 pp.

[65] David Daggett et al. *Revisiting Water Injection for Commercial Aircraft*. Nov. 1, 2004.

[66] B. Durst et al. “BMW Water Injection: Initial Experience and Future Potentials.” In: 38th International Vienna Motor Symposium. Vienna, 2017.

[67] Medhat A. Nemitallah et al. “Review of Novel Combustion Techniques for Clean Power Production in Gas Turbines”. In: *Energy & Fuels* 32.2 (Feb. 15, 2018). Publisher: American Chemical Society, pp. 979–1004. ISSN: 0887-0624. DOI: 10.1021/acs.energyfuels.7b03607.

[68] Klaus Brun et al. “Aerodynamic Instability and Life-Limiting Effects of Inlet and Interstage Water Injection Into Gas Turbines”. In: *Journal of Engineering for Gas Turbines and Power* 128.3 (Mar. 1, 2004), pp. 617–625. ISSN: 0742-4795. DOI: 10.1115/1.2135819.

[69] Tom Tanneberger et al. “Combustion efficiency measurements and burner characterization in a hydrogen-oxyfuel combustor”. In: *International Journal of Hydrogen Energy* 44.56 (Nov. 2019), pp. 29752–29764. ISSN: 03603199. DOI: 10.1016/j.ijhydene.2019.05.055.

[70] Arthur H. Lefebvre McDonell Vincent G. *Atomization and Sprays*. 2nd ed. Boca Raton: CRC Press, Apr. 4, 2017. 300 pp. ISBN: 978-1-315-12091-1. DOI: 10.1201/9781315120911.

[71] E. Amani et al. “Multi-objective CFD optimizations of water spray injection in gas-turbine combustors”. In: *Fuel* 227 (Sept. 2018), pp. 267–278. ISSN: 00162361. DOI: 10.1016/j.fuel.2018.04.093.

[72] A. Farokhipour et al. “A numerical study of NOx reduction by water spray injection in gas turbine combustion chambers”. In: *Fuel* 212 (Jan. 2018), pp. 173–186. ISSN: 00162361. DOI: 10.1016/j.fuel.2017.10.033.

[73] Steven Henry Strogatz. *Nonlinear Dynamics and Chaos: With Applications to Physics, Biology, Chemistry and Engineering*. Google-Books-ID: NZZDnQEACAAJ. Westview, 2000. 498 pp.

[74] *Chaos in an Atmosphere Hanging on a Wall | Mathematics of Planet Earth*. URL: http://mpe.dimacs.rutgers.edu/2013/03/17/chaos-in-an-atmosphere-hanging-on-a-wall/ (visited on 03/21/2024).

[75] Mohammad Farazmand et al. "Extreme Events: Mechanisms and Prediction". In: *Applied Mechanics Reviews* 71.5 (Sept. 1, 2019), p. 050801. ISSN: 0003-6900, 2379-0407. DOI: 10.1115/1.4042065.

[76] Vasilis Dakos et al. "Slowing down as an Early Warning Signal for Abrupt Climate Change". In: *Proceedings of the National Academy of Sciences of the United States of America* 105.38 (2008). Publisher: National Academy of Sciences, pp. 14308–14312. ISSN: 0027-8424.

[77] Kristian Dysthe et al. "Oceanic Rogue Waves". In: *Annual Review of Fluid Mechanics* 40.1 (Jan. 1, 2008), pp. 287–310. ISSN: 0066-4189, 1545-4479. DOI: 10.1146/annurev.fluid.40.111406.102203.

[78] D. R. Easterling et al. "Observed Variability and Trends in Extreme Climate Events: A Brief Review". In: *Bulletin of the American Meteorological Society* 81.3 (2000). Publisher: American Meteorological Society, pp. 417–425. ISSN: 0003-0007.

[79] Mohammad Farazmand et al. "A variational approach to probing extreme events in turbulent dynamical systems". In: *Science Advances* 3.9 (Sept. 2017), e1701533. ISSN: 2375-2548. DOI: 10.1126/sciadv.1701533. arXiv: 1704.04116[nlin,physics:physics].

[80] Angelo Casolaro et al. "Deep Learning for Time Series Forecasting: Advances and Open Problems". In: *Information* 14.11 (Nov. 2023). Number: 11 Publisher: Multidisciplinary Digital Publishing Institute, p. 598. ISSN: 2078-2489. DOI: 10.3390/info14110598.

[81] Steven L Brunton et al. "Machine Learning for Fluid Mechanics". In: (2019).

[82] Kurt Hornik et al. "Multilayer feedforward networks are universal approximators". In: *Neural Networks* 2.5 (Jan. 1, 1989), pp. 359–366. ISSN: 0893-6080. DOI: 10.1016/0893-6080(89)90020-8.

[83] Ian Goodfellow et al. *Deep Learning*. http://www.deeplearningbook.org. MIT Press, 2016.

[84] William L. Hamilton. *Graph Representation Learning*. Synthesis Lectures on Artificial Intelligence and Machine Learning. Cham: Springer International Publishing, 2020. ISBN: 978-3-031-00460-5 978-3-031-01588-5. DOI: 10.1007/978-3-031-01588-5.

[85] Andreas Damianou et al. "Deep Gaussian Processes". In: *Proceedings of the Sixteenth International Conference on Artificial Intelligence and Statistics*. Artificial Intelligence and Statistics. ISSN: 1938-7228. PMLR, Apr. 29, 2013, pp. 207–215.

[86] Ian Goodfellow et al. "Generative Adversarial Nets". In: *Advances in Neural Information Processing Systems*. Vol. 27. Curran Associates, Inc., 2014.

[87] Ian T. Jolliffe et al. “Principal component analysis: a review and recent developments”. In: *Philosophical Transactions of the Royal Society A: Mathematical, Physical and Engineering Sciences* 374.2065 (Apr. 13, 2016). Publisher: Royal Society, p. 20150202. DOI: 10.1098/rsta.2015.0202.

[88] Anirudh Jonnalagadda et al. “A co-kurtosis based dimensionality reduction method for combustion datasets”. In: *Combustion and Flame* 250 (Apr. 2023), p. 112635. ISSN: 00102180. DOI: 10.1016/j.combustflame.2023.112635.

[89] Konduri Aditya et al. “Anomaly detection in scientific data using joint statistical moments”. In: *Journal of Computational Physics* 387 (June 2019), pp. 522–538. ISSN: 00219991. DOI: 10.1016/j.jcp.2019.03.003. arXiv: 1808.04498[physics].

[90] *CS250: K-means Clustering*. Saylor Academy. URL: https://learn.saylor.org/mod/page/view.php?id=55349 (visited on 01/08/2024).

[91] John A. Hartigan. *Clustering Algorithms*. Google-Books-ID: cDnvAAAAMAAJ. Wiley, 1975. 382 pp. ISBN: 978-0-471-35645-5.

[92] Urszula Gołyska. “Machine learning-based identification of precursors of extreme events in chaotic systems”. PhD thesis. 2022.

[93] Andrew Ng et al. “On Spectral Clustering: Analysis and an algorithm”. In: *Advances in Neural Information Processing Systems*. Vol. 14. MIT Press, 2001.

[94] M. E. J. Newman. “Modularity and community structure in networks”. In: *Proceedings of the National Academy of Sciences* 103.23 (June 6, 2006). Publisher: Proceedings of the National Academy of Sciences, pp. 8577–8582. DOI: 10.1073/pnas.0601602103.

[95] Peter Schmid et al. “Analysis and prediction of rare events in turbulent flows”. In: *Center for Turbulence Research* (Dec. 1, 2018).

[96] P J Schmid et al. “Description and detection of burst events in turbulent flows”. In: *Journal of Physics: Conference Series* 1001 (Apr. 2018), p. 012015. ISSN: 1742-6588, 1742-6596. DOI: 10.1088/1742-6596/1001/1/012015.

[97] Loizos Christodoulou et al. “Characterizing the signature of flame flashback precursor through recurrence analysis”. In: *Chaos: An Interdisciplinary Journal of Nonlinear Science* 26.1 (Jan. 1, 2016), p. 013110. ISSN: 1054-1500, 1089-7682. DOI: 10.1063/1.4940154.

[98] Meenatchidevi Murugesan et al. “Detecting the Onset of an Impending Thermoacoustic Instability Using Complex Networks”. In: *Journal of Propulsion and Power* 32.3 (May 2016), pp. 707–712. ISSN: 0748-4658, 1533-3876. DOI: 10.2514/1.B35914.

[99] Tsubasa Kobayashi et al. “Early Detection of Thermoacoustic Combustion Instability Using a Methodology Combining Complex Networks and Machine Learning”. In: *Physical Review Applied* 11.6 (June 14, 2019), p. 064034. ISSN: 2331-7019. DOI: 10.1103/PhysRevApplied.11.064034.

[100] Qiang An et al. “Early Warning Signs of Imminent Thermoacoustic Oscillations Through Critical Slowing Down”. In: *Journal of Engineering for Gas Turbines and Power* 141.5 (May 1, 2019), p. 054501. ISSN: 0742-4795, 1528-8919. DOI: 10.1115/1.4041963.

[101] Urszula Golyska et al. “Clustering-based Identification of Precursors of Extreme Events in Chaotic Systems”. In: ().

[102] Thomas M. Bury et al. “Deep learning for early warning signals of tipping points”. In: *Proceedings of the National Academy of Sciences* 118.39 (Sept. 28, 2021), e2106140118. ISSN: 0027-8424, 1091-6490. DOI: 10.1073/pnas.2106140118.

[103] Anna Asch et al. “Model-assisted deep learning of rare extreme events from partial observations”. In: *Chaos: An Interdisciplinary Journal of Nonlinear Science* 32.4 (Apr. 2022), p. 043112. ISSN: 1054-1500, 1089-7682. DOI: 10.1063/5.0077646. arXiv: 2111.04857[nlin,physics:physics].

[104] Michael McCartney et al. “ONLINE DETECTION OF COMBUSTION INSTABILITIES USING SUPERVISED MACHINE LEARNING”. In: ().

[105] Eustaquio A. Ruiz et al. “Convolutional neural networks to predict the onset of oscillatory instabilities in turbulent systems”. In: *Chaos: An Interdisciplinary Journal of Nonlinear Science* 31.9 (Sept. 2021), p. 093131. ISSN: 1054-1500, 1089-7682. DOI: 10.1063/5.0056032.

[106] Di Qi et al. “Using machine learning to predict extreme events in complex systems”. In: *Proceedings of the National Academy of Sciences* 117.1 (Jan. 7, 2020), pp. 52–59. ISSN: 0027-8424, 1091-6490. DOI: 10.1073/pnas.1917285117.

[107] Junjie Jiang et al. “Predicting extreme events from data using deep machine learning: When and where”. In: *Physical Review Research* 4.2 (Apr. 11, 2022), p. 023028. ISSN: 2643-1564. DOI: 10.1103/PhysRevResearch.4.023028.

[108] Alberto Racca et al. *Data-driven prediction and control of extreme events in a chaotic flow*. Apr. 25, 2022. arXiv: 2204.11682[nlin,physics:physics].

[109] Jiahao ( ) Ren et al. “Predictive models for flame evolution using machine learning: A priori assessment in turbulent flames without and with mean shear”. In: *Physics of Fluids* 33.5 (May 11, 2021), p. 055113. ISSN: 1070-6631. DOI: 10.1063/5.0048680.

[110] Hui Liu et al. “Smart deep learning based wind speed prediction model using wavelet packet decomposition, convolutional neural network and convolutional long short term memory network”. In: *Energy Conversion and Management* 166 (June 15, 2018), pp. 120–131. ISSN: 0196-8904. DOI: 10.1016/j.enconman.2018.04.021.

[111] R. Adnan et al. “Performance and emission analysis of hydrogen fueled compression ignition engine with variable water injection timing”. In: *Energy*. 2nd International Meeting on Cleaner Combustion (CM0901-Detailed Chemical Models for Cleaner Combustion) 43.1 (July 1, 2012), pp. 416–426. ISSN: 0360-5442. DOI: 10.1016/j.energy.2012.03.073.

[112] Hadi Taghavifar et al. “Benchmarking of water injection in a hydrogen-fueled diesel engine to reduce emissions”. In: *International Journal of Hydrogen Energy* 42.16 (Apr. 20, 2017), pp. 11962–11975. ISSN: 0360-3199. DOI: 10.1016/j.ijhydene.2017.02.138.

[113] Saeid Shahpouri et al. “Nitrogen oxides reduction and performance enhancement of combustor with direct water injection and humidification of inlet air”. In: *Clean*

*Technologies and Environmental Policy* 21.3 (Apr. 2019), pp. 667–683. ISSN: 1618-954X, 1618-9558. DOI: 10.1007/s10098-019-01666-4.

[114] Denis Veynante et al. "Turbulent combustion modeling". In: *Progress in Energy and Combustion Science* 28.3 (Mar. 1, 2002), pp. 193–266. ISSN: 0360-1285. DOI: 10.1016/S0360-1285(01)00017-X.

[115] Akira Yoshizawa et al. "A Statistically-Derived Subgrid-Scale Kinetic Energy Model for the Large-Eddy Simulation of Turbulent Flows". In: *Journal of the Physical Society of Japan* 54.8 (Aug. 15, 1985), pp. 2834–2839. ISSN: 0031-9015, 1347-4073. DOI: 10.1143/JPSJ.54.2834.

[116] S Menon. "[35] Effect of subgrid models on the computed interscale energy transfer in isotropic turbulence". In: ().

[117] M. Klein et al. "A digital filter based generation of inflow data for spatially developing direct numerical or large eddy simulations". In: *Journal of Computational Physics* 186.2 (Apr. 2003), pp. 652–665. ISSN: 00219991. DOI: 10.1016/S0021-9991(03)00090-1.

[118] P K Senecal et al. "Multi-Dimensional Modeling of Direct-Injection Diesel Spray Liquid Length and Flam Lift-off Length using CFD an Parallel Detailed Chemistry". In: ().

[119] Stephen R Turns. *Introduction to combustion*. Vol. 287. NY, USA: McGraw-Hill Companies New York, 1996.

[120] J P Legier et al. "Dynamically thickened flame LES model for premixed and non-premixed turbulent combustion". In: ().

[121] Thomas Jaravel. "PREDICTION OF POLLUTANTS IN GAS TURBINES USING LARGE EDDY SIMULATION". Doctorat. Institut National Polytechnique de Toulouse (INP Toulouse), 2016.

[122] Fabrice Charlette et al. "[30] A power-law flame wrinkling model for LES of premixed turbulent combustion Part I: non-dynamic formulation and initial tests". In: *Combustion and Flame* 131.1 (Oct. 2002), pp. 159–180. ISSN: 00102180. DOI: 10.1016/S0010-2180(02)00400-5.

[123] G. Wang et al. "Implementation of a dynamic thickened flame model for large eddy simulations of turbulent premixed combustion". In: *Combustion and Flame* 158.11 (Nov. 1, 2011), pp. 2199–2213. ISSN: 0010-2180. DOI: 10.1016/j.combustflame.2011.04.008.

[124] Gerasimos Theotokatos. *The CFD Development of Non-premixed Dual Fuel Combustion Diesel Engine injected by High-pressure Gas in the Cylinder Chamber – ARCHIE-WeSt*. URL: https://www.archie-west.ac.uk/projects/computational-fluid-dynamics/the-cfd-development-of-non-premixed-dual-fuel-combustion-diesel-engine-injected-by-high-pressure-gas-in-the-cylinder-chamber/ (visited on 12/11/2023).

[125] *Converge CFD v3.1 Manual*. 2023.

[126] Stephen B Pope. "Ten questions concerning the large-eddy simulation of turbulent flows". In: *New Journal of Physics* 6 (Mar. 16, 2004), pp. 35–35. ISSN: 1367-2630. DOI: 10.1088/1367-2630/6/1/035.

[127] Eric Pomraning. "Development of Large Eddy Simulation Turbulence Models". PhD thesis. Dec. 1, 2000. DOI: 10.13140/2.1.2035.7929.

[128] R. I Issa. "Solution of the implicitly discretised fluid flow equations by operator-splitting". In: *Journal of Computational Physics* 62.1 (Jan. 1, 1986), pp. 40–65. ISSN: 0021-9991. DOI: 10.1016/0021-9991(86)90099-9.

[129] C. M RHIE et al. "Numerical study of the turbulent flow past an airfoil with trailing edge separation". In: *Numerical study of the turbulent flow past an airfoil with trailing edge separation* 21.11 (1983). Place: Reston, VA Publisher: American Institute of Aeronautics and Astronautics, pp. 1525–1532. ISSN: 0001-1452.

[130] Anima Anandkumar et al. *Tensor decompositions for learning latent variable models*. Nov. 13, 2014. DOI: 10.48550/arXiv.1210.7559. arXiv: 1210.7559[cs,math,stat].

[131] L. De Lathauwer et al. "Independent component analysis and (simultaneous) third-order tensor diagonalization". In: *IEEE Transactions on Signal Processing* 49.10 (Oct. 2001), pp. 2262–2271. ISSN: 1053587X. DOI: 10.1109/78.950782.

[132] Zhiya Zuo. *Python implementation of Newman's spectral methods to maximize modularity*. original-date: 2017-04-10T22:26:50Z. Dec. 28, 2023.

[133] E. A. Leicht et al. "Community structure in directed networks". In: *Physical Review Letters* 100.11 (Mar. 21, 2008), p. 118703. ISSN: 0031-9007, 1079-7114. DOI: 10.1103/PhysRevLett.100.118703. arXiv: 0709.4500[physics].

[134] Kurt A. Estes et al. "Correlation of sauter mean diameter and critical heat flux for spray cooling of small surfaces". In: *International Journal of Heat and Mass Transfer* 38.16 (Nov. 1, 1995), pp. 2985–2996. ISSN: 0017-9310. DOI: 10.1016/0017-9310(95)00046-C.

[135] Rolf Deneys Reitz. *Atomization and Other Breakup Regimes of a Liquid Jet*. Google-Books-ID: F0_5HAAACAAJ. Princeton University, 1978. 327 pp.

[136] C Trevino. "Ignition Phenomena in Hydrogen and Oxygen Mixtures". In: *Progress in Astronautics and Aeronautics* 131 (1990), pp. 19–43.

[137] Pierre Boivin. "Reduced-kinetic mechanisms for hydrogen and syngas combustion including autoignition". In: ().

[138] Forman A. Williams. "Detailed and reduced chemistry for hydrogen autoignition". In: *Journal of Loss Prevention in the Process Industries*. Hydrogen Safety 21.2 (Mar. 1, 2008), pp. 131–135. ISSN: 0950-4230. DOI: 10.1016/j.jlp.2007.06.002.

[139] Kevin W Thompson. "Time dependent boundary conditions for hyperbolic systems". In: *Journal of Computational Physics* 68.1 (Jan. 1, 1987), pp. 1–24. ISSN: 0021-9991. DOI: 10.1016/0021-9991(87)90041-6.

[140] Kevin W. Thompson. "Time-Dependent Boundary Conditions for Hyperbolic Systems, II". In: *Journal of Computational Physics* 89 (Aug. 1, 1990). ADS Bib-

code: 1990JCoPh..89..439T, pp. 439–461. ISSN: 0021-9991. DOI: 10.1016/0021-9991(90)90152-Q.

[141] T. J Poinsot et al. "Boundary conditions for direct simulations of compressible viscous flows". In: *Journal of Computational Physics* 101.1 (July 1, 1992), pp. 104–129. ISSN: 0021-9991. DOI: 10.1016/0021-9991(92)90046-2.

[142] David H. Rudy et al. "Boundary conditions for subsonic compressible Navier-Stokes calculations". In: *Computers & Fluids* 9.3 (Sept. 1, 1981), pp. 327–338. ISSN: 0045-7930. DOI: 10.1016/0045-7930(81)90005-0.

[143] Horace Lamb. *Hydrodynamics*. In collab. with George A. Smathers Libraries University of Florida. New York,: Dover publications, 1945. 762 pp.

[144] J.D. Naber et al. "Modeling Engine Spray/Wall Impingement". In: *SAE Transactions* 97 (1988). Publisher: SAE International, pp. 118–140. ISSN: 0096-736X.

[145] Manuel A. Gonzalez D. et al. "A Study of Diesel Cold Starting using both Cycle Analysis and Multidimensional Calculations". In: *SAE Transactions* 100 (1991). Publisher: SAE International, pp. 189–208. ISSN: 0096-736X.

[146] L. H. J. Wachters et al. "The heat transfer from a hot wall to impinging water drops in the spheroidal state". In: *Chemical Engineering Science* 21.11 (Nov. 1, 1966), pp. 1047–1056. ISSN: 0009-2509. DOI: 10.1016/0009-2509(66)85100-X.

[147] A. A. Amsden et al. *KIVA-II: A computer program for chemically reactive flows with sprays*. LA-11560-MS. Los Alamos National Lab. (LANL), Los Alamos, NM (United States), May 1, 1989. DOI: 10.2172/6228444.

[148] Nils Froessling. *ON THE EVAPORATION OF FALLING DROPS,* Section: Technical Reports. 1968.

[149] WE Ranz et al. "Evaporation from drops: Part II". In: *Engineering Progress* 48 (1952), pp. 173–180.

[150] B. Abramzon et al. "Droplet vaporization model for spray combustion calculations". In: *International Journal of Heat and Mass Transfer* 32.9 (Sept. 1, 1989), pp. 1605–1618. ISSN: 0017-9310. DOI: 10.1016/0017-9310(89)90043-4.

[151] David P. Schmidt et al. "A New Droplet Collision Algorithm". In: *Journal of Computational Physics* 164.1 (Oct. 10, 2000), pp. 62–80. ISSN: 0021-9991. DOI: 10.1006/jcph.2000.6568.

[152] Scott L. Post et al. "Modeling the outcome of drop–drop collisions in Diesel sprays". In: *International Journal of Multiphase Flow* 28.6 (June 1, 2002), pp. 997–1019. ISSN: 0301-9322. DOI: 10.1016/S0301-9322(02)00007-1.

[153] N. Ashgriz et al. "Collision Dynamics of Two Liquid Drops". In: *Physics of Fluids A: Fluid Dynamics* 1.9 (Sept. 1, 1989), p. 1446. ISSN: 0899-8213. DOI: 10.1063/1.4738835.

[154] Shuhai Hou et al. "Interaction Mechanisms between Closely Spaced Sprays". In: *SAE Technical Papers* (Apr. 14, 2008). DOI: 10.4271/2008-01-0946.

[155] B. J. McKEON et al. “Further observations on the mean velocity distribution in fully developed pipe flow”. In: *Journal of Fluid Mechanics* 501 (Feb. 25, 2004), pp. 135–147. ISSN: 0022-1120, 1469-7645. DOI: 10.1017/S0022112003007304.

[156] B. J. McKEON et al. “A new friction factor relationship for fully developed pipe flow”. In: *Journal of Fluid Mechanics* 538.-1 (Aug. 17, 2005), p. 429. ISSN: 0022-1120, 1469-7645. DOI: 10.1017/S0022112005005501.

# A

# Navier-Stokes Characteristic Boundary Conditions

The NSCBC is based on the eigenanalysis of the Euler equations and they have the intention of purposefully allowing for the pressure waves which are close to the pressure far upstream or downstream the domain to pass through, while reflecting the rest. In the Converge solver, these boundary conditions are implemented following the research of Thompson [139, 140] and Poinsot and Lele [141].

The three-dimensional Euler equations are characterized by five distinct real eigenvalues, reflecting different wave types at the boundaries:

$$\begin{aligned} \lambda_1 &= u, \\ \lambda_2 &= u, \\ \lambda_3 &= u, \\ \lambda_4 &= u - c, \\ \lambda_5 &= u + c, \end{aligned} \tag{A.1}$$

where the first three eigenvalues ($\lambda_1$, $\lambda_2$, and $\lambda_3$) correspond to entropy and vorticity waves, and the remaining two ($\lambda_4$ and $\lambda_5$) to acoustic waves. The propagation speed and direction of these waves are represented by $\lambda$ and $\frac{dn}{dt} = \lambda$, respectively.

At the inlet, where the flow is subsonic, the situation yields four positive and one negative eigenvalue, leading to four incoming and one outgoing wave. This configuration requires setting four variables via physical boundary conditions and one via a numerical boundary condition (BC).

Conversely, at the outlet, the presence of four negative and one positive eigenvalue indicates four outgoing waves and one incoming wave, with numerical BCs specifying four variables and the physical condition determining the fifth.

For updating velocity, density, and pressure each iteration, the correction-based Non-Reflecting Subsonic Outflow Boundary Conditions (NSCBC) approach utilizes the Local One-Dimensional Inviscid (LODI) formulation. If $U = (\rho, p, u, v, w)$ represents the state vector, the time derivative of the residual $R$ is expressed as:

$$\frac{\partial U}{\partial t} = -R. \tag{A.2}$$

The residual predicted at the end of the PISO iteration, $U^{n+1,P}$, is calculated as:

$$R^P = -\frac{U^{n+1,P} - U^n}{dt} \tag{A.3}$$

The correction-based strategy adjusts the incoming waves into corrected waves that match the desired boundary conditions, represented by $C$. The residual $R$ is split into $R = ML$, where $L$ stands for the wave amplitude vector and $M$ denotes a matrix system detailed in [141]:

$$U^{n+1,C} = U^n - dt(R^P - R_{BC}^{in,P} + R_{BC}^{in,C}), \tag{A.4}$$

Utilizing $R_{BC}^{in,P} = ML^{in}$ and $R_{BC}^{in,C} = ML^{in,C}$. For the inlet, where four incoming waves are present, $L^{in} = (0, L_2, L_3, L_4, L_5)$ and $L^{in,C} = (0, L_2^C, L_3^C, L_4^C, L_5^C)$. For the outlet, $L^{in} = (L_1, 0, 0, 0, 0)$ and $L^{inC} = (L_1^C, 0, 0, 0, 0)$. Inlet corrected wave amplitudes $L_i^C$ are calculated using:

$$\frac{\partial u}{\partial t} = -\frac{1}{2\rho c} L_5^C = -K\,(u - u_\infty) \tag{A.5}$$

$$\frac{\partial v}{\partial t} = -L_3^C = -K\,(v - v_\infty) \tag{A.6}$$

$$\frac{\partial w}{\partial t} = -L_4^C = -K\,(w - w_\infty) \tag{A.7}$$

$$\frac{\partial T}{\partial t} = -\frac{T}{\rho c^2} L_2^C = -K\,(T - T_\infty) \tag{A.8}$$

Here, $u_\infty, v_\infty, w_\infty$, and $T_\infty$ are far-field quantities imposed by Dirichlet values. Meanwhile, for the outflow:

$$L_1 = K\,(p - p_\infty)\,, \tag{A.9}$$

where $p_\infty$ is the far-field pressure. The $L_i^C$ is calculated as:

$$\frac{\partial p}{\partial t} = -\frac{1}{2} L_1^C = -K\,(p - p_\infty) \tag{A.10}$$

Far-field values are relaxed using the relaxation constant $K$:

$$K = \sigma\,(1 - M^2)\,\frac{c}{L} \tag{A.11}$$

Here, $M$ is the Mach, $\sigma$ is the tuning parameter, and $L$ is the characteristic length, taken as 0.06 m. The value of $K$ is critical in obtaining an appropriate solution from this model, and thus the tuning parameter should be chosen carefully. High $\sigma$ values can lead to instability or simulation divergence due to large wave amplitude, deviating velocity from the target. Low $\sigma$ values cause a nearly non-reflecting boundary, but the mean solution drifts away due to viscous and transverse terms in the Navier-Stokes equations. An optimal $\sigma$ should impose a nearly non-reflecting behavior while eliminating drift. In this work, the a value of $\sigma = 0.25$ is used, as suggested by Ruby et al. [142].

# B

# Numerical solvers

**Numerical schemes**
The approach used for solving the conservation equations in the Converge software [125] is the Finite Volume Methods (FVM) approach. This method involves partitioning the computational space into discrete cells, where the central point of each cell holds the values of various transported entities. These central values are then updated based on the flux across the cell faces and any contributions from internal sources. When considering the transport of a scalar quantity $\phi$, and applying the Green-Gauss theorem, the process can be represented as follows:

$$\frac{\partial \phi}{\partial t} + \frac{\partial u\phi}{\partial x} = 0 \quad \longrightarrow \quad \frac{\partial \phi}{\partial t} + \frac{1}{V}\int_{\mathrm{S}} u \cdot n\phi \, dS = 0 \tag{B.1}$$

Here, $V$ denotes the volume of the cell, $n$ represents the surface normal, and $S$ indicates the surface area. Then, Equation B.1 is discretized by accounting for the cumulative flux across all faces, as shown:

$$\frac{\partial \phi}{\partial t} + \frac{1}{V}\sum_{i} u_{f,i}\phi_{f,i}S_i = 0 \tag{B.2}$$

To determine the face values of velocity $u_{f,i}$ and the transported quantity $\phi_{f,i}$, extrapolation from adjacent cells is essential. Two primary methods are considered: up-winding from the upstream cell, which enhances stability at the expense of numerical viscosity, and the central difference scheme, which, while more precise, is prone to instability. The Converge solver additionally enables a hybrid approach, blending these two methods. The formula for this blend is given by:

$$\phi_{f,i-\frac{1}{2}} = (1-\beta)\phi_{f,i-1} + \beta\frac{1}{2}(\phi_{f,i-1} + \phi_{f,i}) \tag{B.3}$$

In this expression, $\beta$ regulates the balance between upwinding and central difference. Given hydrogen's high diffusivity and propensity for flashback, minimizing the use of upwind schemes is advisable. In this context, $\beta$ is set to 1 for all transported entities, with the exception of turbulence, where a fully upwind approach is preferred. This decision stems from the fact that central differences preserve strong gradients, thereby enhancing turbulence dissipation. To maintain numerical stability, step limiters are employed, switching to first-order upwind when the monotonicity threshold is not met at the faces. For temporal

derivative discretization, an implicit first-order Euler scheme is chosen, balancing stability and precision while ensuring the conservation of all quantities, including passive ones.

**PISO algorithm**
The PISO (Pressure Implicit with Splitting of Operators) strategy, initially presented by Issa in 1986 [128], represents an approach for resolving transport equations, which emphasizes the correlation between pressure and velocity. This algorithm enhances computational efficiency through the reduction of iterative steps and the utilization of larger time-steps. The PISO algorithm initiates by hypothesizing an initial pressure distribution, derived from a preliminary resolution of the momentum equations. Subsequently, an iterative refinement process is employed, involving the generation of a revised pressure equation and its incorporation into the momentum equations. This iterative sequence continues until the solutions converge within a predefined tolerance threshold. Subsequently, the remaining transport equations are addressed. The PISO algorithm's versatility is evident in its applicability to both incompressible and steady-state scenarios, demonstrating robust stability even when subjected to algorithmic modifications.

The algorithm's execution can be delineated in the following stages, where each additional superscript $^*$ denotes a higher level of temporal accuracy:

- **Predictor Step:** Here, the momentum equation is resolved in a semi-implicit manner. The equation, encapsulating diffusion, convection, and source elements, is expressed as follows, with $H^*$ denoting these collective terms. Intermediate field values during the iterative process are indicated by superscript $^*$, while previous field values bear the superscript $^n$:
$$\frac{\rho^n u_i^*}{dt} - \frac{\rho^n u_i^n}{dt} = -\frac{\partial P^n}{\partial x_i} + H_i^\star \tag{B.4}$$

- **First Correction:** This stage involves updating the velocity field $u^*$ to satisfy the mass conservation. To achieve this, the momentum equation is then reformulated as, based on the adjusted pressure $p^\star$:
$$\frac{\rho^\star u_i^{\star\star}}{dt} - \frac{\rho^n u_i^n}{dt} = -\frac{\partial P^\star}{\partial x_i} + H_i^\star \tag{B.5}$$

- **New Pressure Equation Derivation:** By contrasting the initial and corrected momentum equations and integrating mass conservation principles, a new pressure formulation emerges. Here, $\rho^\star$ is related to pressure as $\rho^\star = P^\star / \left(Z^n R^n T^n\right)$, where Z denotes the compressibility factor, assuming unity for ideal gases. The variable $S$ represents various source terms. The resultant pressure equation is:
$$\frac{\partial^2}{\partial x_i \partial x_i}\left(P^\star - P^n\right) - \frac{\left(P^\star - P^n\right)\phi^n}{dt^2} = \left(\frac{\partial \rho^n u_i^\star}{\partial x_i} - S\right)\frac{1}{dt} \tag{B.6}$$

- **Second Correction:** This involves a further refinement of the velocity field $u_i^{\star\star}$ and pressure $p^\star$, similarly to the previous step. The momentum equation at this stage is simplified to:
$$\frac{\rho^{\star\star} u_i^{\star\star\star}}{dt} - \frac{\rho^n u_i^n}{dt} = -\frac{\partial P^{\star\star}}{\partial x_i} + H_i^\star \tag{B.7}$$

- **Pressure Equation Update:** The final stage involves manipulating the second correction equation to facilitate the computation of the pressure field $p^*$, using the known right-hand side values. The updated velocity $u_i^{\star\star}$ is then determined using Equation B.7. While the iterative process can be extended, a satisfactory accuracy is usually achieved within two iterations.

To improve accuracy, the algorithm also incorporates correction equations for temperature and other transported quantities. Although increasing the number of iterations can improve precision, the discretization of original momentum and transport equations inherently introduces errors of the order $O(\delta t^3)$ and $O(\delta t^2)$ for second and first order schemes, respectively. Therefore, extending the correction resolution beyond two iterations is often unnecessary.

In this specific instance, the PISO algorithm has been implemented with a convergence criterion multiplier set at 20.0, pertaining to the minimum improvement required in residual values per PISO loop iteration. The algorithm stipulates a minimum of two corrections and a maximum of nine, with a tolerance threshold defined at $\Psi_{tol} = 10^{-4}$. The tolerance for each transport equation is computed as follows, where $\Psi^\star$ represents the current correction, and $\Psi^{t-1}$ denotes the preceding correction value:

$$\frac{\left|\Psi^- \Psi^{t-1}\right|}{\left|\Psi^*\right|} < \Psi_{tol} \tag{B.8}$$

**Rhie-Chow Algorithm**
Another important algorithm involved in solving the system of equations is the Rhie-Chow interpolation algorithm [129]. Because all of the transported quantities are placed in the center of the cells, undesirable fluctuations can happen due to the decopuling between pressure and velocity. To account for this, the velocity in the correction steps is now calculated using the spatial pressure gradients across multiple neighbouring cells:

$$u^*_{i+1/2} = \frac{u^*_i + u^*_{i+1}}{2} - \frac{dt}{\rho}\left(\frac{P_{i+1} - P_i}{dx}\right) + \frac{dt}{2\rho}\left(\frac{P_{i+1} - P_{i-1}}{2dx} + \frac{P_{i+2} - P_i}{2dx}\right) \tag{B.9}$$

**Linear solver**
The terminal phase in the computational process involves resolving the entire set of discretized equations for each iteration. This task is accomplished using the SOR (Successive Over-Relaxation) technique, a method noted for its effectiveness in scenarios involving transient, compressible dynamics. The linear equation set is articulated in the matrix form $Ax = b$, with the iterative solution process commencing from an initial estimate denoted by $x_0$. Following each iteration, the algorithm calculates the residual, ensuring its compliance with predefined limits:

$$r_n = \frac{|Ax_n - b|^2}{|b|^2} \tag{B.10}$$

A critical aspect of the SOR method is the introduction of a relaxation factor, $\omega$, which significantly hastens the convergence of the residuals. Iterative procedures often necessitate the application of under-relaxation, linking the subsequent iteration to its predecessor augmented by a proportionally scaled correction. Thus, the ensuing iteration $\phi^{\star\star}$ is derived

from the previous iteration $\phi^\star$, supplemented by the correction, expressed as $\phi^{\star\star} = \phi^\star + \omega\Delta\phi$. The system is then redefined, leading to the following equation:

$$x_i^{k+1} = (1-\omega)x_i^k + \frac{\omega}{a_{ii}}\left(b_i - \sum_{j<i} a_{ij}x_j^{k+1} - \sum_{j>i} a_{ij}x_j^k\right) \tag{B.11}$$

# C

# Spray model

## C.1. Injection size distribution

The injection size distribution chosen for the spray model is the Rosin-Rammler distribution. The selection of this model is based on computational efficiency grounds, as choosing this non-uniform distribution justifies neglecting the break-up and coalescence phenomena, thus simplifying the model. The cumulative probability distribution function is given by:

$$p(r) = 1 - \exp(\zeta^{C_{RR}}) \quad \text{for} \quad 0 < \zeta < \zeta_{max}, \tag{C.1}$$

where $\zeta = r/\tilde{r}$, $\zeta_{max} = \ln 1000^{\frac{1}{C_{RR}}}$ and the upper limit of the radius is imposed using the empirical constant $C_{RR}$. Furthermore,

$$\bar{r} = \Gamma\left(1 - \frac{1}{C_{RR}}\right) r_{\text{Sauter}}, \tag{C.2}$$

where $r_{\text{Sauter}}$ is the Sauter radius and $\Gamma$ is the Gamma function, resulting in a drop radius given by $r = \bar{r}\zeta$.

**Particle motion**

Understanding the path of droplets in the disperse phase is crucial for employing the Lagrangian approach to solve spray dynamics. Initially given momentum at injection, the droplets interact with the gas flow, experiencing forces such as gravity or drag. The particle kinematic evolution, based on Newton's second law, can be expressed as:

$$m_d \frac{dc_i}{dt} = F_{d,i} \tag{C.3}$$

If pressure gradients and body forces are omitted, a simplified definition is given where the acceleration of droplets now primarily depends on the drag force. The mass of a droplet is expressed in terms of the liquid's density, $\rho_l$, and its volume, given by $m_d = \frac{4}{3}\pi\rho_l r^3$. The velocity difference between the droplet and the gas is denoted by $U_i$, calculated as $U_i = u_i + u_i' - c_i$, with $u_i$, $u_i'$, and $c_i$ representing the local mean velocity, velocity fluctuations, and the velocity of the droplet, respectively. The standard expression for the drag force exerted on the droplet is:

$$F_{\text{drag},i} = C_D A_f \frac{\rho_g |U_i|}{2} U_i \tag{C.4}$$

Upon substituting the aforementioned relationships and reorganizing the variables, we derive the final formula for the evolution of the droplet's velocity. The equation incorporates the drag coefficient $C_D$, the density of the gas phase $\rho_g$, and the droplet's radius $r$. Given that the size of the droplet changes over time, primarily due to evaporation, an additional equation is required to describe the changing radius:

$$\frac{dc_i}{dt} = \frac{3}{8}\frac{\rho_g}{\rho_l}C_D\frac{|U_i|}{r}U_i \tag{C.5}$$

The drag coefficient is the final parameter to be defined. While there is an elaborate model for dynamic drag that accounts for changes in the shape of the droplet, a simpler model assuming a spherical droplet shape is utilized for simplicity. The Schiller-Neumann equation is used to estimate $C_D$ based on the Reynolds number for the droplet and gas flow:

$$C_D = \begin{cases} \frac{24}{\mathrm{Re}_d}\left(1 + \frac{1}{6}\mathrm{Re}_d^{2/3}\right) & \mathrm{Re}_d \leq 1000 \\ 0.424 & \mathrm{Re}_d > 1000 \end{cases} \tag{C.6}$$

The Reynolds number, $\mathrm{Re}_d$, is calculated considering the diameter of the droplet, the relative velocity between the droplet and the gas, and the kinematic viscosity of the gas. Note that the calculated drag might be underestimated since droplets, which tend to assume a disk shape in high Weber number flows, exhibit a higher $C_D$ compared to spheres. To address this discrepancy, a correction to the drag coefficient, as proposed by Liu et al., is applied:

$$C_D = C_{D,\mathrm{sphere}}(1 + 2.632y) \tag{C.7}$$

Here, y is the drop distorsion, ranging from 0 to 1, where 0 implies no distortion and 1 implies maximum distortion. For under-damped flows, the function reads as:

$$y(t) = We_c + e^{-\frac{t}{t_d}}\left[(y(0) - We_c)\cos(\omega t) + \frac{1}{\omega}\left(\frac{dy}{dt}(0) + \frac{y(0) - We_c}{t_d}\right)\sin(\omega t)\right] \tag{C.8}$$

where:

$$\begin{aligned} We_g &= \frac{\rho_g u_{rel}^2 r_o}{\sigma} \\ We_c &= \frac{C_F}{C_k C_b}We_g \\ \frac{1}{t_d} &= \frac{C_d}{2}\frac{\mu_l}{\rho_l r_o^2} \\ \omega^2 &= C_k\frac{\sigma}{\rho_l r_o^3} - \frac{1}{t_d^2} \end{aligned} \tag{C.9}$$

and $C_k = 8$, $C_F = 1/3$ and $C_b = 1/2$ are model constants set to match the results of Lamb, 1945 [143]. Furthermore, $\omega$ is the oscillation frequency, $We_g$ is the droplet Weber number, $u_{rel}$ is the relative velocity of the droplet, $\sigma$ is the droplet surface tension, $\mu_l$ is the viscosity of the droplet and finally $r_0$ is the undisturbed droplet radius.

## C.2. Turbulent dispersion

Turbulence plays a crucial role in affecting droplet movement, leading to difficulties in predicting how particles spread out. Due to drag forces, droplets slow down, with their momentum being passed on to the surrounding fluid at smaller scales. In Large Eddy Simulation (LES) studies, estimating the velocity at these smaller scales is critical, and can be approximated using a basic expansion method:

$$u_{\mathrm{sg},i} = C_{\mathrm{les}} \frac{d^2}{24} \frac{\partial^2 \bar{u}_i}{\partial x^2} \tag{C.10}$$

Here, $d$ is the effective cell dimension, derived as $d = \sqrt[3]{V_{\mathrm{cell}}}$, where $V_{\mathrm{cell}}$ is the volume of the computational cell, $\bar{u}_i$ denotes the average velocity in the simulation, and $C_{\mathrm{les}}$ is a predetermined constant. The fluctuating parts of the velocity, $\bar{u}_i'$, are sampled periodically based on the turbulence's characteristic time $t_d$, which is the lesser of two times: the time it takes for a droplet to move through an eddy and the time for the eddy to break apart:

$$t_d = \min\left(\frac{k_{\mathrm{sg}}}{\varepsilon_{\mathrm{sg}}}, c_{ps}\frac{k_{\mathrm{sg}}^{3/2}}{\varepsilon_{\mathrm{sg}}}\frac{1}{\left|u_i + u_i' - u_{\mathrm{dg},i}\right|}\right) \tag{C.11}$$

Here, $c_{ps}$ is an empirical constant, and $k_{\mathrm{sg}}$ and $\varepsilon_{\mathrm{sg}}$ represent the subgrid turbulent kinetic energy and its dissipation rate, respectively, which are calculated from the subgrid velocities and cell size:

$$k_{\mathrm{sg}} = \frac{1}{2} u_{\mathrm{sg},i}^2 \tag{C.12}$$

$$\varepsilon_{\mathrm{sg}} = \frac{k_{\mathrm{sg}}^{3/2}}{d} \tag{C.13}$$

## C.3. Droplet-wall interaction

Despite the short life of droplets before they evaporate, understanding how they impact surfaces is important. This model draws from the work by Naber and Reitz [144] and Gonzalez et al. [145], concentrating on the angled collision of liquid jets against a wall. It adopts a three-dimensional empirical approach, upholding the conservation of mass and momentum. According to the model, the velocity component parallel to the wall does not change, but the perpendicular velocity is critical for determining the impact's outcome. The impact behavior is classified into two regimes based on the Weber number at the moment of impact:

$$We_i = \frac{\rho_l V_n^2 d_0}{\sigma} \tag{C.14}$$

Here, $V_n$ is the velocity perpendicular to the surface. If $We_i < 80$, the droplet bounces back elastically, with the outgoing normal velocity calculated as:

$$V_{n,o} = V_{n,i}\sqrt{\frac{We_o}{We_i}} \tag{C.15}$$

The Weber number for the departing droplet ($We_o$) is determined by the following formula:

$$We_o = 0.678 We_i \exp\left(-0.04415 We_i\right) \tag{C.16}$$

This empirical formula is based on findings by Wachters and Westerling (1966) [146]. For $We_i > 80$, the model applies a jet scenario, where the droplet spreads out tangentially to the surface as a liquid sheet. The thickness of the sheet resulting from the jet's impact is described by:

$$h(\psi) = h_\pi e^{\beta(1-\psi/\pi)} \tag{C.17}$$

In this context, $h_\pi$ is the sheet's height when the droplet impacts the wall at a right angle. The sheet's thickness varies with the impingement angle $\alpha$, a parameter $\beta$, and the angle at which the droplet exits the surface. The equations for these parameters are as follows:

$$\sin\alpha = \left(\frac{e^\beta + 1}{e^\beta - 1}\right)\frac{1}{1+(\pi/\beta)^2} \quad \psi = \frac{\pi}{\beta}\ln\left[1 - n\left(1 - e^{-\beta}\right)\right] \tag{C.18}$$

Here, $n$ represents a randomly chosen number between 0 and 1.

## C.4. Droplet evaporation

The representation of the variation in radius of injected droplets plays a pivotal role in constructing a comprehensive mathematical model for sprays. Ultimately, it dictates absorbed heat by the droplets both for changing their temperature and changing their phase from liquid to gaseous, influencing the temperature in the rest of the flow and in the flame. Droplet evaporation hinges on the interplay between convective mass transfer and diffusion effects, described by the non-dimensional Sherwood number $Sh_D$. The evolution of droplet radius follows Equation C.19, a function dependent on liquid-air mass diffusivity $D$, gas-liquid density ratio $\rho_g/\rho_l$, a mass transfer coefficient scaling factor $\alpha_{\text{spray}}$, and Sherwood number $Sh_D$ [147, 148]:

$$\frac{dr_0}{dt} = -\frac{\alpha_{\text{spray}}\rho_g D}{2\rho_l r_0} B_d Sh_d \tag{C.19}$$

This expression involves the Spalding mass transfer number $B_d$, representing the normalized ratio of water vapor mass fraction $Y_1^*$ to overall vapor mass fraction $Y_1$. Frossling (1938) [148] establishes the correlation for $Sh_d$ incorporating Reynolds and Schmidt numbers under assumptions of spherical droplets, steady evaporation, and saturation vapor concentration. Accounting for the Spalding number, the correlation for $Sh_d$ is:

$$Sh_d = \left(2.0 + 0.6 Re_d^{1/2} Sc^{1/3}\right)\frac{\ln\left(1+B_d\right)}{B_d} \tag{C.20}$$

To accurately determine $Re$ and $Sc$, a valid interpolation temperature for diffusivity coefficient $D$ and gas viscosity $\mu$ is needed. Amsden et al. (1989) [147] propose $\hat{T} = \left(T_{\text{gas}} - 2T_d\right)/3$. Reynolds number considers turbulence fluctuations for each droplet in the gas flow, utilizing droplet diameter $d$ as the length scale. The Schmidt number involves

model constants $D_0$ and $n_0$ determined experimentally:

$$Re_d = \frac{\rho_{\text{gas}} \left| u_i + u_i' - v_i' \right| d}{\mu_{\text{air}}} \tag{C.21}$$

$$Sc = \frac{\mu_{\text{air}}}{1.293 D_0 (\hat{T}/273)^{n_0 - 1}} \tag{C.22}$$

After modeling droplet size evolution, thermal heat transfer to the droplet must be considered. The energy balance equation describes the temperature rate evolution, with $c_l$ as the liquid specific heat and $Q_d$ as the heat conduction rate:

$$\rho_d \frac{4}{3} \pi r^3 c_\ell \frac{dT_d}{dt} - \rho_d 4\pi r^2 R L_V = 4\pi r^2 Q_d \tag{C.23}$$

The heat transfer rate is modeled using the Ranz-Marshall correlation [149], assuming only conduction is significant. It is expressed as a function of interpolation temperature $\hat{T}$, droplet radius, Nusselt number, and a modeling constant $K_{\text{gas}}$:

$$Q_d = \frac{K_{\text{gas}} (T - T_d)}{2r} \text{Nu}_d \quad K_{\text{gas}}(\hat{T}) = \frac{K_1 \hat{T}^{3/2}}{\hat{T} + K_2} \tag{C.24}$$

Finally, the Nusselt number is determined using a correlation analogous to the Sherwood number, replacing the Schmidt number with the Prandtl number:

$$\text{Nu}_d = \left( 2.0 + 0.6 Re_d^{1/2} \text{Pr}_d^{1/3} \right) \frac{\ln(1 + B_d)}{B_d} \quad \text{Pr}_d = \frac{\mu_{\text{gas}}(\hat{T}) c_p(\hat{T})}{K_{\text{gas}}(\hat{T})} \tag{C.25}$$

For droplets smaller than a specified size, a simplified model assumes uniform temperature. For larger droplets, a more comprehensive modeling is performed following Abramzon and Sirignano (1989) [150], accounting for spherically symmetric temperature distribution and potential recirculation effects. The modified Equation 2.52 incorporates partial differentiation:

$$\begin{aligned} \rho c_p \frac{\partial T}{\partial t} &= \frac{1}{r^2} \frac{\partial}{\partial r} \left( k_{\text{eff}} r^2 \frac{\partial T}{\partial r} \right) \\ k_{\text{eff}} \frac{\partial T}{\partial r} \bigg|_{r = R_d} &= h \left( T_g - T(R_d, t) \right) + \rho L_v \frac{dR_d}{dt} \end{aligned} \tag{C.26}$$

Here, $r$ is the distance from the center, $h$ is the droplet-gas convection coefficient, $T_g$ is the gas temperature, $R_d(t)$ is the radius of the droplet, $c_p$ is the droplet specific heat, $L$ is the specific heat of evaporation, $k$ is the droplet thermal conductivity, and $T(R_d, t)$ is the surface temperature. If recirculation effects are considered, the new thermal conductivity $k_{\text{eff}} = \chi k$ is used instead of $k$, where $\chi$ is expressed as:

$$\chi = 1.86 = 0.86 \tanh \left( 2.225 \log_{10} (0.03333 Pe_d) \right) \tag{C.27}$$

Here, $Pe_d$ represents the Peclet number of the droplet.

## C.5. Collision model

The NTC method, introduced by Schmidt and Rutland [151], is the chosen strategy for modeling collisions, based on randomly selecting pairs of droplet parcels within each computational cell. Initially, these parcels are grouped by their cell, and from these groups, pairs are randomly chosen for potential collision analysis. The estimated number of collisions within a given time interval $\Delta t$ is calculated by summing the collision probabilities for all selected pairs:

$$M_{\text{coll}} = \frac{1}{2} \sum_{i=1}^{N} \sum_{j=1}^{N} \frac{V_{i,j} \sigma_{i,j} \Delta t}{V_{\text{total}}} \tag{C.28}$$

In this equation, $N$ is the number of droplets involved, and $\sigma_{i,j} = \pi(r_i + r_j)^2$ calculates the collision cross-sectional area. To better manage collision probability, a factor $qV\sigma$ is applied, where $q$ indicates the number of droplets per cell and $N_p$ the parcels in each cell. Thus, the refined formula for collision counts becomes:

$$M_{\text{coll}} = \sum_{i=1}^{\sqrt{M_{cand}}} q_i \sum_{j=1}^{\sqrt{M_{cand}}} \frac{q_j V_{i,j} \sigma_{i,j}}{(qV\sigma)_{max}} \qquad M_{cand} = \frac{N_p^2 (qV\sigma)_{max} \Delta t}{2V_{\text{total}}} \tag{C.29}$$

By simulating a fraction of the parcel population, this method enhances speed without sacrificing significant accuracy. It also helps in pinpointing pairs of parcels that are likely to collide. A collision is confirmed between parcels $i$ and $j$ if:

$$r < \frac{q_g V_{i,j} \sigma_{i,j}}{(qV\sigma)_{max}} \tag{C.30}$$

where $r$ is a random factor between 0 and 1, and $q_g$ reflects the droplet count in the path of the colliding pairs. Upon meeting this condition, a collision occurs. The nature of the collision—whether it leads to simple contact, merging, stretching, or bouncing back—is determined by the model from Post and Abraham [152], which relies on the Weber number to categorize the interaction. Further, for complex interactions, additional guidelines by Ashgriz and Poo [153] and Hou [154] are consulted to discern between coalescence, stretching, or separation.

# D

# Inlet velocity profile

The mean velocity profile for fully developed turbulent pipe flow is computed based on the studies of McKeon et al. [155][156], where velocity values are derived based on measurements taken with a Pitot probe. Using this experiment, the velocity profile is determined in relation with $y^+$ for multiple regions based on their proximity to the wall. For high Renyolds number, the authors indicate that an inner-layer scaling is given by:

$$U = f'\left(y, u_i, \nu, R\right) \tag{D.1}$$

and an outer-layer scaling by:

$$U_c - U = g'\left(y, u_0, \nu, R\right) \tag{D.2}$$

where $U$ is the mean velocity, $U_c$ is the centerline velocity and $f$ and $g$ denote functional dependencies. Furthermore, $u_i$ and $u_0$ can be taken as $u_\tau$, which is computed as:

$$u_\tau = \sqrt{\frac{\tau_w}{\rho_a}} \tag{D.3}$$

where $\tau_w$ is the wall shear stress computed as:

$$\tau_w = \frac{\lambda}{8}\rho_a U_b^2 \tag{D.4}$$

Here, $U_b$ is the bulk velocity of the inlet flow, which is equal to 200 $m/s$ in order to be consistent with the uniform velocity profile case. Furthermore, for these equation, the ambient density $\rho_a = 5.38\ kg/m^3$ and the kinematic viscosity $\nu = 8.77e-6\ m^2/s$ are taken from the LES simulation. Finally, this leads to the equation for $y^+$:

$$y^+ = \frac{y \cdot u_\tau}{\nu} \tag{D.5}$$

Thus, the regions presented by the authors consist of a power law and a logarithmic law for the inner layer and a another logarithmic law for the outer layer. These are:

$$U^+ = 8.48{y^+}^{0.142} \qquad 0 < y^+ < 300 \tag{D.6}$$

$$U^+ = \frac{1}{0.385} ln(y^+) + 4.15 \qquad 300 < y^+ < 600 \tag{D.7}$$

$$U = U_c(\frac{1}{0.421} ln(\frac{y}{r}) + 1.2) \cdot u_\tau \qquad 600 < y^+ < h/2 \tag{D.8}$$

where $U_c$ is the centerline velocity and $R^+ = \frac{h \cdot u_\tau}{\nu}$. Furthermore, for the first two, the actual velocity is calculated as $U = U^+ \cdot u_\tau$. Finally, to complete the picture, the friction factor is determined as:

$$\frac{1}{\sqrt{\lambda}} = 1.884 \cdot log(Re_D \cdot \sqrt{\lambda}) - 0.331 \tag{D.9}$$

where the diameter based Reynolds number is calculated as follows:

$$Re = \frac{\bar{U} \cdot D}{\nu} \tag{D.10}$$

The resulting velocity profile is shown in Figure D.1. Lastly, it should be mentioned that the centerline velocity was adjusted to $U = 223\ m/s$, such that the bulk velocity calculated by integrating the velocity field is equal to $U_b = 200\ m/s$.

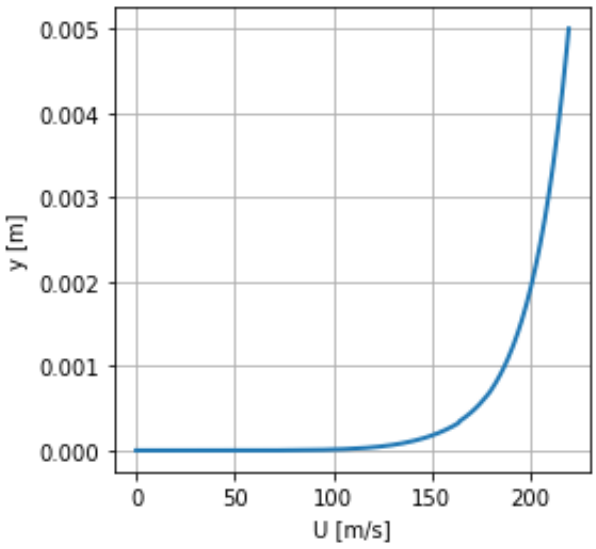


**Figure D.1:** Mean velocity profile for a fully developed pipe flow under the conditions of the LES simulation